

# Degradation of Flexible Cu(In,Ga)Se<sub>2</sub> Solar Cells

Von der Fakultät für Physik und Geowissenschaften  
der Universität Leipzig

genehmigte

D I S S E R T A T I O N

zur Erlangung des akademischen Grades

Doctor rerum naturalium

Dr. rer. nat.

vorgelegt von

Dipl.-Phys. Felix Daume

geboren am 6. Februar 1984 in Leipzig

Gutachter:

Prof. Dr. Marius Grundmann (Universität Leipzig)

Prof. Dr. Marika Edoff (Uppsala Universitet)

Tag der Verleihung:

12. Oktober 2015





# Bibliographische Beschreibung

Daume, Felix

Degradation of Flexible Cu(In,Ga)Se<sub>2</sub> Solar Cells

Universität Leipzig, Dissertation

199 S., 158 Lit., 80 Abb., 17 Tab., 2 Anhänge

## Referat:

Untersuchungsgegenstand dieser Arbeit ist die Degradation flexibler Dünnschichtsolarzellen auf Basis von Cu(In,Ga)Se<sub>2</sub> Absorbern. Zur beschleunigten Alterung unter Laborbedingungen wurden unverkapselte Solarzellen in Klimaschränken Wärme und Feuchte ausgesetzt. Die Auswirkungen von Wärme und Feuchte auf die Solarzellen wurden zunächst durch Messung von Strom–Spannungs–Kennlinien (IV) und Kapazitäts–Spannungs–Charakteristiken (CV) erschlossen. Mittels in–situ Messungen der IV–Kennlinien der Solarzellen unter Wärme und Feuchte konnte die Degradationskinetik untersucht werden. Es gelang zwei Phasen der Alterung, eine anfängliche Verbesserung und die eigentliche Degradation, zu unterscheiden. Außerdem war es dadurch möglich Degradationsraten zu bestimmen. Die Untersuchung der Stabilität der Flächenkontakte erfolgte im Schichtverbund der Solarzelle und separat. Dann wurde der Einfluss von Natrium, einem Bestandteil der Cu(In,Ga)Se<sub>2</sub> Solarzellen, untersucht. Schichtzusammensetzung, Elementprofile und Oberflächenbeschaffenheit wurden mittels Laser–induzierter Plasmaspektroskopie (LIBS), Sekundärionen–Massenspektrometrie (SIMS), Rasterelektronenmikroskopie (SEM) und 3D–Lasermikroskopie gemessen. Die Rolle von Natrium für den Degradationsprozess konnte für zwei unterschiedliche Methoden der Natriumeinbringung in den Absorber (Ko–Verdampfung, Nachbehandlung) beschrieben werden. Schließlich wurde mittels Elektrolumineszenz (EL), Thermographie (DLIT) und der Messung Lichtstrahl–induzierter Ströme (LBIC) die Degradation orts aufgelöst untersucht und Inhomogenitäten detektiert. Aus spannungsabhängigen Elektrolumineszenzaufnahmen gelang es Serienwiderstandskarten zu errechnen. Die Kombination der genannten Messmethoden erlaubte eine Identifizierung dominanter Degradationsprozesse in den flexiblen Cu(In,Ga)Se<sub>2</sub> Solarzellen unter Wärme und Feuchte. Unter anderen wurde die Degradation der Grenzfläche zwischen Absorber und Rückkontakt diskutiert. Die Degradationskinetik konnte beschrieben, Solarzellebensdauern abgeschätzt, die für die Wärme–Feuchte–Stabilität nachteilige Wirkung von Natrium identifiziert und laterale Inhomogenitäten des Degradationsprozesses aufgezeigt werden. Aus der Diskussion der Ergebnisse wurden Vorschläge zur Verbesserung der Wärme–Feuchte–Stabilität abgeleitet.



# Contents

<b>1</b>	<b>Introduction</b>	<b>1</b>
1.1	Motivation . . . . .	1
1.2	Solar Cells . . . . .	2
1.2.1	Materials & Technologies . . . . .	3
1.2.2	Electrical Characteristics . . . . .	6
1.3	Cu(In,Ga)Se <sub>2</sub> Solar Cells . . . . .	9
1.3.1	Cell Design . . . . .	9
1.3.2	The Absorber . . . . .	11
1.3.3	The Role of Sodium . . . . .	16
1.3.4	CIGSe Deposition Techniques . . . . .	18
<b>2</b>	<b>Degradation of Cu(In,Ga)Se<sub>2</sub> Solar Cells: A Literature Survey</b>	<b>21</b>
2.1	Introduction . . . . .	21
2.2	Degradation Conditions . . . . .	26
2.3	Molybdenum Degradation . . . . .	27
2.4	CIGSe Degradation . . . . .	27
2.4.1	Experimental Limitations . . . . .	27
2.4.2	Intrinsic CIGSe Stability . . . . .	28
2.4.3	Extrinsic CIGSe Stability . . . . .	29
2.4.4	Chemical Changes in the Absorber . . . . .	30
2.4.5	Gallium Content . . . . .	30
2.4.6	Sodium Content . . . . .	31
2.5	Buffer Degradation . . . . .	32
2.6	TCO Degradation . . . . .	32
2.7	Influence of the Grid . . . . .	33
2.8	Pn-Junction Changes and Device Behavior . . . . .	35
<b>3</b>	<b>Experimental Methods</b>	<b>39</b>
3.1	Roll-to-Roll Fabrication . . . . .	39
3.2	Characterization . . . . .	40
3.2.1	Current-Voltage Measurements (IV) . . . . .	41
3.2.2	Electroluminescence Imaging (EL) . . . . .	42
3.2.3	Voltage-Dependent Electroluminescence (EL(V)) . . . . .	43

3.2.4	Capacitance–Voltage Measurements (CV)	45
3.2.5	Lock–in Thermography (LIT)	46
3.2.6	Light Beam Induced Current (LBIC)	46
3.2.7	Hall Measurements	47
3.2.8	Transfer Length Measurements (TLM)	47
3.2.9	Scanning Electron Microscopy (SEM)	49
3.2.10	Secondary Ion Mass Spectrometry (SIMS)	49
3.2.11	Laser Induced Breakdown Spectroscopy (LIBS)	50
3.2.12	Scanning Laser Microscopy	51
3.3	Sample Treatment	51
3.3.1	Damp Heat	51
3.3.2	Dry Heat	52
3.3.3	Damp Heat & in–situ IV	52
<b>4</b>	<b>Cu(In,Ga)Se<sub>2</sub> Solar Cells under Damp Heat</b>	<b>53</b>
4.1	Dry versus Damp Heat or the Role of Humidity	53
4.2	Damp Heat	54
4.2.1	Statistics on Electrical Parameters	54
4.2.2	Low–temperature Current–Voltage Characteristics	56
4.2.3	Capacitance–Voltage Characteristics	58
4.3	Degradation Kinetics	59
4.3.1	In–situ Current–Voltage Measurements	60
4.3.2	Kinetics	61
4.3.3	Two Stages	64
4.3.4	Degradation Rates	65
4.4	Planar Contacts	68
4.4.1	Back–Electrode (Mo)	69
4.4.2	Front–Electrode (ZnO:Al)	71
<b>5</b>	<b>The Influence of Sodium</b>	<b>75</b>
5.1	Characterized by LIBS	75
5.2	Electron Microscopy Images	77
5.2.1	Before Damp Heat	77
5.2.2	After Damp Heat	79
5.3	Introduced by Co–Evaporation	84
5.3.1	IV vs. Damp Heat	84
5.3.2	IV vs. Sodium	86
5.3.3	Optimization of the Sodium Content	89
5.4	Introduced by Post–Deposition	92
5.5	Depth Distribution	96
5.6	Surface Roughness	99

---

<b>6</b>	<b>Lateral Inhomogeneities</b>	<b>103</b>
6.1	Electroluminescence Imaging . . . . .	103
6.1.1	EL vs. Damp Heat . . . . .	103
6.1.2	EL vs. Sodium . . . . .	104
6.2	Differential Diagnosis with Different Imaging Techniques . . . . .	107
6.2.1	Shunt . . . . .	107
6.2.2	Severe Shunt . . . . .	110
6.2.3	Corrosion . . . . .	111
6.3	Mapping the Local Series Resistance . . . . .	113
6.3.1	Voltage-Dependant Electroluminescence . . . . .	115
6.3.2	Calculation Method by Hinken et al. . . . .	116
6.3.3	Calculation Method by Breitenstein et al. . . . .	116
6.3.4	Application of Breitenstein's Method after Damp Heat . . . . .	117
<b>7</b>	<b>Discussion</b>	<b>119</b>
7.1	Influence of Damp Heat . . . . .	119
7.1.1	Morphology & Roughness . . . . .	119
7.1.2	Fill Factor and Series Resistance . . . . .	120
7.1.3	The Role of Humidity during Damp Heat . . . . .	120
7.1.4	Appearance of a Roll-over in the IV Characteristic . . . . .	121
7.1.5	New Interpretation of the CV measurements . . . . .	122
7.1.6	The role of the planar contacts . . . . .	125
7.1.7	Kinetics . . . . .	126
7.1.8	Lifetime Assessment . . . . .	129
7.2	Influence of Sodium . . . . .	130
7.2.1	Surface Roughness . . . . .	132
7.2.2	Sodium Depth Distribution . . . . .	133
7.2.3	Electrical Degradation . . . . .	134
7.2.4	Origin of the Degradation . . . . .	135
7.3	Lateral Inhomogeneities During Degradation . . . . .	138
7.3.1	Electroluminescence Imaging . . . . .	138
7.3.2	Differential Diagnosis with Different Imaging Techniques . . . . .	139
7.3.3	Series Resistance Mapping . . . . .	140
7.4	Conclusions . . . . .	144
7.4.1	Theses . . . . .	144
7.4.2	Outlook . . . . .	147
<b>8</b>	<b>Summary</b>	<b>151</b>
<b>A</b>	<b>Solar Cell Data</b>	<b>153</b>

<b>B List of Publications</b>	<b>157</b>
B.1 Research Articles (own and contributed work) . . . . .	157
B.2 Posters (only own) . . . . .	160
B.3 Talks (only own) . . . . .	161
<b>Bibliography</b>	<b>163</b>
<b>Abbreviations &amp; Symbols</b>	<b>177</b>
<b>Acknowledgement</b>	<b>187</b>
<b>Curriculum Vitae</b>	<b>189</b>
<b>Selbstständigkeitserklärung</b>	<b>191</b>

# 1 Introduction

## 1.1 Motivation

At the beginning of the twenty-first century, after sixty years of research, development and small scale production, photovoltaic energy conversion has reached the mass market. Modules are produced in the range of gigawatts (peak) per year and the share of electric energy from photovoltaics is within the range of a few percent of the total annual electricity production in multiple industrialized countries.

While the majority of the market today is based on silicon solar cells,  $\text{Cu(In,Ga)Se}_2$  (CIGSe) solar cells recently gained market share. The latter are based on thin films and can be fabricated on flexible substrates. Since CIGSe solar cells are thinner than human hair, exciting new applications compared to brittle/rigid silicon solar cells are possible. Flexible photovoltaic products become viable and, at the same time, the high specific power (power per weight) allows the application on low-load roofs that may otherwise not allow to harness sunlight via photovoltaics.

As the CIGSe technology matures to production on an industrial scale, its long-term stability becomes increasingly important. Each photovoltaic module loses power over time. The causes for this degradation are manifold and technology-specific. However, increasing the long-term stability by understanding and lowering the degradation of a photovoltaic module is a key strategy for the success of a photovoltaic technology. The electric yield and thus also the revenue of a photovoltaic system depends on the initial power conversion efficiency and its development over time, i.e. its long-term stability (besides the irradiation on the system, of course).

Subject of this thesis is the understanding of the degradation of flexible CIGSe solar cells. While many environmental influences (e.g. UV irradiation, temperature cycles, mechanical load) are known to be detrimental for solar modules, it is known from previous studies that humidity is the most severe threat to a module containing CIGSe solar cells. While the encapsulation within a module is the standard strategy to avoid damage to the solar cells from humidity, it is desirable to increase the long-term stability of the solar cells itself. On the one hand, this is motivated by the cost of the encapsulation, on the other hand does saving on encapsulation and module complexity potentially also yield lower weight and even more flexible products. Therefore, only unencapsulated flexible CIGSe solar cells are studied in this thesis.

Omitting the encapsulation already accelerates the degradation process of the CIGSe solar cell compared to its degradation within a module. Yet, accelerated lifetime tests

are necessary in order to study the degradation behavior within a reasonable amount of time. In this thesis, damp heat testing is used to study the degradation behavior of CIGSe solar cells with respect to humidity as an environmental threat.

The samples studied are flexible Cu(In,Ga)Se<sub>2</sub> solar cells, deposited on flexible plastic substrates. They were fabricated by the company *Solarion AG* in an industrial pilot-production. In order to understand the degradation of these solar cells under damp heat, first, the severity of the degradation will be assessed (physical damage/degradation in the electrical parameters). Subsequently, it will be subject of investigation to identify drivers of the degradation and to study how the degradation proceeds. Furthermore, the role of sodium, which is an important ingredient to CIGSe solar cells, will be studied with respect to the degradation process. Since the individual solar cells investigated have an area of almost 60 cm<sup>2</sup> and are thus fairly large compared to typical laboratory solar cells ( $\approx 1$  cm<sup>2</sup>), the lateral homogeneity of the degradation will be studied as well. Finally, strategies to improve the damp heat stability of the flexible CIGSe solar cells will be derived.

This thesis is divided into eight chapters. While this chapter focuses on fundamentals of solar cells in general and Cu(In,Ga)Se<sub>2</sub> solar cells in particular, a literature review in chapter 2 provides a detailed background about the degradation of Cu(In,Ga)Se<sub>2</sub> solar cells. Chapter 3 describes sample preparation, characterization and accelerated lifetime treatment. Subsequently, three chapters present experimental findings. Chapter 4 gives insights on the influence of damp heat on flexible Cu(In,Ga)Se<sub>2</sub> solar cells and the kinetics of the degradation process. The role of sodium (from the CIGSe absorber) in the degradation process is discussed in chapter 5. Experimental results from imaging techniques that allow to reveal lateral inhomogeneities in the degradation process are presented in chapter 6. All results are discussed in chapter 7 and reviewed in the context of the literature. The conclusions of the discussion are summarized in the form of theses in section 7.4.1 and an outlook is given in section 7.4.2. Chapter 8 summarizes all findings of this dissertation.

## 1.2 Solar Cells

Solar cells are devices designed to absorb the electromagnetic energy carried by photons into chemical energy and to subsequently convert this chemical energy into the electrical energy of charge carriers, thus creating a current and a voltage. Despite of other realizations<sup>1</sup>, today, all common types of solar cells, such as silicon and thin film solar cells (an overview is given in the following section 1.2.1), are realized as pn-junctions in semiconductors<sup>2</sup>.

Electrons in a semiconductor may be excited to higher energy levels under illumination.

---

<sup>1</sup>A detailed description of the physics of solar cells may be found in the book of Peter Würfel [1].

<sup>2</sup>A comprehensive overview on semiconductor physics is given in the book of Marius Grundmann [2].



If the energy of the incident photons is greater than the band gap of the semiconductor, electrons may be lifted above the band gap, i.e. from the valence to the conduction band, leaving a hole in the valence band and thus creating an electron–hole–pair. In order to harness the absorbed energy, electrons and holes need to be separated. In thermodynamic equilibrium (solar cell in the dark), the gradient of the electrochemical potential is zero, the Fermi level is equal throughout the pn–junction, thus the total current (diffusion and drift) is zero (figure 1.1(a)). On the other hand, under illumination, the Fermi level splits up into quasi Fermi levels for the n- and the p–region (figure 1.1(b)). In this non–equilibrium situation, electrons drift towards the n–part of the junction and holes towards the p–part of the junction. The potential difference is measurable as a voltage between the open clamps of the solar cell and when applying a load, a current will be driven by the solar cell.

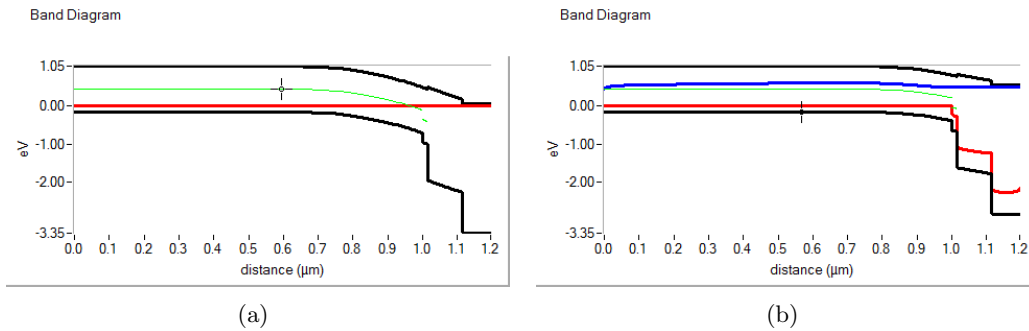


Figure 1.1: Band diagram of a pn–junction (a) in thermodynamic equilibrium (in the dark) with equilibrium Fermi level in red and (b) in the non–equilibrium state (under  $1000 \text{ W/m}^2$  illumination and  $0.5 \text{ V}$  forward bias) with electron Fermi level in blue and hole Fermi level in red. The upper black line depicts the conduction band edge and the lower black line the valence band edge. Based on a SCAPS [3] simulation with the parameter set “example CIGS” included in the software.

### 1.2.1 Materials & Technologies

Since the first solar cell based on a pn–junction was published in 1954 [4], various concepts were developed and different photovoltaic technologies emerged.

The by far largest share of all solar cells produced today is made of mono- or polycrystalline (lateral grain sizes in the centimeter–range) silicon (cf. figure 1.2). The industrial manufacturing process of these first generation solar cells is very well established and takes place on the scale of gigawatts (peak) per year  $\text{GW}_P/\text{y}$ . However, the production of a silicon solar cell has a fairly high energy consumption: In a first step, solar

grade silicon needs to be purified as a raw material from  $\text{SiO}_2$  at very high temperatures. In a second step, wafers have to be sawed from blocks of polycrystalline silicon or ingots of monocrystalline silicon under significant sawing losses. Subsequently the wafers are processed (doping, passivation, metallization, anti-reflex coating) to solar cells. Since silicon is an indirect semiconductor, wafer thicknesses of approximately  $200\ \mu\text{m}$  are used in order to absorb sufficient photons.

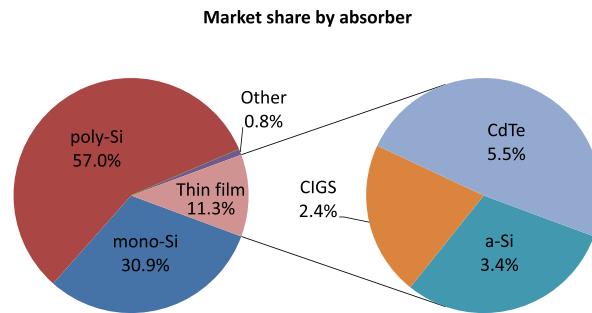


Figure 1.2: Market share of different solar cell technologies in 2011 [5].

Second generation solar cells include the most common inorganic thin film technologies. Semiconductors with direct bandgaps, such as CIGSe or cadmium telluride (CdTe), have higher absorption coefficients thus allowing to use thin absorbers in the micrometer range. Substrates are needed because of the low mechanical stability of the thin absorber layers. Glass is a common choice for rigid devices, flexible thin film solar cells are deposited on metal or plastic foils. Cost reduction potential originates from the inherently lower material consumption as well as from lower demands on the crystal quality since diffusion lengths may be shorter due to the small distances between the point of charge carrier generation and the contacts in the thin film solar cell. Thus, polycrystalline absorber layers with high defect densities in the band gap may be tolerated (compared to the two orders of magnitude thicker silicon solar cells). Deposition techniques yielding the highest efficiencies are vacuum based processes, such as co-evaporation of the constituent elements, sequential deposition of precursors and thermal annealing (rapid thermal processing), sputtering, metal organic chemical vapor deposition, plasma enhanced chemical vapor deposition or atomic layer deposition. Non-vacuum processes include electrodeposition, chemical bath deposition, spraying and screen-printing<sup>3</sup>.

---

<sup>3</sup>An overview on various thin film deposition techniques is given in the book of Poortmans and Arkhipov [6]

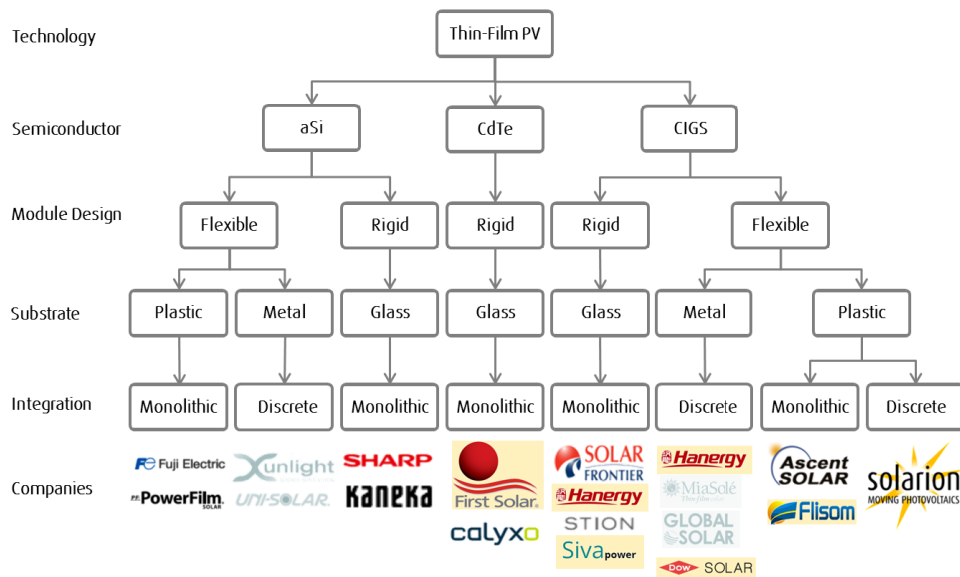


Figure 1.3: Thin film photovoltaic technologies and selected manufacturers (image source: *Solarion AG*).

As illustrated in figure 1.3, thin film photovoltaics has brought up a variety of companies with different approaches in absorber deposition, substrate choice and module design. An overview specifically on the different CIGSe deposition processes is given in section 1.3.4. A list of champion efficiencies for the solar cell technologies that currently dominate the market (figure 1.2) is given in table 1.1.

Third generation solar cells utilize sophisticated inorganic cell concepts or absorbers made from organic materials. Examples for the latter are dye-sensitized solar cells<sup>4</sup> with efficiencies up to 11.9% [8] and organic solar cells, currently reaching 10.7% [8] efficiency. A different approach for inorganic solar cells is the stacking of two, three or more solar cells to create a double, triple or multi junction solar cell. The individual solar cells have different band gaps (e.g. 0.7 eV, 1.1 eV and 1.7 eV) yielding optimized absorption for different photon energies. Thus a multi-junction-solar cell can overcome the Shockley-Queisser limit<sup>5</sup>. The highest efficiency of 37.9% [8] is currently reached with a InGaP/GaAs/InGaAs triple junction solar cell. Solar cells with these sophisticated structures are fairly expensive, thus, their application is often limited to satellites or terrestrial concentrator photovoltaics (where even higher efficiencies may be reached

<sup>4</sup>Also called “Grätzel cell”, named after its inventor Michael Grätzel [7].

<sup>5</sup>The Shockley-Queisser limit is the maximum efficiency for a solar cell that is only limited by radiative recombination [9]. For a single-junction solar cell under terrestrial AM1.5g spectrum a band gap of approximately 1.4 to 1.5 eV is favorable, yielding an efficiency of  $\approx 33\%$ .

Technology	Efficiency [%]	Cell Area	Reference
mono-Si	25.6	143.70 cm <sup>2</sup> (da)	[8]
CIGSe (glass)	21.7	0.50 cm <sup>2</sup>	[10]
CIGSe (polyimide)	20.4	0.52 cm <sup>2</sup> (ap)	[11]
CdTe (glass)	20.4	0.48 cm <sup>2</sup> (da)	[8]
poly-Si	20.4	1.00 cm <sup>2</sup> (ap)	[8]
a-Si	10.1	1.04 cm <sup>2</sup> (ap)	[8]

Table 1.1: Champion (maximum conversion) efficiencies of different single junction solar cell technologies as of September 2014. These efficiencies were mostly demonstrated on small areas.

by concentrating the sunlight to several hundred suns).

### 1.2.2 Electrical Characteristics

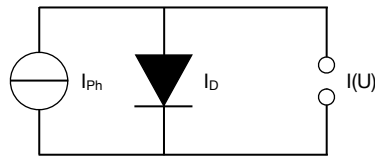


Figure 1.4: Equivalent circuit of an ideal solar cell, consisting of a current source ( $J_{Ph}$ ) and a diode ( $J_D$ ) in parallel.

The electrical behavior of an ideal solar cell under normal operating conditions (DC stimulation) can be described by an equivalent circuit of a current source and a diode (figure 1.4). The current-voltage (IV) characteristic of this parallel circuit of a current source ( $J_{Ph}$ ) and a diode ( $J_D$ ) is described by equation 1.1.

$$J(V) = J_0 \left( \exp \left( \frac{eV}{nkT} \right) - 1 \right) - J_{Ph} = J_D - J_{Ph} \quad (1.1)$$

It represents the IV characteristic of a diode with dark saturation current (density)  $J_0$  and an ideality  $n$ , i.e. the Shockley equation, shifted by the photo current density  $J_{Ph}$ . The latter is called superposition principle.

In a real solar cell, however, loss mechanisms are present that are not represented by the simple equivalent circuit of the ideal solar cell. A common approximation of the real solar cell is given as equivalent circuit in figure 1.5 and described by equation 1.2.

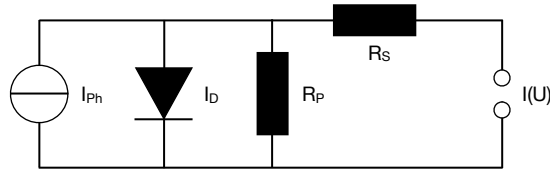


Figure 1.5: Equivalent circuit of a real solar cell, consisting of a current source ( $J_{Ph}$ ), a diode ( $J_D$ ) and a shunt resistor ( $R_P$ ) in parallel, as well as a resistor in series ( $R_S$ ).

$$J(V) = J_0 \left( \exp \left( \frac{e(V - J(V)R_S)}{nkT} \right) - 1 \right) + \frac{V - J(V)R_S}{R_P} - J_{Ph} \quad (1.2)$$

This model extends the equivalent circuit of the ideal solar cell by a shunt resistor  $R_P$  in parallel to the diode (thus also called “parallel resistance”), representing internal losses such as leakage currents through shunts. The additional resistance in series  $R_S$  accounts for ohmic losses, e.g. by current flow through the contacts. The influence of  $R_S$  and  $R_P$  in the IV curve is illustrated in figure 1.6. Either high series resistances or low parallel resistances are detrimental for the fill factor (defined below).

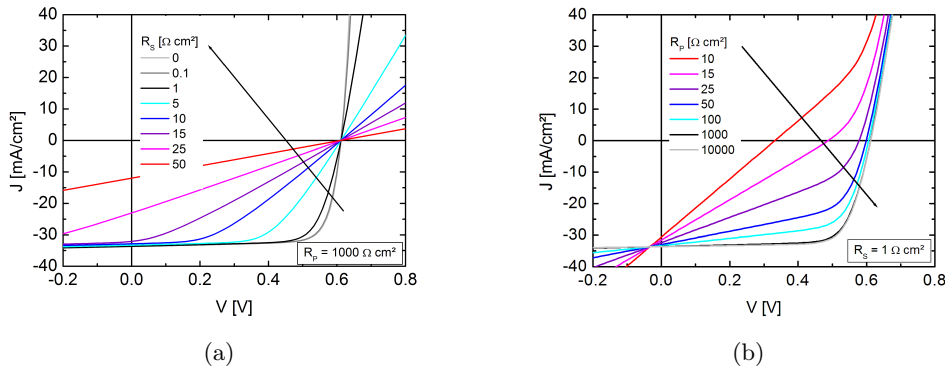


Figure 1.6: Influence of the (a) series resistance  $R_S$  and the (b) parallel (shunt) resistance  $R_P$  on the IV characteristic of a solar cell. Based on a SCAPS [3] simulation with the parameter set “Numos CIGS baseline” included in the software under standard test conditions.

Other features that IV characteristics of some CIGSe solar cells exhibit, such as voltage dependant carrier collection (i.e. photocurrent depending on the voltage) or current blocking effects (e.g. “roll-over” and “red kink”), may be explained by different equiva-

lent circuits [12]. Unless stated otherwise all solar cells in this thesis will be treated with the model in figure 1.5 and their IV characteristics fitted according to equation 1.2.

For better comparability, independent of the area  $A$  of the solar cell, current ( $I$ ) densities  $J = I/A$  are used here instead of currents. “Standard test conditions” are commonly used, to ensure comparability between different measurement stations for IV testing: Solar cells under test shall be kept at a temperature of 25 °C, under an illumination of 1000 W/m<sup>2</sup> with an “AM1.5” spectrum<sup>6</sup>. The latter corresponds to the terrestrial spectrum of the sun under an angle of 41.8° above the horizon. Experimental details about the IV measurement are given in section 3.2.

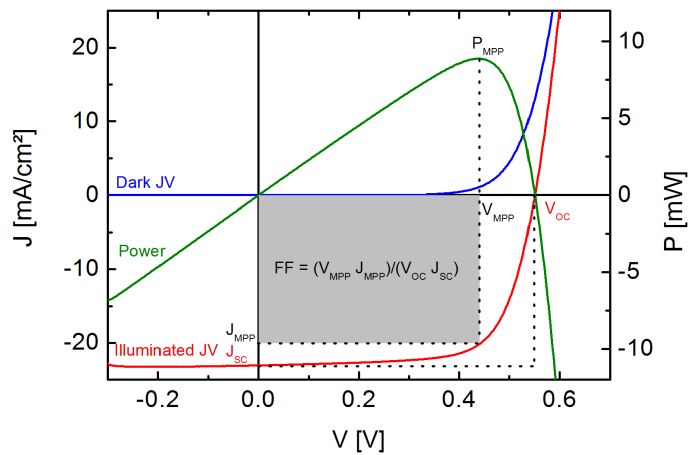


Figure 1.7: Determination of IV parameters from IV (JV) curves

Figure 1.7 shows an IV characteristic and the IV parameters that are typically extracted to describe the electrical behavior of the solar cell. Without a load ( $J = 0$ ), one obtains the open circuit voltage  $V_{OC}$ . If the cell is short-circuited ( $V = 0$ ), the short circuit current density  $J_{SC}$  can be measured. The power  $P$  of the solar cell is the product of voltage and current.

$$P(V) = -V \cdot J(V) \cdot A \quad (1.3)$$

The favorable operating point of the solar cell is at maximum power, i.e. the maximum power point  $P_{MPP}$ . The respective voltage and current density are denoted as  $V_{MPP}$  and  $J_{MPP}$ . A measure for the quality of the solar cell or the squareness of the IV curve,

<sup>6</sup>The notation “AM $x$ ” (air mass  $x$ ) is derived from the angle  $\gamma$  of the sun above the horizon:  $x = 1/\sin \gamma$  [2]. Without the absorption by earth’s atmosphere (e.g. water, ozone, carbon dioxide) the spectrum would be close to a black body at 5800 K and be denoted as “AM0”.

respectively, is obtained by dividing the maximum power by the product of the open circuit voltage and the short circuit current (as illustrated in figure 1.7). This ratio is called fill factor  $FF$ .

$$FF = \frac{P_{MPP}}{V_{OC}J_{SC}A} = \frac{V_{MPP}J_{MPP}}{V_{OC}J_{SC}} \quad (1.4)$$

The power conversion efficiency  $\eta$  of the solar cell describes the fraction of the sunlight that is converted to electricity. Hence it is calculated as the ratio of the maximum power of the solar cell  $P_{MPP}$  to the incident optical power  $P_{opt}$  (illumination).

$$\eta = \frac{P_{MPP}}{P_{opt}} \quad (1.5)$$

## 1.3 Cu(In,Ga)Se<sub>2</sub> Solar Cells

### 1.3.1 Cell Design

All Cu(In,Ga)Se<sub>2</sub> solar cells share a typical design. While the deposition methods for the individual layers vary, the order of the functional layers of a CIGSe thin film solar cell are typically the same (figure 1.8) and their thicknesses similar.

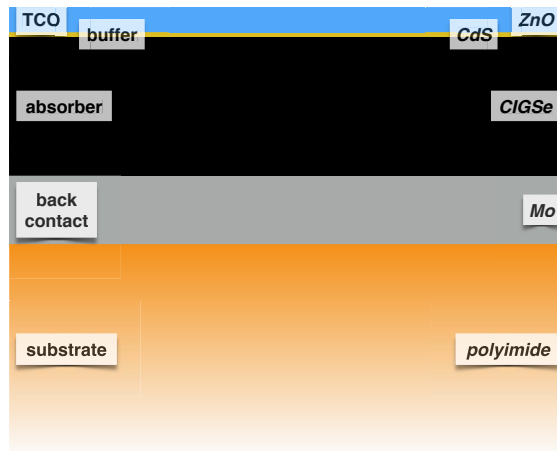


Figure 1.8: Example of a Cu(In,Ga)Se<sub>2</sub> solar cell: layer-stack of a flexible solar cell by Solarion AG (not to scale).

Since the thin film layer stack is not self-sustaining, a **substrate** is needed for the deposition of all subsequent layers. Glass is the standard rigid substrate and in order to provide sodium for the CIGSe absorber (the reason is explained in section 1.3.3), soda-lime glass is the most common material used. Foils out of polyimide, titanium

or steel serve as flexible substrates for specific applications that either require products (modules) with flexibility or low specific weight ( $\text{kg}/\text{m}^2$ ).

The metallic **back contact** of a CIGSe solar cell typically consists of molybdenum. It provides sufficient lateral conductivity for the current generated by the solar cell to be collected and may form an ohmic contact with the CIGSe absorber layer. The Mo layer with an approximate thickness of  $1\ \mu\text{m}$  is typically sputter-deposited. In order to adjust this back contact for better adhesion to the substrate, lateral conductivity, adhesion and ohmic behavior towards the CIGSe layer and sometimes sodium supply (see section 1.3.3), it is often deposited as a multi-layer stack of molybdenum or Mo–alloyed layers in multiple sputter steps.

Subsequently, the  $\text{Cu}(\text{In,Ga})\text{Se}_2$  light-absorbing layer is deposited. In the **absorber**, electrons and holes are separated by incoming photons, contributing the main share of the photo current. It needs to be only 1 to  $2\ \mu\text{m}$  thick (as explained in section 1.3.2) and many techniques have been developed for its deposition (section 1.3.4). Structural properties, existing phases and point defects of this semiconductor are described in section 1.3.2.

A cadmium sulfide (CdS) layer serves as **buffer** on top of the CIGSe absorber. The 30 to 80 nm thick layer is typically deposited in a chemical bath. CdS is an n–type semiconductor, thus serves as the n–part of the pn–heterojunction. Furthermore, the wet chemical process reduces oxidic surface contaminations that may occur after handling the CIGSe absorber in air. The CdS layer reduces the surface roughness and protects from damage during subsequent sputter processes. Additionally, CdS promotes the lattice matching between CIGSe and the transparent conductive oxide (TCO).

Since the top layer of the solar cell needs to collect current laterally (“**front contact**”) and to be transparent (“window layer”) in order to allow photons to reach the absorber, it is made of a transparent conductive oxide (TCO) with a sufficiently large band gap and conductivity. It is typically a bilayer structure to fulfill two purposes.

First, an insulating intrinsic zinc oxide (i-ZnO) layer is sputter deposited (approximately 50 nm). It reduces the severeness of potential shunts (between front contact and back contact through pin–holes in the absorber layer) and, thus, also reduces local inhomogeneities in the absorber thickness. An increase of the series resistance of the solar cell is accepted. The band gap of zinc oxide is approximately 3.4 eV.

Second, a conductive aluminum doped zinc oxide (ZnO:Al) layer is sputter deposited (0.15 to  $1\ \mu\text{m}$ ). This layer is highly n–doped and provides the lateral conductivity in the front contact. The thickness of the ZnO:Al is adjusted to the purpose of the solar cell: For high single cell efficiencies (“champion cells”), a thin TCO reduces light absorption losses and thus increases the photo current whereas for modules (large areas, thus higher currents), a thicker TCO is deposited to reduce ohmic losses.

A different strategy in optimizing the TCO thickness with respect to this trade–off between absorption loss and ohmic loss is an additional **metallic grid** on top on the solar cell. While adding some shading, thus reducing the photo current slightly, it significantly



improves the current collection from the front contact and hence allows to reduce the thickness of the TCO. The concurrent gain from better absorption over-compensates the losses from shading and, in total, increases the current. The grid may be applied via evaporation through a shadow mask or via screen-printing.

Regardless of the type of interconnection between individual solar cells to create a module (either monolithically interconnected or as a single cell approach), an electric contact to the back-electrode has to be realized. The top layers, down to the Mo back contact, may either be removed mechanically, i.e. by scribing with a needle or similar tool for ablation, or by a laser scribing, i.e. by chipping off material with suitable laser frequencies and fluences.

### 1.3.2 The Absorber

#### Crystal Structure

$\text{CuInSe}_2$  (CISE) and  $\text{CuGaSe}_2$  (CGSe), as well as their alloys  $\text{Cu}(\text{In}_{1-x}\text{Ga}_x)\text{Se}_2$  with varying gallium content  $x$ , are I–II–VI<sub>2</sub> compound semiconductors<sup>7</sup>. Their chalcopyrite crystal structure is depicted in figure 1.9(a). Chalcopyrite I–II–VI<sub>2</sub> compound semiconductors include all alloys of  $(\text{Cu},\text{Ag})(\text{Al},\text{Ga},\text{In})(\text{S},\text{Se},\text{Te})_2$ .

Since In and Ga are on the same sublattice in  $\text{Cu}(\text{In},\text{Ga})\text{Se}_2$ , for simplicity, phases and doping will be discussed for  $\text{CuInSe}_2$  in the following.

#### Phases

Due to the number of constituent elements  $\text{CuInSe}_2$  has a variety of possible defects and phases. A common representation of the actual ternary phase diagram between Cu, In and Se is the reduction to a pseudo-binary phase diagram along the tie line between  $\text{Cu}_2\text{Se}$  and  $\text{In}_2\text{Se}_3$ . The phase diagram with proper Cu ratios for photovoltaic applications is given in figure 1.9(b). Four different phases exist in that region of the phase diagram:  $\alpha$ -phase ( $\text{CuInSe}_2$ ),  $\beta$ -phase ( $\text{CuIn}_3\text{Se}_5$ ),  $\delta$ -phase (“high temperature phase”, zinc blende) and  $\text{Cu}_{2-y}\text{Se}$ . The  $\beta$ -phase may be seen as a defect phase of the chalcopyrite structure, i.e. assembled from ordered pairs of copper vacancies ( $\text{V}_{\text{Cu}}$ ) and indium on copper antisites ( $\text{In}_{\text{Cu}}$ ). Similarly, the  $\text{Cu}_{2-y}\text{Se}$  may be seen as chalcopyrite structure assembled from copper on indium antisites ( $\text{Cu}_{\text{In}}$ ) and copper interstitials ( $\text{Cu}_{\text{i}}$ ). The transition from the  $\alpha$ -phase to the  $\delta$ -phase is a rearrangement of the cation sublattice (Cu, In) [14].

At room temperature, the for photovoltaic applications desirable  $\alpha$ -phase of  $\text{CuInSe}_2$  expands only over a fairly narrow range of 24.5 to 25.0% of Cu along the  $\text{Cu}_2\text{Se}$ – $\text{In}_2\text{Se}_3$  tie line. Remarkably, this preferred composition is below the stoichiometric point of

<sup>7</sup>A more detailed overview about the  $\text{Cu}(\text{In},\text{Ga})\text{Se}_2$  absorber may be found in my diploma thesis [13], which this section is based on, or in books [6, 12, 14].

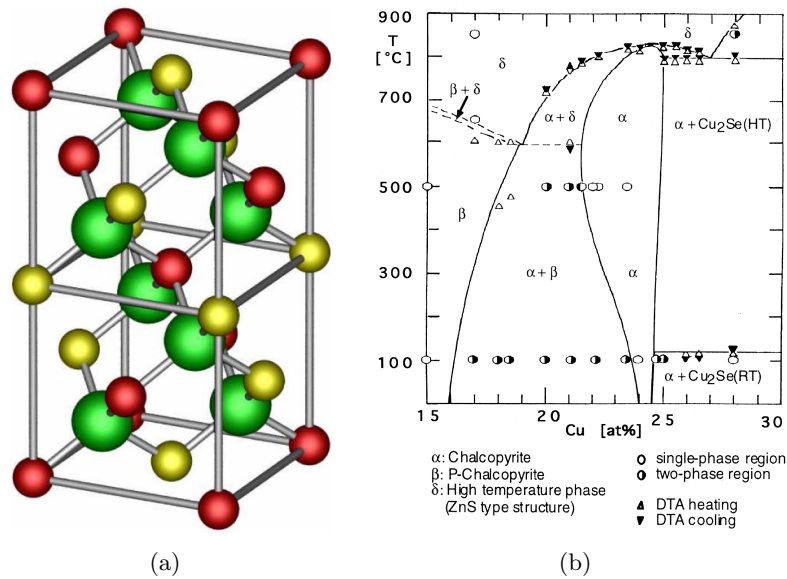


Figure 1.9:  $\text{CuInSe}_2$ : (a) schematic illustration of the chalcopyrite crystal structure (unit cell; Cu atoms in red, In atoms in yellow, Se atoms in green) [2] (b) pseudo-binary phase diagram along the tie line between  $\text{Cu}_2\text{Se}$  and  $\text{In}_2\text{Se}_3$  of the ternary compound [15]

25% copper. In fact, typical copper contents for  $\text{CuInSe}_2$  absorbers are between 22 to 24%, thus during deposition (at temperatures above 400 °C) the material is purely  $\alpha$ -phased and only after cooling down to room temperature the absorber drops into the  $\alpha + \beta$ -phase region with a tendency to phase segregation. However, if indium is partly substituted by gallium, i.e. in  $\text{Cu}(\text{In,Ga})\text{Se}_2$ , or if sodium is added during growth, the  $\alpha$ -phase is broader [16].

Absorbers with more than 25% of copper tend to segregate into an  $\alpha$ -phase and  $\text{Cu}_{2-y}\text{Se}$  regions. The metallic behavior of the latter can cause shunts in the CIGSe solar cell, thus a copper rich stoichiometry is less favorable for CIGSe solar cells. On the other hand, the  $\beta$ -phase is slightly n-conductive, thus too low copper contents are also not favorable since the whole absorber may lose its p-conduction [17].

## Defects & Doping

Due to the polycrystalline nature of all commercially used CIGSe absorbers higher dimensional structural defects, such as dislocations and stacking faults, are of minor importance within the grains and only one dimensional defects, i.e. point defects, will be discussed. Given the three constituent elements as well as the possibility of a vacancy

Position Element	Cu	In	Se	i
Cu		$\text{Cu}_{\text{In}}$	$\text{Cu}_{\text{Se}}$	$\text{Cu}_i$
In	$\text{In}_{\text{Cu}}$		$\text{In}_{\text{Se}}$	$\text{In}_i$
Se	$\text{Se}_{\text{Cu}}$	$\text{Se}_{\text{In}}$		$\text{Se}_i$
V	$\text{V}_{\text{Cu}}$	$\text{V}_{\text{In}}$	$\text{V}_{\text{Se}}$	

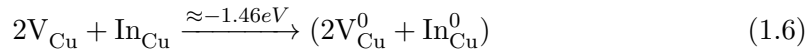
Table 1.2: Point defects in the  $\text{CuInSe}_2$  lattice. Elements are denoted as in the periodic table, “V” is a vacancy and “i” means interstitial. Antisites, e.g. indium on copper site, are denoted as  $\text{In}_{\text{Cu}}$ . Electronically, the point defects create acceptors (white table cells) or donors (grey table cells). The selenium vacancy  $\text{V}_{\text{Se}}$  may either be donor or acceptor.

and an interstitial, 12 point defects are possible in CISE (table 1.2).

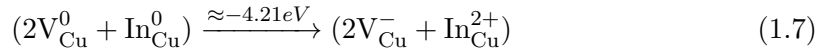
As mentioned in the previous section, CISE absorbers are typically grown copper poor, hence point defects may be expected in the lattice. Assuming a copper content of 24% and a density of  $41.3 \text{ atoms/nm}^3$  (in the case of CISE [15]), a point defect density of  $4 \times 10^{20}/\text{cm}^3$  can be expected, which is orders of magnitude above measured net doping concentrations ( $10^{16}$  to  $10^{17} \text{ 1/cm}^3$ ) and above an acceptable density of recombination centers for photovoltaic applications.

Nonetheless, extrinsic doping is uncommon for CISE solar cells, instead, intrinsic doping via point defects is the standard approach for doping. Since p-type absorbers are grown copper poor under selenium over-pressure, and absorbers grown copper rich but selenium deficient tend to be n-type [17, 18, 19], the copper vacancy  $\text{V}_{\text{Cu}}$  is held for the main acceptor in CISE and the selenium vacancy  $\text{V}_{\text{Se}}$  for the main donor (in n-type CISE or the main compensating donor in p-type CISE). In copper poor CISE, the formation energy of  $\text{V}_{\text{Cu}}$  is actually slightly below zero [20], i.e. the spontaneous formation of copper vacancies, causing a shallow acceptor ( $\approx 30 \text{ meV}$ ) in the band gap, is possible. The energetic positions of the point defects are listed in table 1.3.

One of the most important features of the defect physics in CISE is the formation of defect pairs or defect complexes. The formation of



and its charging



is energetically favorable. Even the interaction between two defect pairs is possible. A defect complex of two pairs of  $(2\text{V}_{\text{Cu}}^- + \text{In}_{\text{Cu}}^{2+})$  has a binding energy of  $\approx -0.4 \text{ eV}$ .

Acceptor		Donor	
Point Defect	Energy [meV]	Point Defect	Energy [meV]
$V_{\text{Cu}}$	30	$\text{Se}_{\text{Cu}}$	20
$V_{\text{In}}$	40	$\text{In}_{\text{Cu}}$	35–45
$V_{\text{Se}}$ (covalent)	45	$\text{Cu}_i$	55
$\text{Cu}_{\text{In}}$	45–55	$\text{In}_i$	70
$\text{Se}_i$	55–60	$\text{In}_{\text{Se}}$	85–95
$\text{Se}_{\text{In}}$	80	$V_{\text{Se}}$ (ionic)	115
$\text{Cu}_{\text{Se}}$	110–130		

Table 1.3: Energetic position of point defects, i.e. the energetic distance between the valence (conduction) band and the acceptor (donor) level in the band gap. Energies determined from photoluminescence measurements [21]

Adding up the binding energies from the point defects ( $4V_{\text{Cu}}$  and  $2\text{In}_{\text{Cu}}$ ) to the charged defect complex yields an energy gain of  $\approx 6.1$  eV. The electronic behavior of this defect complex differs from the individual point defects: The defect complex ( $2V_{\text{Cu}}^0 + \text{In}_{\text{Cu}}^0$ ) has no electronic state in the band gap. Considering the fact that forming these pairs and complexes is energetically favorable and that they do not introduce electronic states in the band gap (which might act as recombination centers), we can understand why CISE and CIGSe absorbers have good electric properties allowing photovoltaic applications despite a huge number of point defects due to off-stoichiometric growth.

The abundance of defects causes another peculiarity of  $\text{CuInSe}_2$ , namely the existence of the ordered defect compound (ODC; also denoted as “OVC”, ordered vacancy compound). Depending on the density of defect complexes, CISE rearranges into compounds like  $\text{CuIn}_3\text{Se}_5$ ,  $\text{CuIn}_5\text{Se}_8$ ,  $\text{Cu}_2\text{In}_4\text{Se}_7$  and  $\text{Cu}_3\text{In}_5\text{Se}_9$ . The ODC is presumably n-type [22] or p-type [23] or p-type with an n-type surface [24]. Taking into account that the ODC is reported to be at the surface of the CISE absorber, the question needs to be raised where the pn-junction of the CISE solar cell is located. Under the assumption of an (at least at the surface) n-type ODC, a “buried homojunction” is possible, in contrast to the general assumption of a heterojunction between CdS (n-type) and CISE (p-type).

In conclusion, the defect physics of CISE explains outstanding properties of this semiconductor that allow the use as a photovoltaic absorber with good efficiencies, i.e. the possibility of intrinsic p- or n-doping, tolerance (electronically) towards deviations from the ideal stoichiometry and the benign nature of (some of) the point defects and the complexes they form.

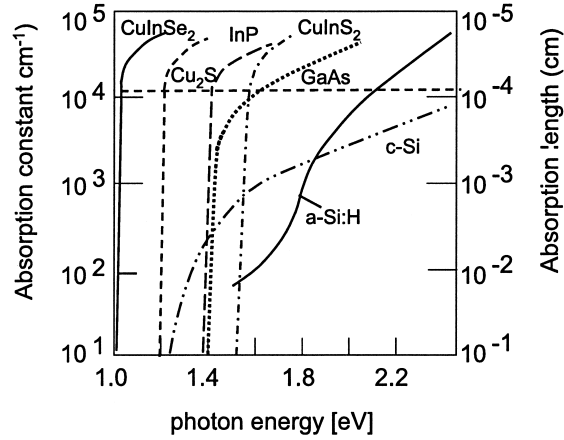


Figure 1.10: Absorption coefficients of different solar cell absorber materials [14]. The absorption edges result from the respective band gap of the material. The significantly lower absorption coefficients of crystalline silicon (c-Si) are due to its indirect band gap (in contrast to the direct band gap materials as CIGSe).

### Electrical Properties

The high absorption coefficients of  $\text{Cu}(\text{In,Ga})\text{Se}_2$  (cf. figure 1.10), due to its direct band gap, allow the deposition as a thin film absorber. By varying the gallium content  $x$ , the band gap  $E_g$  can be tuned between 1.05 eV ( $\text{CuInSe}_2$ ) and 1.70 eV ( $\text{CuGaSe}_2$ ) [25]. It can be calculated by equation 1.8 while the reported bowing parameters  $b$  vary between 0.11 eV and 0.24 eV for co-evaporated (see section 1.3.4) polycrystalline CIGSe absorbers [26].

$$E_g(x) = (1 - x)E_g(\text{CuInSe}_2) + xE_g(\text{CuGaSe}_2) - bx(1 - x) \quad (1.8)$$

As mentioned in section 1.2.2, the optimum band gap for a single junction solar cell under the illumination of an AM1.5 spectrum is around 1.5 eV. According to equation 1.8, this corresponds to a gallium content of  $x = 0.8$  for  $\text{Cu}(\text{In,Ga})\text{Se}_2$  solar cells. However, CIGSe solar cells with a gallium content  $x$  of about 0.1 to 0.3 with band gaps between 1.1 eV and 1.2 eV yield the highest efficiencies [27]. A reduction of the minority carrier diffusion length from 0.8 to 0.1  $\mu\text{m}$  was found to cause a voltage dependent light generated current which is responsible for the gap between expected and measured open circuit voltage ( $E_g - eV_{OC}$ ) at higher gallium contents [28]. A correlation between the difference  $E_g - eV_{OC}$  and the defect concentration in the bulk of the CIGSe was found [27].

Besides doping, the mobility  $\mu$  of the charge carriers is a fundamental parameter for the electrical behavior of a semiconductor. It critically depends on the growth conditions and

morphology of the absorber. Polycrystalline p-type CIGSe absorbers have hole mobilities from 1 to 200 cm<sup>2</sup>/(V s) [29] and single crystals up to 1000 cm<sup>2</sup>/(V s) [14].

Charge carrier lifetimes  $\tau$  are around 40 ns for high efficiency solar cells [30]. If the CIGSe absorber is in contact with air, the lifetime decreases by a factor of 10 within less than 1.5 h and by factor of 100 within a day [30]. Diffusion lengths  $L_D$  are in the  $\mu\text{m}$  range [31].

### 1.3.3 The Role of Sodium

Doping CIGSe absorbers with sodium is essential to reach top efficiencies. By comparing different substrates Hedström et al. found that growing CIGSe on soda–lime glass significantly increases the open circuit voltages and fill factors of CIGSe solar cells compared to a growth on sodium–free substrates [32]. Since that discovery, many research groups are studying the influence of sodium on CIGSe solar cells and in the meanwhile various methods were developed to incorporate about 0.1 at% of Na in the final CIGSe film in order to reach an optimum in efficiency [33].

The first known source of sodium is the substrate of the solar cell, i.e. soda–lime glass containing up to 15 % Na<sub>2</sub>O [12]. Molybdenum grain boundaries and Mo oxide phases in the back contact appear to serve as diffusion channels that allow sodium from the substrate to diffuse to the absorber at high temperatures during the CIGSe deposition [34]. By varying the sputter parameters of the molybdenum, the properties of the back may be tuned to different sodium permeabilities [35].

However, for sodium free substrates (such as polyimide) or to precisely control the amount of sodium that may be present during CIGSe growth, different strategies were developed. One approach is to deposit a sodium blocking layer onto the substrate (if the latter contains sodium) and to subsequently deposit a sodium doped back contact, e.g. by sputtering molybdenum from a sodium doped molybdenum target [36, 37]. A different strategy is to deposit a sodium containing precursor layer (NaF, Na<sub>2</sub>S, Na<sub>2</sub>Se) before CIGSe deposition [38]. Another approach is to co–evaporate from a sodium containing source (NaF, Na<sub>2</sub>S, Na<sub>2</sub>Se) during CIGSe growth [39]. Since Na<sub>2</sub>S and Na<sub>2</sub>Se are hygroscopic and difficult to handle, NaF is used in most labs and industrial processes, either as precursor or in co–evaporation. A completely different sodium incorporation strategy, that yields top efficiencies as well, is to grow sodium free absorbers and to subsequently add sodium in a post–treatment. Typically, NaF is evaporated onto the “cold” (room–temperature or similar) CIGSe layer and then annealed at elevated temperatures ( $\approx 400^\circ\text{C}$ ) in order to enable a diffusion process into the absorber layer [40].

The introduction of sodium has manifold influences on the CIGSe layer, either during growth or on a previously sodium free grown CIGSe layer. While for the latter scenario sodium seems to be beneficial anyway, the effect of sodium during growth depends on the processing conditions. For sequential processes [41] and bilayer co–evaporation processes [38], the grain size increases significantly upon addition of sodium during growth.

In contrary, for a three-stage co-evaporation process, which naturally yields large grains, a decreased grain size with sodium doping was observed [39]. Further influences of the morphology were reported; with increasing sodium content the [112]-orientation of the grains is favored in the polycrystalline layer [42]; the width of the  $\alpha$ -phase is widened [43]. Furthermore, the presence of sodium during absorber growth reduces the diffusion of In and Ga in the growing film [44, 39].

Besides its influence on the growth of the CIGSe layer, sodium changes the electrical properties of the absorber. Due to an increased net doping (p), the conductivity of the CIGSe is increased significantly. An incorporation of about 0.1 at% of sodium in the CIGSe layer typically leads to an increase in conductivity by one order of magnitude [12]. It was reported that CIGSe films doped with Na exhibit a larger hole concentration in the light-soaked state than Na free films, i.e. they are more susceptible to a persistent light-induced conductivity increase [45].

The 0.1 at% Na that are typically incorporated in the CIGSe film, correspond to approximately  $2 \times 10^{19}/\text{cm}^3$ . Changes in the net doping of about  $1 \times 10^{16}/\text{cm}^3$ , however, are orders of magnitude below that value. With secondary ion mass spectrometry (SIMS) mappings it was shown that Na is located mainly at the grain boundaries [34]. High-resolution Auger spectroscopy confirmed that finding, along with the observation of oxygen situated at the grain boundaries [46]. In attempts to diffuse sodium in bulk  $\text{CuInSe}_2$  crystals, the sodium concentration in the bulk was below the detection limit. Instead, large Na concentrations were found at the surface [47]. The latter observation was made on CIGSe/CdS interfaces as well [48]. In conclusion, the high concentrations of sodium needed for high-efficiency devices are not soluble in the CIGSe crystal, instead, most of the Na is at the grain boundaries. Accordingly, calculations showed that  $\text{Na}_x\text{Cu}_{1-x}\text{InSe}_2$  has a positive mixing enthalpy, thus large amounts of Na lead to precipitations [49]. Experimentally observed precipitates are  $\text{Na}_2\text{Se}_x$  ( $x = 1, 2, 3, 4, 6$ ) compounds in CIGSe [50]. Figure 1.11 includes a phase diagram of sodium-selenium compounds.

These influences of sodium doping are at least partially an electronic effect since the possibility of a post-deposition treatment proves that the increased carrier concentration due to Na doping is not (completely) caused by structural influences of the Na during crystal growth. The origin of the increased conductivity may either be (a) in the grain interior where Na reduces the compensation by passivation of donors or by acting as an acceptor and thus increasing the p-doping or (b) at the grain boundaries where Na passivates donor states.

Regarding scenario (a): According to calculations by Wei et al. [49],  $\text{Na}_{\text{In}}$  is a deep acceptor level and thus ruled out as the decisive defect.  $\text{Na}_{\text{Cu}}$  has no electronic level in the band gap and is therefore electronically inactive in CIGSe. The formation of  $\text{Na}_{(\text{In},\text{Ga})}$  on the other hand is exothermic and introduces acceptor levels, hence, the removal of  $\text{In}_{\text{Cu}}$  donors could be the main influence of Na doping leading to lower compensation and higher p-doping.

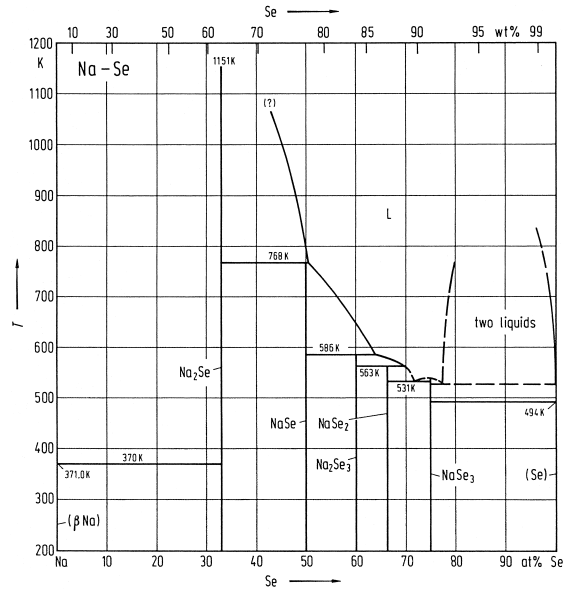


Figure 1.11: Phase diagram of sodium–selenium compounds [29]

Regarding scenario (b): According to the grain boundary passivation model by Cahen et al. [51], sodium acts as a catalyst for the oxidation of dangling In bonds. Thus, by oxygenation, the amount of compensating donors at the grain boundaries is reduced. In total, the net hole concentration in the CIGSe absorber increases. The model is supported by experimental observations of concurrent sodium and oxygen signals [46, 52].

Recent publications show that combined Na and K post-treatments yield the highest efficiencies ever reported [53, 54, 55]. The discussion which effect of sodium is dominating for which type of absorber is ongoing in the scientific community and the scope of it, most likely, has to be broadened now from “sodium doping” to “alkali doping” (or treatment, respectively) in order to come to a satisfying understanding of this key factor in manufacturing high-efficiency CIGSe solar cells.

### 1.3.4 CIGSe Deposition Techniques

The Cu(In,Ga)Se<sub>2</sub> absorber layer is the core layer of a CIGSe solar cell and also the layer with the biggest variety of deposition techniques. Choices that go along with the suitable coating technique include the deposition temperature (depending on the substrate choice), Ga-grading (flat or sophisticated), proportion of sulphur to selenium and alkali supply (from the substrate, from the back contact, precursor layer, co-evaporation, post-treatment). This variety leads to a diversity of startups and companies that are offering CIGSe based products, each with individual intellectual property about their



specific CIGSe layer [56].

There are two fundamental approaches to deposit CIGSe: (1) thermal co-evaporation of all the constituent elements, i.e. Cu, In, Ga, Se, onto a substrate with suitable growth temperature (400 to 600 °C) and (2) rapid thermal processing (RTP) of precursors, i.e. Cu, In, Ga precursors that are deposited onto the cold substrate and that are subsequently selenized, i.e. annealed under Se atmosphere at high temperatures. Since the chalcopyrite absorber always crystallizes under selenium-supply, it should be denoted that co-evaporated absorbers grow “bottom-up”, i.e. from the back contact towards the (later) absorber surface, while RTP absorbers crystallize “top-down”, i.e. the precursor (and thus later absorber) surface selenizes first. For both approaches various fashions exist, of which only some basic ones shall be mentioned here.

### Co-evaporation

In the case of co-evaporation the metals may be evaporated from point or linear evaporation crucibles, resulting in different layer homogeneities and material yields. The substrate temperature depends on the material. For glass, temperatures above 500 °C may be used (industrial manufacturers: *Solibro*, *Manz*), for plastic substrates, temperatures well below 500 °C must be used (industrial manufacturers: *Flisom*, *Solarion*). In order to retain a good CIGSe crystal quality at low deposition temperatures, *Solarion AG* introduced the ion beam assisted deposition process (see section 3.1 for more details). In either case, elemental gradients may be tuned by different subsequent evaporation steps in batch-like fabrication with fixed substrate configurations or by specific evaporator sequences in continuous manufacturing (moving individual substrate or roll-to-roll deposition).

### Rapid Thermal Processing

In the case of RTP, the CIGSe deposition methods mainly differ in the precursor deposition method. Classically Cu, In and Ga are sputter-deposited (industrial manufacturers: *SolarFrontier*, *Avancis*). By starting with a specific stack of the Cu and In/Ga precursor layers, elemental gradients may be tuned as well. Recently, new precursor deposition techniques have been investigated and commercialized, such as electro-deposition (industrial manufacturers: *Nexcis*, *Solopower*) and printing of inks (industrial manufacturers: *Nanosolar*, *International Solar Electric Technology*).



## 2 Degradation of Cu(In,Ga)Se<sub>2</sub> Solar Cells: A Literature Survey

This chapter is an excerpt of the review paper “Stability of Cu(In,Ga)Se<sub>2</sub> Solar Cells: A Literature Review”<sup>1</sup> by Mirjam Theelen (*TNO* Eindhoven) and Felix Daume. While the paper provides a comprehensive overview over all degradation aspects of Cu(In,Ga)Se<sub>2</sub> solar cells, this chapter summarizes the most important knowledge about the individual layers and gives a detailed review on the degradation of the pn-junction and the electrical behavior of the solar cell after degradation.

### 2.1 Introduction

For large scale market introduction of CIGSe modules, product performance stability, alongside with initial costs and efficiency, are important prerequisites (cf. figure 2.1).

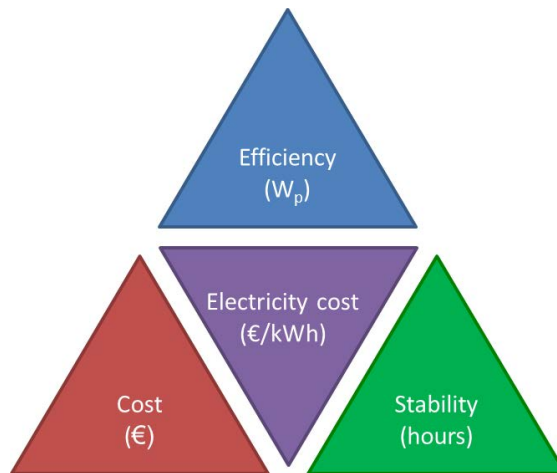


Figure 2.1: The three main parameters determining the cost competitiveness of electricity from PV panels.

For the thin film PV industry, the long term field performance of PV modules is especially hard to control, because predicting their lifetime is a complicated process.

<sup>1</sup>Manuscript in preparation [57] (cf. appendix B).

However, most suppliers provide a guarantee that the modules will still provide at least 90 % of their initial efficiency after 10 years or 80 % after 25 years [58]. Various degradation rates of CIGSe modules, as obtained from field testing, are shown in table 2.1.

<b>Period</b>	<b>Location</b>	<b>Producer or <i>Comment</i></b>	<b>Rate (%/a)</b>	<b>Reference</b>
2006–2011	Nicosia, Cyprus	Würth	1.9...2.4	[59]
2005–2007	Florida		4.5...5.1	[60]
2003–2010	Magdeburg, Germany	Würth	0	[61]
1990 (2002)– 2008	Colorado, USA		0.2...2.3	[62]
2005–2008	Colorado, USA	<i>With Bias</i>	2.5...4.7	[62]
2006–2011	Colorado, USA	Shell Solar	0	[63]
n/a	Colorado, USA		0...3.7	[63]
2001 (10 months)	South–Africa		48	[64]
2001–2003	South–Africa		8.1	[64]
2003–2007	Widderstall, Germany	ZSW	0.2	[65]
until 1990 (17.5 months)	Colorado, USA	Siemens Solar	4.1	[66]
1988–2006	Colorado, USA	Siemens Solar	-0.2...1.7	[67]
2003–2006	Japan	Showa Shell Sekiyu	0	[68]
2007–2009 (13 months)	Port Elizabeth, South–Africa		-1.8...4.1	[69]

Table 2.1: Literature overview of degradation rates (percent per year) of CIGSe modules obtained by field tests at different locations.

Table 2.1 shows that the recently tested modules vary from very stable (no degradation after seven years) to very vulnerable to outdoor exposure. It should be noted that the degradation rates are not linear, in fact large differences between years can be observed. These mixed results show that a general statement about the module lifetime of CIGSe PV cannot be made at this moment. The main reason for this limited knowledge can be found in:

1. Limited field experience with CIGSe modules, which mostly have not been in the field for a long time.
2. Results from field experiments can vary greatly, as is shown in table 2.1. Degradation

tion depends on many parameters such as module production techniques, module type, production year, orientation of the panel and climate of the installation location, as well as installation parameters like the applied voltage. So far, not enough field testing data is available to apply reliable statistics.

3. Lessons learned for crystalline silicon (for both field and accelerated testing) cannot always be applied to CIGSe modules due to deviations in module design and composition.

More information about the field performance of many types of PV modules, including CIGSe can be found in the review by Jordan and Kurtz [70]. In general, table 2.1 and the references [70, 58] show that some CIGSe modules show excellent outdoor stability, while other modules degrade very quickly. When the change of the individual PV parameters of the degraded modules was studied, it was observed that the efficiency decrease was mostly caused by deterioration of the fill factor ( $FF$ ), while small changes in the open circuit voltage ( $V_{OC}$ ) and minimal changes in the short circuit current ( $I_{SC}$ ) were also observed [62, 70].

In order to better predict the lifetime and reliability of CIGSe modules, they are exposed to accelerated lifetime testing (ALT) according to International Electrotechnical Commission (*IEC*) module testing procedure 61646 [71]. These tests should ideally show whether the requirements related to performance stability are met. However, literature reveals that a positive outcome of the *IEC* tests not always indicates that the PV module can stand the predicted outdoor conditions [70, 72]. This weak correlation between tests and reality is currently specifically a challenge for thin film PV including CIGSe [73]. The latter PV technology shows different failure mechanisms from crystalline silicon modules, which were used to define the ALT sequences over many years. As described in reference [72], these procedures have been optimized multiple times, based on field experience, while the optimization process for thin film PV only started recently.

The degradation of CIGSe modules can be caused by non-cell type specific reasons, like connection wires or junction box corrosion which can also be found in other types of PV modules, as well as CIGSe specific causes. Table 2.2 shows an overview of failure modes leading to CIGSe module degradation, and a global categorization whether they are specific for CIGSe or also observed for other (thin film) modules.

When the circumstances leading to CIGSe-specific degradation were studied, humidity was often a key factor. ALT tests including liquid or gaseous water, like damp heat tests (exposure to 85% relative humidity (RH) at 85 °C) are the tests which are most often failed by CIGSe PV. It was therefore concluded that CIGSe is very sensitive to humidity ingress. Furthermore, sensitivity to e.g. temperature (shocks), electrical bias and illumination has been found, but the impacts of these loads are not necessarily detrimental.

Degradation data of unencapsulated CIGSe solar cells were taken from various literature sources [57]. Linear degradation rates for damp and dry heat treatments that

<b>Failure Modes</b>	<b>CIGSe Specific</b>	<b>Impact</b>	<b>Possible Failure Mechanisms</b>
<i>Cell degradation</i>			
Pn-junction: Increase of recombination	yes	Loss in $FF$ , $J_{SC}$ and $V_{OC}$	Diffusion of dopants, impurities and electromigration
Shunting	yes	$R_P$ decrease	Diffusion of metals, impurities
TCO, Mo degradation	yes	$R_S$ increase	Corrosion, diffusion
Delamination of back contact	yes	$J_{SC}$ decrease	Lamination stress
<i>Module degradation</i>			
Interconnect resistance: ZnO:Al/Mo or Mo	yes	$R_S$ increase	Corrosion, electromigration
Interconnect degradation: shunting across isolation scribe	yes	$R_P$ decrease	Corrosion, electromigration
Busbar failure	no	$R_S$ increase or open circuit	Corrosion, electromigration
Solder joint	no	$R_S$ increase or open circuit	Fatigue, coarsening (alloy segregation)
Encapsulation: delamination	no	$FF$ , $J_{SC}$ losses or open circuit	Surface contamination, UV degradation, hydrolysis of silane/glass bond, warped glass, “dinged” glass edges, thermal expansion mismatch
Encapsulation: loss or hermetic seal	no		
Encapsulation: glass breakage	no		
Encapsulation: Loss of high-potential isolation	no		

Table 2.2: Summary of failure modes as observed for CIGSe based photovoltaics (modified but based on reference [74]).

were calculated from these data and compared in figure 2.2(a). A histogram of the linear degradation rates of unencapsulated CIGSe solar cells under damp heat is given in figure 2.2(b).

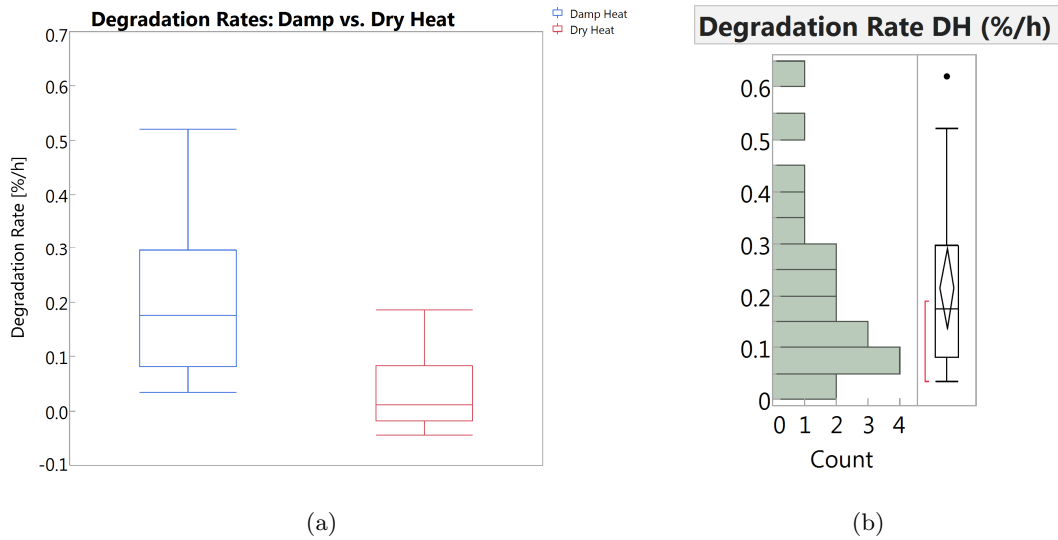


Figure 2.2: (a) Linear degradation rates of unencapsulated CIGSe solar cells under damp heat (blue; median degradation rate = 0.175 %/h) and dry heat (red; median degradation rate = 0.012 %/h). (b) Histogram of the linear degradation rates of unencapsulated CIGSe solar cells under damp heat. The 20 data points each were taken from a literature review paper [57].

In order to protect the CIGSe cells against water ingress, encapsulation is applied in modules. For rigid modules, glass is an excellent encapsulation material, while for flexible modules often expensive inorganic/organic multi-stack materials are chosen. Although this enhances the lifetime of the CIGSe modules, it also leads to higher costs and hinders the large scale market introduction of flexible modules. Therefore, intrinsically stable CIGSe cells and modules would be very attractive. They would contribute to lower production costs due to reduced encapsulation costs and accelerate the introduction of flexible CIGSe modules to the market. Knowledge about intrinsically more stable CIGSe material might thus also help CIGSe producers that are currently producing stable, but relatively expensive modules.

## 2.2 Degradation Conditions

In the sections below, the results of various types of accelerated lifetime tests are described. The most important tests are introduced here:

1. “Standard” damp heat exposure at 85 °C at 85 % relative humidity. According to *IEC* standard 61646 [71], 1000 h exposure to these conditions should mimic 25 years field exposure in Miami. However, the similarities between field and accelerated testing are still under debate. In this thesis – as in most publications – the term “damp heat” refers to these conditions unless other damp heat conditions are explicitly stated.
2. “Mild” damp heat, e.g. 60 °C at 90 % relative humidity [75]. It should be noted that the relative water concentration is higher than for 85 °C at 85 % relative humidity, but the absolute water concentration is lower, due to lower saturation concentrations at lower temperatures.<sup>2</sup>
3. “Dry heat”, which is mostly 85 °C or 90 °C combined with a low relative humidity grade (e.g. 10 % relative humidity).
4. Combined damp heat and illumination testing [68], which can also allow the in-situ monitoring of the degradation behavior [76]. Furthermore, damp heat can also be combined with UV exposure [77]. It should be noted that the temperature and humidity conditions as reported in a combined damp heat illumination experiment are generally the chamber conditions instead of the sample conditions. This is caused by additional sample heating due to the illumination, which also leads to a reduction in the relative humidity of the sample. Therefore, when comparing between damp heat and damp heat illumination experiments, these deviations should be taken into account.

It should be noted that the temperatures used during accelerated lifetime testing (typically 85 °C) are much higher than typical environmental temperatures. However, module temperatures are often higher than the environmental temperature. McMahon et al. measured the temperatures at the back of modules in New Mexico as high as 71 °C [74].

It is important to note that the accelerated lifetime tests sometimes include the removal of samples from the climate chamber for analysis purposes. The samples are then returned to the chamber several hours or days later. These actions could lead to the introduction of drying stains (evaporation of surface water due to the lower humidity

---

<sup>2</sup>Example: 85 % relative humidity at 60 °C correspond to 103 g/m<sup>3</sup>, while 85 % relative humidity at 85 °C correspond to 241 g/m<sup>3</sup> (according to <http://hyperphysics.phy-astr.gsu.edu/hbase/kinetic/relhum.html>).



of ambient air) and stress related effects, due to large and fast temperature and humidity changes. On the other hand, this “drying effect” can also be positive, e.g. due to intermediate drying of the samples, as described by Pern et al. [78].

## 2.3 Molybdenum Degradation

When molybdenum and selenized molybdenum are exposed to water and oxygen, especially under elevated temperatures, black and blue stains can occur on the metallic molybdenum surface. These stains contain oxidized molybdenum ( $\text{MoO}_2/\text{MoO}_3$ ). These oxides are badly conducting and reflecting, which likely has a negative impact on the solar cell [79]. Furthermore, the molybdenum oxide layer can crack, while needles can also be formed. The formation of a thick layer of non-conductive molybdenum oxide likely leads to a sudden and complete disappearance of the conductivity when measured from the top. The degradation effects are the most severe for molybdenum deposited at high deposition pressures, thereby forming more porous molybdenum layers. Selenized molybdenum also degrades in damp heat via the formation of molybdenum oxide, but this process occurs slower, probably since the molybdenum has already reacted with selenium in this case [80].

Although the oxide formation seems very detrimental for later deposited solar cells, mild oxidation could actually result in slightly improved efficiency. When CIGSe is deposited on oxidized molybdenum, this likely leads to reduction of the molybdenum oxide ( $\text{MoO}_3 \longrightarrow \text{MoO}_2$ ) as well as transformation into  $\text{MoSe}_2$  [81].

Various references reported on the presence of sodium, which likely plays a role in molybdenum degradation. It can occur e.g. in the form of needles on the molybdenum surface, but it is also possible that it intercalates via a reduction reaction into  $\text{MoO}_3$ , thereby forming  $\text{Na}_x\text{MoO}_3$  [82].

## 2.4 CIGSe Degradation

### 2.4.1 Experimental Limitations

When investigating the properties of a CIGSe absorber in a solar cell under ALT conditions, one faces the challenge of revealing properties of one specific layer within a stack of interacting layers. This is particularly the case since creating model samples, i.e. an “isolated” CIGSe layer, of similar quality than within the actual device is nearly impossible. For example, if one lifts of the top of the solar cell from the back contact, buffer and TCO (more conductive than CIGSe) are still underneath the CIGSe thus making electrical measurements on CIGSe alone difficult. If, on the other hand, one stops the solar cell manufacturing process after absorber deposition (or chemically etches away layers from the top), creating a sample substrate / molybdenum / CIGSe, the much

more conductive molybdenum back contact causes the same problems (in the case of etching, an additional challenge is to stop the etching process right at the absorber surface). Another option would be the growth of CIGSe directly onto an alternative, non-conducting substrate. In that case, however, the crystal growth would be different, no MoSe<sub>2</sub> could form and the layer properties were not comparable to a real device anymore. Apart from the fact that the absorber properties are most likely different from the CIGSe layer in the solar cell, the aforementioned techniques are destructive. Thus, the comparison of the IV properties of the as-prepared and aged solar cells as well as the individual layer properties at the same time is impossible. Some of the most valuable structural analysis techniques, such as SIMS, impose the same limitations.

Therefore, electrical measurements are typically performed on complete devices, which is also necessary to obtain the very basic information about the conversion efficiency from IV measurements. The main challenge is to separate the influences of all individual layers (from substrate to TCO) in the interpretation of these electrical measurements. A common tactic to do so is to investigate a series of samples, that were manufactured the same way, except for some intentional variation in the absorber layer (e.g. alkali doping, gallium grading, thickness). By comparing the results of the electrical measurements from different samples, conclusions of the influence of the absorber and its composition on the stability of the solar cell are possible.

In this literature review it will be differed between stability issues measurable in the CIGSe absorber (this section) and those only measurable due to the pn-junction between CIGSe and buffer (cf. section 2.8). The stability of CIGSe will be discussed with respect to extrinsic effects such as damp heat but, at first, the intrinsic stability, i.e. without ALT conditions, will be discussed briefly.

#### 2.4.2 Intrinsic CIGSe Stability

Intrinsic instabilities of Cu(In,Ga)Se<sub>2</sub>, i.e. defect metastability, the mobility of copper as a constituent element and interface reactions between the layers of the final device, are potentially detrimental for the long-term stability of a CIGSe solar cell. Guillemoles et al. [83], however, argue that these fundamental instabilities are actually beneficial to the device: Possible interface reactions (back contact/absorber, absorber/buffer, buffer/window) are thermodynamically or kinetically limited. In contrast to a-Si:H solar cells, defect metastabilities are self-annealed at room temperature, and actually beneficial to the cell performance. They actually increase the doping level in the absorber. Regarding the point defects in CIGSe, there are two important features: the presence of a large defect pool and the possibility of ionic migration. Their synergetic action makes CIGSe a radiation hard and impurity tolerant material. The radiation hardness is based on the mobility of copper within the chalcopyrite lattice. It provides means to level out defect related gradients in the chemical potential of the material. Cu related defect complex pools buffer electronic and chemical changes. Via migration of Cu, defects ap-

pearing anywhere in the absorber may be passivated. The necessary reaction energies are low enough to permit this passivation at room temperature. In that sense, the stability of CIGSe is not static but dynamic or, as Guillemoles et al. [83] put it, CIGSe is strong because it is flexible. In that sense, they call it a “smart material”, which is by their definition “capable of sensing changes in its environment and responding to them”.

As described by [84], the point defect related self-healing mechanisms lead to a characteristic stability, i.e. CIGSe resists changes in its carrier concentration and opposes the creation of deep defect centers. Self-healing is inherent to CIGSe that was prepared under selenium excess pressure which leads to p-type CIGSe with hole concentrations between  $1 \times 10^{15}/\text{cm}^3$  and  $1 \times 10^{17}/\text{cm}^3$ , irrespective of deviations from stoichiometry (which may be in the percentage range). The point defect interaction at high point defect concentrations is not too large, thus deforming the lattice only minimally and thus allowing a wide non-stoichiometric range. In the case of  $\text{CuInSe}_2$ , this range exists along the  $\text{Cu}_2\text{Se}-\text{In}_2\text{Se}_3$  tie line for  $\text{Cu}/\text{In} < 1$ . These compounds, so called ordered vacancy compounds (OVC or ODC), have a crystal structure that may be derived from CIGSe by leaving some cationic (Cu) sites empty. They may also be understood as ordered arrays of point defects ( $\text{In}_{\text{Cu}}, 2V_{\text{Cu}}$ ). Since the atoms of the cationic species in CIGSe are much smaller than those of the anionic species, only defects on the cationic sites (and selenium vacancies) seem to have low formation energies; they may be created with minimal distortion [84].

### 2.4.3 Extrinsic CIGSe Stability

As mentioned in the introduction, the stability of non-encapsulated CIGSe solar cell is mainly threatened by humidity [84]. Many research groups report a reduction of the open circuit voltages and the fill factors of their CIGSe solar cells after artificial aging with damp heat [85, 86, 87, 88].

Lower open circuit voltages after DH may be caused by changes inherent to the CIGSe absorber such as point defects, doping, defects, elemental diffusion, oxidation or grain boundaries. Or, they may be related to the properties of the pn-junction, e.g. band bending, Fermi level pinning or interface defect states. Either way, these effects are typically studied by electrical measurement techniques, e.g. admittance spectroscopy, which rely on the existence of a pn-junction, thus they will be discussed in the respective section (2.8).

Increases in the fill factor after DH can typically be traced back to increased series and diminished parallel resistances of the solar cell. A typical failure mode for the parallel resistance is shunting within an isolation scribe. An increase in the series resistance may have different causes, as it is the sum of various contributions including the different sheet and contact resistances as well as the grid. The contributions of the back contact (section 2.3), the TCO (section 2.6) and the grid (section 2.7) are discussed separately. Wennerberg et al. found that the increase in the sheet resistance alone did not explain

the decrease in fill factor [85].

#### 2.4.4 Chemical Changes in the Absorber

Various studies have investigated the changes in the absorber in full solar cells due to degradation (cf. section 2.8), but as described above, not many sources have studied the individual absorber.

Pern et al. exposed the separate absorber for 15 min to 5 h to damp heat and for 8 to 12 months to the laboratory atmosphere [89]. Both the 5 h damp heat and the air exposure led to the formation of many spots. The spotty areas showed low Ga, Cu and Se concentrations, while the concentration of Na was relatively high. It was expected that hydrolysis or oxidation led to these degradation processes. These spots did not have an impact on the optical properties between 250 to 900 nm, while a peak shift in the interference pattern in the infrared region with unknown cause was observed.

Scanning Kelvin Probe and Atomic Force Microscopy (AFM) showed that small spots occurred on the AFM images after 1 to 5 h of damp heat exposure. It was also observed that the work function had lost its correlation with the grain geometric feature due to damp heat exposure. After 5 h, the initially well defined work function images became blurred, which could be a result of the electronic property breakdown of the CIGSe grains.

Solar cells were made from the absorbers exposed to ambient conditions and to 15 to 30 min of damp heat. The cells exposed to ambient conditions showed a severe decrease of all solar cell parameters, while the damp heat degradation showed a much smaller decrease of only  $V_{OC}$  and  $FF$ .

The degradation of bare CIGSe under damp heat or under ambient conditions fits with the large decrease in carrier lifetime observed by Metzger et al. [30], who studied air exposed CIGSe absorbers by Time Resolved Photo Luminescence (TRPL). This degradation process can be prevented by CdS deposition, which leads to absorbers that are stable in the air for months.

Suggestions about the possible degradation products on the absorbers were made by Würz et al. [90] who reported the formation of Cu(OH)<sub>2</sub> on CuGaSe<sub>2</sub> solar cells that were stored under ambient conditions for months. Heske et al. [91] reported the formation of sulfate, which resulted from the damp heat induced oxidation of sulfur in Cu(InGa)(SeS)<sub>2</sub> solar cells.

#### 2.4.5 Gallium Content

Malmstroem et al. investigated the influence on different absorber compositions on the damp heat stability of their Cu(In<sub>1-x</sub>Ga<sub>x</sub>)S solar cells [92]. They found the lowest efficiency drop after 800 h of damp heat for gallium contents of  $x = 0.4$  (−27%). Without

gallium ( $x = 0$ ) the efficiency drop was the largest ( $-92\%$ ), while pure  $\text{CuGaSe}_2$  cells ( $x = 1$ ) degraded by  $64\%$ .

### 2.4.6 Sodium Content

Alkali supply – typically sodium – to the CIGSe absorber either as a precursor, during growth or in a post-treatment, is essential to achieve high efficiency CIGSe solar cells. It turns out that sodium is a factor in the long-term stability of CIGSe solar cells as well [50, 93].

According to Braunger et al. [50], the oxidation of  $\text{CuInSe}_2$  or  $\text{Cu(In,Ga)Se}_2$  is accelerated in the presence of sodium. The oxidation of the absorber (at high temperatures) has little or no effect on the efficiency, but absorbers oxidized in humid air (at room temperature) show a drastic decrease in performance. Braunger et al. describe, that reactions of sodium with selenium species are possible at very low temperatures. For  $T < 500\text{ }^\circ\text{C}$ , sodium polyselenides ( $\text{Na}_2\text{Se}_x$ ;  $x \in \{1, 2, 3, 4, 6\}$ ) and for  $T > 500\text{ }^\circ\text{C}$  sodium monoselenide ( $\text{Na}_2\text{Se}$ ) are formed. CIGSe grown on soda lime glass substrates, i.e. in the presence of sodium, showed less indium or gallium oxides at the surface, but more elemental selenium and selenium oxides, compared to CIGSe grown on sodium-free substrates. As humidity was found to promote the degradation,  $\text{H}_2\text{O}$  catalyzed reactions for the incomplete oxidation of  $\text{Na}_2\text{Se}_x$  (which is present as precipitate / intergranular segregation in the polycrystalline CIGSe film) in air were suggested:

- $\text{Na}_2\text{Se}_x + \frac{1}{2}\text{O}_2 \longrightarrow \text{Na}_2\text{O} + x\text{Se}$
- $\text{Na}_2\text{Se}_x + \frac{3}{2}\text{O}_2 \longrightarrow \text{Na}_2\text{SeO}_3 + (x-1)\text{Se}$
- $\text{Na}_2\text{Se}_x + \frac{1}{2}\text{O}_2 + \text{CO}_2 \longrightarrow \text{Na}_2\text{CO}_3 + x\text{Se}$

Accordingly, a  $\text{H}_2\text{O}$  and Na catalyzed reaction pathway of the absorber was suggested:

- $2\text{Cu(In}_{1-x}\text{Ga}_x\text{)Se}_2 + \frac{3}{2}\text{O}_2 \longrightarrow 2\text{'Cu}^{\text{I}}, + (1-x)\text{In}_2\text{O}_3 + x\text{Ga}_2\text{O}_3 + 4\text{Se}$

Since Braunger et al. detected a partial oxidation of selenium in their degraded samples, they assumed another reaction pathway:  $\text{Se} + \text{O}_2 \longrightarrow \text{SeO}_2$  [50]. The presence of water lead to the hydrolysis of the oxides, i.e. the formation of  $\text{In(OH)}_3$ ,  $\text{Ga(OH)}_3$ ,  $\text{H}_2\text{SeO}_3$  and  $\text{NaOH}$ . In conclusion, Braunger et al. found sodium to promote an enhanced removal of selenium from the absorber layer via the formation of  $\text{Na}_2\text{Se}_x$  compounds [50]. During degradation, the oxidation of the absorbers lead to the oxidation of both, CIGSe and  $\text{Na}_2\text{Se}_x$ . If that oxidation was incomplete, an increased production of elemental selenium from CIGSe and  $\text{Na}_2\text{Se}_x$  (in the above described reactions) occurred which severely affected the device performance.

## 2.5 Buffer Degradation

Wennerberg et al. studied the degradation of the window layer with model structures, i.e. substrate (glass/silicon) / CdS (no/one/two chemical bath deposition dips) / (ZnO) [85]. Window layers grown without CdS buffer were more stable (regarding the sheet resistance) under damp heat conditions. Furthermore, the TCO sheet resistance degradation was enhanced by an increasing CdS buffer thickness.

CIGSe solar cell on glass with chemical bath deposited CdS buffer layers were studied with respect to their degradation behavior under damp heat (100 h, 1000 h) by Schmidt et al. [87]. IV measurements revealed that, besides  $V_{OC}$  (as discussed in section 2.8), most significantly the  $FF$  degrades. The degeneration of the ZnO/CdS window layer was considered as likely explanation. Decreasing ZnO conductivity with increasing duration of damp heat was argued to lead to the observed losses in  $FF$ . The authors stated that different ZnO deposition techniques and various CdS thicknesses lead to more or less degeneration of the ZnO/CdS window layer.

Heske et al. analyzed ZnO/CIGSSe and ZnO/CdS/CIGSSe interfaces by XES (soft X-ray emission spectroscopy) [91]. The authors observed the formation of a sulphate species at or near the ZnO/CdS and the ZnO/CIGSSe interface after damp heat treatment. In both cases, sulphur atoms diffuse into the ZnO layer and form a sulphate species there (such as ZnSO<sub>4</sub>). In contrast, a series of similar samples that were treated with dry heat showed no evidence for sulphur oxidation or sulphate formation. Thus, Heske et al. concluded that the source of oxygen for the sulphate formation is predominately the ambient humidity rather than the ZnO layer. The authors propose that the losses in FF observed by Schmidt et al. [87] and the commonly observed increase in ZnO resistivity are enhanced by a change in the electronic and chemical structure at and near the ZnO/(CdS)/CIGSSe interface, as well as by the altered electronic properties of the ZnO film containing a detectable fraction of ZnSO<sub>4</sub> “contamination” in the vicinity of the interface [91].

## 2.6 TCO Degradation

Several types of TCO are candidate as front electrode for CIGSe solar cells, of which sputtered aluminum doped zinc oxide is the most important, while ITO can also be used. An enhanced resistivity of aluminum doped zinc oxide is often found to be the main cause of solar cell degradation and is mostly driven by mobility decrease [94]. This is mostly caused by the diffusion of “foreign” species from the atmosphere into the grain boundaries. The migration of, among others, H<sub>2</sub>O and CO<sub>2</sub> can lead to the formation of molecules like Zn(OH)<sub>2</sub> and Zn<sub>5</sub>(CO<sub>3</sub>)<sub>2</sub>(OH)<sub>6</sub>, which can form a potential barrier at the grain boundaries [95]. Adsorption of these species is also a possibility.

More stable aluminum doped zinc oxide layers can be deposited by higher thicker

layers, deposition temperatures and doping concentrations or post-deposition treatments at elevated temperature [96]. Furthermore, the increase in resistivity can largely be reversed by annealing at vacuum or a reducing atmosphere at elevated temperatures [97]. The roughness of the substrate also influences the aluminum doped zinc oxide stability. Since samples on rough substrates are less stable, rough underlying layers within the CIGSe cell can also negatively impact the stability of the aluminum doped zinc oxide [98].

The more expensive ITO is generally more stable than aluminum doped zinc oxide. Further positive effects on the stability can be found in higher substrate temperatures and lower partial pressures of oxygen [99]. Degradation of ITO can be caused by the migration of water and alkali elements into the layer. It was also observed that decomposition of the layer into tin and indium containing materials occurred. Furthermore, the degradation of both aluminum doped zinc oxide and ITO was often accompanied by the formation of spots [100].

Interaction between the TCO and encapsulation also plays a large role for CIGSe module stability. A good barrier can prevent the ingress of atmospheric species into the TCO. It was reported that alongside to the materials designed as water barrier, intrinsic zinc oxide, ITO and SnO<sub>2</sub> did also show barrier properties.

## 2.7 Influence of the Grid

Generally, grids are used to overcome the limitations in the conductivity of TCOs. By providing an additional low-resistance path for current collection, they reduce the overall series resistance of the cell and thus ohmic power losses. As any other part of the solar cell, grids are subject to degradation but, at the same time, a strategy to deal with a degrading solar cell. In a gridded solar cell or module, the ohmic losses in the TCO can be controlled by varying the spacing between the grid fingers. By trading off some initial power, more specifically some current density, since the shading increases when decreasing the finger distance [101], the module efficiency can be kept at a higher level after damp heat, because the additional grid fingers compensate for the increasing sheet resistance of the TCO. From that point of view, the gridded module design is preferable from a long-term performance point of view [86]. Wennerberg et al. pointed out further advantages of a gridded module such as less inactive area (the cell stripes in a monolithically interconnected module can be wider), higher tolerance for variations, a cheaper TCO process (thinner TCO is possible) and improved degrees of freedom in the module geometry [102]. Nevertheless, the authors noted that the benefits of a gridded module have to outweigh the cost of an (additional) grid deposition in order to pay off in production.

A typical grid for solar cells in many research labs consists of a thin nickel layer (e.g. of 50 nm thickness), followed by a thick aluminum layer (e.g. 2 to 3 μm thickness) that are typically applied by some evaporation method. Wennerberg et al. reported that this

structure corroded considerably and led to uncertainty in the interpretation of changes in the IV characteristics [85]. A modified grid structure, however, with an additional Ni capping (50 nm) improved the stability. No visual degradation was observed after 1000 h of damp heat and the IV statistics became tighter.

A different grid application technology is screen-printing. Typically, polymer matrices with silver particles are printed and subsequently annealed. Britt et al. report that silver containing grid fingers exhibited visual signs of corrosion after 50 h of damp heat [103]. Widespread defects were found on the surface of damp heat treated stainless steel/Mo/CIGSe/CdS samples. These pinhole like defects consisted of sodium, oxygen and carbon in their core. It was hypothesized that shunting paths were produced if a silver grid would be printed on top of these pinholes. It remained unclear and subject to further investigation whether such a pinhole defect could form and would be harmful to the solar cell performance if a TCO and a grid, respectively, were applied before damp heat.

Elowe et al. studied direct cell inorganic coatings as an approach to increase the cell stability motivated by the perspective of a simplified encapsulation package [104]. Reactively sputtered SiN<sub>x</sub> layers were investigated because of their chemical stability, high density and transparency in the visible spectrum. Model samples consisting out of a glass (soda lime glass) substrate, an aluminum layer that allows monitoring of water vapor transmission through the package by optical changes due to oxidation of the aluminum, ITO, an electron beam evaporated Ni/Al grid (total grid thickness 1.6 μm) and a 150 nm silicon nitride layer were prepared. After 47 h of accelerated lifetime testing (100 % relative humidity at 115 °C), a significant oxidation of the aluminum layer was found in the vicinity of the silver grid lines in contrast to the majority of the ITO/SiN<sub>x</sub> surface. After 380 h of aging, the degradation near the grid lines had proceeded severely, i.e. ruptures, fissures and delamination of the protecting silicon nitride layer was observed. Elemental mapping revealed an oxidation of the SiN<sub>x</sub> layers near the grid lines. Furthermore, significant quantities of sodium were found in the top layers of the grid region. A close relationship between oxidation of the silicon nitride layer and migration of sodium species such as NaOH and Na<sub>2</sub>O from the glass to these regions was concluded. The cracking is at first observed in the regions of the silver grid since there the residual compressive stress within the SiN<sub>x</sub> layer is the largest (higher mismatch of the coefficients of thermal expansion than outside the grid region). It was predicted that mitigating the sodium migration to the top layer and an improved interface integrity could overcome the observed failure mechanism. The postulation was experimentally confirmed by introducing a 10 nm thin TaN<sub>x</sub> layer between ITO and SiN<sub>x</sub> thus mitigating sodium diffusion, hindering oxidation of the SiN<sub>x</sub> film and significantly improving the stability of the samples. Applied to CIGSe solar cells (following the process by *NREL*), 90 % of the initial performance could be retained after 1900 h under damp heat (85 % relative humidity at 85 °C) on average.

Pern et al. report that a standard metallic grid of a 3 μm aluminum layer on top of a



50 nm nickel layer are unstable under damp heat [105]. The stack is subject to hydrolytic corrosion within 50 to 100 h of damp heat thus becoming highly resistive. Since nickel was known to be more stable against oxidation and hydrolysis than aluminum, Pern et al. prepared solar cells with nickel only grids. At a grid thickness of 0.2 to 0.3  $\mu\text{m}$ , the solar cells with nickel only grid showed a lower efficiency (compared to those with standard Ni/Al grid) due to the higher resistivity of nickel. At nickel grid thicknesses of 1.6 to 1.8  $\mu\text{m}$ , the devices offered comparable efficiencies. Due to high mechanical stress some of the nickel only grids exhibited cracking and peeled off resulting in damaged or failed devices. However, 4–point resistance measurements on simple test structures consisting of a 0.1  $\mu\text{m}$  thin nickel layer showed no change in resistance after 50 to 100 h of damp heat thus motivating further optimization of a potential grid purely out of nickel.

## 2.8 Pn–Junction Changes and Device Behavior

As mentioned in section 2.4.3, CIGSe solar cells mainly suffer from  $V_{OC}$  and  $FF$  losses after damp heat ALT. In this section, models that have been introduced in literature to explain these changes are reviewed.

After 1000 h of DH on 0.5  $\text{cm}^2$  sized CIGSe solar cell on glass substrates, Schmidt et al. observe a decrease in  $V_{OC}$  of about 5 to 20 % and, more severely, approx. a 40 % decrease in  $FF$  while  $J_{SC}$  remains constant [87]. The drop in  $FF$  is ascribed to the decreasing conductivity of the ZnO after DH treatment. By temperature dependent IV measurements, the dominant recombination mechanism was determined to be defect states in the bulk of the CIGSe absorber. Admittance spectroscopy was carried out and interpreted with the method by Walter et al. [106]. The N1 signature which is commonly observed by many authors shifted to higher activation energies after 100 h of DH. Furthermore, the N2 signature, shifted to higher activation energies and almost doubled in density ( $6 \times 10^{16}/(\text{cm}^3 \text{ eV})$ ).

The signature N1 was interpreted as an interface defect: Upon damp heat, the decreasing ZnO conductivity was believed to lead to a wider space charge region width  $w$  which leads to a shift of the voltage drop across the pn–junctions towards the n region of the cell and thus to an increase of the energetic distance between the electron Fermi level and the conduction band  $\Delta E_{F_n}$  (see figure 2.3). This change is equivalent to a decrease of the type inversion (and might also be caused by changes in the defect density at the interface [107]) resulting in an increased interface barrier  $\Phi_b^n$  for electrons. For barriers  $\Phi_b^n$  higher than 0.5 eV, according to Rau et al. [17], the series resistance is affected and thus the fill factor will decrease for increasing  $\Delta E_{F_n}$  and  $\Phi_b^n$ .

The signature N2 in admittance measurements was interpreted as a (deep) bulk defect in the CIGSe absorber [87]. It was held responsible for the decrease in the  $V_{OC}$  after damp heat, since bulk recombination was identified via temperature dependent IV measurements as the main recombination mechanism and admittance measurements

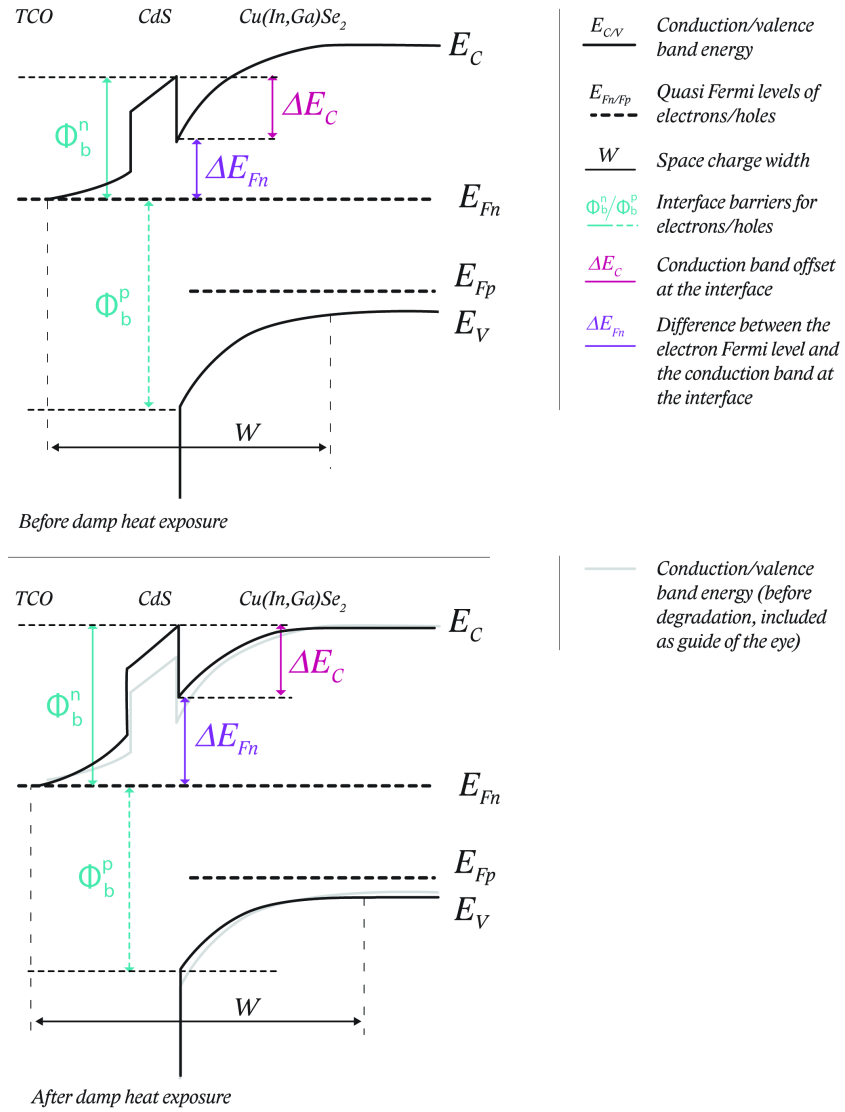


Figure 2.3: Band diagram of a ZnO/CdS/CIGSe solar cell. Black lines: before damp heat, gray lines: after damp heat treatment (assuming a decreasing ZnO and absorber conductivity). Figure adopted from Schmidt et al. [87].

proved an increase in the density of N2 after DH. The relationship between  $V_{OC}$  and the bulk defect density was given (see figure 2.4) and compared to the theoretical relation for a diode ideality of  $A = 2$  at room temperature (dashed line in figure 2.4). Schmidt et al. conclude that changes, i.e. increased recombination, in the bulk or at the grain boundaries are responsible for the  $V_{OC}$  loss [87].

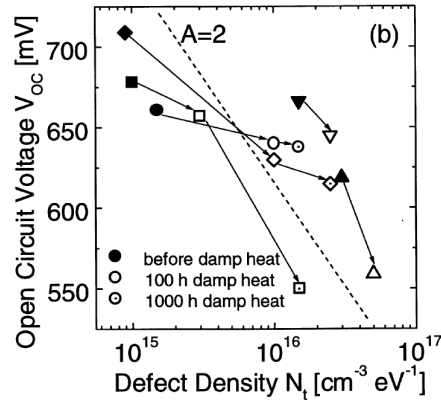


Figure 2.4: Correlation between open circuit voltage  $V_{OC}$  and defect density  $N_t$  of bulk defect  $N_2$  for different cells before, after 100 h and after 1000 h of damp heat exposure. The theoretical dependence for a diode ideality factor  $A = 2$  is given by the dashed line. (Figure taken from [87].)

Deibel et al. observed  $V_{OC}$  and  $FF$  losses on non-encapsulated cells after 438 h of damp heat [88]. Capacitance voltage measurements revealed a reduced net doping after damp heat. From admittance spectroscopy, deep level transient spectroscopy (DLTS) and temperature dependent IV measurements it was concluded that the concentration of observed bulk defects increased after damp heat. An increase in the activation energy of the electronic defect state was measured. The Fermi level pinning at the absorber/buffer interface was lifted after DH and the high band bending (of the as grown cells) reduced [108]; thus  $V_{OC}$  was diminished after damp heat.

Igalson et al. characterized CIGSe sample on glass of the same type as Wennerberg et al. [109, 85]. The solar cells were characterized with IV, admittance spectroscopy and deep level transient spectroscopy (DLTS) prior and after 1000 h of DH. The diode ideality factor increased after DH. The temperature dependence of the diode ideality after damp heat indicated that trapping related tunneling replaced thermally activated emission. An increase in the series resistance as well as a decrease in the parallel resistance was observed. Contact degradation and humidity-leakage due to grain boundaries were given as possible explanations; however, changes in the electronic properties of the absorber could not be excluded as origin.

Via admittance spectroscopy, as well as DLTS and reverse-DLTS, two defects were identified: N1, occurring in a temperature range between 100 K and 240 K, corresponding to the minority carrier signal of the emission from electron traps at or close to the interface and N2, occurring at higher temperatures and only in the damp heat treated devices, being a majority carrier signal. Additionally, the signature N3, an electron trap occurring above 300 K and thus too deep to be detected via admittance spectroscopy, was detected via DLTS in the damp heat treated samples.

The activation energy of N1 was interpreted as the energetic distance of the Fermi level from the conduction band at the interface. Apart from previous interpretations of N2 as a major recombination center in the bulk of the absorber [17], Igalson et al. [109] interpret N2 as a feature originating from the capture of electrons by deep traps (N3). The main effect of damp heat is the creation of midgap donor type defects which are responsible for the  $V_{OC}$  and  $FF$  losses. The origin of the N3 level, introduced by DH, was speculated to be the  $O_{Se}$  defect which, according to theoretical predictions by Zhang et al. [20] is a deep donor.

Deibel et al. [110] found that the net doping of the absorber is reduced after damp heat treatment of the cells (from  $5.5 \times 10^{15}/\text{cm}^3$  down to  $2.5 \times 10^{15}/\text{cm}^3$  after 144 h of DH). Accordingly, the width of the space charge region increased (from around 300 nm before to 600 nm after 144 h of DH). It was also reported that the dominant defect measured with admittance spectroscopy shifts to higher activation energies after damp heat treatment (50 meV before to 195 meV after 144 h of DH) which was interpreted as an interface response, i.e. the activation energy being the difference between the conduction band minimum and the electron Fermi level at the interface. Deibel et al. report that the density of interface states reduces by a factor of two and that the Fermi level appears to be unpinned after DH. The authors claim that the combination of these effects represent a major part of the damp heat induced device degradation that, from an IV point of view, mainly implies  $V_{OC}$  and  $FF$  reduction [108].

Malmstroem et al. compare CIGSe solar cell treated with damp and dry heat, each for 800 h [92]. Two different manifestations of the degradation were found in IV measurements: Blocking behavior and the enhancement of a second diode with high ideality factor. Together they explain the observed losses in  $FF$ ,  $V_{OC}$  and  $J_{SC}$  (see section 2.4.5 for numeric examples). The second diode exhibited tunneling characteristics and was found to be more dominant under illumination. It was suggested that this second diode can be attributed to tunneling-enhanced recombination at the CdS/CIGSe interface. The influence of that diode or recombination mechanism respectively is more important for CIGSe solar cells with high gallium contents and under illumination.

## 3 Experimental Methods

### 3.1 Roll-to-Roll Fabrication

CIGSe solar cells at *Solarion AG* are deposited on a polyimide **substrate**. This plastic foil is 25  $\mu\text{m}$  thin and has a grammage of 41  $\text{g}/\text{m}^2$  [111]. Due to the flexibility of the substrate all necessary deposition steps (see section 1.3.1 for the general design of CIGSe solar cells) can be realized on roll-to-roll equipment (schematically shown in figure 3.1).

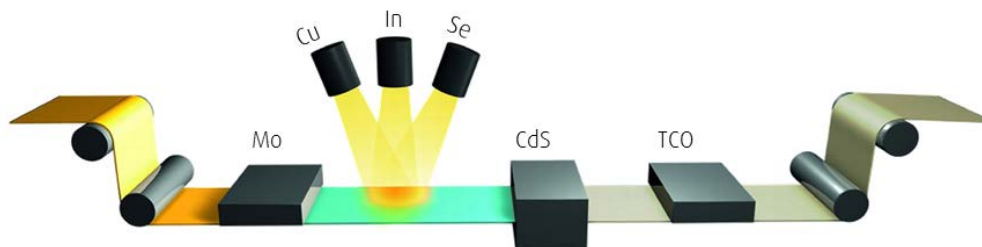


Figure 3.1: Schematic of the *Solarion AG* roll-to-roll deposition process.

The molybdenum **back contact** is sputter deposited in a bilayer structure for better homogeneity with a total thickness of approximately 1  $\mu\text{m}$ .

The CIGSe **absorber** of about 1.6  $\mu\text{m}$  thickness is deposited in a unique ion beam assisted deposition process [111, 112]. While Cu, In and Ga are (co-) evaporated directly onto the substrate, Se vapor is transferred into an ion beam source that cracks large Se molecules into smaller molecules, ionizes (mainly  $\text{Se}^+$ ,  $\text{Se}_2^+$ , also  $\text{Se}_2^{2+}$  [113]) and accelerates them towards the substrate, thus increasing the reactivity of Se on the deposition surface, where the  $\text{Cu}(\text{In,Ga})\text{Se}_2$  is formed. The additional energy input<sup>1</sup> by the Se ion beam enables the deposition of CIGSe already below the thermal limit of the polyimide substrate of approximately 450  $^\circ\text{C}$ . Sodium is provided via co-evaporation from a NaF source during a late stage of the CIGSe deposition. The amount of evaporated sodium can be tuned with the NaF crucible temperature  $T_{\text{NaF}}$ .

The CdS **buffer** layer of about 50 to 80 nm thickness is deposited in a wet chemical process.

<sup>1</sup>The influence of the ion energy on the structural properties of the CIGSe film as well as the formation of electrically active defects was subject to the thesis of Hendrik Zachann [114].

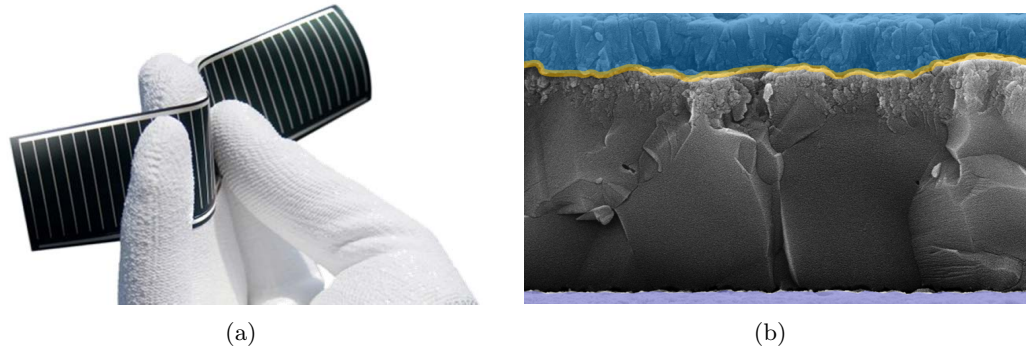


Figure 3.2: (a) Photograph of a flexible  $\text{Cu}(\text{In,Ga})\text{Se}_2$  solar cell by *Solarion AG*. (b) SEM cross section image (see section 3.2.9) of a solar cell by *Solarion AG*. Layers from bottom to top: Mo back contact (purple), CIGSe absorber (gray), CdS buffer (yellow), ZnO window layer (blue).

The **transparent conductive oxide** (window) is a bilayer structure. About 50 nm of *i*-ZnO are deposited by radio frequency sputtering, subsequently approximately 300 nm of ZnO:Al are deposited by direct current sputtering.

Since *Solarion AG* follows a single cell approach for the cell interconnection within the module, individual cells have to be defined from the web with all its functional layers. During **converting**, first, CIGSe, CdS and TCO are locally removed by mechanical scribing (interconnects to the Mo back contact). Second, a metallic grid is silk-screen printed on top of the TCO<sup>2</sup>. After tempering the printed silver conductive paste, individual solar cells (with scribed contacts and printed grid) are cut out of the web (figure 3.2(a)).

A high resolution cross section scanning electron microscopy image of a *Solarion* solar cell is shown in figure 3.2(b) whereas more details about the *Solarion* process may be found elsewhere [111]. Stoichiometries, sodium contents and IV parameters of all solar cells that were studied in this thesis are listed in appendix A.

## 3.2 Characterization

The characterization methods that were applied to the samples in this thesis are briefly discussed in this section. As most of them are standard methods to characterize semiconductors, solids or solar cells, only specific configurations, settings and parameters are described. Fundamental principles of the characterization of semiconductors and of thin

---

<sup>2</sup>Contacting flexible  $\text{Cu}(\text{In,Ga})\text{Se}_2$  solar cells via printed conductive polymers was subject to the thesis of Christian Scheit [115].

film solar cells may be found in the literature<sup>3</sup>.

### 3.2.1 Current–Voltage Measurements (IV)

The current–voltage measurement (IV) is the basic characterization method for any solar cell. Basic parameters such as the power output under different biases, the ideal working point (maximum power point) and the conversion efficiency can be extracted from the IV characteristic. Details about the relevance and interpretation of the electrical characteristic can be found in section 1.2.2.

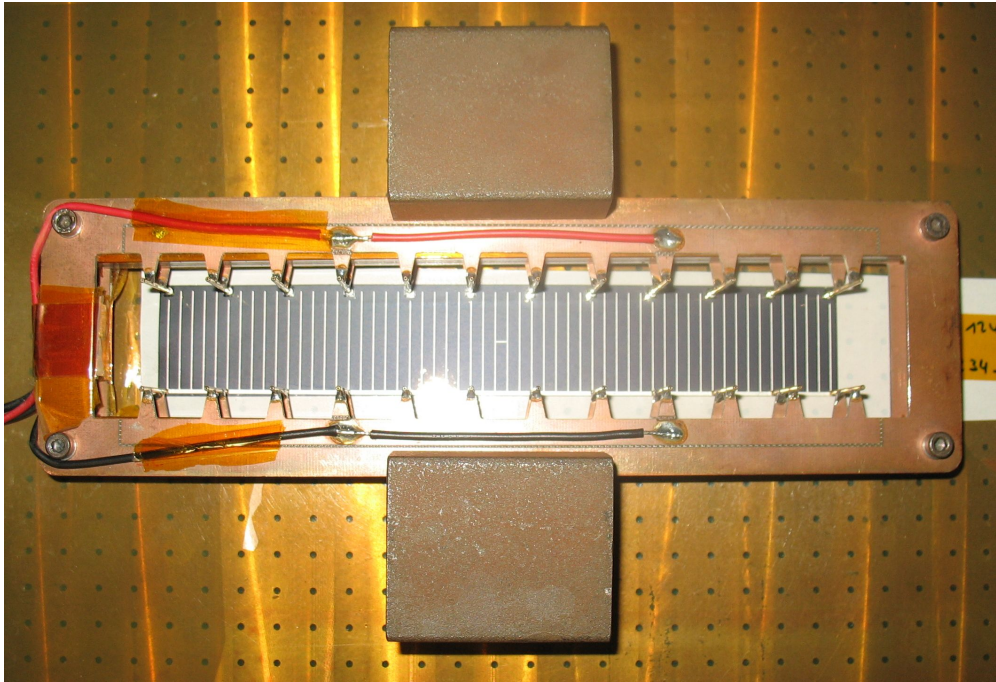


Figure 3.3: Photo of a solar cell (with a size of 190.5 mm times 31 mm) by *Solarion AG* that is contacted in four–point configuration. The upper row of measurement tips contacts the back contact (scribed areas), the lower row contacts the front contact (busbar). Symmetrically, two of each of the 12 measurement tips are used for measuring the voltage whereas ten conduct the current.

All IV measurements were performed under a steady state solar simulator. Standard

<sup>3</sup>General principles and methods for the characterization of semiconductors are described in the book of Grundmann [2]. A comprehensive overview of characterization techniques for thin film solar cells is given in the book edited by Abou-Ras, Kirchartz and Rau [116]. Quantum efficiency, current–voltage, and admittance measurements are reviewed with regard to aspects of interpretation unique to the thin-film solar cells in the paper by Hegedus and Shafarman [117].

test conditions, i.e. an illumination of  $1000 \text{ W/m}^2$ , an AM1.5 spectrum and a sample temperature of  $25^\circ\text{C}$ , were applied. An HMI (hydrargyrum medium-arc iodide) lamp was used as light source. A good thermal contact of the solar cells to the temperature-stabilized sample stage was enabled by suction to that stage. The solar cells under test were contacted by gold plated measuring tips in a four-point configuration in order to allow a good ohmic contact and to eliminate the influence of the contact resistance (between measuring tip and sample) on the measurement (as shown in figure 3.3). A *Keithley 2601A SourceMeter* [118] was used to sweep IV curves; the electrical measurement conditions are listed in table 3.1.

Quantity	Range
voltage	$-0.3$ to $1.2 \text{ V}$
current limit	$2.2 \text{ A}$
steps	500
NPLC <sup>4</sup>	1

Table 3.1: Measurement conditions for IV sweeps

The measurements were controlled, recorded and evaluated with a *Matlab* program (“Solarion IU Mess- & Fit”). This program allowed to extract the open circuit voltage, the short circuit current density, the fill factor and thus the efficiency. Under the assumption of an equivalent circuit of the solar cell diode with a shunt and a series resistance (as depicted in figure 1.5), these resistances could be determined, as well as the diode ideality factor and the saturation current density could be fitted according to the method described by Hegedus et al. [117].

#### 3.2.2 Electroluminescence Imaging (EL)

Electroluminescence imaging is applying a current to the solar cell and recording an image of the emitted light that arises from the recombination of electrons and holes in the solar cell. Since the light emission, according to the reciprocity theorem, is inverse to the absorption, an EL image is a map marking more (brighter) and less (darker) efficient areas of the solar cell. However, the (local) intensity of the electroluminescence is not only determined by the recombination processes in the absorber, but also by e.g. the optical properties of the cell surface (roughness, reflectivity), the transmission coefficient of the TCO and the resistances of the contacts (and thus the local voltages).

The EL images were taken with a *Sensovation coolSamBa HR-830* camera [119]. Pixel binning ( $3 \times 3$ ) was used to increase the sensitivity of the CCD-detector, while trading of

---

<sup>4</sup>The number of power line cycles (NPLC) corresponds to the integration time for one step in the IV sweep. An NPLC value of 1 implies the integration over one period of the power grid’s AC voltage ( $230 \text{ V}$  at  $50 \text{ Hz}$ ), i.e.  $0.02 \text{ s}$ .



resolution: Images with  $1108 \times 834$  pixels were recorded from the CCD with a  $3326 \times 2504$  resolution.

The ambient temperature was room temperature (approximately 298 K) and the EL measurements were performed in a dark environment. In order to ensure a homogeneous current injection, the solar cells were contacted in two-point configuration, i.e. each tip of the frame that was contacting the solar cell supplied current. Thus, only the current flow into the cell could be measured accurately. To also know the voltage drop across the cell, dark IV curves were measured before EL testing, providing the appropriate voltage reading the current that was supplied for EL.

### 3.2.3 Voltage-Dependent Electroluminescence (EL(V))

One way of optimizing the solar cell efficiency is the reduction of inherent losses in the cell<sup>5</sup>. Having access to spatially resolved information of electrical parameters such as the series resistance is desirable and allows the systematic improvement of certain functional parts or layers in the cell. The evaluation of electroluminescence (EL) images is a versatile and convenient method since data acquisition is fast and non-destructive. Several methods are known from literature to calculate mappings of the series resistance from EL images taken at different voltages. In this thesis two of these methods that have been demonstrated on crystalline silicon solar cells are applied to CIGSe solar cells manufactured by *Solarion AG*.

The first method by Hinken et al. [121] requires a series of EL images taken at different but similar voltages as it uses the derivative of the luminescence signal with respect to the voltage to calculate the series resistance mapping. The second method by Breitenstein et al. [122] relies on an iterative calculation requiring only two EL images taken at different voltages to obtain the series resistance mapping as well as the saturation current mapping.

As described in section 3.2.2, the EL images were taken with a *Sensovation coolSamBa HR-830* camera [119] operating at a resolution of  $1108 \times 834$  pixels. The exposure time was 60 s, the ambient temperature was 298 K and dark field images were taken and subtracted from each EL image in order to remove the background.

To obtain spatially resolved information on solar cell parameters like the series resistance, the solar cell is assumed to be a two-dimensional network of parallelly operating equivalent circuits (i.e. a diode with a series and a parallel resistance) in both calculations. The number of equivalent circuits is determined by the resolution of the camera since each pixel is representing and imaging one of these circuits. For each equivalent circuit  $i$  a local diode equation (ideality factor of  $n = 1$  is assumed)

$$J_i = J_{0,i} \cdot \exp\left(\frac{eV_i}{kT}\right) \quad (3.1)$$

<sup>5</sup>This section is based on one of my conference papers [120].

and an exponential dependence of the local luminescence signal  $\Phi_i$  on the local voltage  $V_i$  is assumed

$$\Phi_i = C_i \cdot \exp\left(\frac{eV_i}{kT}\right). \quad (3.2)$$

Figure 3.4 depicts the dependance of the EL intensity on the applied voltage and temperature.

Hinken's approach relies on the derivative of the luminescence signal with respect to the voltage thus making it necessary to capture multiple EL images at different voltages. The series resistance mapping is calibrated under the assumption of  $J_{0,i}/C_i$  being laterally homogeneous.

Breitenstein's method uses an iterative approach requiring only two EL images, cyclically calculating  $j_{0,i}$ ,  $R_{S,i}$  and  $V_{i,1}$ . The local proportionality factor  $C_i$  is split up in a global scaling factor  $f$  and the local saturation current density  $j_{0,i}$ :  $C_i = f/j_{0,i}$ . The series resistance mapping ( $f$  respectively) is scaled such that the average of all local series resistances from the mapping is equal to the global value of the series resistance extracted from the current-voltage characteristic (IV) of the solar cell.

The derivation and details of both calculation methods can be found in the original publications by Hinken et al. [121] and Breitenstein et al. [122].

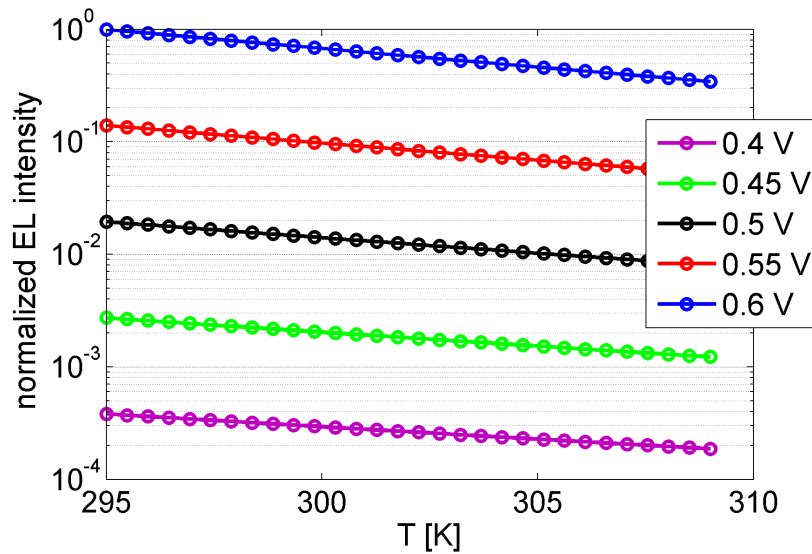


Figure 3.4: Simulation of the EL intensity  $\phi_{EL}$  in dependance on the applied voltage  $V$  and temperature  $T$  ( $\phi_{EL} \propto \exp\left(\frac{eV}{kT}\right)$ ). All intensities are normalized to the value obtained at 0.6 V and 295 K

### 3.2.4 Capacitance–Voltage Measurements (CV)

The capacitance of the diode (solar cell) is typically analyzed using the depletion approximation [2]. The precisely defined and fully depleted (i.e. no free carriers present) space charge region ends abruptly. While the charge density remains constant within the depletion region, its width  $w$  will vary with the applied bias. Neglecting densities of deep states that may actually be present in thin–film semiconductors, the capacitance  $C$  solely originates from the depletion edge. Similarly to a planar plate capacitor it is given by equation 3.3, where  $A$  is the area of the device,  $\epsilon_0$  the vacuum permittivity and  $\epsilon$  the dielectric constant of the semiconductor.

$$C = \epsilon\epsilon_0 \frac{A}{w} \quad (3.3)$$

For an abrupt, one–sided junction<sup>6</sup> or Schottky junction the depletion width  $w$  (or space charge region width) may be described by equation 3.4 where  $V_{DC}$  is the applied bias,  $N_d$  the doping concentration,  $e$  the elementary charge and  $V_{bi}$  the build–in voltage [116].

$$w = \sqrt{\frac{2\epsilon\epsilon_0(V_{bi} - V_{DC})}{eN_d}} \quad (3.4)$$

Measuring the capacitance  $C$  with respect to the applied DC bias  $V_{DC}$  and plotting  $C^{-2}$  versus  $V_{DC}$  (Mott–Schottky plot), the slope yields the CV density  $N_{CV}$  (equation 3.5) that is equal to  $N_d$  under the aforementioned assumptions. A one–dimensional profile of the doping density  $N_d(x)$  through the thickness of the semiconductor<sup>7</sup> may be acquired by using equation 3.5 where  $x = \epsilon\epsilon_0 A / C(V_{DC})$  (from equation 3.3).

$$N_d = N_{CV} = \frac{-2}{A^2\epsilon\epsilon_0 e} \left[ \frac{\partial}{\partial V_{DC}} \left( \frac{1}{C(V)^2} \right) \right]^{-1} \quad (3.5)$$

All CV measurements were carried out with an *Agilent 4284A* [123] impedance analyzer at room temperature in the dark. The capacitances were measured at 10 kHz with voltage biases ranging from 0.3 to  $-1$  V and an AC oscillation amplitude of 50 mV. From the capacitance measured at reverse bias voltages, a profile of the net doping,  $N_d$ , could be derived [117] under the common assumption of  $\epsilon = 10$  for the dielectric constant [124]. All net dopings given refer to the value obtained this way at zero bias voltage.

<sup>6</sup>Typically an one–sided junction is assumed for the case of a  $n^+ - p$  Cu(In,Ga)Se<sub>2</sub> solar cell since the doping of the buffer (n) exceeds that of the absorber (p) by orders of magnitude.

<sup>7</sup> $x$  is measured through the depth of the film while  $x = 0$  is at the interface.

### 3.2.5 Lock-in Thermography (LIT)

Lock-in thermography (LIT) may be used as a tool to locate and investigate shunts in solar cells. According to the lock-in principle, the technique is based on the application of a periodically pulsed bias voltage to the solar cell in the dark and by measuring the temperature modulation of its surface with a sensitive infrared (IR) camera [125]. Thereby, the leakage current through a shunt generates a maximum in the temperature distribution since the local maximum in current density causes a local maximum in heat generation.

The image acquisition typically averages over many periods  $N$  each containing many individual images  $n$  (frames) [126]. The thermography setup allows two operation modes, dark lock-in thermography (DLIT) and illuminated lock-in thermography (ILIT), differing in the excitation of the solar cell. In a DLIT measurement, the solar cell is contacted and a pulsed bias voltage is applied. In contrast, in an ILIT measurement the solar cell does not need to be contacted and is periodically illuminated with a LEDs to generate charge carriers.

The Lock-in thermography setup at *Solarion AG* is a commercial *TDL 640 SM* system by *Thermosensorik GmbH* with an InSb IR camera. The applied measurement parameters for the thermography measurements are listed in table 3.2.

Quantity	Range
lock-in frequency	10 Hz
number of periods $N$	1500
frames per period $n$	10
voltage	-0.5 V

Table 3.2: Measurement parameters for lock-in thermography

### 3.2.6 Light Beam Induced Current (LBIC)

Light beam induced current (LBIC) measurements yield a map that indicates the contribution of each point of the solar cell to the total current. While the current output is measured under short circuit condition the solar cell is scanned locally with a light spot. The LBIC image visualizes which parts of the solar cell are capable of producing high currents and which parts suffer from losses such as recombination.

The employed setup consists of a laser light source (670 nm,  $\approx 1$  mW) mounted on a *DriveSet M30* x-y-stage by *Systec*. The positioning accuracy of the x-y-stage was approximately 25  $\mu\text{m}$  while it could move in steps of 10  $\mu\text{m}$ . The setup shields the solar cell from residual illumination. The current output of the solar cell was measured with a *Keithley 2000* multimeter under short circuit condition [127].

### 3.2.7 Hall Measurements

Hall measurements allow the determination of the specific electrical resistance  $\rho$ , the charge carrier concentration  $n$  and the mobility  $\mu$  of the charge carriers within a semiconductor. The measurement employs the Hall effect, i.e. the measurement of a voltage  $V_H$  across an electric conductor (distance  $d$ ), transverse to an electric current  $I$  in the conductor and perpendicular to a magnetic field  $B_z$ .

$$R_H = \frac{d}{IB_z} \Delta V_H \quad (3.6)$$

Hall coefficients  $R_H$  (equation 3.6) were determined at Universität Leipzig. That setup for Hall measurements works with a magnetic field of 0.43 T and includes automated data analysis (for the specific electrical resistance  $\rho$ , carrier concentration  $n$  and mobility  $\mu$ ) based on a *Matlab* program [128]. From the Hall coefficient the charge carrier concentration  $n$  can be calculated according to equation 3.7.

$$R_H = \frac{1}{nq} \quad (3.7)$$

The mobility  $\mu$  is then calculated via the electric conductivity  $\sigma$  (equation 3.8).

$$\sigma = \frac{1}{\rho} = qn\mu \quad (3.8)$$

### 3.2.8 Transfer Length Measurements (TLM)

Transfer length measurements (TLM) allow the determination of the sheet resistance of a thin conductive layer as well as the contact resistance with it at the same time. A specific test structure is required, i.e.  $n > 5$  line shaped contacts in parallel on top of the thin conductive layer. The resistance measurement is done in a four point configuration. While a current  $I$  is applied to the outermost contacts (contact 1 and  $n$ ), voltage drops are measured between the inner contacts ( $V_{2,3}$ ,  $V_{2,4}$ , ...). From the voltage drops and the current, the resistances between the inner contacts can be calculated:  $R_{i,j} = V_{i,j}/I$ . Finally, these resistances are plotted versus the distances  $l_{i,j}$  between the respective contacts. A linear fit yields *slope* and *intercept* from which sheet resistance  $R_{sheet}$  ( $= slope \times sample\ width$ ) and contact resistance  $R_C$  ( $= intercept$ ), i.e. the resistance between the line shaped contacts and the thin conductive layer, can be calculated.

The TLM method was applied to the back and front contact of complete solar cells in this thesis. For the measurement of the **front contact**, the grid on top of the TCO was used as a test structure. The grid fingers were carefully disconnected from the busbar with a scalpel before the measurement in order to have individual contact lines on top of the TCO.

### 3 Experimental Methods

---

Since the TCO is connected to a stack of (semi-) conducting layers underneath (cf. figure 1.8), it had to be ensured that the current for the resistance measurement of the TCO is only flowing within that layer. By limiting the voltage (during the resistance measurements) to 0.3 V the solar cell diode remained below its threshold voltage and thus blocking. In addition, the resistances  $R_{i,j}$  between the contacts were determined from a linear fit of the measurement of an IV curve ( $-0.3$  to  $0.3$  V, 100 data point) between the contacts. This extended procedure allowed to check the IV characteristics for linearity (which was the case for all measurements) indicating the measurement of an ohmic contact. Hence the requirement of the measurement that the current flows within the TCO layer (and does not cross the pn-junction to spread within the metallic back contact) could be ensured.

At the molybdenum **back contact** no line contacts were available, nor could they be introduced to the complete solar cell. However, the scribed areas that allow an electric contact to the molybdenum back contact within the complete solar cell could be used for the measurement. As shown in figure 3.5, the scribing areas were used as TLM contacts to apply current and to measure voltage drops. In contrast to line shaped contacts, the point contacts do not inject the current homogeneously into the TCO. However, test measurements showed that the voltage drops  $R_{i,j}$  between neighbouring scribing areas are almost identical, except for  $R_{1,2}$  and  $R_{11,12}$  (which include the contacts where the current is applied and which are not included in the TLM fit anyway). This indicates that the inhomogeneous current injection does not impede the application of the TLM method for the given sample geometry. Additionally, the TLM fit ( $R_{i,j}$  versus  $l_{i,j}$ ) was linear for all back contact measurements, indicating a good ohmic contact without non-linear effects.

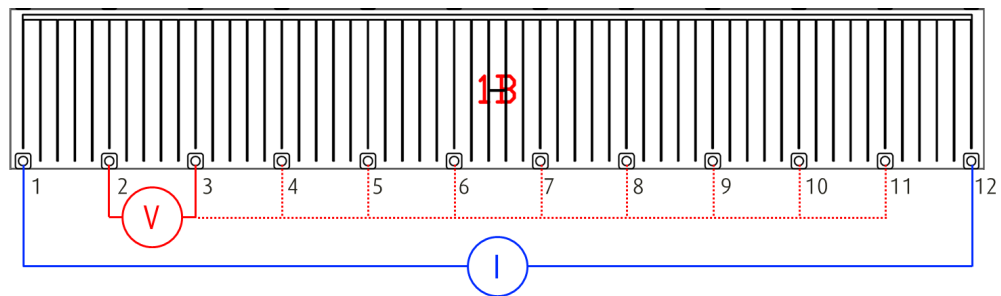


Figure 3.5: Schema of the Transfer Length Method (TLM). The current is applied between the outer contacts (1 and 12). Voltages are measured between contact 2 and 3, 4, ... 11, respectively.

### 3.2.9 Scanning Electron Microscopy (SEM)

SEM is commonly applied to thin film solar cells providing insights into layer thicknesses, surface topographies and other features of the thin film layer stack with a resolution down to 1 nm. Secondary (up to 50 eV) or back-scattered (up to the energy of the primary electrons) electrons emitted from the sample upon (primary) electron radiation are used for imaging, i.e. the primary electron beam is deflected to scan a certain area of the sample. Due to their very small exit depths of a few nanometers and since the secondary electron yield depends on the tilt of a given surface element, secondary electrons are used to image the surface topography [116].

The scanning electron microscopy (SEM) images in this thesis were taken with an *Ultra 55* microscope with field emission gun by *Carl Zeiss*. The microscope is located at the Leibniz Institute of Surface Modification in Leipzig, Germany. The settings of the SEM (acceleration voltage of the electron beam, working distance, magnification) are imprinted within the images. All samples were coated with a very thin (nanometer range) gold film for better surface conductivity in order to avoid charging effects.

### 3.2.10 Secondary Ion Mass Spectrometry (SIMS)

During SIMS ionized species (atoms, molecules, clusters) are sputtered from a sample surface into vacuum, accelerated by an electric field and analyzed with respect to their energy and mass. It is one of the most sensitive composition depth-profiling techniques available. SIMS is best for analyzing trace impurity depth profiles in known matrices (e.g. Na in  $\text{Cu(In,Ga)Se}_2$ ) or measuring relative changes in a matrix constituent in the absence of major changes in the chemistry of the matrix [116].

SIMS was performed with an *ION-TOF "TOF.SIMS 5"* at the Leibniz Institute of Surface Modification in Leipzig, Germany. For the analysis of positive ions (e.g.  $\text{Cu}^+$ ,  $\text{In}^+$ ,  $\text{Ga}^+$ ) a crater of  $300\ \mu\text{m} \times 300\ \mu\text{m}$  was sputtered with a 2 keV oxygen ion beam. For the analysis of negative ions (e.g.  $\text{O}^-$ ,  $\text{F}^-$ ) this crater was sputtered with a 2 keV cesium ion beam. In either case, the analyte was sputtered from a  $50\ \mu\text{m} \times 50\ \mu\text{m}$  surface within this crater by a 15 keV gallium ion beam.

Since sputter rates depend on the ablated material and since different samples might vary slightly in layer thicknesses, the sputter time (from surface to substrate or molybdenum back contact, respectively) for each sample is different. Thus, in order to compare the elemental profiles of various samples conveniently, the sputter time axes of all samples are scaled such that characteristic features in the SIMS profile match (e.g. the drop of the zinc signal at the TCO/CdS interface, the cadmium peak within the CdS buffer or the rise of the molybdenum signal at the CIGSe/Mo interface).

Naturally SIMS yields counts per second as signal and a conversion to stoichiometry is only possible if the material specific sputter rates are known. This is particularly complicated for multi-layer stacks such as our thin film solar cells. However, knowing

the overall stoichiometry (from external XRF measurements) it is possible to re-scale the SIMS profiles at least for one layer (here: Cu(In,Ga)Se<sub>2</sub>). For this purpose, the integrals of the elemental counts (Cu, In, Ga, Se) over the absorber region are normalized to the known stoichiometry. Hence the SIMS data can be represented as stoichiometry (strictly valid only for the absorber) versus sputter depth (with arbitrary units due to the scaling described above).

#### 3.2.11 Laser Induced Breakdown Spectroscopy (LIBS)

LIBS is a laser spectroscopic method capable of rapid, contactless elemental analysis of a specimen<sup>8</sup>. The laser is used dually, as a tool for ablation and excitation for analysis.

In order to ablate the analyte, a pulsed laser is focused onto the surface of the solar cell. The radiation energy (above  $1 \times 10^9$  W/cm<sup>2</sup>) locally heats up the material and evaporates it. Within the analyte vapor and the surrounding gas atmosphere a plasma is generated. In that plasma, excited atoms and ions spontaneously emit radiation. Subsequently, the plasma decays and emits element specific radiation. This radiation is detected with a spectrometer and analyzed spectrally and temporally. Due to the ablation of the material, the solar cell is left with a crater, thus LIBS is considered as a destructive method for chemical analysis.

The lifetime of the plasma after one laser induced breakdown spectroscopy (LIBS) shot is in the order of a few microseconds. The delay between the edge of the laser pulse and the rising of the plasma emission is less than a nanosecond. For a couple of ten to hundreds of nanoseconds the plasma predominantly emits a continuous spectrum. After this distinct maximum in radiation the plasma mostly emits characteristic radiation from atomic transitions around 3 eV.

Typically, a spectrum is integrated over a certain integration time  $t_{int}$ . To discard the peak of continuous radiation, a delay  $t_{delay}$  is introduced between the laser pulse and the onset of the integration interval. The position of peaks in the measured spectra (intensity vs. wavelength) is allocated on the basis of tabulated data. The height of a peak is a measure of the concentration of the respective element. However, since it depends on other factors, such as the energy of the laser pulse, plasma temperature, sample surface and detector response function as well, the ratio of an analyte peak to the peak of a predominant element in the specimen is a more reliable measure.

In this thesis LIBS is used to determine the sodium content of CIGSe solar cells (in relation to copper, indium or gallium). The applied measurement parameters are listed in table 3.3.

---

<sup>8</sup>The description of LIBS is adopted from the book of Reinhard Noll [129]



Parameter	Value
laser	Nd:YAG
wavelength	1064 nm
pulse energy	50 mJ
pulse width	7 ns
integration time $t_{int}$	200 $\mu$ s
delay time $t_{delay}$	0.3 $\mu$ s
shots	100

Table 3.3: Measurement conditions for LIBS

### 3.2.12 Scanning Laser Microscopy

Scanning laser microscopy upgrades the capability of a conventional optical microscope by the ability to render three dimensional images. For that purpose a laser is scanning the surface of the sample from different distances. If the surface of the sample is in focus the highest laser intensity is detected. Thus information on the sample topography are obtained and a 3D image can be calculated. Different representations of the measurement are possible, e.g. the plain optical image, a superposition of optical and laser scanning image or a height map from the laser scanning image.

The laser scanning microscopy images in this thesis were obtained with a *Keyence VK-X210* at Universität Leipzig. The optical magnification was  $150\times$  and the laser had a power of 0.95 W at a wavelength of 408 nm ( $\approx 3$  eV). The CIGSe solar cell samples were placed on glass object plates for better handling under the microscope.

## 3.3 Sample Treatment

### 3.3.1 Damp Heat

According to a standard of the *International Electrotechnical Commission*, IEC 61646, “damp heat” refers to 85 % relative humidity at 85 °C. Unless stated otherwise, all damp heat treatments in this thesis were performed under these conditions. The cells were treated in a commercially available climate chamber by *CTS GmbH*. More details about damp heat may be found in section 2.

The samples received the damp heat treatment under open circuit conditions and without intentional illumination (the climate chamber has a small window). In order to accelerate the degradation process compared to module degradation experiments and to study aging of the bare solar cells, none of them was encapsulated.

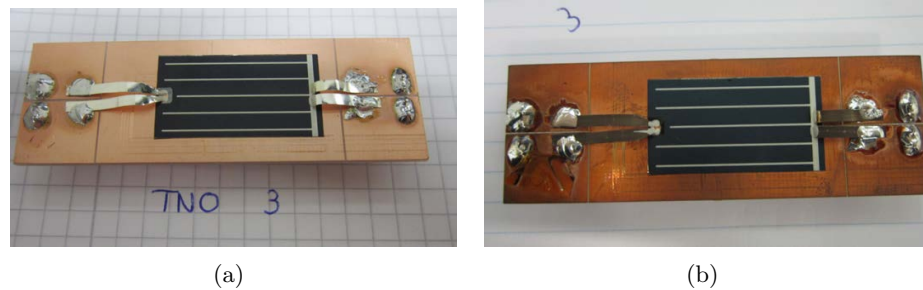


Figure 3.6: Sample holders for the hybrid degradation setup at *TNO Eindhoven* for in-situ IV measurements under damp heat. (a) Before and (b) after 730 h (1 month) of damp heat.

#### 3.3.2 Dry Heat

In section 4.1 a comparison between damp and dry heat treatment of the samples is presented. The samples treated with “dry heat” were kept in a convection oven at 85 °C. While the humidity was not controlled actively, a humidity below 10 % can be assumed<sup>9</sup>.

#### 3.3.3 Damp Heat & in-situ IV

In-situ IV measurements under damp heat conditions were done in a unique setup at *TNO Eindhoven* in the Netherlands<sup>10</sup>. The “hybrid degradation setup” [130] consists of a damp heat chamber (temperature chamber model ARL-1100 by *ESPEC GmbH*) with a 80 × 80 cm<sup>2</sup> window in the flank. A solar simulator by *Eternal Sun B.V.* illuminates up to 12 samples of a size of approximately 5 cm<sup>2</sup> that are placed perpendicular to the incident illumination inside the climate chamber. Thus the samples are exposed to illumination, temperature and humidity at the same time<sup>11</sup>. Each sample is placed on an individual sample holder (cf. figure 3.6) that is equipped with a temperature sensor. A shutter in front of the window allows to shade the samples temporarily. Current-voltage measurements can be performed with a *Keithley 2440 5A* source meter and a *National Instruments PXI-1011* multiplexer to switch between the samples.

---

<sup>9</sup>The samples were put into the convection oven at room temperature which was then locked and heated up. Even if the relative humidity at room temperature (25 °C) was 100 %, assuming a constant water vapor density, at 85 °C the relative humidity would be approximately 8 %.

<sup>10</sup>I gratefully acknowledge the cooperation with Mirjam Theelen that allowed these measurements and the experimental support by Henk Steijvers in the lab (both from *TNO Eindhoven*).

<sup>11</sup>Due to the illumination the actual sample temperature ( $\approx 100$  °C) differs from the nominal damp heat condition (85 °C).

## 4 Cu(In,Ga)Se<sub>2</sub> Solar Cells under Damp Heat

This first out of three chapters presenting experimental findings deals with the influence of damp heat on the electrical behavior of the Cu(In,Ga)Se<sub>2</sub> (CIGSe) solar cell as a device. In section 4.1 the role of humidity as part of the damp heat treatment will be discussed. Section 4.2 investigates the influence of damp heat on the electrical properties of the cell. Statistics on IV data (section 4.2.1) and low temperature IV data (see section 4.2.2) as well as CV data (section 4.2.3) will be presented. In section 4.3 the kinetics of the degradation process is analyzed and degradation rates for the investigated solar cells are given. Section 4.4 gives insight into the role of the back contact and the window layer for the degradation of the solar cell. The influence of the absorber and specifically its sodium content on the degradation of the Cu(In,Ga)Se<sub>2</sub> solar cell will be discussed in chapter 5.

### 4.1 Dry versus Damp Heat or the Role of Humidity

During damp heat testing the solar cell is exposed to an atmosphere of 85% relative humidity at 85 °C. For a better understanding of how these artificial aging conditions affect the solar cell it is important to discriminate between the influence of heat and humidity. Thus, two similar sets of samples were treated with either heat or damp heat (for experimental conditions see section 3.3.2 and 3.3.1, respectively).

In figure 4.1 results of the IV measurements of three samples each are shown comparing damp and dry heat treatment. The set of samples exposed to dry heat showed no significant aging effect in any of the IV parameters whereas the set of samples exposed to damp heat showed a degradation behavior. While the open circuit voltage and the short circuit current remained unaffected mainly the fill factor and the efficiency were influenced.

Regarding the damp heat treatment, the diode related internal parameter  $V_{OC}$  as a measure for the CIGSe/CdS junction quality and  $J_{SC}$ , being related to carrier collection, did not change significantly. Thus, the observations from figure 4.1 suggest that the performance after aging was limited by a decreasing fill factor caused by the detrimental influence of an increased series resistance (as discussed in the next section and shown in figure 4.3(b)). The  $R_S$  values determined from the IV characteristics confirmed an increase by a factor of 1.4. Since this change was only be observed for samples exposed

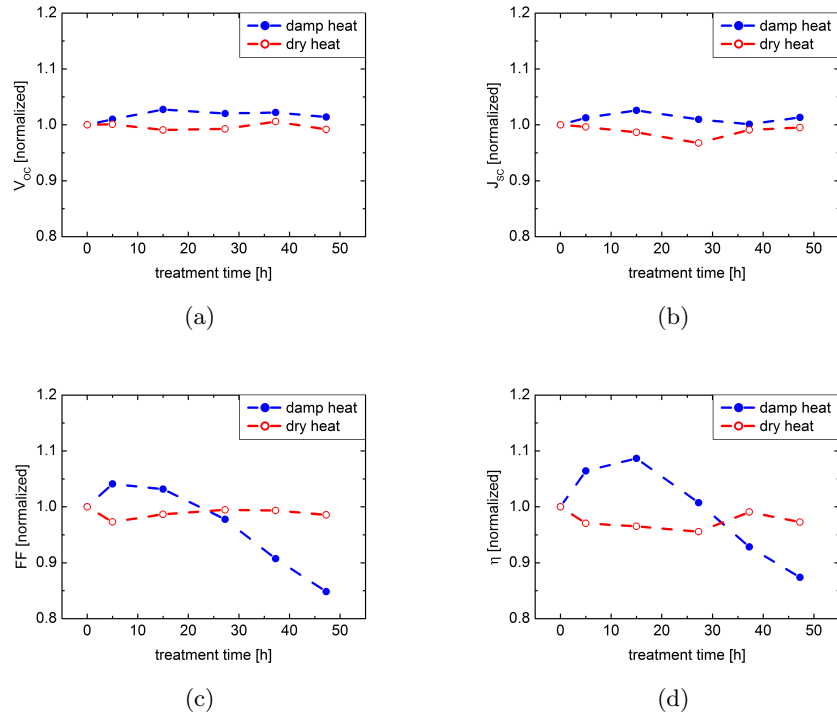


Figure 4.1: Comparison of damp and dry heat treatment; average of three samples each; (a) open circuit voltage (b) short circuit current density (c) fill factor (d) efficiency; all values are scaled to initial (0 h) value

to damp heat, it can be concluded that moisture plays a key role in the degradation process.

In contrast to the overall degradation of the damp heat samples, intermediate increases in fill factor and efficiency were observed after 5 h and 15 h of damp heat treatment. More experimental data on this observation can be found in section 4.2.1 and 4.3.3 while their discussion is to be found in section 7.1.

## 4.2 Damp Heat

### 4.2.1 Statistics on Electrical Parameters

In order to show the influence of damp heat on the electrical behavior of flexible  $\text{Cu}(\text{In,Ga})\text{Se}_2$  thin film solar cells a random sample of 82 solar cells was drawn out of the production of *Solarion AG* (for a description of the roll-to-roll manufacturing

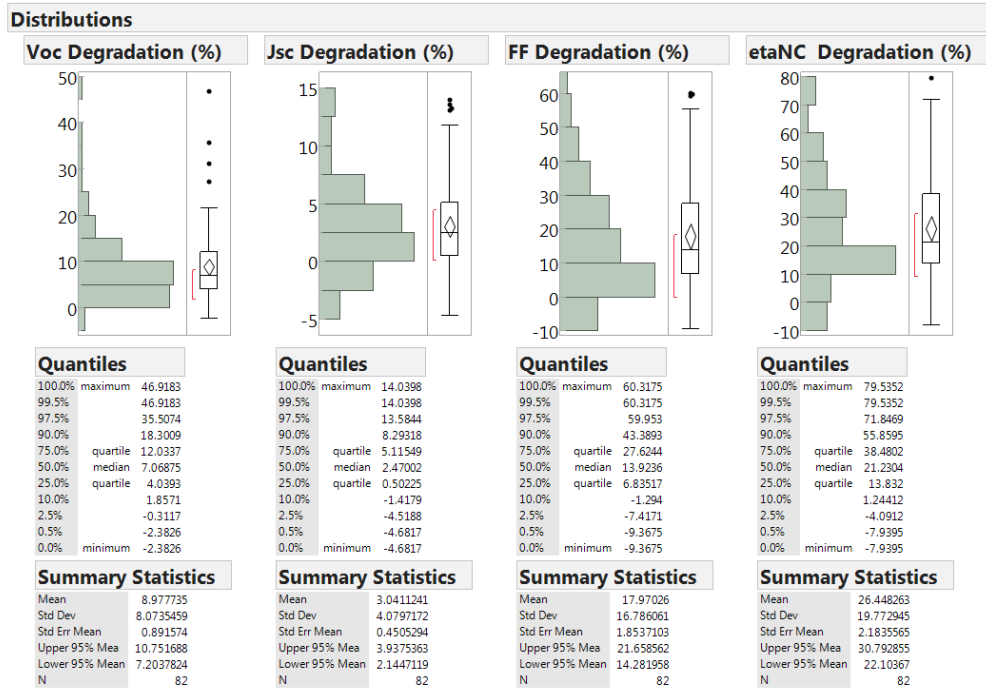


Figure 4.2: Statistics of IV parameters of 82 solar cells after 75 h of damp heat.

process see 3.1). IV was measured at the solar simulator (see section 3.2.1) before and after 75 h of damp heat treatment (see section 3.3.1).

The degradation after (damp heat) treatment is defined according to equation 4.1, where  $X$  is one of the IV parameters, e.g. open circuit voltage [V] ( $V_{OC}$ ), short circuit current density [ $\text{mA}/\text{cm}^2$ ] ( $J_{SC}$ ), fill factor ( $FF$ ) or efficiency [%] ( $\eta$ ).

$$\text{degradation}(X) = \frac{X_{\text{initial}} - X_{\text{treated}}}{X_{\text{initial}}} \quad (4.1)$$

In figure 4.2, the statistical distribution of the degradation is shown for  $V_{OC}$ ,  $J_{SC}$ ,  $FF$  and  $\eta$ . On average, the open circuit voltage degrades around 9% and the short circuit current density around 3%. Compared to  $FF$  and  $\eta$  the distribution of  $V_{OC}$  and  $J_{SC}$  degradation is tighter. The  $FF$  degrades around 18% and the efficiency around 26% on average. For all four IV parameters, outliers have a certain influence on the average degradation, as the mean values are always above the median. From that statistics it is clear that the degradation of the fill factor is the strongest contribution to the overall efficiency degradation of the solar cell.

It should be noted that some solar cells (statistically one out of 40) actually increase their efficiency after damp heat (i.e. negative degradation in figure 4.2). An increase in

$V_{OC}$ ,  $J_{SC}$  and  $FF$  was observed for a small fraction of the samples, respectively. Further experimental findings on this non-intuitive observation can be found in section 4.3.3 while their discussion is in section 7.

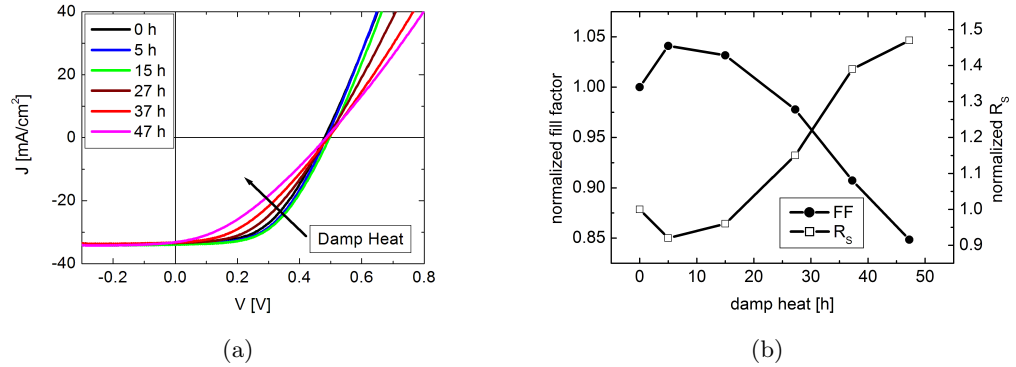


Figure 4.3: Example of IV curves of a flexible solar cell after different damp heat exposure times (cumulative) (a) IV curves vs. damp heat exposure (b) Extracted  $FF$  &  $R_s$  vs. damp heat exposure time

While the details of the degradation kinetics shall be presented in section 4.3, figure 4.3(a) shows an example of IV curves of one solar cell measured after different damp heat exposure times. In accordance with the statistical data (figure 4.2) we observe no significant change in  $V_{OC}$  nor  $J_{SC}$ . However, the curvature of the IV characteristic changes with increasing damp heat exposure and the fill factor decreases (see figure 4.3(b)). The comparison of the series resistance to the fill factor, as shown in figure 4.3(b), reveals the origin of the fill factor decline, i.e. the increase of the series resistance.

## 4.2.2 Low-temperature Current-Voltage Characteristics

Temperature dependant IV measurements were done in a range from 50 to 300 K on standard  $\text{Cu(In,Ga)Se}_2$  solar cells. Due to the spatial limitations of the cryostat<sup>1</sup> that was used to cool the solar cells they had to have a size of only around  $1 \text{ cm}^2$ . The samples were characterized before and after 5 h, 15 h, 30 h and 50 h of damp heat.

Figure 4.4 shows a set of IV curves of the same sample taken after different periods of damp heat. At room temperature (300 K; see figure 4.4(a)) the degradation of the IV characteristic follows the pattern described in section 4.2.1, i.e. the open circuit voltage and the short circuit current remain fairly constant but the fill factor decreases (due to

<sup>1</sup>More details about the low temperature measurement setup may be found elsewhere [13].

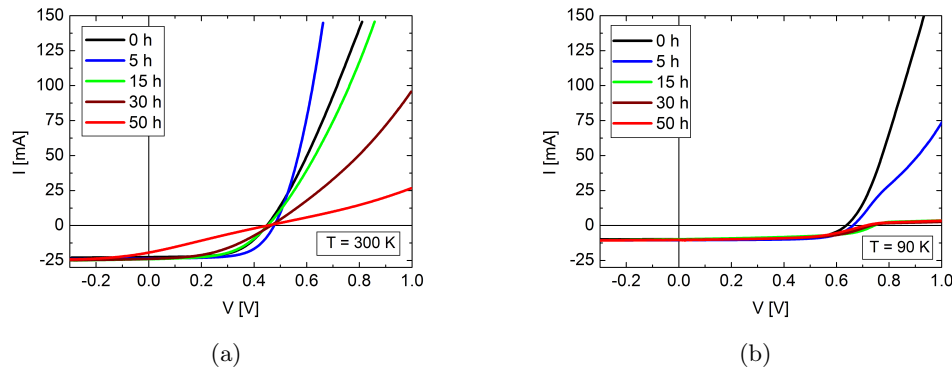


Figure 4.4: IV measurements (a) at 300 K and (b) at 90 K after different damp heat durations (cumulative).

an increase in the series resistance that was observed for this sample as well). After 50 h of damp heat the sample barely exhibits a diode-like IV characteristic typical for a solar cell; the fill factor has diminished to 25 % and the IV curve is almost ohmic.

At low temperatures (90 K; see figure 4.4(b)) and after damp heat exposure a roll-over becomes apparent. This current blocking behavior of the cell in forward direction can be seen in the first quadrant of the IV plot in figure 4.4(b) for all damp heat exposures starting at the measurement after 5 h of damp heat. The equivalent circuit model (figure 1.5) introduced in section 1.2.2 cannot fit the roll-over characteristic. However, an extension of the equivalent circuit by another element, consisting of a diode ( $I_{RO}$ ) and a parallel (shunt) resistor  $R_{RO}$ , that models the blocking behavior in forward direction and is thus applied opposed to the main diode can model the observed roll-over behavior (figure 4.5).

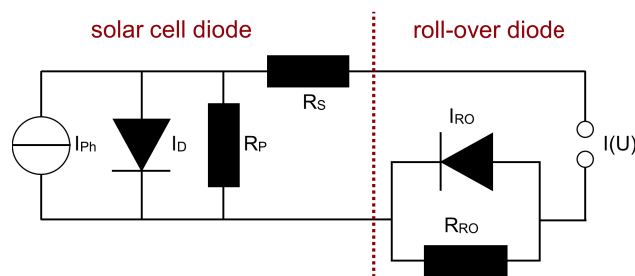


Figure 4.5: Equivalent circuit for a solar cell (as shown in figure 1.5) with an additional (blocking) “roll-over” diode

The IV data for all measured temperatures and all damp heat exposures of that

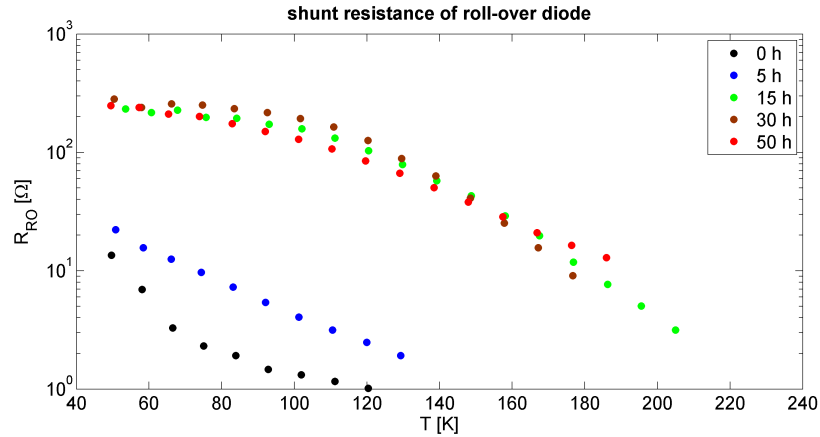


Figure 4.6: Extracted roll-over resistances  $R_{RO}$  according to equivalent circuit from figure 4.5 for different temperatures of the IV measurement and different damp heat exposures (cumulative).

sample were fitted to the roll-over equivalent circuit model (from figure 4.5). The roll-over resistance was extracted and plotted in figure 4.6. If the roll-over resistance  $R_{RO}$  increases, the roll-over effect, i.e. the current blocking in forward direction, becomes larger<sup>2</sup>. Figure 4.5 shows clearly that the roll-over effect increases with longer damp heat exposure. In addition, the roll-over already becomes visible at higher temperatures.

### 4.2.3 Capacitance–Voltage Characteristics

Capacitance–voltage measurements (CV) were carried out according to the procedure described in section 3.2.4. A profile of the net doping was derived from each CV measurement and the net doping at zero bias voltage  $N_d$  was extracted as a parameter to compare different cells. The samples were prepared with different sodium contents in the absorber (batch 2A–1173, cf. section 5.3.1).

In figure 4.7 the influence of the sodium content on the net doping  $N_d$  of the absorber, averaged over more than 150 cells in total, is depicted (no damp heat). It is evident from the graph that the net doping increases with increasing sodium content.

In a cyclic approach consisting of CV measurements alternating with periods of damp heat exposure a time resolved insight into the degradation process was obtained. Two sets of Cu(In,Ga)Se<sub>2</sub> solar cells (six cells each) with different sodium contents were exposed to damp heat and for comparison to dry heat as well (cf. section 4.1). In

<sup>2</sup>The larger the roll-over resistance  $R_{RO}$  the more current flows through the roll-over diode  $I_{RO}$  thus increasing the blocking behavior in forward direction.



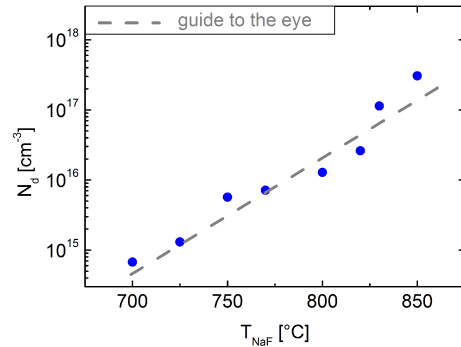


Figure 4.7: Net doping  $N_d$  of the absorber in dependence of the sodium content (denoted as  $T_{NaF}$ ) in the  $\text{Cu}(\text{In,Ga})\text{Se}_2$  layer. Averaged values of more than 150 cells in total are depicted.

section 5.3.1 the degradation of the IV parameters of the same samples is described and further details about the samples may be found (cf. table 5.2).

The trend of the capacitance (at zero bias) under damp heat treatment is plotted in figure 4.8(a). This rather unusual representation of the CV data will be used in the discussion (section 7) to explain the degradation behavior of our solar cells.

The more common representation of the CV data, the net doping of the absorber as derived from the CV, is shown in figure 4.8(b). In accordance with figure 4.7, the samples with  $11.33\times$  sodium content exhibit a higher net doping, as more sodium was supplied during CIGSe deposition. Apparently, for the samples with  $0.52\times$  sodium content, the net doping remains unaffected under dry heat treatment, while there is a slight decrease for the samples with  $11.33\times$  sodium content. Exposure to damp heat significantly decreases the apparent net doping for both sample sets. Thereby, this effect is much more pronounced for the samples with higher sodium content ( $11.33\times$ ).

### 4.3 Degradation Kinetics

In this section data from in-situ IV measurements of solar cells under damp heat will be presented. Testing the cells under these conditions of artificial aging — without interruptions — allows an undisturbed insight into the degradation kinetics of the solar cells.

The data shown here were obtained with the setup described in section 3.3.3. The presented IV measurements were done in 150 steps in the range of  $-0.3$  to  $1.2$  V with a current limit of 350 mA.

The samples differed in their sodium content. One set of three samples had a low

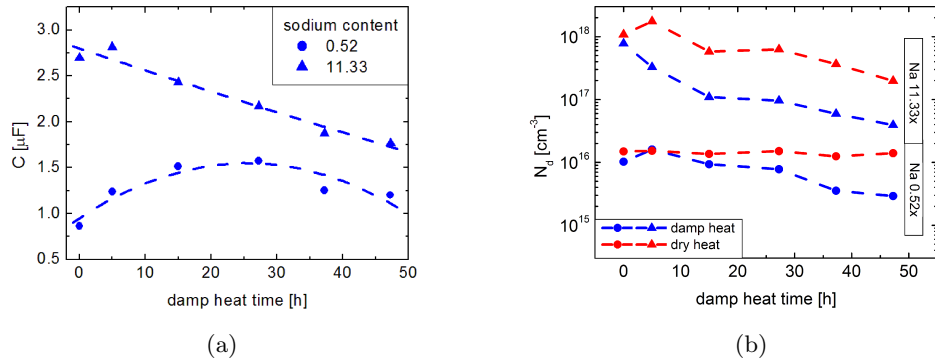


Figure 4.8: CV measurements after damp heat exposure (a) capacitance  $C$  and (b) net doping  $N_d$  at  $V = 0$  V. Sodium contents as normalized from LIBS.

sodium content<sup>3</sup>, i.e.  $0.44\times$  (normalized from LIBS, cf. section 3.2.11 and 5.1) or characterized by the sodium fluoride crucible temperature during CIGSe deposition  $T_{\text{NaF}} = 710^\circ\text{C}$  (cf. section 1.3.4 and 3.1), respectively. The other two sets of samples (three solar cells each) had a medium, i.e.  $0.66\times$  ( $T_{\text{NaF}} = 735^\circ\text{C}$ ), and a high, i.e.  $0.86\times$  ( $T_{\text{NaF}} = 760^\circ\text{C}$ ), sodium content.

### 4.3.1 In-situ Current–Voltage Measurements

The hybrid degradation setup was used to study the degradation kinetics of 12 samples for approximately one month. During the first three days each solar cell was IV tested 15 times per hour (every 4 min). Later on the solar cells were measured six times per hour (every 10 min).

Figure 4.9 illustrates how the treatment influences the solar cells in their IV behavior. The experimental run started in the dark at room temperature with a dry atmosphere. First, the solar simulator was switched on. That results in a shift of the dark IV curve by the magnitude of the short circuit current to the illuminated IV curve along the current axis (cf. step 1 in figure 4.9(a)). Second, the setup was heated from room temperature to  $85^\circ\text{C}$ . The temperature dependance of the IV curve, mainly with respect to the open circuit voltage, could be observed (cf. step 2 in figure 4.9(a)). Finally, the setup provided a damp atmosphere with 85% relative humidity at  $85^\circ\text{C}$ . Under these standardized artificial aging conditions a gradual change in the IV curve, mainly in the

<sup>3</sup>The terms “low”, “medium” and “high” are used as a convenient nomenclature for the different sodium contents in this section. They do not imply an absolute measure for the sodium content in a CIGSe solar cell. A detailed analysis of the sodium content in the present samples compared to those in other samples is given in section 5.1.

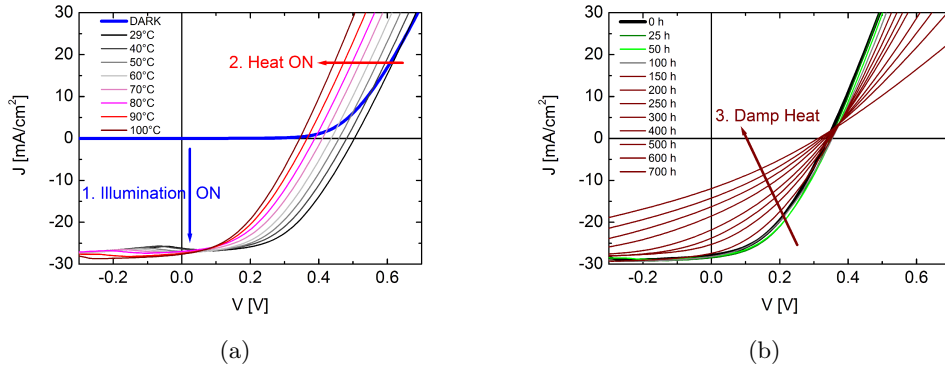


Figure 4.9: IV curves measured (a) at room temperature in the dark, after switching on the solar simulator and during heating (b) in-situ under damp heat. The CIGSe solar cell had a sodium content of 0.44 (normalized from LIBS;  $T_{NaF} = 710^\circ\text{C}$  respectively).

series resistance (and thus a lower slope under positive forward currents), was observed (cf. step 3 in figure 4.9(b)).

### 4.3.2 Kinetics

From each curve of all IV measurements during the degradation experiment (and for all samples), the open circuit voltages, short circuit current densities, fill factors and efficiencies were derived (cf. figure 4.10 and 4.11, respectively). All parameters exhibit a certain temperature dependant behavior. However, for  $V_{OC}$  it is most prominent as shown by the steep drop during the first 15 h of the experiment, when the temperature was ramped up from room temperature to  $85^\circ\text{C}$  (cf. figure 4.10(a)). It is possible to derive temperature coefficients for all IV parameters from this period<sup>4</sup>.

The time resolved trends in the IV parameters reveal the degradation kinetics of the solar cell under damp heat (figure 4.10 and 4.11).

For the **open circuit voltage**  $V_{OC}$ , three different classes of samples clearly evolve from the data. They can be differed by their respective sodium content (as marked in figure 4.10(a) and 4.10(b)). The samples with a low sodium content of  $0.44 \times$  ( $T_{NaF} = 710^\circ\text{C}$ ) have the lowest  $V_{OC}$  before damp heat, followed by the samples with a high sodium content of  $0.86 \times$  ( $T_{NaF} = 760^\circ\text{C}$ ) and  $0.66 \times$  ( $T_{NaF} = 735^\circ\text{C}$ ). This may be explained by two factors: The increasing  $V_{OC}$  with increasing sodium content that was (and is widely) observed at room temperature and the decrease in  $V_{OC}$  with temperature (temperature

<sup>4</sup>A paper on the *Determination of the Temperature Dependency of the IV Characteristics of CIGS Solar Cells* is in preparation [131] (cf. appendix B).

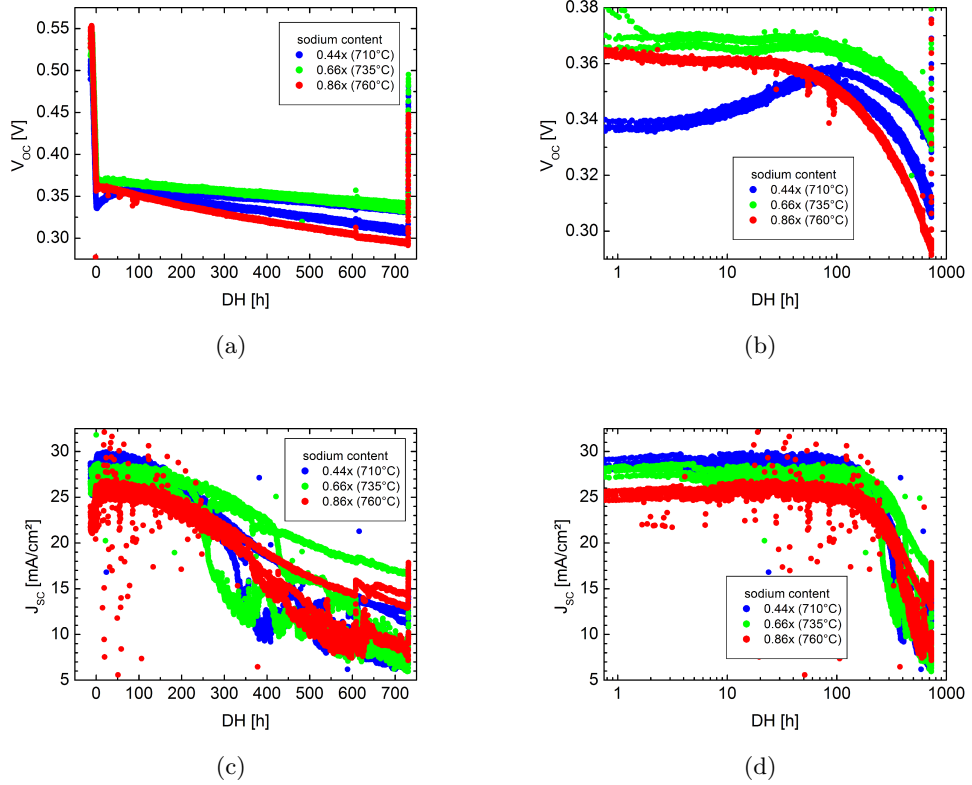


Figure 4.10: Extracted IV parameters (from top to bottom:  $V_{OC}$ ,  $J_{SC}$ ) from in-situ IV measurements under damp heat. Three samples were measured per sodium content (given as normalized value from LIBS and  $T_{NaF}$ ). Note the origin of the DH timescale being the onset of the damp heat, i.e. after heating up the climate chamber (cf. figure 4.9), thus the heating period cannot be seen in the semi-logarithmic representation (right column).

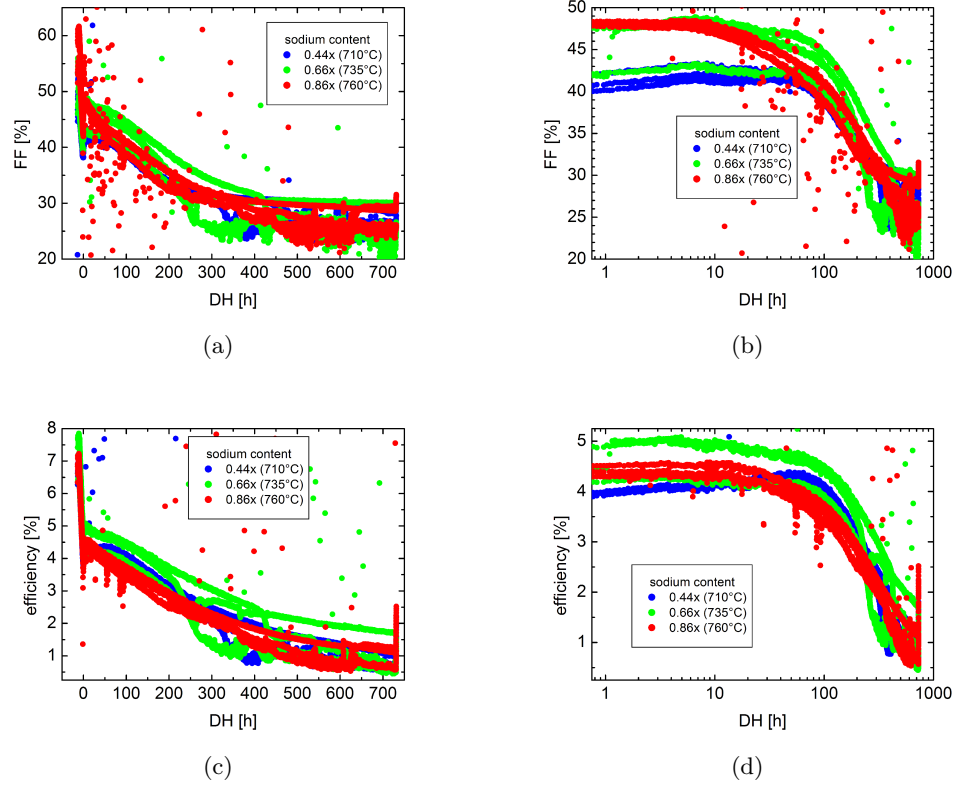


Figure 4.11: Extracted IV parameters (from top to bottom:  $FF$ , efficiency) from in-situ IV measurements under damp heat. Three samples were measured per sodium content (given as normalized value from LIBS and  $T_{NaF}$ ). Note the origin of the DH timescale being the onset of the damp heat, i.e. after heating up the climate chamber (cf. figure 4.9), thus the heating period cannot be seen in the semi-logarithmic representation (right column).

coefficient). While clearly observed for all samples, the latter was lowest for the samples with a medium sodium content ( $0.66\times$  or  $T_{NaF} = 735^\circ\text{C}$ , respectively) in this experiment. The temperature driven  $V_{OC}$  decrease compared to the  $V_{OC}$  degradation under damp heat can be easily seen in figure 4.10(a)). Specifically for the samples with low sodium content an initial increase in  $V_{OC}$  was observed after the onset of damp heat (cf. figure 4.10(b)). This will be discussed in section 4.3.3.

Figure 4.10(c) shows the degradation of the **short circuit current density**. As the temperature coefficients for  $J_{SC}$  are rather low, compared to those of  $V_{OC}$ , and positive with increasing temperature,  $J_{SC}$  exhibits only a small increase during temperature ramp up (i.e. the first 15 h of the experiment). Figure 4.10(d) gives a semi-logarithmic representation of the data. From that representation of the data we can see that most cells do not show a severe degradation for about 200 to 300 h, however, after that period, the short circuit currents of all samples break down, irrespective of their sodium content.

Figure 4.11(a) and 4.11(b) illustrate the time dependent behavior of the **fill factor**. Cells with initially higher fill factor (those with higher sodium content) suffer from a higher temperature coefficient during heat up. From the onset of damp heat up to about 100 h, there are two groups of samples, one showing higher fill factors but a more pronounced degradation compared to the other group that, in fact, exhibits almost no  $FF$  degradation. After 100 h, the samples from the latter group begin to decrease more severely, then all samples degrade in  $FF$  until about 300 to 400 h. At that time, fill factors of around 25 % are reached, indicating the destruction of the device in terms of its function as a solar cell (with a diode-like IV curve).

The degradation behavior of the **efficiency** of the cells is shown in figure 4.11(c) and 4.11(d). All solar cells drop in efficiency during heat-up. The actual efficiency degradation with damp heat, likewise the  $FF$ , turns from a slight decrease to a more severe decrease after approximately 100 h of damp heat.

### 4.3.3 Two Stages

As mentioned in section 4.3.2, three different classes of samples with different sodium contents can be differed by their degradation behavior. Especially for the open circuit voltage and the fill factor differences in the aging process between these classes can be observed.

All samples with low sodium content show an increase in  $V_{OC}$  before a final decrease sets in (cf. figure 4.10(a)). This suggests that there is a superposition of a beneficial and a deteriorating mechanism involved in the damp heat degradation process. For the samples with medium sodium content this behavior can barely be observed, however,  $V_{OC}$  decreases not immediately after the onset of damp heat but the decrease is delayed for about as long as the  $V_{OC}$  increases for the samples with low sodium content (for approximately 50 h). For the samples with the highest sodium contents, the decrease of  $V_{OC}$  starts more or less immediately with the onset of damp heat.

This observation shall be used to differ between two stages in the degradation process, as indicated in figure 4.12(a) and 4.12(b). **Stage 1**, being characterized by an initial improvement of the IV parameters (here  $V_{OC}$ ). This stage is distinct for  $V_{OC}$  for the samples with low sodium content and is suppressed for high sodium contents. **Stage 2** is characterized by a steady decrease of the IV parameters. It is, for all observed samples, a final stage of the aging process that ends with the “death” of the solar cell, i.e. an ohmic instead of a diode-like IV characteristic ( $FF = 25\%$ ).

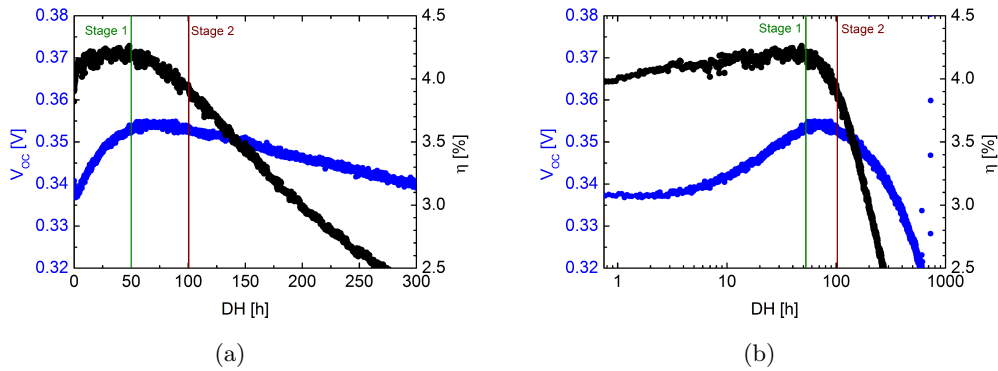


Figure 4.12: Two Stages of the aging process as observed with in-situ IV measurements under damp heat. (a) Linear time scale, (b) Logarithmic time scale. The CIGSe solar cell had a sodium content of 0.44 (normalized from LIBS;  $T_{NaF} = 710\text{ °C}$  respectively).

#### 4.3.4 Degradation Rates

For all four IV parameters,  $V_{OC}$ ,  $J_{SC}$ ,  $FF$  and efficiency, linear degradation rates were extracted. To ensure an appropriate data quality, only measurements with fill factors above 30% were taken into account. This, on the one hand, discards all measurements later than approximately 300 h (when the device is broken anyway) and, on the other hand, filters out outliers. The degradation rates were fitted for stage 2 only since stage 1 was seen explicitly for the samples with low sodium content only. A linear regression was used, that worked perfectly for  $V_{OC}$  and which served as a very good approximation for  $J_{SC}$ ,  $FF$  and efficiency. An example for the linear fit in the range of 100 to 300 h is given in figure 4.13. Decreasing IV parameters, i.e. negative slopes in the linear regression of the respective IV parameter vs. time, yield positive degradation rates (cf. equation 4.1).

These degradation rates are shown in figures 4.14(a), 4.14(b), 4.14(c), 4.14(d) and denoted in table 4.1 for the respective IV parameters. The open circuit voltage has degradation rates ranging from 42.5 to 106.7  $\mu\text{V/h}$ . Samples with initially higher sodium

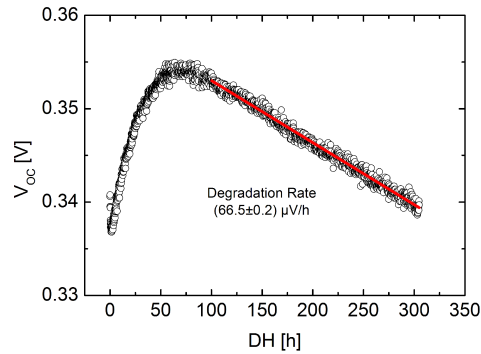


Figure 4.13: Example of a linear fit of the degradation rate in stage 2 of the aging process under damp heat. The  $V_{OC}$  data are taken from a sample with low sodium content, i.e.  $0.44\times$  (cf. figure 4.10(a)).

content show a more pronounced  $V_{OC}$  degradation. The short circuit current density degrades at rates ranging from  $11.8$  to  $40.7 \mu\text{A}/(\text{cm}^2 \text{h})$ . The  $J_{SC}$  degradation is more pronounced for samples with lower sodium content. The fill factor degradation rates are about  $0.039$  to  $0.071$  %-pts/h. Samples with low and high sodium content exhibit a less severe degradation, whereas the samples with medium sodium content exhibit a slightly more pronounced degradation. The maximum power output of the cell (proportional to efficiency under constant illumination), which combines all aforementioned trends, degrades at rates ranging from  $7.1$  to  $10.0 \mu\text{W}/(\text{cm}^2 \text{h})$ . The influence of the sodium content on these degradation rates is within the level of confidence for these rates (calculated from the means over the three samples of sodium class).



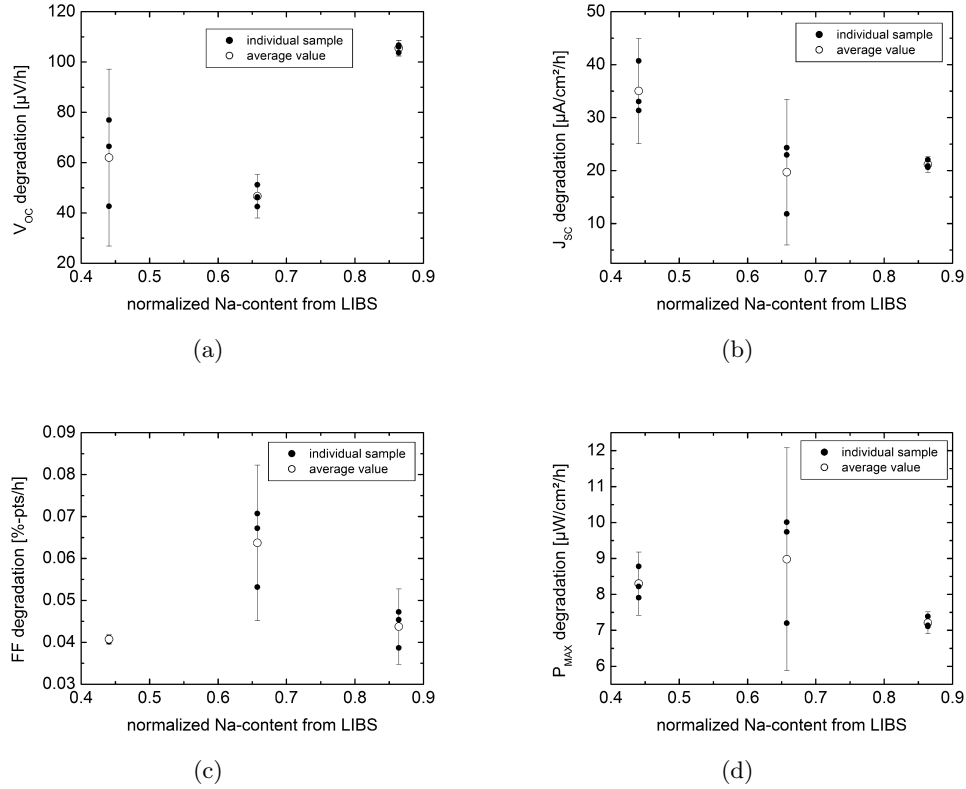


Figure 4.14: Linear degradation rates from in-situ IV measurements under damp heat. The respective IV parameters were fitted in the range of 100 to 300 h, i.e. stage 2 of the aging process. The numerical values are listed in table 4.1. Error bars for the arithmetic averages equal twice the standard deviation of the individual degradation rates for each sodium content. The sodium contents are given as normalized values from LIBS (cf. section 5.1).

Na-content	$V_{OC}$ degr. [ $\mu\text{V}/\text{h}$ ]	$J_{SC}$ degr. [ $\mu\text{A}/(\text{cm}^2 \text{ h})$ ]	$FF$ degr. [%-pts/h]	$P_{MPP}$ degr. [ $\mu\text{W}/(\text{cm}^2 \text{ h})$ ]
0.44	77.0	40.7	0.040	8.8
0.44	66.5	31.4	0.041	7.9
0.44	42.6	33.1	0.041	8.2
0.66	51.2	24.3	0.071	10.0
0.66	42.5	23.0	0.067	9.7
0.66	46.3	11.8	0.053	7.2
0.86	106.0	20.9	0.047	7.1
0.86	106.7	20.6	0.045	7.1
0.86	103.7	22.0	0.039	7.4
averages per sodium content				
0.44	62.0	35.0	0.041	8.3
0.66	46.7	19.7	0.064	9.0
0.86	105.5	21.2	0.044	7.2

Table 4.1: Degradation rates under damp heat of different IV parameters of unencapsulated CIGSe solar cells obtained from the linear regression of in-situ IV measurements versus time during stage 2 of the aging process (cf. figure 4.14). Sodium contents as normalized from LIBS.

## 4.4 Planar Contacts

In section 4.2.1 it was carved out that the degradation of the fill factor is the main contribution to the drop in the solar cell’s efficiency during a damp heat treatment. Furthermore, an increase in series resistance was identified as the origin for this degradation (cf. figure 4.3). In this section the influence on damp heat on the resistances of the planar contacts of the solar cell will be discussed since they contribute predominantly to the solar cell’s series resistance.

Section 4.4.1 investigates the degradation of the back contact, that causes approximately one quarter of the series resistance, while section 4.4.2 presents data on the degradation behavior of the front contact that contributes roughly three quarters to the overall series resistance of the solar cell<sup>5</sup>.

<sup>5</sup>Internal estimation based on power losses within the solar cell (*Solarion AG*). The biggest contribution to the overall front contact resistance is the resistivity of the grid and the contact resistance between grid and TCO while the TCO resistance itself has a smaller influence.

#### 4.4.1 Back–Electrode (Mo)

In this section the degradation behavior of the molybdenum back contact is investigated. On the one hand, measurements of the molybdenum sheet resistance within actual solar cells are presented in order to study the degradation of the back contact in its working environment. Transfer length measurements at the back contact scribes (cf. figure 3.5) were employed (see section 3.2.8 for details about the measurement). On the other hand, Hall measurements on plain molybdenum layers were done before and after damp heat to investigate the degradation behavior of the molybdenum layer itself.

##### Transfer Length Measurements

Figure 4.15 shows sheet resistance measurements of the molybdenum layer within the solar cell carried out with the transfer length method. Three solar cells each were measured before and after 0 h (control group), 15 h and 50 h of damp heat. The average sheet resistances of the solar cells in each damp heat class are plotted in figure 4.15(a) while the average relative change in sheet resistance after damp heat is plotted in figure 4.15(b).

Within the level of confidence of the measurements (derived from the standard deviation between the different samples in each class) no change in sheet resistance could be observed due to damp heat treatment. Before and after damp heat treatment, the average molybdenum sheet resistance was  $116 \text{ m}\Omega/\square$ .

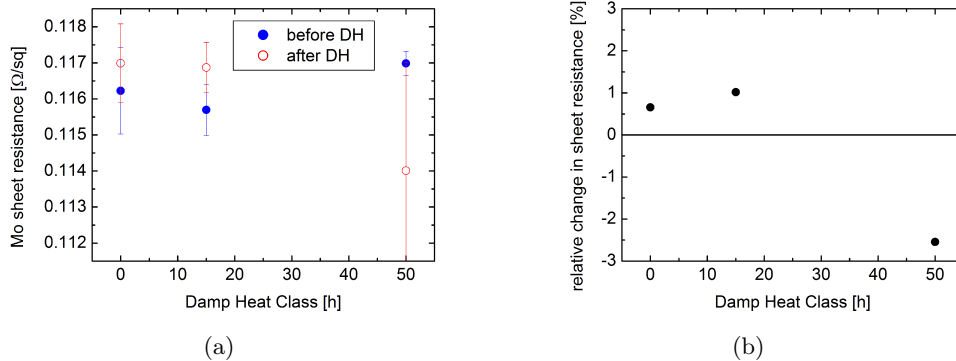


Figure 4.15: TLM measurements of the sheet resistance of the molybdenum back contact of solar cells (three solar cells per damp heat class) before and after damp heat exposure. (a) Average sheet resistance and (b) average relative change in sheet resistance. The molybdenum sheet resistance does not change within the level of confidence of the measurement.

With a different set of samples this experimental procedure was extended to longer damp heat exposure (figure 4.16). The sheet resistances of the solar cell in each damp

heat class is plotted in figure 4.16(a) while the relative change in sheet resistance after damp heat is plotted in figure 4.16(b).

The average molybdenum sheet resistance was  $114 \text{ m}\Omega/\square$  before and  $119 \text{ m}\Omega/\square$  after damp heat. This apparent increase in sheet resistance of the molybdenum back contact after damp heat is within the level of confidence of the measurement. In particular it should be noted that the apparent increase in sheet resistance does not correlate with the damp heat exposure time (cf. figure 4.16(b)) hence suggesting an offset in the measurement rather than a damp heat induced effect.

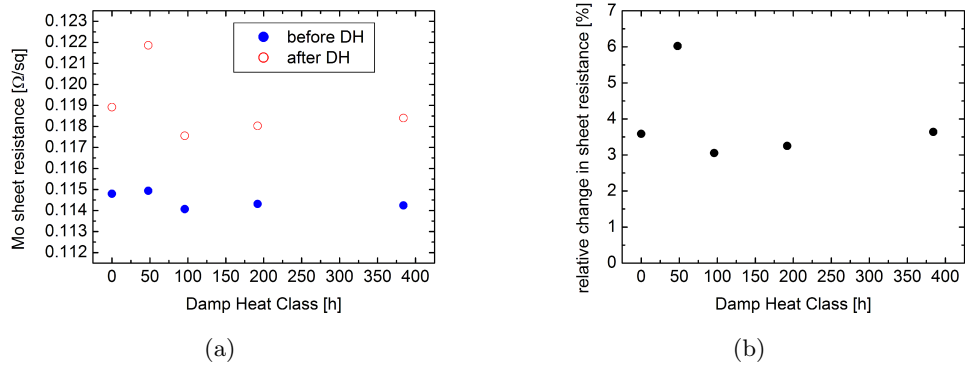


Figure 4.16: TLM measurements of the sheet resistance of the molybdenum back contact of solar cells (one solar cell per damp heat class) before and after extended damp heat exposure. (a) Sheet resistance and (b) relative change in sheet resistance. The molybdenum sheet resistance does not change within the level of confidence of the measurement.

### Hall Measurements

Hall measurements were conducted at room temperature on molybdenum layers of approximately  $1 \mu\text{m}$  thickness deposited on polyimide plastic foil. The deposition parameters were identical to those of the back contact of a solar cell. The square shaped samples with a size of  $1 \text{ cm}^2$  were exposed to damp heat for 0 h (reference), 15 h or 50 h. The Hall measurement was conducted in a 0.43 T magnetic field with a measurement current of 100 mA. The specific resistances  $\rho$  of the molybdenum layers deduced from the Hall measurements are shown in figure 4.17(a).

The resistance of the molybdenum layer changed due to damp heat. After 50 h it had increased by less than 5% compared to the initial resistance, however, after 15 h of damp heat the increase was 33% (cf. figure 4.17(b)). The more pronounced increase in resistance after 15 h compared to 50 h of damp heat remained difficult to explain.

Since all three samples were cut out of a larger, homogeneously coated polyimide foil at neighbouring positions, similar initial resistances should be assumed. The increase in resistance after 15 h was driven by a 31 % decrease in mobility, however this decrease was below the level of confidence of the measurement of the mobility. Regardless of the assumption of similar initial resistances, small deviations in the mobilities of the non-treated samples are the most likely explanation for the apparently different degradation behavior after 15 h and 50 h of damp heat, respectively. Overall, the Hall measurements seem to confirm a low degradation of the molybdenum back contact after damp heat.

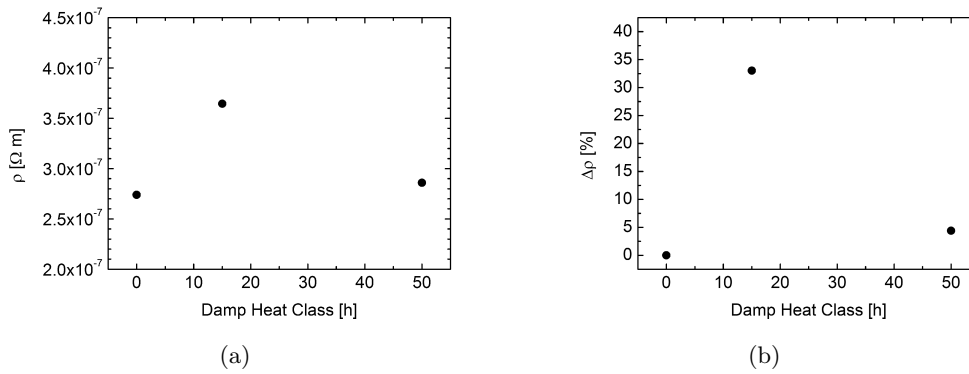


Figure 4.17: Hall measurement of molybdenum layers on polyimide before and after damp heat. (a) Specific resistance  $\rho$  (b) change in the specific resistivity  $\Delta\rho$ .

#### 4.4.2 Front-Electrode (ZnO:Al)

##### Transfer Length Measurements

Figure 4.18 shows sheet resistance measurements of the front contact carried out with the transfer length method on complete solar cells as described in section 3.2.8. A comparison of the TCO sheet resistance before and after damp heat for the same cell is not feasible since the TLM measurement destroys the grid thus making necessary monitoring IV measurements impossible.

Sheet resistances of the TCO in each damp heat class are plotted in figure 4.18(a). The sheet resistance of the TCO seems to drop linearly under damp heat exposure and between 0 to 50 h the apparent drop is about 15 %. However, this trend is below the level of confidence of the measurement (as deduced from the uncertainty of slope and intercept of the TLM fit) and thus insignificant.

The contact resistance between grid and TCO was determined via TLM as well (cf. figure 4.18(b)). Apparently, this contact resistance seems to increase upon damp heat ex-

posure. However, even the 70 % increase between 0 to 50 h is below the level of confidence of the measurement.

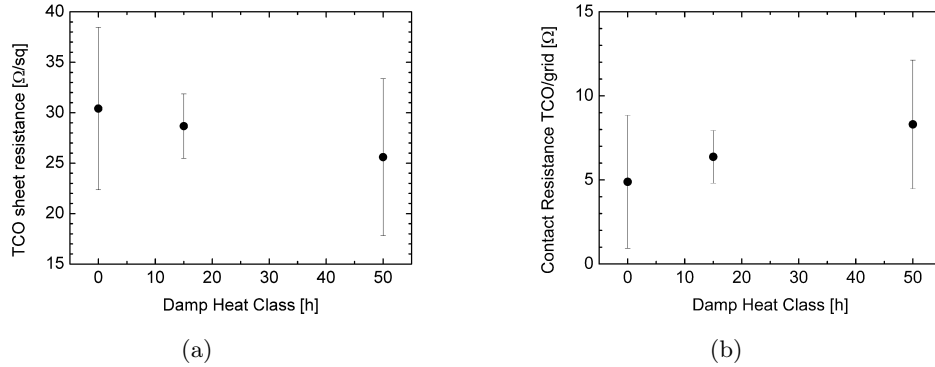


Figure 4.18: TLM measurements of the sheet resistance of the ZnO:Al front contacts of solar cells (one solar cell per damp heat class) before and after damp heat exposure. (a) Sheet resistance of the TCO and (b) contact resistance between TCO and grid. The apparent trend in both resistances is below the level of confidence of the measurement.

Since the apparent trends in figure 4.18 were below the level of confidence of the measurement, the experimental procedure was repeated with a different set of samples for an extended damp heat exposure (cf. figure 4.19).

As plotted in figure 4.19(a) the sheet resistances of the TCO increased significantly with damp heat. An exponential growth fits the degradation of the TCO sheet resistance due to damp heat perfectly.

In figure 4.19(b) the contact resistance between grid and TCO is plotted. It increased significantly after damp heat exposure, too. Up to 192 h (8 days) it fits to an exponential increase as well. At 384 h (16 days) the degradation had slowed down, however the contact resistance had increased 62-fold compared to the initial value.

### Hall Measurements

Hall measurements were conducted at room temperature on square shaped samples ( $1\text{ cm}^2$ ) with ZnO:Al layers that were deposited with identical deposition parameters as for complete solar cells. However, a PEN plastic foil served as substrate. The samples were exposed to damp heat for 0 h (reference), 15 h or 50 h. The ZnO:Al layer thickness was approximately 400 nm. The Hall measurement was conducted in a 0.43 T magnetic field with a measurement current of 10 mA. The specific resistances  $\rho$  of the ZnO:Al TCO layers deduced from the Hall measurements are shown in figure 4.20(a).

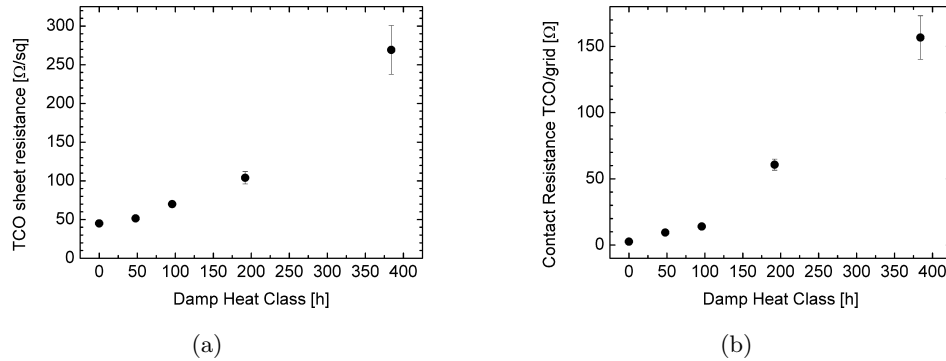


Figure 4.19: TLM measurements of the sheet resistance of the ZnO:Al front contacts of solar cells (one solar cell per damp heat class) before and after extended damp heat exposure. (a) Sheet resistance of the TCO and (b) contact resistance between TCO and grid. Both resistances increase significantly after damp heat.

The resistance of the ZnO:Al layer degraded under damp heat. As shown in figure 4.20(b) it had increased by 11% after 15 h and by 27% after 50 h of damp heat compared to the initial resistance. Nearly identical initial resistances can be assumed since all three samples were cut out of a larger, homogeneously coated PEN foil at neighbouring positions. The increase in resistance might be explained by a slight drop in carrier concentration after damp heat. However, this change is below the level of confidence of the measurement.

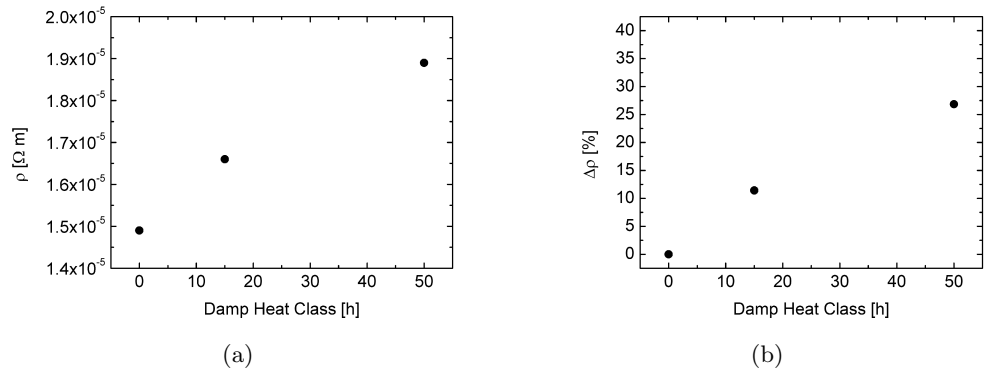


Figure 4.20: Hall measurement of TCO on flexible substrate before and after damp heat.  
(a) Specific resistance  $\rho$  (b) change in the specific resistivity  $\Delta\rho$ .



## 5 The Influence of Sodium

It is well known for  $\text{Cu(In,Ga)Se}_2$  solar cells that sodium has an influence on the device characteristics (cf. section 1.3.3). However, regarding the influence of sodium on the long term stability of these solar cells, no comprehensive study has been published so far (cf. section 2.4.6). In this chapter, the damp heat stability of CIGSe solar cells with different sodium contents (cf. section 5.1) is analyzed. Structural aspects will be discussed on the basis of electron microscopy images (section 5.2) and elemental depth profiles from SIMS (section 5.5). Different incorporation methods of the sodium, i.e. co-evaporation (section 5.3) and post-deposition (section 5.4) will be considered. By using the example of the co-evaporation incorporation method, an optimization of the sodium content with respect to damp heat stability will be shown (cf. section 5.3.3).

### 5.1 Characterized by LIBS

In order to characterize the sodium content of our  $\text{Cu(In,Ga)Se}_2$  solar cells LIBS measurements were carried out. The full layer stack of the sample (either as a complete solar cell or pieces that were cut out of it) was subjected to the laser shots. The samples were characterized with the parameters described in section 3.2.11.

Indium was chosen as reference element for the quantification of sodium since the indium content (as measured with XRF during film deposition) has a very low variation coefficient among all samples. Thus the sodium content is given as peak ratio of sodium to indium of the respective sample. For sodium, the area under the peak at 588.995 nm was used, for indium the area under the 451.131 nm peak, respectively.

Table 5.1 lists the sodium contents for all samples in this thesis. In order to make the sodium content easily comparable among different samples, the peak ratios were normalized to one specific sample<sup>1</sup> (cf. table 5.1). For all samples in this thesis, the sodium content is given in this fashion (denoted as “normalized from LIBS”), in addition to the corresponding sodium fluoride evaporator temperature. In figure 5.1 these normalized sodium contents are plotted versus the sodium fluoride evaporator temperatures. Figure 5.2 depicts a linear regression of the normalized sodium content from LIBS vs. the NaF evaporator temperature.

As expected, for all samples, the detected global sodium content in the sample increases with increasing sodium fluoride evaporator temperature (cf. table 5.1 and fig-

---

<sup>1</sup>See section 5.3.3 for the reason why this sodium content was chosen as reference.

Process	Method	$T_{NaF}$ [°C]	Speed [cm/min]	Na/In	Na normalized
2A-1173	Co-Evaporation	775		0.0681	0.52
2A-1173	Co-Evaporation	825		1.4948	11.33
2A-1209	Co-Evaporation	740		0.0810	0.61
2A-1209	Co-Evaporation	760		0.0990	0.75
2A-1209	Co-Evaporation	780		0.1320	<b>1.00</b>
2A-1209	Co-Evaporation	800		0.1385	1.05
2A-1209	Co-Evaporation	820		0.1726	1.31
2A-1225	Co-Evaporation	710		0.0571	0.43
2A-1225	Co-Evaporation	735		0.0942	0.71
2A-1225	Co-Evaporation	760		0.1506	1.14
2A-1233	Co-Evaporation	710		0.0582	0.44
2A-1233	Co-Evaporation	735		0.0868	0.66
2A-1233	Co-Evaporation	760		0.1140	0.86
2A-1234	Post-Deposition		80	0.0185	0.14
2A-1234	Post-Deposition		24	0.0289	0.22
2A-1234	Post-Deposition		12	0.0337	0.26
2A-1234	Post-Deposition		6	0.0625	0.47
2A-1234	Post-Deposition		3	0.1010	0.77
2A-1234	Post-Deposition		1.5	0.1108	0.84

Table 5.1: Sodium content from LIBS for samples with NaF incorporation via co-evaporation (NaF evaporator temperature) or post-deposition (web speed during NaF deposition). Na/In peak ratio obtained from the area under the Na peak at 588.995 nm and the In peak at 451.131 nm.

ure 5.1). This confirms that not only the amount of sodium offered increases with higher NaF evaporator temperature but also the amount incorporated in the solar cell (absorber). At an NaF evaporator temperature of 825 °C, one sample from process 2A–1173 showed an unusually high sodium content compared to the trend suggested by all other data points (cf. figure 5.1(a)). Therefore it was excluded from the fit in figure 5.2.

An analysis of spatial distribution of the sodium from SIMS elemental depth profiling is given in section 5.5.

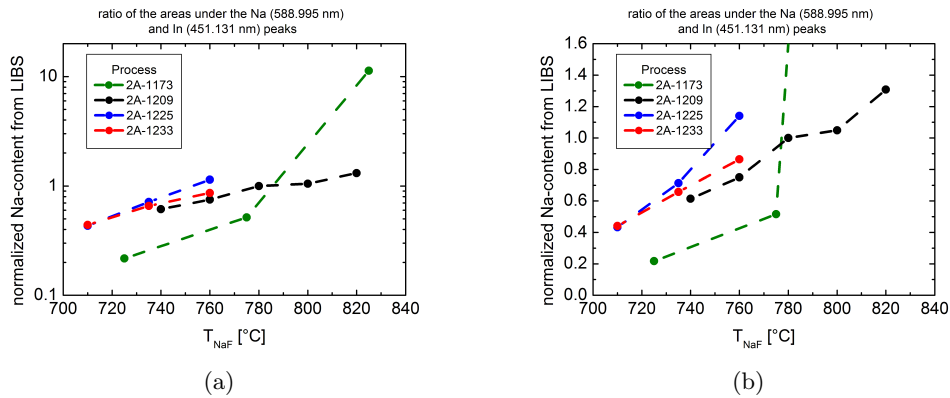


Figure 5.1: Sodium content from LIBS of all samples plotted (a) logarithmically (b) linearly vs. the NaF evaporator temperature.

## 5.2 Electron Microscopy Images

### 5.2.1 Before Damp Heat

Scanning electron microscopy (SEM) images were taken in order to assess the morphology of the solar cells with respect to the influence of sodium and damp heat. On the one hand, images were taken at different magnifications from the surface of the solar cell (“top view”) to get information about the surface texture. On the other hand, the flexible solar cell samples were pulled apart thus allowing to image the breaking edges (“cross section”). The latter images yield information about the layer stack and particle sizes.

Samples from two different manufacturing runs (2A–1173, 2A–1209) were studied by SEM as described in section 3.2.9. During the absorber deposition, in both runs, the amount of sodium was varied in order to study the influence of sodium on the solar cell properties.

Cross sectional SEM images of samples from process 2A–1173 with three different sodium contents are shown in figure 5.3. They nicely depict the general micro–structure

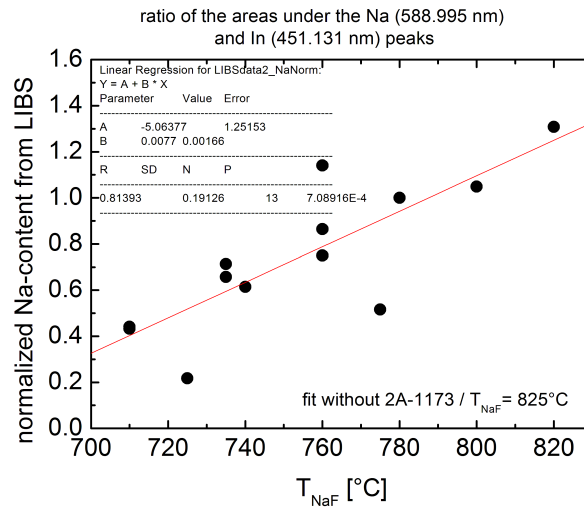


Figure 5.2: Fit of the sodium content from LIBS vs. NaF evaporator temperature for all samples, except 2A-1173  $T_{NaF} = 825^{\circ}C$

of a flexible Cu(In,Ga)Se<sub>2</sub> cell by *Solarion AG* that has been introduced in figure 3.2(b). From the bottom to the top, the different layers appear as follows. The molybdenum has a columnar bilayer structure. On top of it, the CIGSe appears with much larger particles (grains or grain boundaries cannot be seen from secondary electron contrast in SEM). It is not possible to see the only tens of nanometers thin CdS buffer layer. However, the craggy top layer is the transparent conductive oxide. Generally, the structure is the same for all three samples. For the highest sodium content (right image) the CIGSe appears to have smaller particle sizes.

Top view SEM images from process 2A-1173 are shown in figure 5.4 for all three sodium contents (left to right) at different magnifications (from top to bottom). The texture of the cell surfaces is similar as seen at any magnification. It is not completely flat but has a cauliflower like texture. There is a slight tendency towards a flatter surface that can be seen particularly for the highest sodium content (easier at 10000× and 20000× magnification). This appears to be a consequence of the slightly smaller particle sizes in the CIGSe absorber layer that have been seen in the cross section for the highest sodium content (figure 5.3) as mentioned in the previous paragraph.

Top view SEM images from process 2A-1209 with five different sodium contents are shown in figure 5.5 at different magnifications (from left to right). As for the samples from the previous process (figure 5.3) these surfaces have a typical cauliflower like texture. For the different samples, from top to bottom in figure 5.5, different sodium contents were incorporated during absorber deposition. A tendency towards a flatter surface with increasing sodium content can be seen particularly well for the highest

magnification ( $20000\times$ ). The sample with the highest sodium content (normalized from LIBS: 1.3;  $T_{NaF} = 820^\circ\text{C}$ ) is an exception from that trend.

Cross sectional SEM images of samples from process 2A–1209 are shown in figure 5.6(a). Alike the samples from the previous process run (figure 5.3) these cross sections reveal the general micro-structure of our flexible  $\text{Cu}(\text{In,Ga})\text{Se}_2$  solar cells. By judging the surface that can be seen grazingly from these images the trend regarding their texture can be confirmed. However, inferring that texture from particle sizes (e.g. of the absorber) appears impossible for these samples.

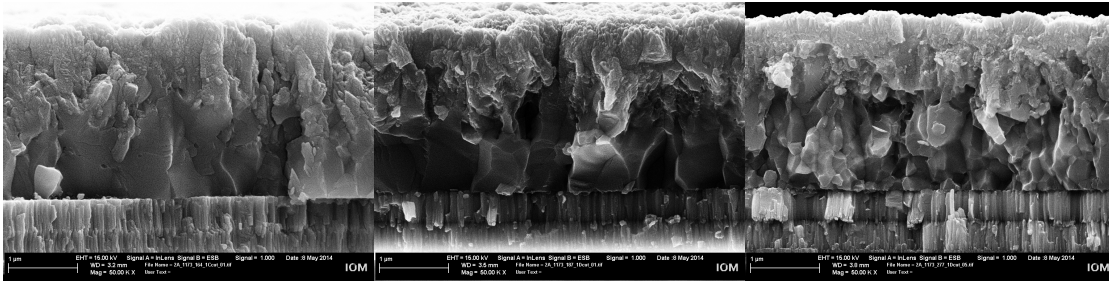


Figure 5.3: SEM images of cross sections of CIGSe solar cells from process 2A–1173. From left to right, the cells differ in sodium content — normalized from LIBS ( $T_{NaF}$ ): 0.2 ( $725^\circ\text{C}$ ), 0.5 ( $775^\circ\text{C}$ ), 11.3 ( $825^\circ\text{C}$ ). Magnification  $50000\times$ .

### 5.2.2 After Damp Heat

Figure 5.6(b) presents SEM cross section images from process 2A–1209 after 85 h of DH for three out of five sodium contents. These samples are cut out of neighbouring (referring to the position on the web during production; cf. section 3.1) solar cells compared to those from figure 5.6(a). Thus, a comparison of the morphology of similar material is possible before (figure 5.6(a)) and after damp heat. For none of the sodium contents a difference can be seen.

A comparison of top-view SEM images from process 2A–1209 before & after DH is given in figure 5.7 at different magnifications. In accordance with the cross sectional appearance no difference can be seen in the surface texture of the samples before and after damp heat.

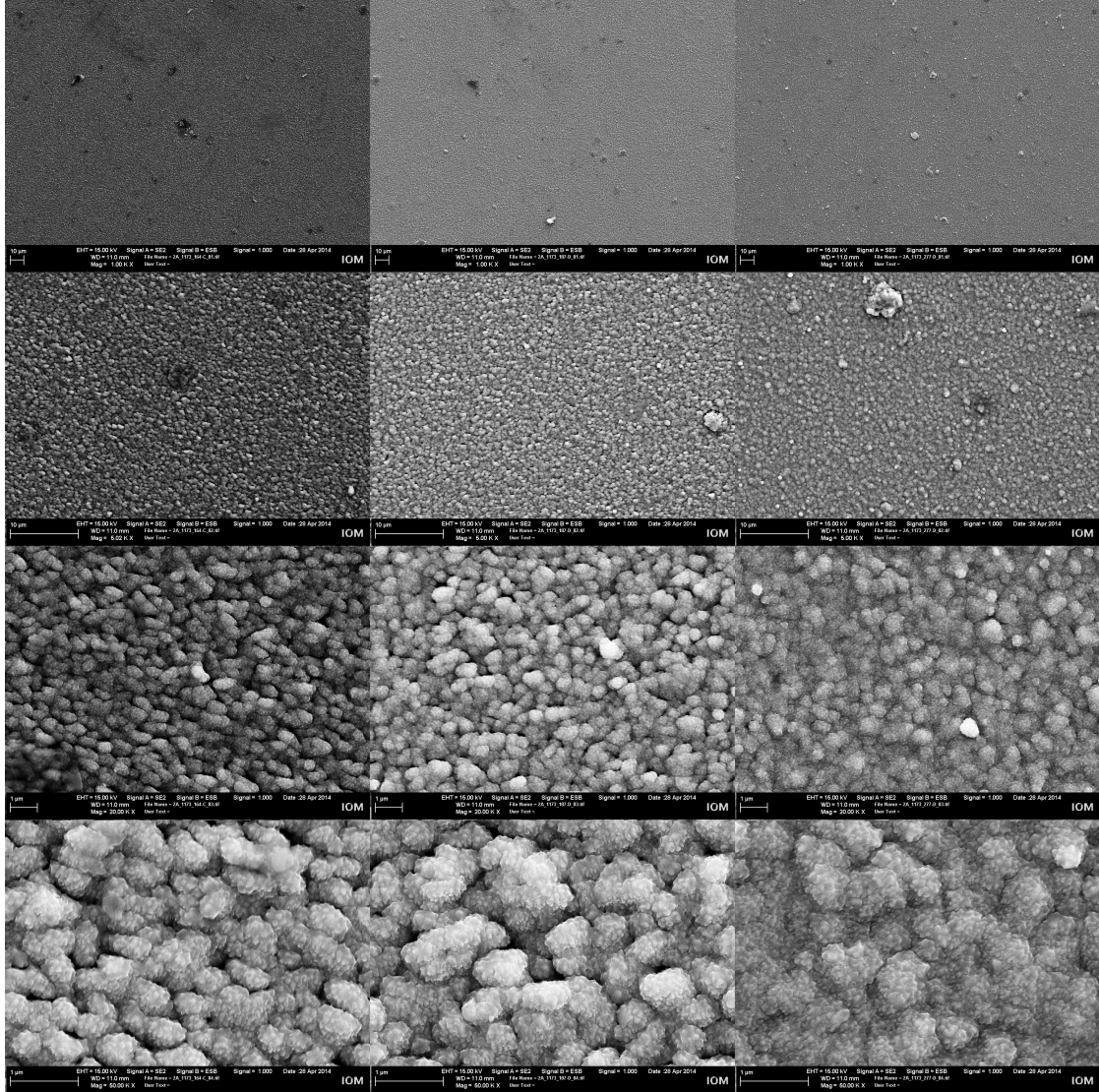


Figure 5.4: SEM images of the surface of CIGSe solar cells from process 2A-1173. From left to right column, the cells differ in sodium content — normalized from LIBS ( $T_{NaF}$ ): 0.2 (725 °C), 0.5 (775 °C), 11.3 (825 °C). From top to bottom increasing magnification: 1000 $\times$ , 5000 $\times$ , 20000 $\times$  and 50000 $\times$ .

## 5.2 Electron Microscopy Images

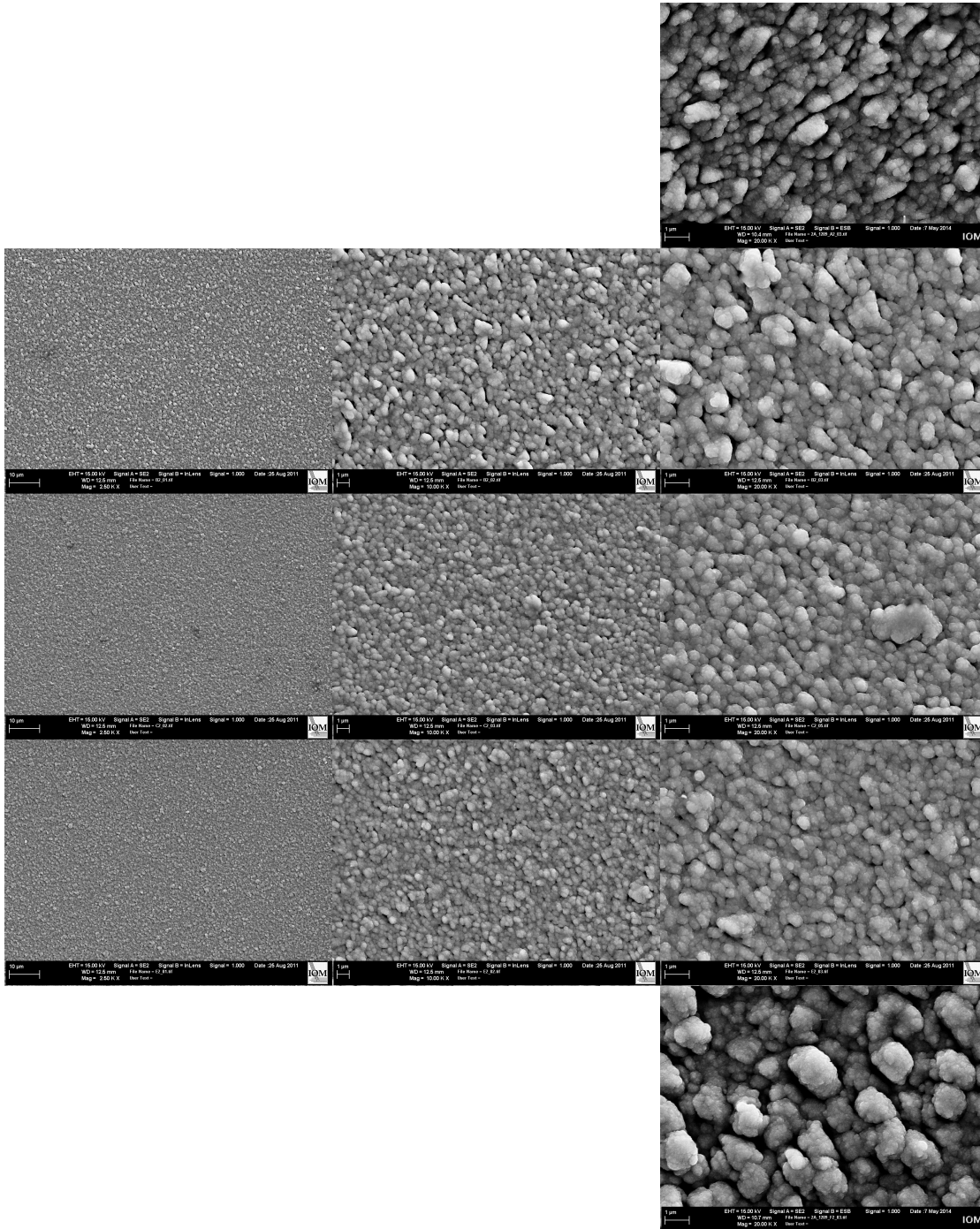


Figure 5.5: SEM images of the surface of CIGSe solar cells from process 2A-1209. From top to bottom, samples differ in Na content; normalized from LIBS ( $T_{NaF}$ ): 0.6 (740 °C), 0.8 (760 °C), 1.0 (780 °C), 1.1 (800 °C) and 1.3 (820 °C). From left to right increasing magnification: 2500 $\times$ , 10000 $\times$  and 20000 $\times$ .

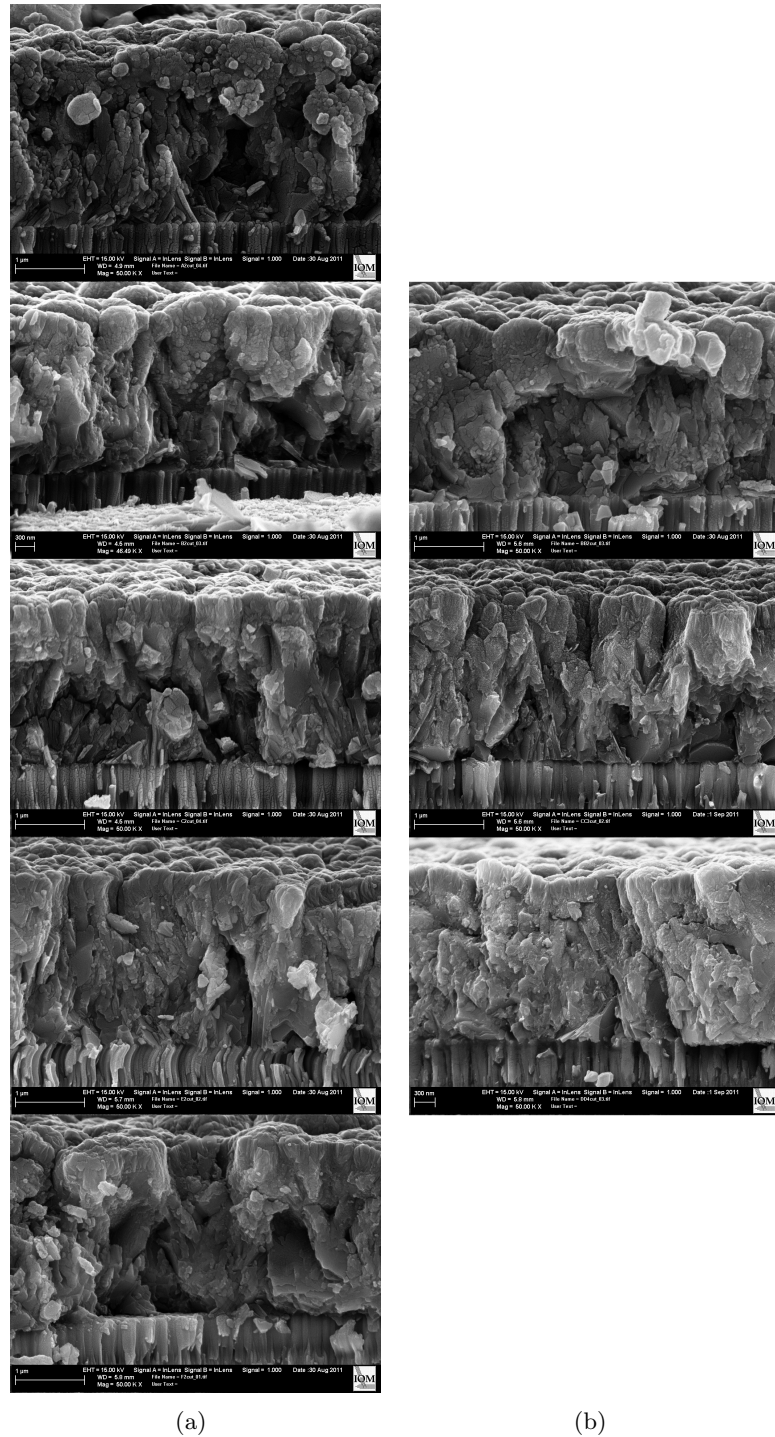


Figure 5.6: SEM images of the cross section of CIGSe solar cells from process 2A-1209. (a) Before, (b) after 85 h of damp heat. From top to bottom, samples differ in Na content; normalized from LIBS ( $T_{NaF}$ ): 0.6 (740 °C), 0.8 (760 °C), 1.0 (780 °C), 1.1 (800 °C) and 1.3 (820 °C). Magnification 50000 $\times$ .



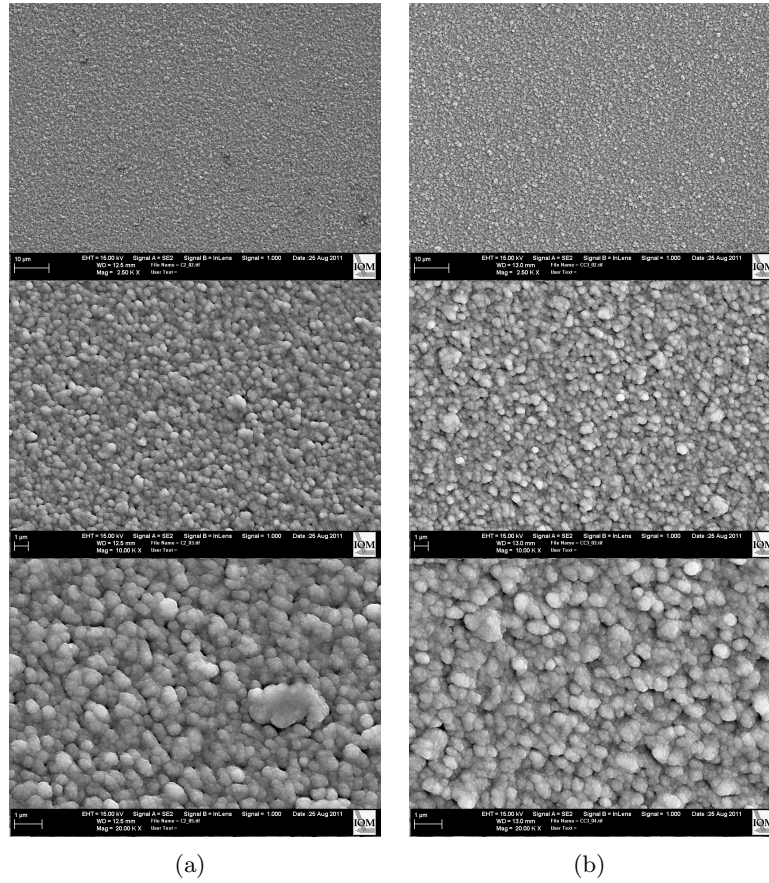


Figure 5.7: SEM images of the surface of CIGSe solar cells from process 2A-1209. (a) Before damp heat, (b) after 85 h of damp heat. From top to bottom increasing magnification: 2500 $\times$ , 10000 $\times$  and 20000 $\times$ . Sodium content — normalized from LIBS ( $T_{NaF}$ ): 1.0 (780 °C).

### 5.3 Introduced by Co-Evaporation

In this section, IV data with respect to damp heat of three different sample sets from different manufacturing runs are presented. In order to obtain information on the damp heat stability of the bare solar cells rapidly, all samples were unencapsulated.

No damage was visible on the cells after damp heat. As shown in the previous section, high-resolution electron microscopy images (cross section and top view) showed no differences either. Thus, the damp heat treatment up to 50 to 85 h discussed here lead to mild damage only, i.e. no physical damage such as delamination, but with a clear influence on the IV characteristic, i.e. the electrical properties.

#### 5.3.1 IV vs. Damp Heat

The first experiment (batch 2A–1173) is a cyclic approach consisting of IV measurements alternating with periods of damp heat exposure. This simple procedure yields time resolved insight into the degradation process albeit less detailed than the in-situ experiment that was described in section 4.3. Two sets of Cu(In,Ga)Se<sub>2</sub> solar cells (six cells each) with different sodium contents were exposed to damp heat (see table 5.2 for cell information and selected IV data).

Sample ( $T_{NaF}$ )	Sodium normalized	Average initial efficiency	Degradation (after 50 h DH)	Number of samples
775 °C	0.52	8.3 %	13 %	6
825 °C	11.33	10.0 %	63 %	6

Table 5.2: Samples of batch 2A–1173 for experiment 1 on the influence of sodium on the damp heat stability. Normalized sodium contents from LIBS (cf. section 5.1). Initial efficiency is averaged over six samples with the respective sodium content.

Time resolved data on the degradation behavior of the samples with respect to the sodium content in the Cu(In,Ga)Se<sub>2</sub> absorber layer are presented in figure 5.8. Both sets of samples show a decrease of efficiency and fill factor under exposure to damp heat. The behavior of the fill factor appears to be driven by the series resistance (cp. figure 5.9). However, only for the cells with lower sodium content (0.5×) we observe a slight increase in efficiency and fill factor before the overall decline dominates (cf. figure 5.8(d) and 5.8(c)). Furthermore, the degradation is much more pronounced for the samples with higher sodium content (11.3×). As we have seen before, for the samples with 0.5× sodium content, the open circuit voltage and the short circuit current density do not decline (cf. figure 5.8(a) and 5.8(b)). For the samples with 11.3× sodium content the same is true, except for the dip after 5 h of damp heat (cf. figure 5.8(b) and 5.8(d)).

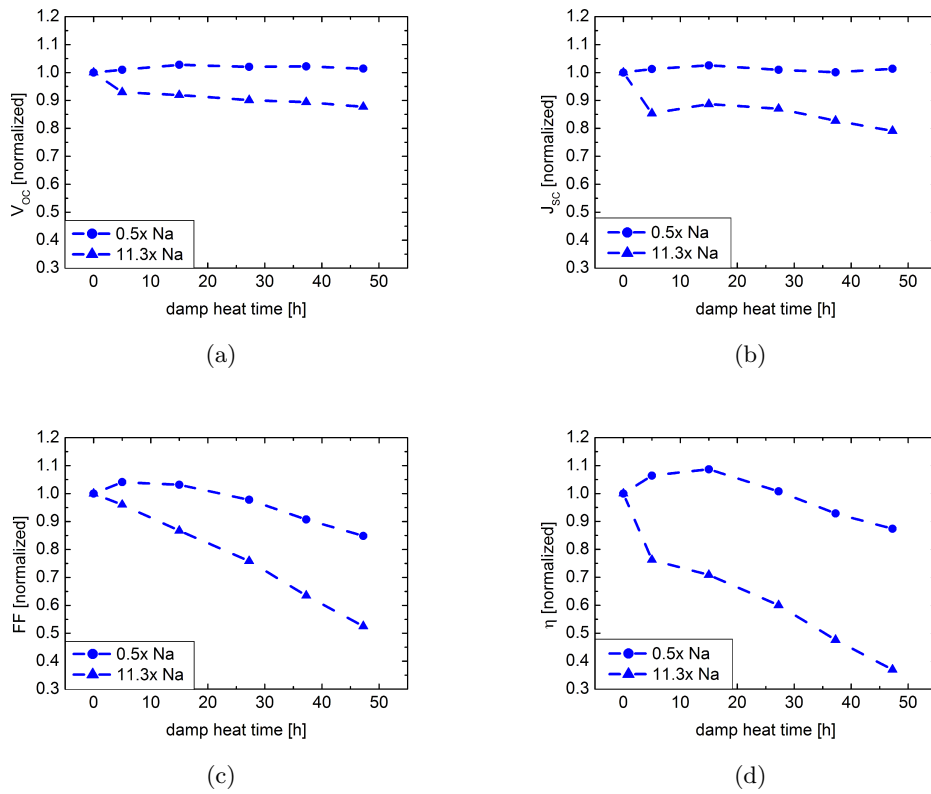


Figure 5.8: Damp heat treatment of the set of samples with sodium content  $0.5\times$  and  $11.3\times$ ; (a) open circuit voltage (b) short circuit current density (c) fill factor (d) efficiency; all values are scaled to initial (0h) value

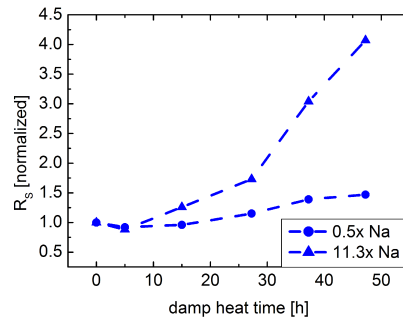


Figure 5.9: Damp heat treatment of the set of samples with sodium content  $0.5\times$  and  $11.3\times$ . Series resistance vs. damp heat exposure. All values are scaled to initial (0 h) value.

### 5.3.2 IV vs. Sodium

In a second experiment (batch 2A–1225) samples with three different sodium contents were prepared to reproduce the findings about the influence of the sodium content on the damp heat stability of the CIGSe solar cells (cf. section 5.3.1). Sodium was supplied via co–evaporation thus the amount of sodium was set by tuning the NaF crucible temperature ( $710\text{ }^\circ\text{C}$ ,  $735\text{ }^\circ\text{C}$  and  $760\text{ }^\circ\text{C}$ ) during CIGSe deposition. In table 5.3 information on the cells and selected IV data are given.

Sample ( $T_{NaF}$ )	Sodium normalized	Average initial efficiency	Degradation (after 50 h DH)	Number of samples
$710\text{ }^\circ\text{C}$	0.43	9.2 %	4 %	6
$735\text{ }^\circ\text{C}$	0.71	10.8 %	7 %	12
$760\text{ }^\circ\text{C}$	1.14	11.2 %	33 %	6

Table 5.3: Samples of batch 2A–1225 for experiment 2 on the influence of sodium on the damp heat stability. Normalized sodium contents from LIBS (cf. section 5.1).

Figure 5.10 shows the IV behavior of these cells. Prior to damp heat, the efficiency of the solar cells increases with sodium content. This is mainly due to a significant increase in the open circuit voltage and the fill factor. Additionally there is a slight beneficial decrease of the series resistance with increasing sodium content, whereas the short circuit current drops for the highest sodium content ( $1.14\times$ ).

After 50 h of damp heat, all cells have degraded in terms of efficiency. From figure 5.10, the IV parameters after damp heat may be easily compared for the different sodium contents whereas figure 5.11 allows a more convenient comparison for the IV behavior of

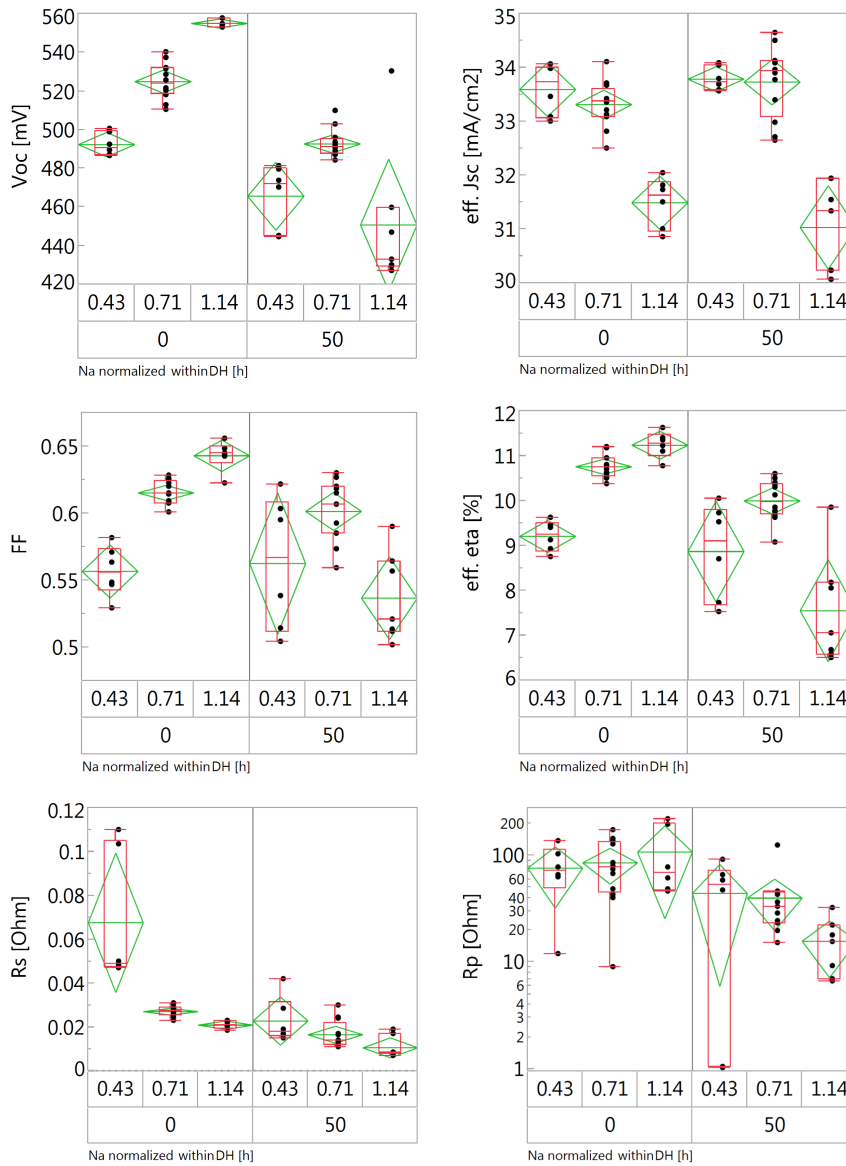


Figure 5.10: IV parameters of cells with co-evaporated sodium. All IV parameters are plotted versus the sodium content (as normalized from LIBS: 0.43 to 1.14) and are grouped by the damp heat exposure (0 or 50 h). The red box indicates the lower and upper quartiles (lower and upper box boundary), the median (red bar in between) and outliers (red vertical lines). The center of each green diamond in the graph denotes the group mean and its edges indicate a  $2\sigma$  (95 %) confidence interval.

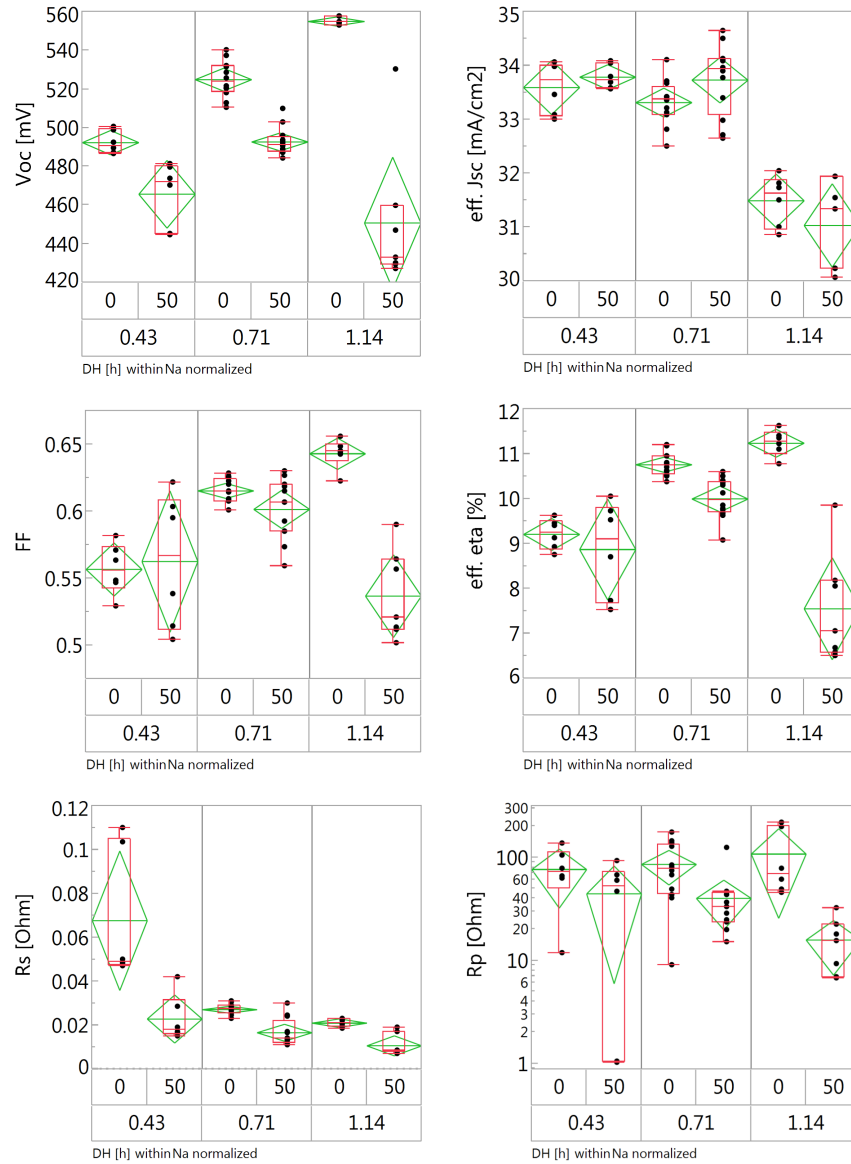


Figure 5.11: IV parameters of cells with co-evaporated sodium. All IV parameters are plotted versus damp heat exposure (0 or 50 h) and are grouped by the sodium content (as normalized from LIBS: 0.43 to 1.14). The red box indicates the lower and upper quartiles (lower and upper box boundary), the median (red bar in between) and outliers (red vertical lines). The center of each green diamond in the graph denotes the group mean and its edges indicate a  $2\sigma$  (95 %) confidence interval.

the samples, with one particular sodium content, before and after damp heat. The cells with the lowest sodium content ( $0.43\times$ ) exhibit the least degradation while the drop in efficiency increases with sodium content (figure 5.11). Generally, the degradation can be attributed to a drop in the open circuit voltage, a drop in the fill factor and a drop in the parallel resistance, each of them more pronounced for higher sodium contents ( $0.71\times$  and  $1.14\times$ ). For all samples, the short circuit current remains nearly constant, after damp heat. The series resistance seems to drop for all three sodium contents, however for  $0.43\times$  Na, the scattering is quite large before damp heat, and for the  $0.71\times$  and  $1.14\times$  Na samples, the drop is quite small.

In summary, the observation from section 5.3.1, i.e. a more pronounced degradation for samples with higher sodium contents, could be reproduced.

### 5.3.3 Optimization of the Sodium Content

The previous findings on cell efficiency and damp heat degradation with respect to sodium content (section 5.3.1 and 5.3.2) suggest that the sodium content may be chosen to either reach good initial efficiencies (generally, more Na seems to be better as long as not exceeding a certain threshold) or to minimize the degradation (as shown in the previous two sections, less sodium appears to be better).

In order to verify that and to find an optimum sodium content, a third experiment (batch 2A–1209) was conducted: CIGSe solar cells with five different sodium contents were prepared (by NaF co-evaporation with crucible temperatures of  $740^\circ\text{C}$ ,  $760^\circ\text{C}$ ,  $780^\circ\text{C}$ ,  $800^\circ\text{C}$  and  $820^\circ\text{C}$ ) and artificially aged by 85 h of damp heat. Table 5.4 lists information on the samples and selected IV data.

Sample ( $T_{\text{NaF}}$ )	Sodium normalized	Average initial efficiency	Degradation (after 85 h DH)	Number of samples
$740^\circ\text{C}$	0.61	6.8 %	55 %	3
$760^\circ\text{C}$	0.75	8.3 %	59 %	3
$780^\circ\text{C}$	1.00	9.2 %	62 %	3
$800^\circ\text{C}$	1.05	8.9 %	67 %	3
$820^\circ\text{C}$	1.31	5.8 %	90 %	3

Table 5.4: Samples of batch 2A–1209 for experiment 3 to optimize the sodium content for a balance between initial efficiency and damp heat stability. Normalized sodium contents from LIBS (cf. section 5.1).

In figure 5.12 normalized IV parameters for these samples, initially and after damp heat, are plotted versus the sodium content. Before damp heat, a NaF crucible temperature of  $780^\circ\text{C}$  (Na  $1.00\times$ ) yields the most efficient cells (all values in figure 5.12(a) and 5.12(b) are scaled to the initial values of this group). This optimum results from the

trends that comes along with increasing sodium content:  $V_{OC}$  increases (figure 5.12(a)),  $J_{SC}$  decreases for higher sodium contents (figure 5.12(a)) and the fill factor exhibits a maximum at a NaF crucible temperature of 780 °C (Na 1.00×) as well (figure 5.12(b)).

The damp heat degradation diminishes all IV parameters. For low sodium contents (0.61× or  $T_{NaF} = 740$  °C) the open circuit voltage is nearly unaffected by damp heat, however for cells with higher sodium contents, the degradation in  $V_{OC}$  is more pronounced. The short circuit current drops for all groups while the drop is largest for the highest sodium content (1.31× or  $T_{NaF} = 820$  °C). For the samples from the latter group, the degradation in the series resistance, i.e. a strong increase of  $R_S$  (figure 5.12(c)), causes the fill factor to drop significantly (figure 5.12(b)) and thus influences  $J_{SC}$  as well (cf. figure 1.6). At the same time the parallel resistance is diminished (figure 5.12(c)) leading to a lower value of  $V_{OC}$ . The fill factor drops for all groups after damp heat treatment and this drop is larger for higher sodium contents.

Looking at the overall efficiency, the degradation is clearly stronger for cells with higher sodium content (figure 5.12(d)). On the one hand, this confirms previous findings. On the other hand, since this trend in efficiency is opposite to the higher initial efficiencies with higher sodium contents, an optimum in efficiency after damp heat arises (figure 5.12(b)). In this experiment the optimum after damp heat coincides with the optimum before damp heat, i.e. cells with 1.00× Na or  $T_{NaF} = 780$  °C yield the highest efficiencies before and after 85 h of damp heat. Thus the sodium contents from LIBS were normalized to this particular value (cf. section 5.1).

This coincidence allows to optimize the initial cell efficiency as well as the long term stability at the same time. Nevertheless it is very likely that the two optima do not match for any given damp heat time. As a consequence from the two trends described above it can be expected that cells with higher sodium contents are better suited for short damp heat exposure and cells with lower sodium contents are better suited for long damp heat exposure. In any case, the sodium content may be used to optimize the CIGSe solar cell for highest initial efficiency and long-term stability.



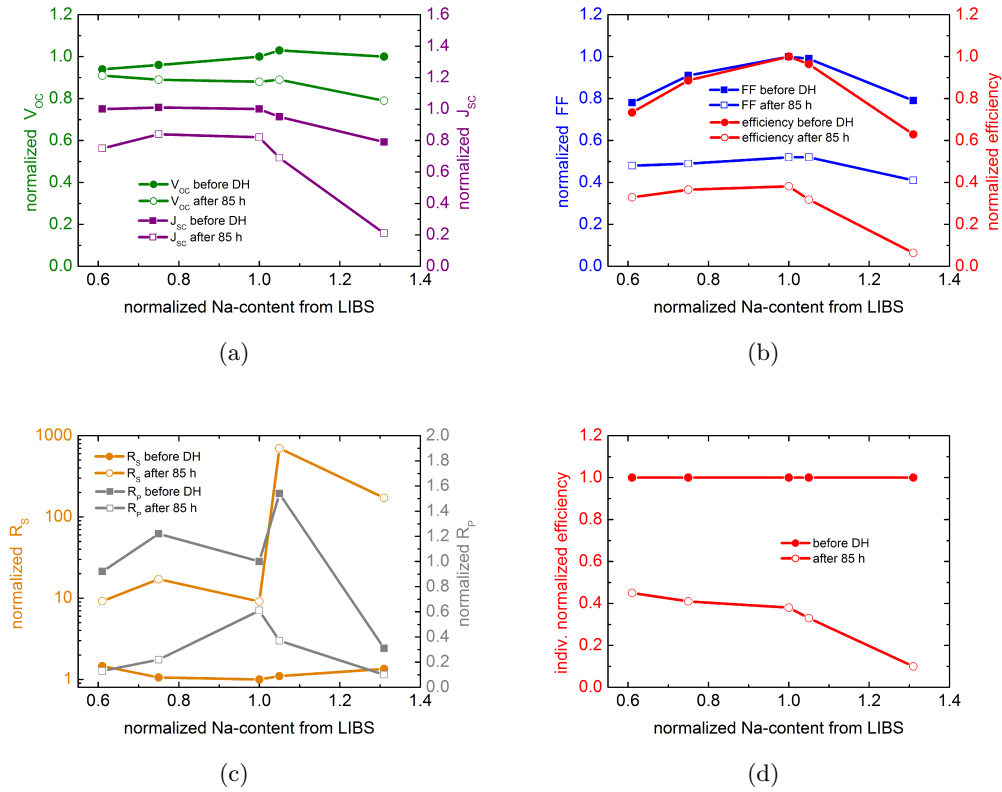


Figure 5.12: IV parameters versus sodium content (normalized from LIBS). (a)  $V_{OC}$  and  $J_{SC}$ , (b)  $FF$  and efficiency, (c)  $R_S$  (note the logarithmic scale) and  $R_P$  are normalized to their highest respective values before damp heat. (d) shows the efficiency normalized to the maximum of each sodium group.

## 5.4 Introduced by Post-Deposition

As remarked in section 1.3.3 the post-deposition treatment is an alternative method to introduce sodium to the  $\text{Cu(In,Ga)Se}_2$  absorber. In this section the damp heat stability of CIGSe solar cells with respect to their sodium content introduced in a post-deposition treatment of the absorber is investigated. Similarly to the first experiment about co-evaporated sodium (section 5.3.1) a cyclic approach consisting of IV measurements alternating with periods of damp heat exposure was chosen to yield a time resolved insight into the degradation process.

In order to conduct this experiment, a CIGSe absorber was grown without sodium supply (batch 2A-1234). Subsequently, NaF was evaporated onto the deposited absorber at a fixed crucible temperature. The amount of sodium to be deposited was tuned by adjusting the web speed during that post-deposition step. Thereby, lower web speeds cause thicker NaF layers on the absorber and, after annealing (at 200 °C), a higher sodium content in the sample. This was confirmed by LIBS measurements of the sodium content of the finished cells (as shown in figure 5.13). In table 5.5 information on the samples and selected IV data are given.

Sample $v$ (cm/min)	Sodium normalized	Avg. initial efficiency	Degradation (50 h DH)	Degradation (200 h DH)	No. of samples
80	0.14	5.2 %	-7 %	-22 %	6
24	0.22	7.2 %	-10 %	-9 %	11
12	0.26	6.7 %	-8 %	-14 %	12
6	0.47	8.7 %	2 %	8 %	14
3	0.77	10.1 %	4 %	35 %	12
1.5	0.84	11.1 %	6 %	36 %	12

Table 5.5: Samples of batch 2A-1234 to study the damp heat stability with respect to the sodium content from post-deposition. Normalized sodium contents from LIBS (cf. section 5.1). Note that negative degradation means an actual increase of the efficiency.

For each group of samples, corresponding to a specific sodium content, the open circuit voltages (figure 5.14(a)), short circuit current densities (figure 5.14(b)), fill factors (figure 5.14(c)), efficiencies (figure 5.15(a)), series resistances (figure 5.15(b)) and parallel resistances (figure 5.15(c)) were derived.

Before damp heat (0 h) the open circuit voltage increases (on average) from 400 to 510 mV with increasing sodium content (figure 5.14(a)). The damp heat degradation behavior is different for each sodium content. For low sodium contents (0.14 $\times$ )  $V_{OC}$  increases, for medium contents (0.47 $\times$ ) it remains constant and for high sodium contents (0.84 $\times$ ) it decreases with increasing damp heat exposure (as indicated with arrows in

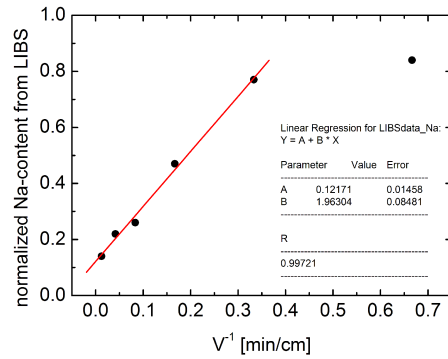


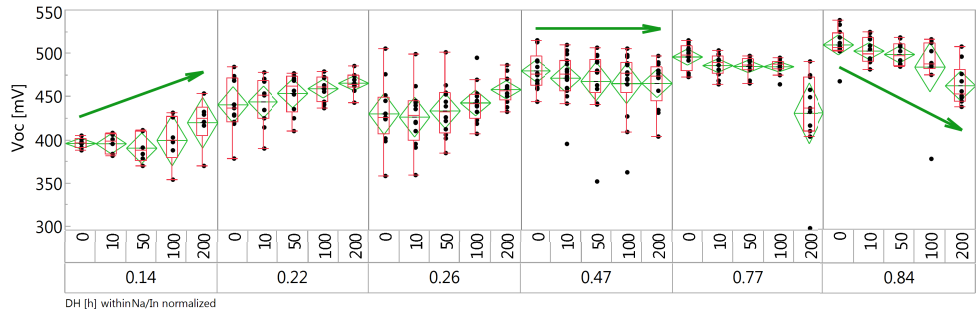
Figure 5.13: Sodium content of the Na post-deposition samples as obtained from LIBS plotted versus the inverse web speed  $v^{-1}$  during NaF post-deposition.

figure 5.14(a)).

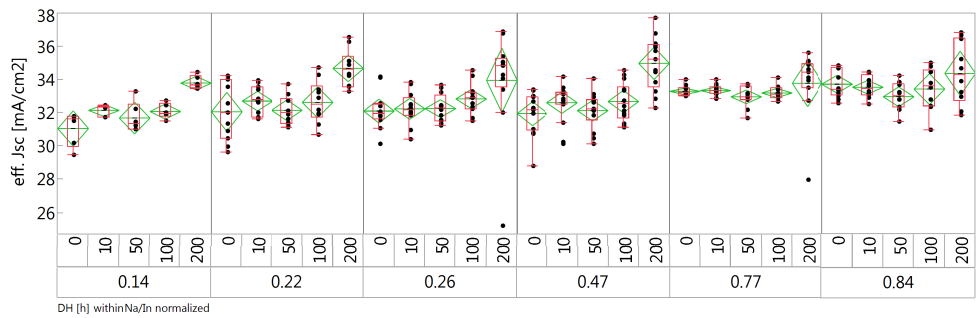
The short circuit current density is initially, i.e. at 0 h damp heat, at around  $32 \text{ mA/cm}^2$  for low up to medium sodium contents (figure 5.14(b)). Only for Na  $0.77\times$  and Na  $0.84\times$  it rises up to approximately  $33.5 \text{ mA/cm}^2$ . Under damp heat,  $J_{SC}$  seems to rise slightly for all sodium contents. However, the most prominent group causing this apparent trend,  $J_{SC}$  after 200 h of damp heat (for all sodium contents), is very likely an outlier caused by a deviation in the intensity of the solar simulator. As these measurements were taken over a longer period of time (time in damp heat plus time for transfer and measurement), the aging of the light source might cause such a drift. However, since this potential drift in intensity and spectrum of the solar simulator mainly affects the photo current, other IV parameters but  $J_{SC}$  were still determined reliably.

Initially, the fill factors increase with increasing sodium content from 42 to 64 % (figure 5.14(c)). The degradation behavior of the fill factor is very distinct: for low sodium contents ( $0.14\times$ ) it remains nearly constant with damp heat up to 200 h. The higher the sodium content, the clearer a different degradation behavior becomes prominent: After 10 h of damp heat, the fill factor has increased up to 10 %, only then an actual degradation starts. This decrease in  $FF$  becomes increasingly prominent with increasing sodium content. In figure 5.14(c) these trends are indicated with arrows.

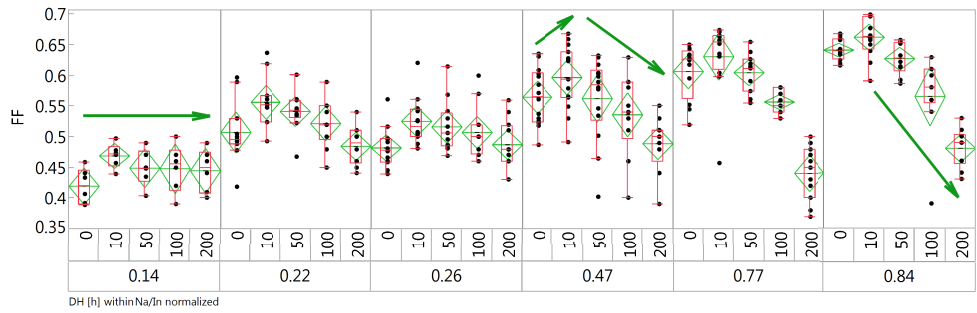
The parallel resistance is very similar for all cells, initially (figure 5.15(c)). For low sodium contents ( $0.14\times$ )  $R_P$  remains constant, but with increasing sodium content, a drop in  $R_P$  becomes more severe and for medium ( $0.47\times$ ) to high ( $0.84\times$ ) sodium contents  $R_P$  drops up to one order in magnitude. The series resistance decreases initially with sodium content (figure 5.15(b)). The drop from the lowest ( $0.14\times$ ) to the highest sodium content ( $0.84\times$ ) exceeds one order in magnitude. After 10 h of damp heat,  $R_S$  dropped for all sodium contents. For longer damp heat exposure,  $R_S$  remains constant at



(a)



(b)



(c)

Figure 5.14: IV parameters of samples with sodium post-deposition. (a)  $V_{OC}$ , (b)  $J_{SC}$  and (c)  $FF$  are plotted versus the time in damp heat (0 to 200h) and grouped by sodium content (normalized from LIBS: 0.14 to 0.84). The center of each green diamond in the graph denotes the group mean and its edges indicate a  $2\sigma$  (95%) confidence interval. The edges of the red boxes indicate the upper and lower quartiles of each group, the red bar in between the median and the red lines mark outliers.

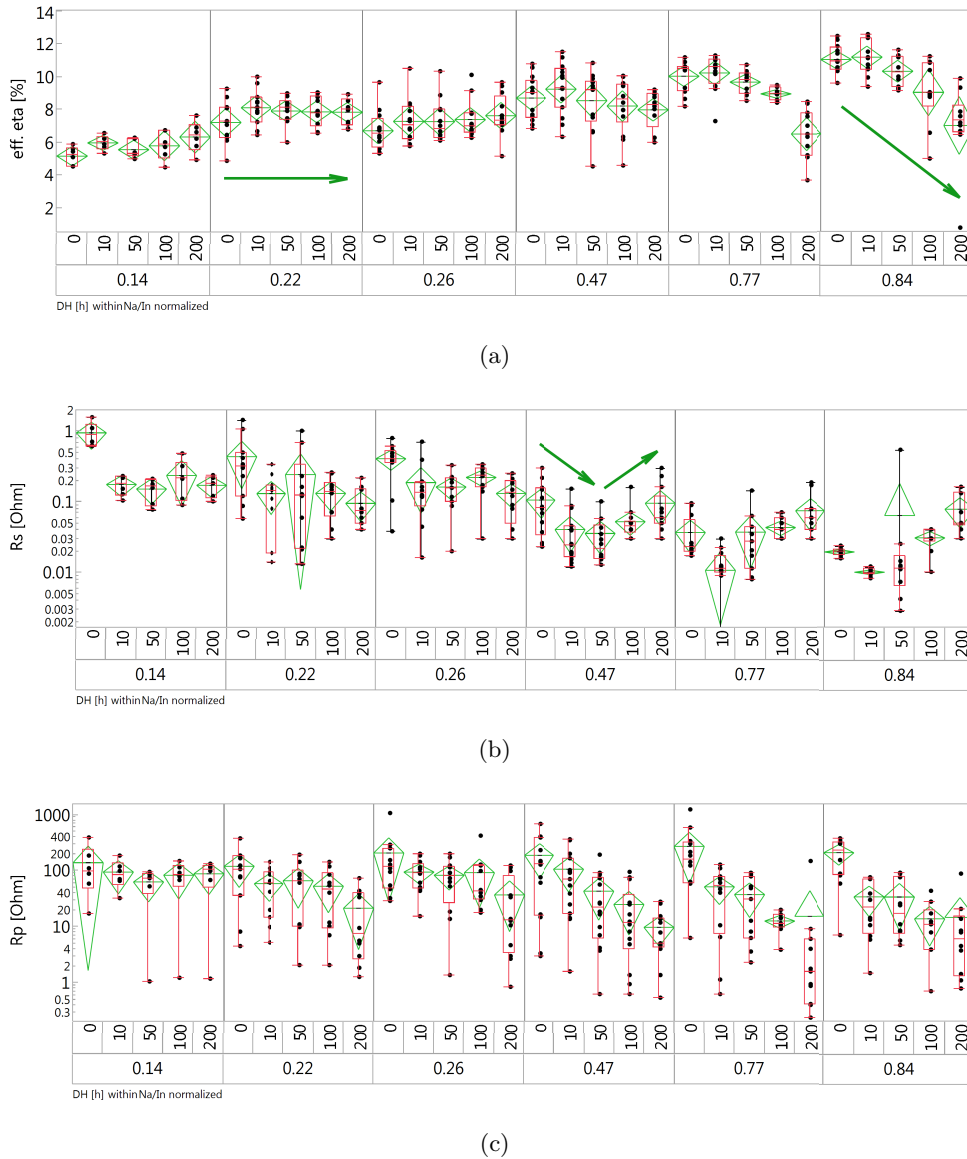


Figure 5.15: IV parameters of samples with sodium post-deposition. (a) efficiency, (b)  $R_S$  and (c)  $R_P$  are plotted versus the time in damp heat (0 to 200 h) and grouped by sodium content (normalized from LIBS: 0.14 to 0.84). The center of each green diamond in the graph denotes the group mean and its edges indicate a  $2\sigma$  (95 %) confidence interval. The edges of the red boxes indicate the upper and lower quartiles of each group, the red bar in between the median and the red lines mark outliers.

lower sodium contents (up to Na 0.26×) while, for higher sodium contents,  $R_S$  increases again (up to one order of magnitude for the highest sodium content). The pattern of initial  $R_S$  decrease, followed by a persistent  $R_S$  increase (indicated with arrows in figure 5.15(b)) correlates with the degradation behavior of the  $FF$  for medium and higher sodium contents (figure 5.14(c)).

The efficiency ( $\eta = V_{OC} \times J_{SC} (\times A) \times FF$ ) reflects the product of the aforementioned trends. Initially, the efficiency clearly increases with sodium content from 5.2 to 11.1%. Regarding the damp heat stability, cells with low (0.14×) up to medium (0.47×) sodium content show almost no degradation in efficiency at all, whereas cells with higher sodium contents (0.77× and 0.84×) exhibit a degradation.

## 5.5 Depth Distribution

In order to assess the elemental gradients of the CIGSe constituents as well as the distribution of trace elements such as sodium, fluorine and oxygen within the absorber and the whole solar cell secondary ion mass spectrometry (SIMS) measurements were performed. A set of samples with different sodium contents ( $T_{NaF} = 760^\circ\text{C}$ ,  $780^\circ\text{C}$  and  $800^\circ\text{C}$  or Na 0.75×, 1.00×, 1.05× as normalized from LIBS; see table 5.4 for more details on the samples) were measured via SIMS for their elemental depth gradients. The measurements were performed and the data processed as described in section 3.2.10.

Figure 5.16 shows the obtained gradients of the CIGSe constituents copper (red), indium (blue), gallium (green) and selenium (black) as well as relevant elements in minor concentrations, such as sodium (black), oxygen (blue) and fluorine (red). For all sodium contents, SIMS measurements were carried out before and after 85 h damp heat treatment (profiles in “bleached” colors).

In all SIMS measurements, typical device features were detected: Between 200 s to 300 s sputter time, the signals of copper, indium and gallium become evident (figures 5.16(a), 5.16(c) and 5.16(e)). At the same time the zinc (not shown) and oxygen signals decrease (figures 5.16(b), 5.16(d) and 5.16(f)), indicating the interface between TCO (ZnO) and absorber (CIGSe). As the polycrystalline material does not have flat interfaces, i.e. the roughness is defined by the grain morphology (see section 5.2 for SEM images and section 5.6 for measurements of the surface roughness), interfaces do not cause sharp transitions with sputter time in the SIMS signal. Instead, the elemental profiles are smeared out, making it difficult to precisely determine the depths of thin (compared to the average roughness) layers, such as the CdS buffer. At around 1000 s sputter time, the signals of the absorber constituents decrease and the molybdenum signal (not shown) increases, indicating the detection of the back contact interface, i.e. between CIGSe and molybdenum.

For all sodium contents, a slight gallium grading towards the back electrode was detected. This is an intentionally build-in grading of the absorber in order to create a

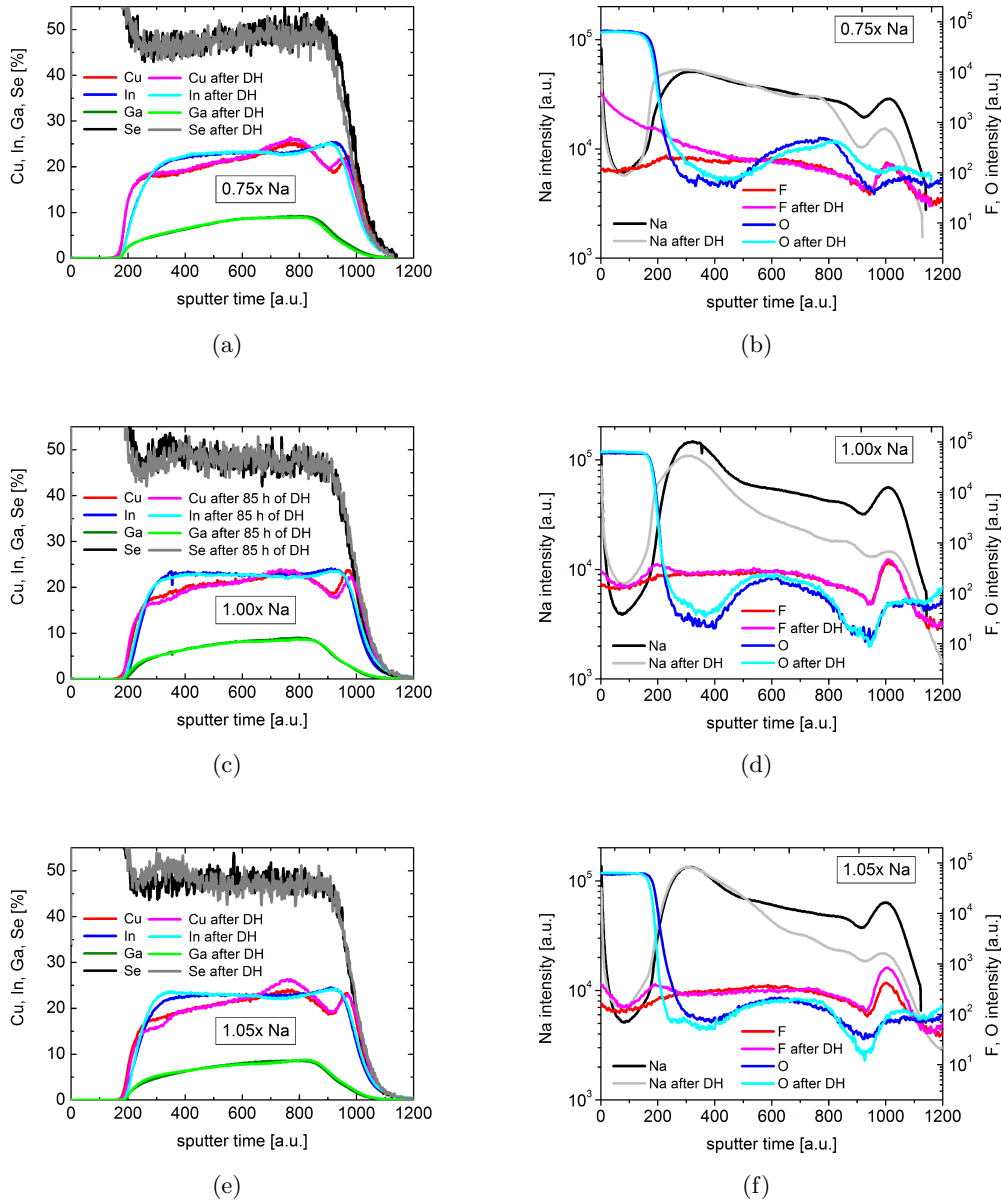


Figure 5.16: Elemental depth profiles from SIMS on solar cells with different sodium contents (co-evaporation; normalized sodium contents from LIBS denoted on the graphs) before and after 85 h of damp heat. The sputtering was done from the TCO surface (sputter time = 0) down to the back contact (sputter time  $\approx$  1000). (a), (c), (e) depict the chemical gradients of the CIGSe constituents. (b), (d), (f) depict sodium, oxygen and fluorine that are only contained in small quantities in the absorber.

back-surface (electric) field that helps collecting charge carriers by inducing an additional electron drift towards the space charge region and a hole drift towards the back electrode, respectively. Aside from the interface regions, the indium signal behaves inversely proportional to the gallium signal, which is, for a single-phase chalcopyrite crystal, plausible since indium and gallium share the same sublattice of the crystal.

It becomes clear that, for all sodium contents, the profiles of copper, indium, gallium and selenium do not change with damp heat treatment. This strongly indicates that the chalcopyrite CIGSe crystal itself is stable under damp heat treatment. Only for the Na 1.05× sample, a slight difference in the copper profiles before and after damp heat was detected. The latter might be caused by a slight initial stoichiometry deviation at a different lateral position of the measurement spot on the sample.

Sodium is present throughout the absorber for samples of all sodium contents (figures 5.16(b), 5.16(d) and 5.16(f)). The amount of sodium decreases from the front towards the back of the absorber. At the CdS/CIGSe- ( $\approx 200$  s to 300 s) and at the CIGSe/Mo-interfaces ( $\approx 1000$  s) an aggregation of sodium was found for all samples. Compared to the Na 0.75× sample, this aggregation is more pronounced for the Na 1.00× and Na 1.05× samples. In fact, also the overall sodium signal increases from the Na 0.75× to the Na 1.05× sample which is obvious from the preparation of the samples (variations of  $T_{NaF}$  lead to different amounts of sodium incorporated into the absorber). Nevertheless, this expectation could nicely be proven by integrating the sodium signal from SIMS over the full absorber thickness (figure 5.17).

After damp heat, sodium is the only (here observed) element that exhibits a different depth distribution. For the Na 0.75× sample, the sodium aggregation at the CIGSe/Mo-interface is much smaller after damp heat treatment (figure 5.16(b)). For higher sodium contents, i.e. the Na 1.00× (figure 5.16(d)) and Na 1.05× (figure 5.16(f)) samples, the aggregations seems to have almost vanished. For the latter two samples, the overall sodium gradient from front to back is also much steeper compared to before damp heat. The sodium might therefore have been transported (diffusion as an ion, or as a compound in solution, e.g. NaF) towards the back contact and substrate. In figure 5.17 the integral amounts of sodium after damp heat are shown as well. The observation of less sodium in the absorber becomes evident.

Fluorine is fairly evenly distributed before damp heat, throughout the whole device (including TCO), with one exception. For all samples, fluorine aggregates at the CIGSe/Mo-interface (figures 5.16(b), 5.16(d) and 5.16(f) at  $\approx 1000$  s). Since sodium is also present and similarly aggregated, the presence of NaF as a compound may be suspected. In contrast to the sodium aggregation, this fluorine aggregation does not diminish after damp heat. Instead, for the Na 1.00× and Na 1.05× sample, a small amount of fluorine aggregates at the CdS/CIGSe-interface after damp heat. For the Na 0.75× sample, the measurement seems to be dominated by the artifact of an increasing fluorine content towards the sample surface (this SIMS measurement was done later compared to all other measurements). Looking closely at the sodium signal after damp heat at



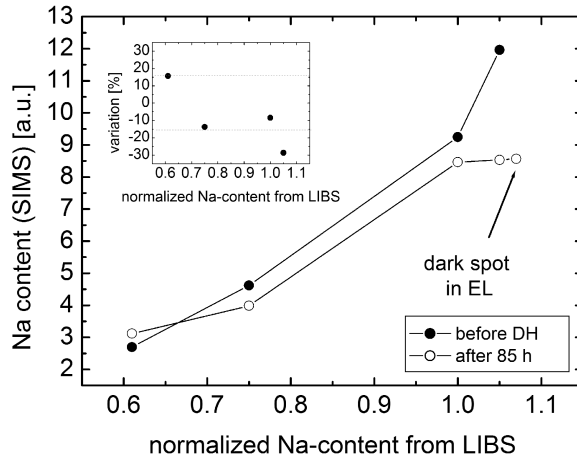


Figure 5.17: Integral sodium content from SIMS profiles (figure 5.16) plotted versus the NaF crucible temperature during CIGSe deposition. Filled circles indicate the amount of sodium before damp heat, open circles indicate the amount after 85 h of damp heat. Inset: change of the sodium content after damp heat for each NaF crucible temperature compared to before damp heat.

the exact position of the fluorine aggregation after damp heat (CdS/CIGSe-interface), also the sodium signal is higher as compared to before damp heat (figures 5.16(d) and 5.16(f)). Again, the presence of NaF might be suspected, possibly as a consequence of an aforementioned transport-process during damp heat.

Oxygen (figures 5.16(b), 5.16(d) and 5.16(f)) is present in the whole sample. Up to a sputter depth of 200 s to 300 s it may be attributed to the zinc oxide TCO. Further into the device, the oxygen signal increases in the absorber, then decreases again. Starting at the interface CIGSe/Mo it increases again. Only here, a little different distribution could be observed after damp heat: Slightly more oxygen is present after degradation, which might indicate a partial oxidation of the molybdenum.

## 5.6 Surface Roughness

Scanning laser microscopy (cf. chapter 3.2.12) was used to characterize the surface roughness of the Cu(In,Ga)Se<sub>2</sub> solar cells. The samples under investigation were taken from the batch (2A-1209) whose damp heat stability was investigated in section 5.3.3. They were identical to the samples of this batch which were used for LIBS characterization (cf. section 5.1).

In figure 5.18 height images from laser scanning microscopies of five samples with

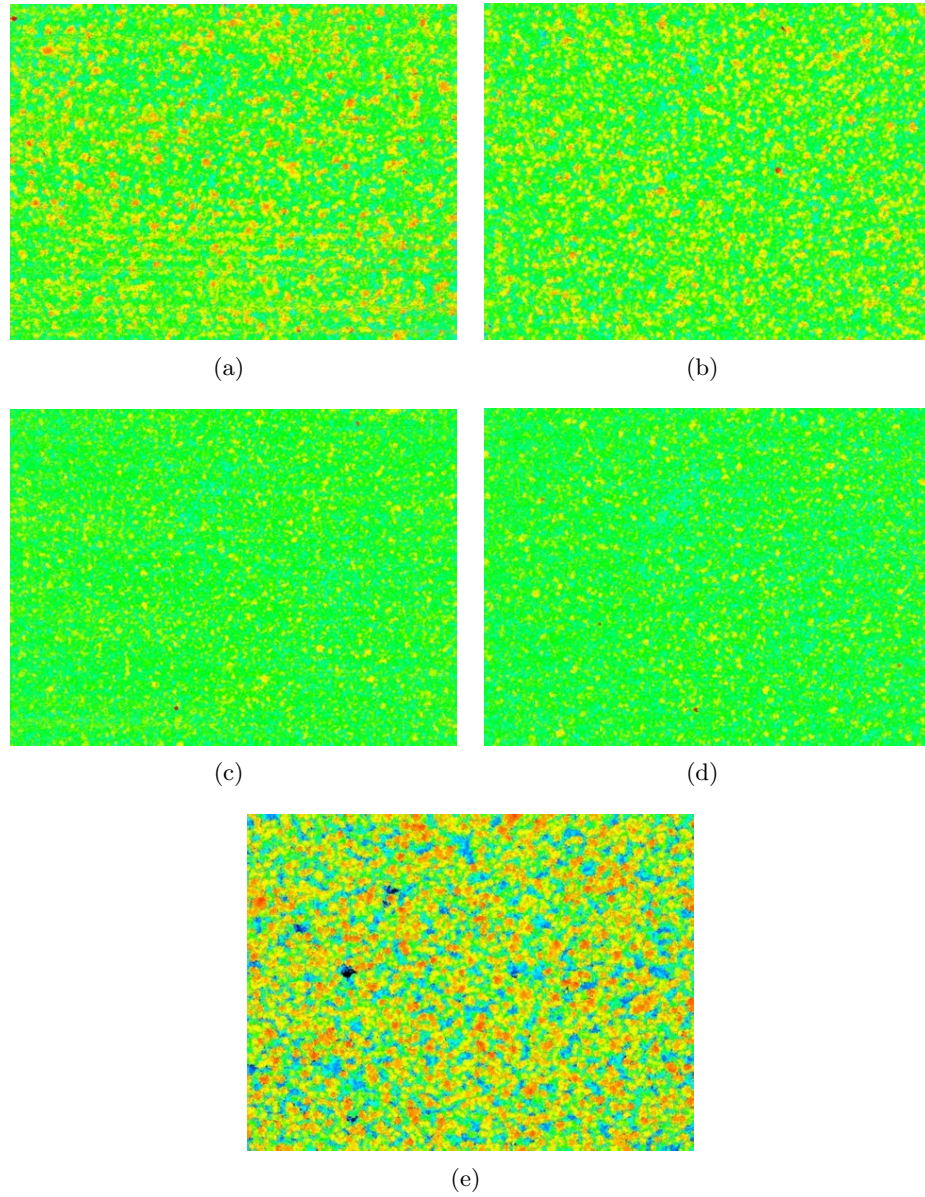


Figure 5.18: Scanning laser microscopy of surfaces of CIGSe solar cells with different sodium contents (as normalized from LIBS): (a)  $0.61\times$  (b)  $0.75\times$  (c)  $1.00\times$  (d)  $1.05\times$  (e)  $1.31\times$ . The height is color coded with a range of  $1.5\mu\text{m}$  from valley to peak (color scale: black – blue – cyan – green – yellow – red). The width of each image section is approximately  $100\mu\text{m}$ . For details about the samples see table 5.4 in section 5.3.3.

different sodium contents ( $0.61\times$  to  $1.31\times$  as normalized from LIBS) are shown. Curvatures of the background (of the image) were removed and the scaling of the height is the same for all images, i.e. a range of  $1.5\ \mu\text{m}$  from valley to peak (color scale: black – blue – cyan – green – yellow – red). From these height profiles a decreasing roughness with increasing sodium content is observable (figure 5.18(a) to figure 5.18(d)). Apparently the sample with the highest sodium content ( $1.31\times$ ) is an exception from that trend showing the highest roughness.

The mean square roughness  $R_{sq}$  was calculated from the laser scanning microscopy images. The values are given in table 5.6 and plotted versus the sodium content in figure 5.19(a).

Sample ( $T_{NaF}$ )	Sodium normalized	$R_{sq}$ [nm]	$R_{sq}$ normalized
740 °C	0.61	164	1.62
760 °C	0.75	141	1.40
780 °C	1.00	101	1.00
800 °C	1.05	102	1.01
820 °C	1.31	303	3.00

Table 5.6: Mean square roughness  $R_{sq}$  of the samples from batch 2A–1209. For details about the samples see table 5.4 in section 5.3.3.

In section 5.2.1 the trend towards a flatter solar cell surface with increasing sodium content was already recognized by judging the SEM images of this batch (cf. figure 5.5). The sample with the highest sodium showed an exceptionally high surface roughness in the SEM image as well. In order to quantify that visual impression the free *Gwyddion* software [132] was used to calculate the roughness from the top view SEM images (figure 5.5). Due to the lack of a height scale in the SEM images only a relative quantification was possible. Figure 5.19(b) shows the normalized mean square roughness from scanning laser microscopy as well as from SEM images in comparison. For both determination methods the roughness was normalized to the value of the sample with the best IV performance (before and after 85 h) of damp heat, i.e. Na  $1.00\times$  (cf. section 5.3.3). The relative roughness obtained from the two methods is in very good agreement. Both are rendering the trend to less rough surfaces with higher sodium content, both with the exception of the sample with the highest sodium content ( $1.31\times$ ).

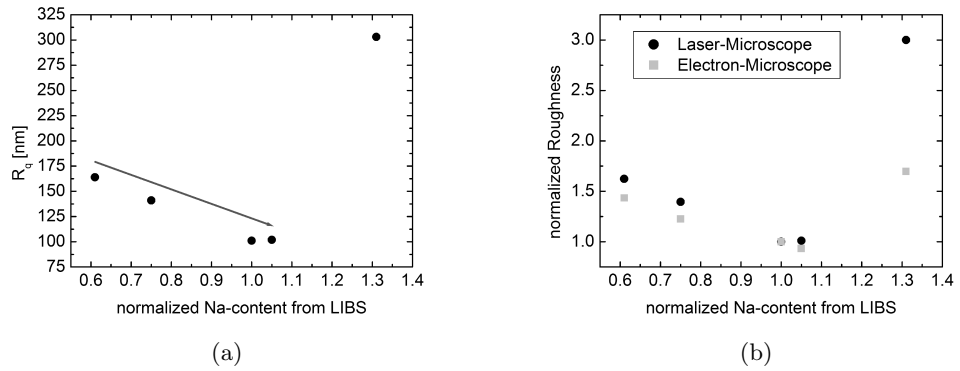


Figure 5.19: Roughness of the solar cell surface. (a) Mean square roughness obtained from scanning laser microscopy images (figure 5.18) and (b) normalized mean square roughness from scanning laser microscopy as well as SEM images (figure 5.5) analyzed with the *Gwyddion* software [132] plotted versus the sodium content (normalized from LIBS). For details about the samples see table 5.4 in section 5.3.3.

## 6 Lateral Inhomogeneities

Thin film coating processes in the order of square meters need not necessarily result in perfectly homogeneous layers. Except for the microscopy images, all characterization methods for solar cells (e.g. IV) employed in the previous chapters were incapable of showing possible influences of lateral inhomogeneities on the properties of the solar cell. In order to study the lateral homogeneity of CIGSe solar cells (with a size of  $\approx 59\text{ cm}^2$  that was cut out of a web of aforementioned dimensions; cf. section 3.1) measurement methods with lateral resolution such as electroluminescence (EL), dark lock-in thermography (DLIT) or light beam induced current (LBIC) must be employed.

### 6.1 Electroluminescence Imaging

#### 6.1.1 EL vs. Damp Heat

Electroluminescence images of solar cells whose IV characteristics before and after damp heat were discussed in section 5.3.1 were recorded as described in section 3.2.2. These Cu(In,Ga)Se<sub>2</sub> solar cells of batch 2A-1173 had a size of 126 mm by 31 mm ( $\approx 39\text{ cm}^2$  total area). The exposure time for EL imaging was 90 s and the supplied current of 1 A ( $25.6\text{ mA/cm}^2$  based on the total area or  $31.0\text{ mA/cm}^2$  based on the active area) was in the order of the short circuit current of the samples.

In figure 6.1 and 6.2, EL images after different damp heat exposures are shown for those solar cells for two different sodium contents, i.e.  $0.52\times$  and  $11.33\times$  (as normalized from LIBS; cf. section 5.1), respectively. The dark vertical line in each EL image is the busbar and the thinner dark horizontal lines are the grid fingers on top of the solar cell (cf. figure 1.8). Interruptions in the vertical stripe on the right of the busbar is shading from the contacting tips. The current injection was distributed over 10 tips on each side of the cell (front contact, i.e. the busbar, and back contact; the latter is not visible in the EL images).

The overall EL intensity of all cells under damp heat treatment decreased with increasing damp heat exposure. However, it remained unaffected for the samples under dry heat (not shown here; for a comparison of the IV data see section 4.1). The decrease in EL intensity is much more pronounced for the samples with higher sodium content ( $11.33\times$ ; cf. figure 6.2) than for the samples with lower sodium content ( $0.52\times$ ; cf. figure 6.1). For the samples with  $11.33\times$  sodium content an effect can be observed that is barely visible for the samples with  $0.52\times$  sodium content: the formation of darker

cloud-like areas within the cell (cf. figure 6.2) after 15 h of damp heat. They appear to be caused by a locally more severe degradation and are thus a sign for a laterally inhomogeneous degradation process.

### 6.1.2 EL vs. Sodium

For a closer look on the influence of the sodium content on the electroluminescence of the CIGSe solar cells EL images of samples whose IV characteristics were discussed in section 5.3.2 were recorded as described in section 3.2.2. These Cu(In,Ga)Se<sub>2</sub> solar cells of batch 2A-1225 had a size of 190.5 mm by 31.0 mm ( $\approx 59 \text{ cm}^2$  total area). The exposure time for EL imaging was 90 s and the pixel binning  $2 \times 2$  (cf. section 3.2.2). The supplied current of 1.8 A ( $30.4 \text{ mA/cm}^2$  based on the total area or  $35.6 \text{ mA/cm}^2$  based on the active area) was slightly above the short circuit current of the samples.

In figure 6.3 and 6.4, EL images of solar cells with three different sodium contents, i.e.  $0.43\times$ ,  $0.71\times$  and  $1.14\times$  (as normalized from LIBS; cf. section 5.1) are shown before and after 50 h of damp heat treatment, respectively. The busbar (dark horizontal line at the top of the cell), the grid fingers (thinner dark vertical lines) and the scribed areas (square shaped dark areas at the bottom of the cell) are visible in all EL images. Specifically in figure 6.3(c) the contacting tips on the long sides of the cell are visible (12 on each side, the busbar and the back contact scribing areas, respectively).

From figure 6.3 it is evident that the overall EL intensity of the solar cell increases with increasing sodium content. This is in good agreement with the trend in IV parameters with respect to the sodium content (as shown in figure 5.10 and discussed in section 5.3.2). A comparison of figure 6.3 and figure 6.4 allows to compare the influence of 50 h damp heat on the overall EL intensity. As seen for the samples in section 6.1.1 the EL intensity decreases due to damp heat exposure. After damp heat, the sample with  $0.71\times$  sodium content shows the highest EL intensity. This reflects the trend in the IV parameters with respect to sodium after damp heat (as shown in figure 5.10 and discussed in section 5.3.2). In figure 6.4(b), i.e. the EL image after damp heat of the sample with  $0.71\times$  sodium content, a darker area is visible. They look similar, however more severe, than the dark cloud-like areas in figure 6.2(c) to 6.2(f). In order to identify the origin of the dark spots, the EL image of the sample in figure 6.4(b) will be compared to other laterally resolved measurement methods in section 6.2.

In order to verify the findings on the dependence of the EL signal on the sodium content of the CIGSe absorber, EL images of samples with five different sodium contents in the range of  $0.61\times$  to  $1.31\times$  were recorded. Their respective IV characteristics before and after 85 h of damp heat treatment were shown in section 5.3.3. The samples of batch 2A-1209 had a size of 126 mm by 31 mm ( $\approx 39 \text{ cm}^2$  total area). The exposure time for EL imaging was 60 s and the supplied current of 1 A ( $25.6 \text{ mA/cm}^2$  based on the total area or  $28.4 \text{ mA/cm}^2$  based on the active area) was slightly below the short circuit current of the solar cells.

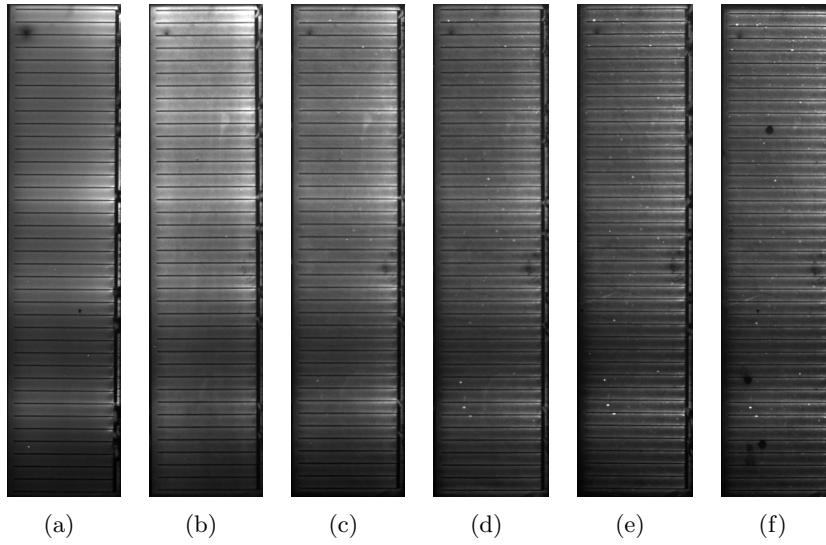


Figure 6.1: Electroluminescence images of a sample with  $0.52\times$  sodium content from batch 2A-1173 (IV data shown in section 5.3.1). EL after different damp heat exposures: (a) 0 h (b) 5 h (c) 15 h (d) 27 h (e) 37 h (f) 47 h.

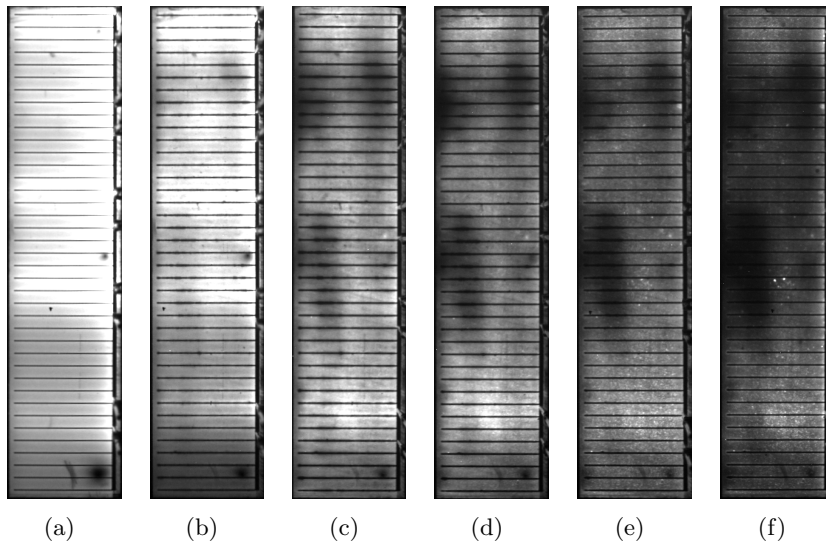


Figure 6.2: Electroluminescence images of a sample with  $11.33\times$  sodium content from batch 2A-1173 (IV data shown in section 5.3.1). EL after different damp heat exposures: (a) 0 h (b) 5 h (c) 15 h (d) 27 h (e) 37 h (f) 47 h. Darker cloud-like spots appear after 15 h of damp heat.

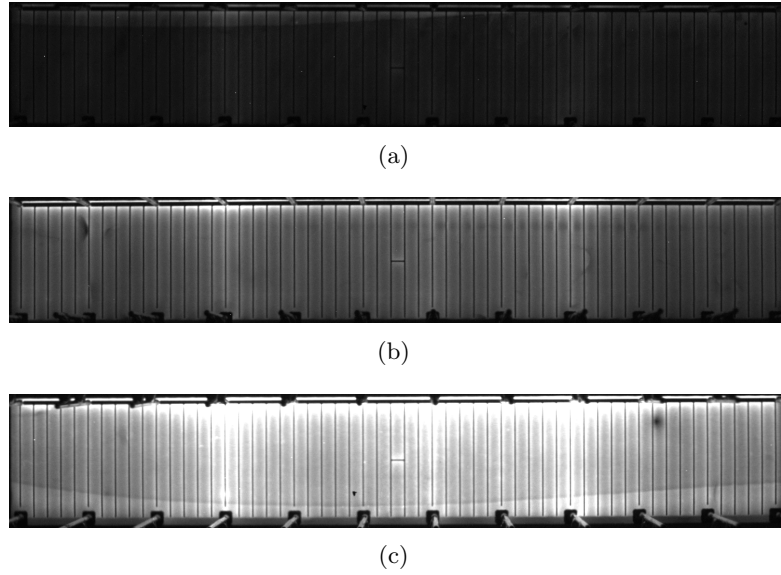


Figure 6.3: Electroluminescence images from batch 2A-1225 before damp heat (IV data shown in section 5.3.2). EL for cells with different sodium content (as normalized from LIBS): (a)  $0.43\times$  (b)  $0.71\times$  (c)  $1.14\times$ .

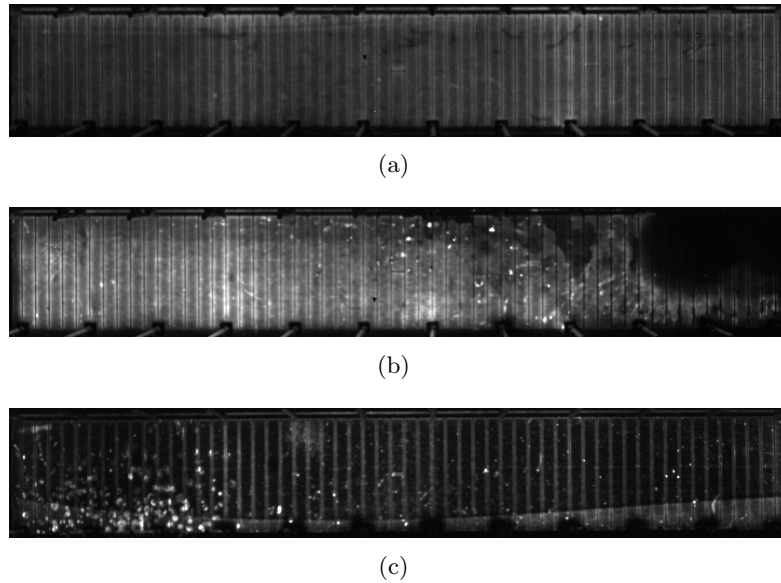


Figure 6.4: Electroluminescence images from batch 2A-1225 after 50 h of damp heat (IV data shown in section 5.3.2). EL for cells with different sodium content (as normalized from LIBS): (a)  $0.43\times$  (b)  $0.71\times$  (c)  $1.14\times$ .



In figure 6.5 the EL images of samples with five different sodium contents, i.e.  $0.61\times$ ,  $0.75\times$ ,  $1.00\times$ ,  $1.05\times$  and  $1.31\times$  (as normalized from LIBS; cf. section 5.1), are shown before and after 85 h of damp heat treatment, respectively. The general features of the cell that are mapped in the EL image such as busbar and back contact scribing areas are similar to figure 6.3 and 6.4 and were described before.

The EL images from batch 2A–1209 confirm the trends that have been found for the other two previous batches (2A–1173 and 2A–1225): (i) With increasing sodium content in the absorber the EL intensity of the solar cells increases. Although the sample with the highest sodium content in this batch ( $1.31\times$ , cf. figure 6.5(i)) is an exception from that trend (before damp heat), the overall trend in the EL intensity with respect to sodium content matches the trend in the IV parameters for these samples (the efficiency drops for the highest sodium content as well; cf. figure 5.12 in section 5.3.3). (ii) The EL intensity drops for all samples, i.e. all sodium contents, after damp heat treatment (cf. figure 6.5). (iii) Even the formation of darker cloud-like areas in the EL image after damp heat that has been observed for some samples previously could be reproduced (figure 6.5(h)).

## 6.2 Differential Diagnosis with Different Imaging Techniques

Differential diagnosis is identifying failure mechanisms by combining the conclusions from complementary measurement methods such as EL, LBIC and DLIT while the measurement result of each individual method allowed multiple conclusions. In this section, the advantage of combining these three laterally resolved measurement techniques is demonstrated in order to identify three different failure mechanisms. The samples were selected from batch 2A–1225. IV parameters were shown in section 5.3.2 and EL images for all three sodium contents in section 6.1.2.

Electroluminescence (EL) images were recorded with the parameters given in section 6.1.2 following the procedure described in section 3.2.2. light beam induced current measurements were carried out with the setup described in section 3.2.6. Lock-in thermography images were obtained with the measurement parameters given in table 3.2 as described in section 3.2.5. During lock-in thermography the cell was under a reverse bias ( $V_{bias} = -0.5\text{ V}$ ) thus the operational mode was DLIT.

### 6.2.1 Shunt

Figure 6.6(a) shows the EL image of a  $\text{Cu(In,Ga)Se}_2$  solar cell with a sodium content of  $0.71\times$  (as normalized from LIBS) in the absorber. The cell was not treated with damp heat. Characteristic features of the solar cell are apparent in the EL image such as the busbar (dark horizontal line at the top of the cell), the grid fingers (thinner dark vertical lines) and the scribed areas (square shaped dark areas at the bottom of the cell) in the EL image. The light emitted via electroluminescence is not distributed completely

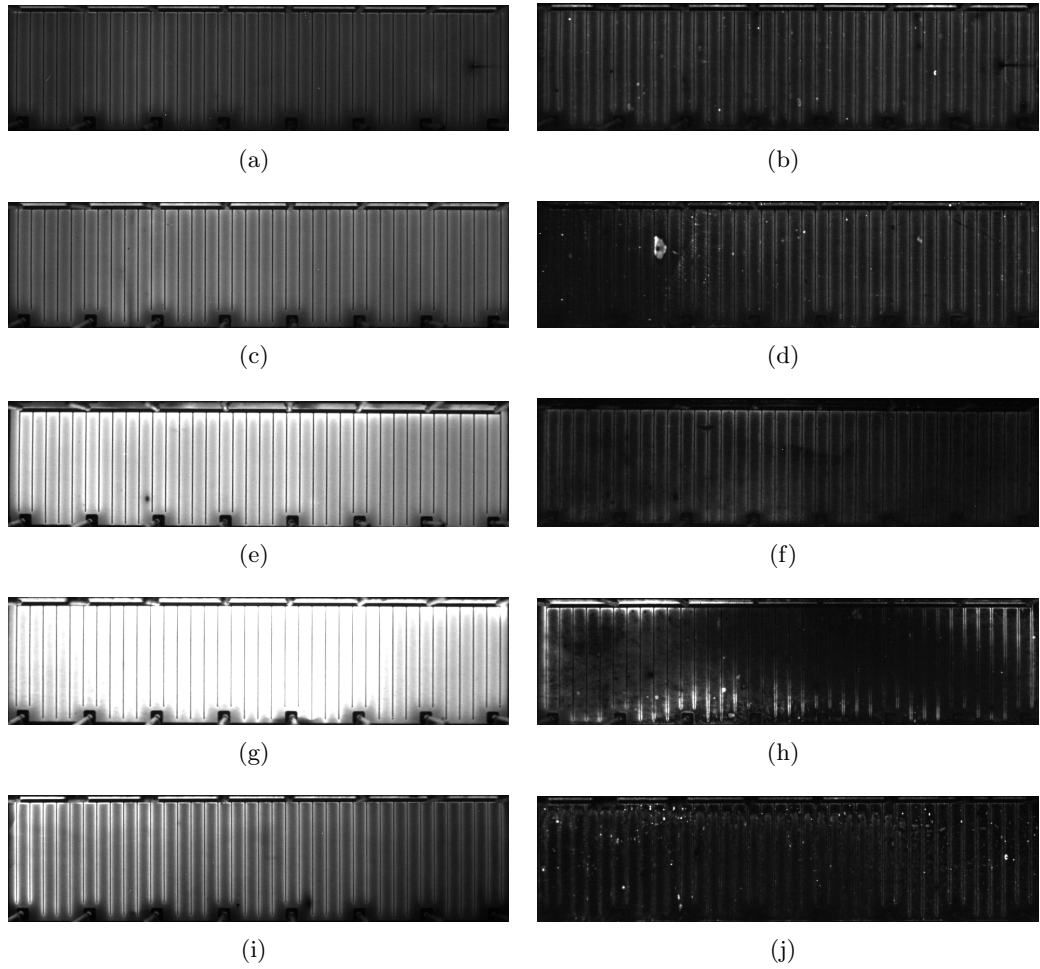


Figure 6.5: Electroluminescence images of samples from batch 2A-1209 with different sodium contents before and after 85 h of damp heat (IV data shown in section 5.3.3; sodium contents as normlized from LIBS). (a) Na  $0.61\times$  before DH (b) Na  $0.61\times$  after DH (c) Na  $0.75\times$  before DH (d) Na  $0.75\times$  after DH (e) Na  $1.00\times$  before DH (f) Na  $1.00\times$  after DH (g) Na  $1.05\times$  before DH (h) Na  $1.05\times$  after DH (i) Na  $1.31\times$  before DH (j) Na  $1.31\times$  after DH.

homogeneous. Close to the busbar and to the grid fingers the intensity is slightly higher. This is due to the voltage distribution across the cell (cf. equation 3.2). The limited conductivity of the planar contacts, namely the TCO (since its sheet resistance is about two orders of magnitude above the back contact), leads to a voltage drop in the local voltage compared to the applied external voltage. Thus, the local EL intensity drops with increasing distance from the grid and especially from the busbar (both have a higher conductivity than the planar contact). Additionally, the EL intensity is higher close to some of the measurement tips that are contacting the busbar (e.g. the fourth and the ninth from the left). This is an indication of a slightly non-uniform current distribution onto the 12 measurement tips probably caused by slightly different contact resistances between the tips and the busbar. All these features are normal and can be observed on every sample. On the contrary, a non desirable feature in the EL in figure 6.6(a) is the dark spot in the lower part of the cell at the third grid finger from the right. The width of that spot equals about the distance between two grid fingers. Since emission of light (electroluminescence) and absorption (operation as a solar cell) are reciprocal processes, the area of the solar cell with the dark spot in EL will contribute less to the solar cells power output under illumination.

Figure 6.6(b) shows the LBIC image of the same solar cell. Almost the whole area of the solar cell contributes evenly to the total current (red color). Only three spots contribute less: the spot at the third grid finger from the right (yellow) which appeared dark in EL and two spots (yellow, green) that are caused by a partial shading from the contacting tips. The pixels in the vicinity of the spot at the third grid finger from the right (more precisely, the areas on the solar cell that are imaged by each pixel) contribute about 75 % of the current (per pixel) compared to the majority of the area of the solar cell that contributes homogeneously.

Figure 6.6(c) shows the DLIT image of the sample. Since it is recorded under a reverse voltage bias ( $V_{bias} = -0.5\text{ V}$ ) it reveals shunts as bright spots while the rest of the solar cell's area remains dark. Shunts are spots where the local parallel resistance  $R_P^{i,j}$  of the solar cell diode is dramatically reduced<sup>1</sup> (cf. figure 1.5). Thus a current can flow in reverse direction although the solar cell diode is blocking. The current concentrates on the spot with reduced parallel resistance and thus heats up the solar cell locally hence making the shunt visible as a temperature difference in the DLIT image. Besides a few minor bright spots which are very small shunts, figure 6.6(c) reveals a shunt at the same position that was a characteristic spot in the EL and the LBIC image.

It can be concluded that the spot that was observed in EL, LBIC and DLIT is a shunt close to the third grid finger from the right. The lock-in thermography image

---

<sup>1</sup>The physical origin of a shunt is a short circuit between front and back contact. Such a short may for example be generated if the absorber has small pinholes which are covered (filled) with the TCO. Thus, a direct pathway for the current between the front and the back contact is created. A short circuit may also be induced due to damage to the solar cell (mechanically or by thermal breakdown of the pn-junction due to high reverse voltages).

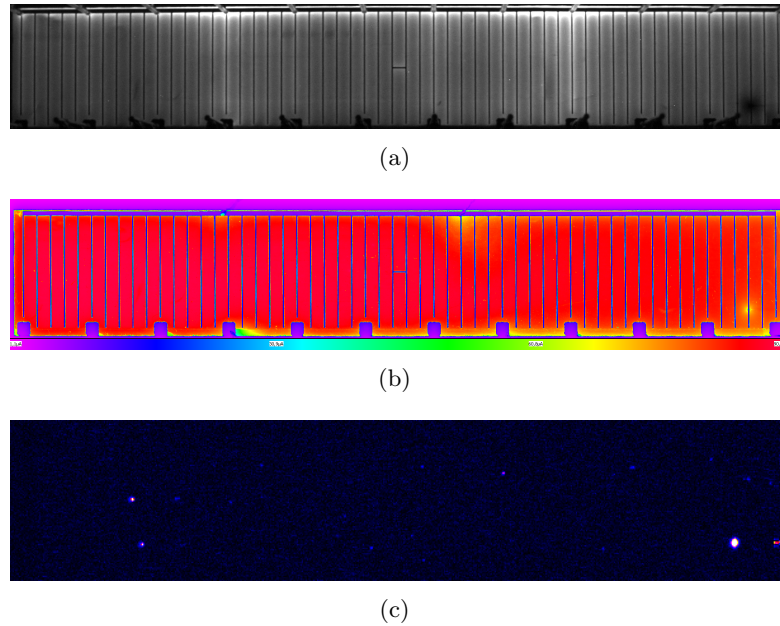


Figure 6.6: Different imaging techniques applied to a solar cell with shunt (at the third grid finger from the right) that is visible in (a) EL (b) LBIC and (c) DLIT. Sample from batch 2A-1225 with a sodium content of  $0.71\times$  (as normalized from LIBS) without damp heat treatment.

(figure 6.6(c)) clearly showed that. Due to the shunt the voltage drops significantly at that location resulting in the reduced electroluminescence signal that was observed experimentally (figure 6.6(a)). In the LBIC image the shunt appears as a spot with lower contribution to the overall current because only a fraction of the current generated in the vicinity of the shunt reaches the outside contacts (and is measured) while the other fraction flows directly through the shunt (figure 6.6(b)).

### 6.2.2 Severe Shunt

Figure 6.7(a) shows the EL image of a  $\text{Cu}(\text{In,Ga})\text{Se}_2$  solar cell with a sodium content of  $0.43\times$  (as normalized from LIBS) in the absorber. The cell was exposed to 50 h of damp heat. The overall EL intensity is very low. On the one hand, this can be explained by the drop of EL intensity due to damp heat treatment that was shown in section 6.1.2. Characteristic features of the solar cell that were discussed in the previous section (6.2.1) are barely visible in figure 6.7(a). On the other hand, the similar sample (same sodium content, same batch) that was shown in figure 6.4(a) had a higher overall EL intensity even after damp heat. Looking carefully at the EL image in figure 6.7(a), one can see

that the right part of the solar cell is completely dark – except for a bright spot at the busbar – while busbar and grid fingers are faintly visible in the middle and on the left side of the cell. The origin of the bright spot seems to be below the busbar since there is also some light visible above while most of the light is emitted below the busbar.

Figure 6.7(b) shows the LBIC image of this solar cell. There is a distinct gradient in the intensity of the LBIC signal from the left to right of the solar cell. The right side (blue color) does not contribute to current output of the solar cell.

Figure 6.7(c) shows the DLIT image of the sample. It clearly reveals a shunt at the same position where the bright spot appeared in the EL image. The spot diameter of the shunt is wider and appears white (highest intensity) thus showing a higher intensity than the shunt from the previous example (in figure 6.6(c)).

Bearing the DLIT image in mind the spot on the right side of the solar cell in figure 6.7 can be identified as a severe shunt. Not only the larger appearance in the DLIT image justifies the term “severe”. Most of all its position, i.e. under or at the busbar, makes this shunt detrimental for the solar cell. A significant portion of the generated current under illumination flows through the shunt and does not reach the outer contacts of the solar cell causing the pattern in the LBIC image (figure 6.7(b)) that was described above. Contrariwise does the cell not emit any electroluminescence on the right side of the solar cell because the potential difference between front and back contact drops (almost) fully at the busbar leaving the whole area along the grid fingers on the right side of the solar cell dark (figure 6.7(a)). The fact that a bright spot is visible in EL at the position of the shunt is another indication for its severely detrimental influence: The heat due to the current flow through the shunt reaches a level high enough so that the sensitivity of the EL camera is sufficient to detect tails of the spectrum of the heat emission<sup>2</sup>.

### 6.2.3 Corrosion

Figure 6.8(a) shows the EL image of a  $\text{Cu(In,Ga)Se}_2$  solar cell with a sodium content of  $0.71\times$  (as normalized from LIBS) in the absorber. The cell was exposed to 50 h of damp heat and is the same sample as in figure 6.4(b). The EL image reveals a number of inhomogeneities. Close to the grid fingers the EL intensity is higher than in between. This characteristic has been discussed in section 6.2.1, however, it is more pronounced than in figure 6.6(a) since the TCO conductivity is presumably lower after damp heat exposure and thus the voltage drops along the planar contacts are larger. Furthermore, a number of darker areas as well as smaller spots are visible in the EL image, indicating a laterally inhomogeneous degradation. However, the most prominent

---

<sup>2</sup>The infrared camera used for DLIT (cf. section 3.2.5) is most sensitive in the spectral range between  $5\ \mu\text{m}$  and  $1\ \mu\text{m}$  whereas the camera used for EL (cf. section 3.2.2) is most sensitive in the spectral range below  $1\ \mu\text{m}$

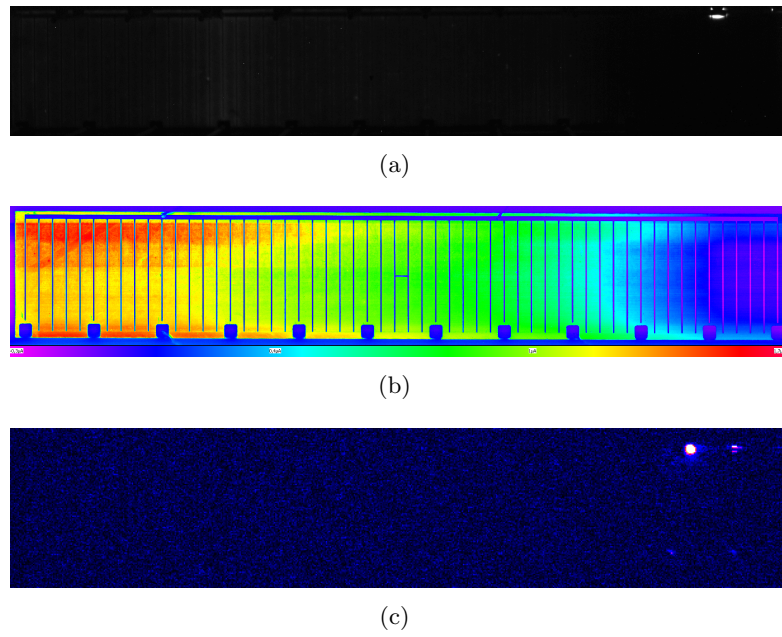


Figure 6.7: Different imaging techniques applied to a solar cell with a severe shunt close to the busbar that affects the (a) EL (b) LBIC and (c) DLIT images. Sample from batch 2A-1225 with a sodium content of  $0.43\times$  (as normalized from LIBS) after 50 h of damp heat.

feature in figure 6.8(a) is the dark spot in the top right corner of the solar cell. No electroluminescence is emitted there indicating severe degradation.

Figure 6.8(b) depicts the mapping of the current contributions from different areas of the solar cell as obtained from LBIC. While most of the solar cell contributes fairly homogeneously, the upper right corner of the solar cell which appeared black in the EL image does not contribute to the current at all.

Figure 6.8(c) shows the DLIT image of this sample. A few smaller shunts are distributed across the solar cell. However, no significant shunt can be observed in the vicinity of the upper right corner of the solar cell, which remains black in EL and does not contribute to the solar cell's current output according to LBIC. This is in contrast to the previous two examples of failures (section 6.2.1 and 6.2.2) where (severe) shunts could be identified as cause for such an observation.

Looking at the vicinity of the upper right corner of the present sample the EL image (figure 6.8(a)) and the LBIC image (figure 6.8(b)) reveal another important difference to the failure pattern of a shunt that was discussed before. On the contrary to figure 6.6(a) and figure 6.7(a) the intensity of the electroluminescence does not fade out smoothly towards the dark area, it rather drops abruptly at the circumference of the dark area in figure 6.8(a). The same abrupt drop can be observed in the LBIC signal in figure 6.8(b) as compared to the shunt in figure 6.6(b) and 6.7(b).

The distinct boundary of the dark area in the upper right corner of figure 6.8 eliminates a shunt (which could not be shown in DLIT anyway) as possible explanation since a shunt would cause a gradient in the potential distribution which would then lead to a fading EL intensity. The dark area in the upper right corner of the solar cell in figure 6.8 may either be the result of non-radiative recombination due to a degradation of the pn-junction or be the consequence of a lack of charge carrier injection into the pn-junction. The latter may either be caused by a corrosion (and thus a severely increased resistivity) of the planar contacts (back or front contact) or their respective interfaces with the pn-junction (Mo/CIGSe or CdS/TCO).

## 6.3 Mapping the Local Series Resistance

As introduced in section 3.2.3 voltage-dependent electroluminescence images provide a data base for the calculation of series resistance mappings, i.e. the local series resistance  $R_s^{x,y}$  at a given point  $(x, y)$  on the solar cell. Two calculation methods will be utilized (Hinken et al. in section 6.3.2 and Breitenstein et al. in section 6.3.3) below<sup>3</sup>. For both methods *Matlab* programs were developed in order to automatize the calculation. A comparison of the two methods as well as an assessment of the validity of the measurement can be found in section 7.3.3.

<sup>3</sup>Section 6.3 is based on a conference paper by Daume et al. [120].

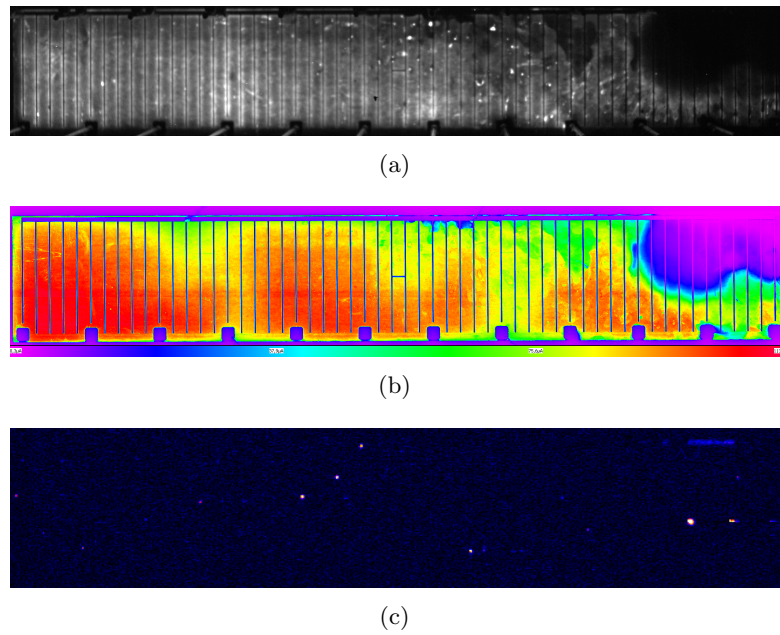


Figure 6.8: Different imaging techniques applied to a solar cell with a corroded area that is visible in the (a) EL and (b) LBIC image of while the (c) DLIT image remains unaffected. Sample from batch 2A-1225 with a sodium content of  $0.71\times$  (as normalized from LIBS) after 50 h of damp heat.



### 6.3.1 Voltage-Dependant Electroluminescence

For the Hinken calculation method 17 EL images with voltage differences of 10 mV in the range of 0.54 V (5.5 mA/cm<sup>2</sup>) to 0.7 V (27.6 mA/cm<sup>2</sup>) were captured in random order. For the iterative Breitenstein calculation method only two images were necessary, the employed EL images at 0.59 V (11.0 mA/cm<sup>2</sup>) and 0.69 V (26.1 mA/cm<sup>2</sup>) are shown in figure 6.9.

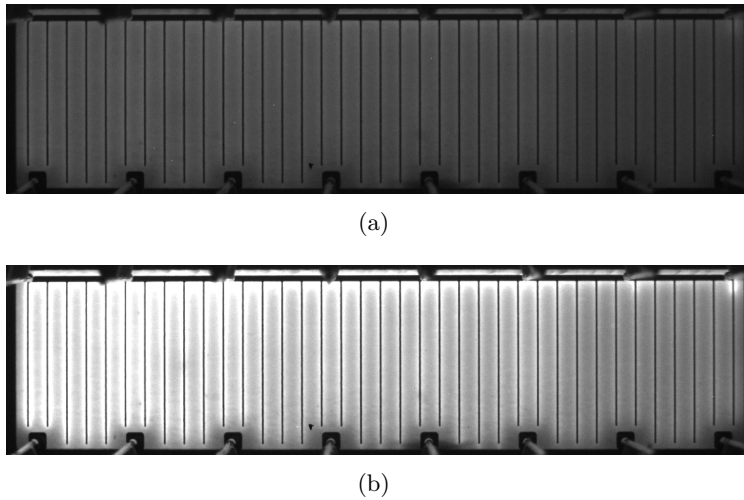


Figure 6.9: Electroluminescence images of the same sample from batch 2A-1209 (find the corresponding IV data in section 5.3.3 and more EL images in section 6.1.2) with a  $1.05\times$  sodium content (as normalized from LIBS) at (a) 0.59 V and at (b) 0.69 V. The thin dark vertical lines are shades of the grid and the dark horizontal line on the top is a shade of the busbar of the solar cell.

For the calculation (via both methods) it is crucial to know the voltage at the pn-junction of the solar cell. Since the solar cells were contacted in a two-point configuration during EL imaging (in order to ensure a homogeneous current injection through all contacting tips) measuring the voltage at the terminals would have led to readings disturbed by the contact resistance between tips and the solar cell as well as the resistance of the wires. Thus, the voltage readings were taken from an independent IV measurement in four-point configuration in the dark and the respective current readings for a given voltage were taken as a setting for the current source during EL imaging. Thus, independently of the voltage at the terminals of the solar cell that was necessary to drive the current setting, the voltage at the pn-junction as well as the injected current were known.

### 6.3.2 Calculation Method by Hinken et al.

The series resistance mapping obtained with the method by Hinken et al. that was introduced in section 3.2.3 is shown in figure 6.10.

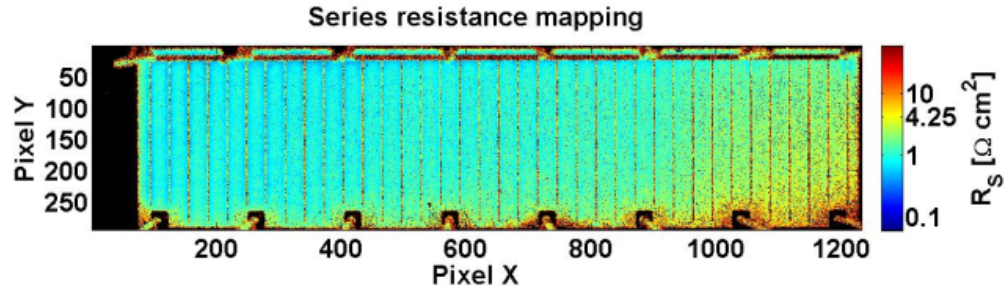


Figure 6.10: Series resistance mapping calculated with Hinken's method.

The series resistance  $R_S$  seems to be fairly homogeneously distributed, with some notable features (besides the dark vertical lines that are shades of the grid). The series resistance is higher in the lower right area of the solar cell which seems plausible in comparison to the EL image that also showed a lower electroluminescence in that area of the solar cell (compare figure 6.9 and figure 6.10). Looking carefully, one can also observe that the series resistance is slightly higher between the grid fingers (which is better visible in figure 7.5 and will be discussed below).

### 6.3.3 Calculation Method by Breitenstein et al.

Figure 6.11 depicts the series resistance mapping obtained with Breitenstein's method that was introduced in section 3.2.3.

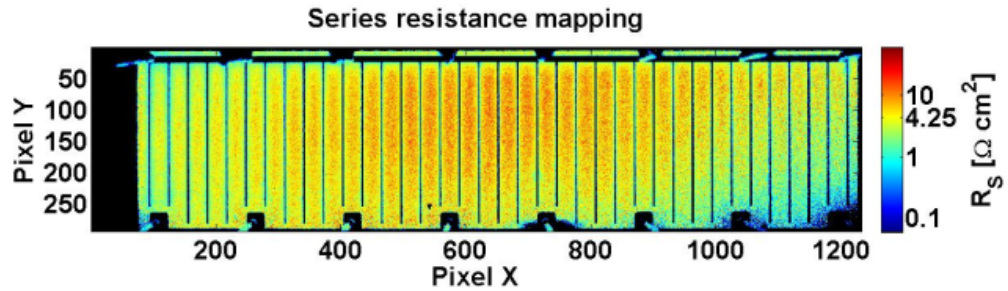


Figure 6.11: Series resistance mapping calculated with Breitenstein's method.

Like in figure 6.10 the series resistance shows maxima between the grid fingers which are slightly more pronounced here. Also, the lower right area of the mapping differs from

the rest of the image. However, applying Breitenstein's calculation method the series resistance drops in this area. This seems to be in contradiction with the original EL image that was darker in that area.

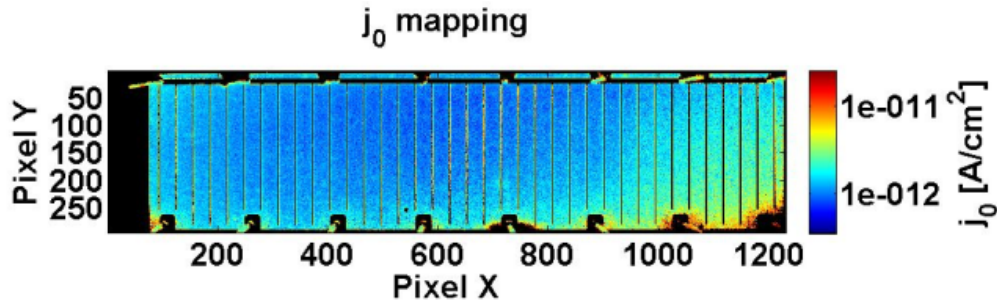


Figure 6.12: Mapping of the saturation current density  $j_0$  calculated with Breitenstein's method.

The saturation current mapping (figure 6.12) provided by this calculation method provides a possible explanation for that apparent contradiction: An increase in the saturation current density can be observed in exactly this area of the solar cell. The lower EL intensity can therefore be explained by a change of the local diode characteristic since a higher  $j_0$  diminishes the luminescence intensity. Breitenstein's method thus allows to locally differ between influences of the pn-junction (CIGSe/CdS) since  $j_0$  is a diode parameter and parasitic ohmic effects of the series resistance resulting from the contacts.

#### 6.3.4 Application of Breitenstein's Method after Damp Heat

In figure 6.13 the EL image of a solar cell is shown that has been exposed to 37 h of damp heat. It is the same sample as in figure 6.2. The application of Breitenstein's calculation method provides a series resistance mapping (figure 6.14) and a mapping of the saturation current density (figure 6.15) of this solar cell. As described above, the average of the series resistance map has been scaled to the series resistance obtained from the IV measurement, i.e.  $6.25 \Omega \text{ cm}^2$ .

According to Breitenstein's calculation method, the dark spots in the EL image (figure 6.13) do not result from an increased series resistance. Instead, a locally increased saturation current density (figure 6.15) causes the EL intensity to drop in these areas. It is therefore likely that besides other damage to the cell (like contact corrosion) the properties of the pn-junction suffered from the damp heat treatment, with an emphasis in the area of the dark spots. However, it should be noted that the average of the saturation current density map does not match the value obtained from the IV measurement.

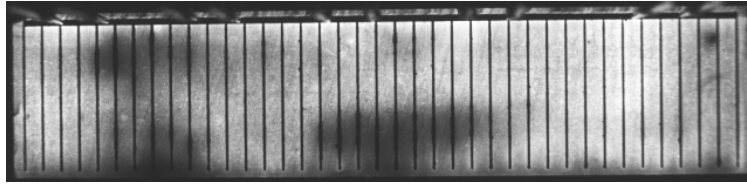


Figure 6.13: Electroluminescence image of a sample from batch 2A-1173 (find the corresponding IV data in section 5.3.1 and more EL images in section 6.1.1) with a  $11.33\times$  sodium content (as normalized from LIBS) of a sample that has been exposed to 37 h of damp heat. The EL image was taken at 0.78 V ( $28.0 \text{ mA/cm}^2$ ).

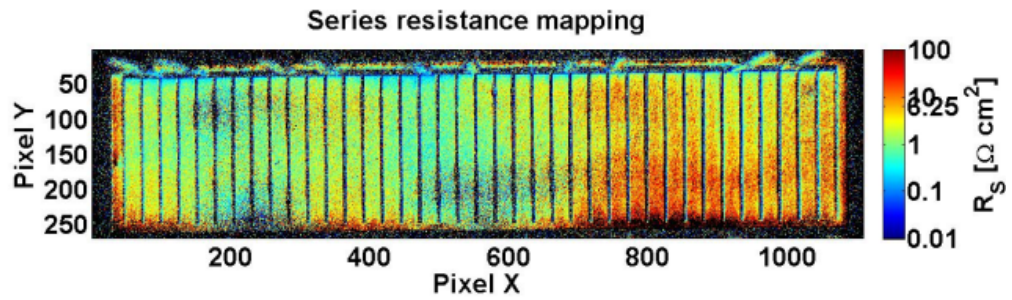


Figure 6.14: Series resistance mapping of a sample that has been exposed to damp heat calculated with Breitensteins's method.

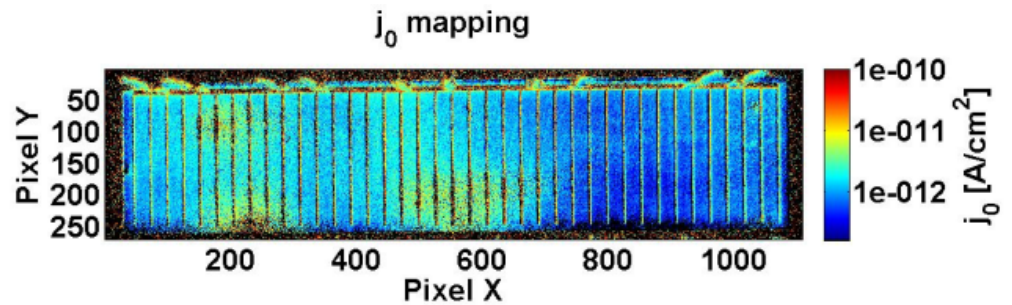


Figure 6.15: Mapping of the saturation current density  $j_0$  of a sample that has been exposed to damp heat calculated with Breitensteins's method.

## 7 Discussion

The previous chapters have shown the influence of damp heat on flexible Cu(In,Ga)Se<sub>2</sub> solar cells (chapter 4), the influence of the sodium content of a CIGSe solar cell on its damp heat stability (chapter 5) and lateral inhomogeneities that appear in the degradation process (chapter 6). In this chapter, all findings will be discussed with respect to the current state of the literature regarding the stability of Cu(In,Ga)Se<sub>2</sub> solar cells under damp heat exposure that was reviewed in chapter 2.

Section 7.1 will discuss the influence of damp heat on the solar cell properties in terms of structure and electrical behavior. While a detailed discussion of the influence of sodium on the properties and the long-term stability of the Cu(In,Ga)Se<sub>2</sub> solar cell is subject in section 7.2, the fact that the initial sodium content of the solar cell does influence its stability under damp heat (cf. section 5.3) is employed in the discussion in section 7.1 already. Section 7.3 discusses lateral inhomogeneities during the degradation process. Finally, in section 7.4 all findings of this thesis are summarized in the form of theses and an outlook is given.

### 7.1 Influence of Damp Heat

#### 7.1.1 Morphology & Roughness

No obvious physical damage was observed after exposure of flexible Cu(In,Ga)Se<sub>2</sub> solar cells to damp heat (cf. section 5.3).

The morphology of the solar cells was evaluated with scanning electron microscopy (cf. section 5.2). No differences were found between untreated solar cells and those exposed to damp heat (up to 85 h). The surface morphology (cf. figure 5.7) as well as the appearance of the cross-sections (cf. figure 5.6) was identical.

SIMS measurements of the elemental depth gradients showed no changes in the profiles of copper, indium, gallium and selenium after damp heat exposure hence indicating that the chalcopyrite crystal is stable under damp heat (cf. section 5.5). Differences were found in the sodium gradient, i.e. a reduction of an initial aggregation at the CIGSe/Mo interface after damp heat (further discussion in section 7.2.2). While the sodium content showed a correlation with the roughness of the solar cell surface initially (cf. figure 5.19; discussion in section 7.2.1), the change in the sodium gradient after damp heat exposure did not change the roughness of the surface.

It can be concluded that damp heat only induced “mild” changes. Exposure to damp heat had no influence on the morphology or surface roughness of the Cu(In,Ga)Se<sub>2</sub> solar cells. Certainly, influences on the electrical properties were revealed which will be discussed in the following sections. This is in agreement with the literature, where most papers report on degradation in the electrical behavior of the solar cells after damp heat exposure cf. section 2.

### 7.1.2 Fill Factor and Series Resistance

In order to screen the degradation<sup>1</sup> behavior of the Cu(In,Ga)Se<sub>2</sub> solar cells studied in this thesis (cf. section 3.1) statistical analysis of the change in IV parameters after 75 h exposure to damp heat (compared to the initial IV parameters) was carried out (section 4.2.1). While the overall efficiency of the solar cells degraded by 26 % on average, only a small degradation was observed in the open circuit voltage (9 % degradation) and in the short circuit current (3 % degradation; cf. figure 4.2). The IV parameter that was most influenced by the degradation was the fill factor (18 % degradation). This was clearly visible in the IV parameters of the damp heat treated solar cells, as shown in figure 4.3(a). While both, parallel (if too low) and series (if too high), resistances have a detrimental influence on the fill factor and thus the efficiency of the solar cell (cf. figure 1.6), the degradation in the fill factor could be correlated with an increase in series resistance after damp heat exposure (figure 4.3(b)).

A decreasing fill factor of the solar cell after exposure to damp heat was reported in the literature before (cf. section 2.4.3). It was commonly accompanied by a decrease in the open circuit voltages of the solar cells. Such a decrease in the open circuit voltage is an indication for a degradation of the pn-junction (cf. section 2.8). However, for the samples in this thesis the degradation of the fill factor was twice as big as the degradation in open circuit voltage after 75 h exposure to damp heat (cf. figure 4.2). It could be shown that an increasing series resistance was the driver for the increase in fill factor. Thus a severe degradation of the pn-junction seems unlikely or is outranked by a different degradation mechanism which affects the series resistance.

The observed increase in series resistance naturally draws attention to the planar contacts, i.e. the back and the front contact, of the solar cell. As mentioned in section 4.4, the latter contributes three quarters to the overall series resistance while the molybdenum back contact layer contributes about one quarter of the total series resistance. The degradation behavior of both planar contacts will be discussed below.

### 7.1.3 The Role of Humidity during Damp Heat

In order to better understand the role of humidity in the standardized damp heat test on the stability of CIGSe solar cells, a comparison to dry heat was conducted (cf. sec-

---

<sup>1</sup>For the definition of the term “degradation” see equation 4.1.

tion 4.1). It was found that, while exposed for the same time, the samples degraded under damp heat and remained stable in their IV parameters under dry heat (cf. figure 4.1). It can be concluded that humidity has a leading role in the degradation of CIGSe solar cells.

This result agrees with previous findings by Malmström et al. [92] who reported that Cu(In,Ga)Se<sub>2</sub> solar cells treated up to 800 h of damp heat degraded by approximately 25% while they were stable under dry heat when exposed for that period. From similar results Wennerberg concluded in his PhD thesis that “humidity is a primary catalyst to the mechanisms involved in the degradation process” [133].

One of the main implications of the role of humidity in the degradation process of Cu(In,Ga)Se<sub>2</sub> solar cells is the strategy of encapsulation in order to protect the solar cells from humidity and thereby increasing their life time.

#### 7.1.4 Appearance of a Roll-over in the IV Characteristic

A roll-over was observed in the IV characteristic at low temperatures after damp heat treatment (section 4.2.2). In order to fit the respective IV curves the equivalent circuit model was extended by a second (blocking) “roll-over diode”, in parallel with a “roll-over resistance”  $R_{RO}$  (cf. figure 4.6). This roll-over resistance increases with extended exposure to damp heat thus increasing the influence on the roll-over diode in the IV characteristic.

The roll-over is a current blocking behavior in forward direction. According to the book of Scheer and Schock [12] the origin of the additional blocking diode resulting in a saturation of the current in forward direction can be explained in different ways:

- Back contact barrier: The forward current of the main diode is limited by the saturation current of the back contact diode (“blocking diode”). This roll-over shows up in light and dark IV curves. The back contact exhibits a non-ohmic electrical behavior. This can be caused by [134]:
  - increased defect concentration at the back contact (since the absorber growth starts here)
  - band bending due to the MoSe<sub>2</sub> layer between molybdenum back contact and Cu(In,Ga)Se<sub>2</sub> absorber
- Acceptor states at the buffer/window interface: blocking of the diode current due to an electron barrier at the interface (which is fixed due to Fermi level pinning). Only the photo current can pass the barrier. This roll-over shows up in the IV curve under illumination.
- Positive conduction band offset at the buffer/window interface.

Since the roll-over was observed during IV measurements in the dark, acceptor states at the buffer/window interface can be ruled out as a potential explanation. No measurements of the band structure were available in order to check for the third potential explanation. Without an immediate proof we will assume a back contact barrier as explanation for the observed roll-over effect. This is different to the interpretation of an observed roll-over by Malmstroem et al. (cf. section 2.8). Yet, in the further discussion evidence will be presented that confirm this assumption.

In the literature it was reported that the MoSe<sub>2</sub> layer, which is formed by selenization of the plain molybdenum back contact at the beginning of the Cu(In,Ga)Se<sub>2</sub> deposition, is beneficial for the formation of an ohmic back contact [135]. Assuming the presence of a MoSe<sub>2</sub> layer within our samples (which could be shown via transmission electron microscopy for similar samples), the following explanation for the observed occurrence of a roll-over after damp heat exposure of the solar cell is suggested.

Initially the MoSe<sub>2</sub> enables an ohmic back contact. The MoSe<sub>2</sub> layer is damaged during damp heat exposure, i.e. by chemical reactions at the interface between molybdenum back contact and CIGSe absorber layer<sup>2</sup>. The chemical reactions could, for instance, reduce the MoSe<sub>2</sub> layer thickness (locally or throughout the whole back contact). Ultimately, regardless of the exact chemical process, the ohmic nature of the not damp heat treated back contact interface is altered to a more diode-like electrical characteristic. Following this argument, the roll-over diode in the equivalent circuit model (cf. figure 4.5) is formed by the non-ohmic back contact interface and the roll-over effect appears in the IV characteristic of the solar cell after damp heat treatment.

### 7.1.5 New Interpretation of the CV measurements

The derivation of net doping profiles from CV measurements typically contributes to the understanding of doping within the CIGSe absorber. In section 4.2.3 the influence of the sodium content on the net doping, as derived from CV measurements was investigated. It was shown that the net doping of the absorber increases with increasing sodium content (cf. figure 4.7). Described by many authors, this is commonly attributed to a decrease of the degree of compensation in the CIGSe absorber (for instance, since sodium suppresses donor type In<sub>Cu</sub> antisites [17]).

Capacitance-voltage measurements were carried out after damp heat aging as well and the net doping of the absorber was derived from the CV data (figure 4.8(b)). In accordance with figure 4.7, the samples with 11.33× sodium content exhibited a higher net doping than the samples with 0.52× sodium content since more sodium was supplied during CIGSe deposition. For the samples with the lower sodium content, the net doping remained unaffected under dry heat treatment, while there was a slight decrease for the samples with the higher sodium content. Exposure to damp heat significantly decreased

---

<sup>2</sup>Further details on the degradation at the Mo/CIGSe interface can be found in the discussion below (“New Interpretation of the CV measurements”) and in section 7.2.4.



the apparent net doping for both sets of samples. This effect was much more pronounced for the samples with higher sodium content (11.33×).

First, an attempt is made to explain the trend in the capacitance data in terms of doping, but motivated by the contradiction of this interpretation with the IV data, a new explanation will be proposed<sup>3</sup>.

The more pronounced decrease of the net doping with higher sodium content (figure 4.8(b)) fits well with the more pronounced degradation of the whole cell in terms of fill factor and efficiency (cf. figure 5.8). As a simple model, one could imagine that sodium is “washed out” of the cell by the water under damp heat conditions. Thus, degradation is solely visible (and sodium-dependent) in the presence of water, whereas in dry heat, the samples remain unaffected. One may then speculate that the decrease in net doping for samples with higher sodium content (11.33×) under dry heat treatment (figure 4.8(b)) is explained by the influence of ambient air humidity during measurement, due to the hygroscopic nature of compounds, like sodium selenide. When the sodium content decreases, the degree of compensation in the material increases again, thereby having a detrimental effect on the net doping (figure 4.7). The CV measurements showed that along with the decrease of net doping, the width of the space charge region increased. If one assumes a fixed charge carrier diffusion length, the short circuit current density should increase along with the width of the space charge region under damp heat treatment, due to a better carrier collection in the absorber.

Nevertheless,  $J_{SC}$  remains nearly constant. Dropping the assumption of a fixed diffusion length (which is rather unlikely, since the carrier lifetime in CIGSe decreases already under atmospheric conditions [30]), the increase in the space charge region width had to compensate for the decrease in diffusion length completely in order to leave  $J_{SC}$  unaffected. This rather unlikely relationship motivates to look for an alternative explanation of all collected data. Moreover, the apparent decrease in net doping for the damp heat treated solar cells contradicts their stable open circuit voltages.

The standard interpretation of the capacitance data is based on strong simplifications of the device: with the impedance analyzer, the complex resistance of the sample is measured. Under the assumption of a parallel equivalent circuit of a capacitor (formed by the space charge region of the pn-junction) and a parallel resistance, a capacitance value is obtained. According to the again simplified interpretation as a plain plate-type capacitor, the capacitance  $C$ , depends on the distance of the plates (i.e., the width of the space charge region  $w$ ) and the area  $A$  of the capacitor (i.e., the area of the pn-junction):

$$C = \epsilon\epsilon_0 A/w \quad (7.1)$$

(where  $\epsilon$  is the dielectric constant of the CIGSe absorber and  $\epsilon_0$  the vacuum permittivity). Since not only the junction, but also the front and back contacts of the solar

---

<sup>3</sup>The argument on this interpretation of capacitance-voltage measurements of flexible Cu(In,Ga)Se<sub>2</sub> solar cells after damp heat exposure was published in a research paper [93] (cf. appendix B).

cell extend over this area, it is likely that the non-idealities of these contacts have an influence on the measurement.

Therefore, a new explanation of all measured data based on the corrosion of the planar contacts is proposed.

Sodium in the CIGSe solar cell in conjunction with water leads to the corrosion of both planar contacts: the ZnO:Al window layer and the molybdenum back contact. However, it seems more likely that the latter process and, especially, the degradation of the Mo/CIGSe interface is responsible for the sodium-related degradation of the solar cells, since it is known from elemental depth profiling (SIMS, cf. section 5.5) that sodium tends to aggregate at the back contact interface [136, 137]. With SIMS measurements on a similar set of samples, a decrease of the sodium aggregation at the Mo/CIGSe interface after damp heat treatment was found [137]. Since water is necessary for the described corrosion mechanism, it was observed in the samples treated with damp heat, but not in the samples treated with dry heat. As the polyimide substrate is permeable to water [138], the ingress from the back side of the cell is another possible path for water to enter the cell besides the top (window layer) surface. The columnar structure of the molybdenum layer (resulting from the columnar growth during the sputter process) might even provide capillary-like channels for water to propagate.

Literature suggests that only well defined Mo/CIGSe interfaces with an intermediate MoSe<sub>2</sub> layer [139] result in good ohmic contacts [135]. A partially corroded back contact (interface) will then presumably exhibit a significantly increased (contact) resistance. The partial corrosion of the back contact interface then results in a lower effective interface area  $A$  between molybdenum and Cu(In,Ga)Se<sub>2</sub>. Looking from this perspective, **the changes in the net doping in figure 4.8(b) are an artifact from the reduced area  $A$  of the model capacitor.** Figure 4.8(a) shows the change in capacitance of the two sets of samples under damp heat treatment. The samples show a decrease of the capacitance with damp heat time, consistent with our explanation. However, for the samples with lower sodium content ( $0.52\times$ ), the capacitance shows an initial increase consistent with the observation of an initially increasing efficiency. This effect could be related to water ingress into the CIGSe absorber, possibly having a positive influence on the efficiency, similar to the one of water vapor during CIGSe growth [140]. Therefore, damp heat exposure could lead to a superposition of the enhancing effect on the absorber and the detrimental effect on the back contact, resulting in the efficiency (figure 5.8(d)) and capacitance maxima (figure 4.8(a)) for the samples with  $0.52\times$  sodium content. For the samples with  $11.33\times$  sodium content, the back contact corrosion seems to be dominant; hence, no initial increase in efficiency or capacitance can be observed.

The idea of a dominating back contact corrosion also explains the EL data better than the reduced net doping, which should affect the absorber and, therefore, the EL signal uniformly over the whole area  $A$ . Certainly that would be in contradiction to the observation of localized darker areas arising in the EL images under damp heat treatment (cf. section 6.1.1, e.g. figure 6.2). On the other hand, since the occurrence of corrosion

will most likely be dominated by inhomogeneities of the water ingress resulting from, e.g., percolation behavior at grain boundaries or pinholes in the layer stack and inhomogeneities in the initial sodium distribution, the more pronounced corrosion in certain areas is consistent with our explanation. Quantitative support for our explanation is provided by the comparison of the effects of damp heat on the capacitance and the EL signal. An image analysis (measuring the two disjoint areas after defining a brightness threshold in figure 6.2(f)) yields that approximately 20 % of the cell area belongs to dark spots. This estimation is rough, since it is difficult to define an appropriate threshold. However, the fraction of dark spots is well within the same order of magnitude as the change in capacitance of approximately 40 % for the set of samples with  $11.33\times$  sodium content.

Considering this argumentation, the effect of the back contact corrosion seems to be the main degradation mechanism in the long run for our samples, however, the presented explanation does not rule out other degradation mechanisms related to the absorber itself or one of the various other layers and interfaces. Other aging mechanisms might even be present in our experiment (as hinted at by the intermediate increase in efficiency for the samples with the lower sodium content), but they are superimposed by the described corrosion effect.

### 7.1.6 The role of the planar contacts

As stated in section 4.4 and 7.1.2, the measured increase of the series resistance of the CIGSe solar cells due to damp heat exposure is the main driver for the degradation of the IV characteristic. Since the planar contacts predominantly contribute to the series resistance of the solar cell their degradation behavior was investigated in separate experiments (cf. section 4.4).

#### “Ex-situ” Measurement (on Model Substrates)

Hall measurements of plain molybdenum back contacts (on polyimide substrates) and plain aluminum doped zinc oxide layers (on model substrates) were carried out in order to study the damp heat stability of the individual layers. Measurements of the specific resistivity were compared before and after damp heat exposure.

No significant degradation of the plain back contact layer was found after 50 h of damp heat. The specific resistance of the molybdenum layer increased by less than 5 % compared to untreated layers (cf. figure 4.17). After the same exposure to damp heat the specific resistance of plain aluminum doped zinc oxide layers had increased by 27 % (cf. figure 4.20).

### “In-situ” Measurement (within Solar Cells)

For measuring the degradation of the molybdenum back contact and the aluminum doped zinc oxide front contact within the actual solar cell, transfer length measurements were carried out on both layers on complete solar cells. The procedure was described in section 3.2.8.

In two separate experiments, for damp heat exposures up to 384 h (16 days), no significant increase of the molybdenum sheet resistance could be determined.

The TLM measurements of the aluminum doped zinc oxide front contact did not yield significant results for damp heat exposures up to 50 h. In another experiment with an extended damp heat exposure (up to 384 h), it was found that sheet resistivity as well as the contact resistance between TCO and grid increased significantly. The TCO sheet resistance had increased 6-fold while the contact resistance to the grid had increased 62-fold.

### Conclusion

A degradation of the bulk of the molybdenum back contact could be excluded. Resistivity measurements of bare molybdenum layers as well as of the back contact of CIGSe solar cells show no significant degradation. A degradation of the interface between the back contact and the absorber of the solar cell, however, cannot be ruled out as a potential origin of the observed increases in  $R_S$  after damp heat since the measurements carried out were not sensitive to that contact resistance.

Resistivity measurements of bare aluminum doped zinc oxide layers as well as of the front contact of CIGSe solar cells show a significant degradation. While the sheet resistance of the aluminum doped zinc oxide front contact increased by almost one order of magnitude, the contact resistance between aluminum doped zinc oxide and grid increased by almost two orders of magnitude after extended damp heat exposure of the bare solar cells.

Since the front contact contributes the biggest share to the overall series resistance of the solar cell (cf. section 4.4) it can be concluded that the observed degradation of the front contact (ZnO:Al and contact resistance with the grid) contributes significantly to the increase in  $R_S$  that was observed in IV measurements.

Moreover, it can be concluded that the degradation of the solar cell is a superposition of different degradation paths. Besides the likely degradation of the CIGSe/Mo interface (cf. section 7.1.4 and 7.1.5) the degradation of the front contact could be identified as another degradation path of the CIGSe solar cell.

#### 7.1.7 Kinetics

A hybrid degradation setup (cf. section 3.3.3) was employed to measure IV characteristics of flexible CIGSe solar cells during damp heat degradation. As shown in section 4.3,

the following insights were obtained from these in-situ measurements (cf. figure 4.10 and 4.11):

- The  $FF$  and  $V_{OC}$  may increase after short damp heat exposure.
- Two stages of aging can be distinguished under damp heat; an initial improvement followed by a continuous degradation.
- Linear degradation rates for unencapsulated flexible CIGSe solar cells were determined for the first time.

The first finding is remarkable and not intuitive. Actually, degradation is the general expectation upon applying a procedure of accelerated aging, such as damp heat. Hypotheses about the origin of the initial increases in  $FF$  and  $V_{OC}$  during stage 1 of the aging process of the solar cell will be discussed below.

Stage 1, the initial improvement, refers to a period of about 50 h after the onset of damp heat (in this experiment). Stage 2, the continuous degradation starts about 100 h after the onset of damp heat (in this experiment). The occurrence of stage 1 depended on the sodium content of the samples (cf. section 4.3.3). Stage 1 was more pronounced for low sodium contents. At higher sodium contents,  $FF$  and  $V_{OC}$  remained rather constant instead of an increase during stage 1. The discussion of further experiments on the role of sodium during the degradation process can be found in section 7.2. All aspects regarding the continuous degradation of the solar cell in stage 2 are subject to the discussion in this chapter.

The third finding, degradation rates for stage 2, is novel. No reports on degradation rates of flexible CIGSe solar cells (unencapsulated) have been found in the literature. The high relevance of the degradation rates for the estimation of lifetimes will be discussed in section 7.1.8.

In contrast to the differences in the degradation behavior between CIGSe solar cells with different sodium content (cf. section 7.2), the degradation rates of the power output (cf. figure 4.14(d)) are not significantly different between the cells with different sodium contents in the in-situ measurements. It appears that the main difference between the cells with different sodium contents in the in-situ experiment is the characteristic of stage 1, i.e. how (when) the degradation starts (rather than its progression). The measurement of the efficiency versus damp heat exposure in the cyclic damp heat approach in section 5.3.1 indicated similar degradation rates in stage 2 already (cf. figure 5.8(d)), however, the in-situ IV measurements under damp heat were able to verify that indication numerically.

### **Initial Improvement**

A couple of hypotheses to explain the initial increase in open circuit voltage and fill factor will be discussed here.

One might argue that the increase of  $V_{OC}$  and fill factor is caused by **light-soaking** [17] since the in-situ IV measurements go along with an illumination of  $1000 \text{ W/m}^2$ . In contrast, an initial increase in fill factor and thus in efficiency was observed for samples that were damp heat treated in the dark as well (cf. section 5.3.1).

Since the current collecting grid on top of the TCO is silk-screen printed (cf. section 3.1), another explanation is tempting. Due to the elevated temperature during damp heat, the conductive paste undergoes a further curing thus increases the **conductivity of the grid**. The latter reduces the series resistance of the solar cell and thus the fill factor increases. It is, however, not explicable why humidity should be relevant for that curing. In contrast, solar cells that were only treated with (dry) heat did not show an initial increase in fill factor and efficiency (cf. section 4.1).

An alternative explanation can be deduced from the observations by Ishizuka et al. [140]. They reported increases in  $V_{OC}$ ,  $J_{SC}$  and efficiency of CIGSe solar cells that were grown under the **introduction of water vapor during absorber deposition**. The improvements were thought to be related to annihilation of donor defects arising from selenium vacancies by incorporation of oxygen from the water vapor [140]. One might therefore argue that the presence of humidity has a beneficial influence on the CIGSe absorber. Thus, the solar cell benefits as well, until detrimental influences on other layers of the solar cell (e.g. the planar contacts or various interfaces) become dominant. The latter would mark the transition between stage 1 and stage 2 in the aging process. However, it is dubious whether water can be beneficial for the absorber within the complete solar cell, i.e. after the growth is completed. Insights into the chemistry of the effect observed by Ishizuka et al. were necessary to evaluate that hypothesis.

Since these three hypotheses have flaws they can be ruled out as exclusive explanations for the initial improvement. Thus a new explanation based on the **migration of copper ions** is suggested. During the in-situ degradation experiment, the samples were constantly illuminated and between the IV measurements, i.e. most of the time, under open circuit condition (no external load was attached to the solar cell). Under these conditions, the internal electric field<sup>4</sup> could lead to a drift of copper ions from the CdS/CIGSe interface towards the bulk of the absorber (cf. figure 7.1). Thus, the ODC region at the interface depletes further from copper. The band gap thus increases locally (at the interface) and thereby also the open circuit voltage of the solar cell. This increase in  $V_{OC}$  characterizes stage 1 as long as the superposition with degrading mechanisms does not dominate the aging process.

The observation of an initial improvement of CIGSe solar cells was reported once in the literature. While it was not addressed in the discussion, the data published by Britt et al. show an initial increase in  $V_{OC}$ ,  $FF$  and power output of CIGSe solar cells on steel substrates within a flexible packaging (module) under damp heat [103]. While the initial increase in the maximum power output was as high as 9% (after 200 h) no explanation

---

<sup>4</sup>The internal electric field is present in the dark as well.

was suggested. After 1000 h the same samples had degraded by 20 % compared to their initial power output. Although these solar cells had a different substrate compared to our samples and were encapsulated within modules, the observation of an initial increase in performance might be a universal feature of (flexible) CIGSe solar cells and demands further investigation.

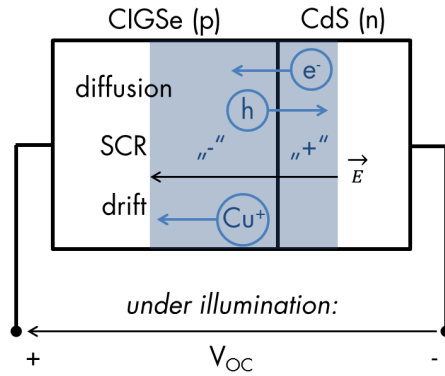


Figure 7.1: Hypothesis about the increase of  $V_{OC}$  during stage 1 of the aging process of the solar cell (cf. section 4.3.3). Under illumination and open circuit conditions, the internal electric field (within the space charge region, SCR) could lead to a drift of  $\text{Cu}^+$  ions from the CdS/CIGSe interface towards the bulk of the absorber. Thus, the ODC region at the interface depletes further from copper. Hence the band gap increases locally (at the interface) and thereby the open circuit voltage of the solar cell as well.

### 7.1.8 Lifetime Assessment

Assuming a linear degradation rate  $R_D$  over the entire lifetime of a solar cell or module, the lifetime  $t_L$  can be calculated according to equation 7.2 for a given lifetime limit  $L_D$  [72]. The end of lifetime is reached (“lifetime limit”) if the power output drops below a certain percentage  $L_D$  of the initial power output.

$$t_L = \frac{100\% - L_D}{R_D} \quad (7.2)$$

In figure 7.2 relations between lifetime and typical degradation rates for photovoltaic modules are shown. This relation is of high relevance since manufacturers typically guarantee certain power outputs of their photovoltaic modules after 10 or 25 years (cf. section 2). According to a literature review of 2000 degradation rates (for all PV technologies) by Jordan and Kurtz [70], the average module degradation rate was 0.8 %/year and

the median 0.5 %/year. Both rates allow to meet commercial warranties (such as 80 % of the initial power output after 25 years).

Based on the degradation rates (cf. table 4.1) that were determined from in-situ IV measurements under damp heat (cf. section 4.3.4), the lifetime  $t_L$  of the solar cell can be calculated as a function of the lifetime limit  $L_D$  according to equation 7.2. As an example, the average of the degradation rates for all three sodium contents in table 4.1 was taken ( $8.2 \mu\text{W}/(\text{cm}^2 \text{h})$ ). Assuming a  $58 \text{ cm}^2$  solar cell with an initial power of 600 mW (approximately 10 % efficiency), the relative degradation rate is 1.9 %/day. Figure 7.3 shows the relation between lifetime limit and lifetime at this given degradation rate. Note the lower lifetimes in figure 7.3 in comparison to figure 7.2. The degradation rate employed for the calculation applies for unencapsulated CIGSe solar cells (cf. section 4.3.4) rather than modules that provide protection against environmental influences.

Knowing the degradation rate of the solar cells within a photovoltaic module it becomes feasible to estimate the lifetime of the module. However, besides data on the climate that the module is exposed to, the permeability of the module package needs to be known. For flexible CIGSe modules Coyle et al. found that (for diffusion-controlled processes, such as moisture ingress) the lifetime scales with the square root of the ratio of characteristic package diffusion time divided by the cell degradation rate [141]. Since the estimation of module lifetimes is beyond the scope of this thesis, solely the following outlook shall be given. The above calculated degradation rate for unencapsulated flexible CIGSe solar cell of 1.9 %/day translates into 691 %/year. Assuming that a power output of the module of 80 % of its initial power shall be guaranteed after 25 years, a module degradation rate of 0.8 %/year must not be exceeded. In order to achieve the necessary protection of the solar cell, the module package thus has to slow down the degradation process 864-fold, i.e. by almost three orders of magnitude, compared to the unprotected solar cells.

## 7.2 Influence of Sodium

Within the framework of this thesis multiple sets of solar cells with varying sodium content were investigated (cf. chapter 5). The sodium was incorporated into the solar cell via co-evaporation of NaF during  $\text{Cu}(\text{In,Ga})\text{Se}_2$  absorber deposition or via post-deposition on a sodium free absorber. In the case of co-evaporation, the sodium content was controlled by tuning the NaF evaporator temperature whereas in the case of post-deposition the absorber (the with Mo and CIGSe coated polyimide web, respectively) was pulled across a NaF evaporator with fixed evaporation temperature at different speeds. By measuring the overall sodium content in the solar cells via LIBS it could be shown for both incorporation methods that more sodium is incorporated into the sample the more sodium is offered (cf. section 5.1).



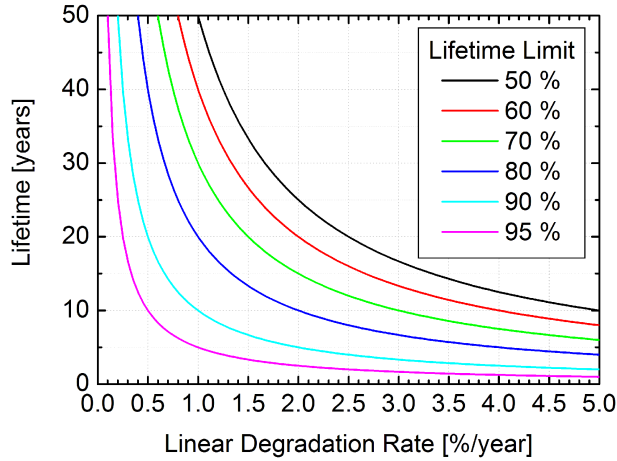


Figure 7.2: Lifetime  $t_L$  of a solar cell or module vs. degradation rate as calculated from equation 7.2. A linear degradation rate  $R_D$  is assumed for the whole lifetime. The values chosen are representative for photovoltaic modules (i.e. with protection against environmental influences).

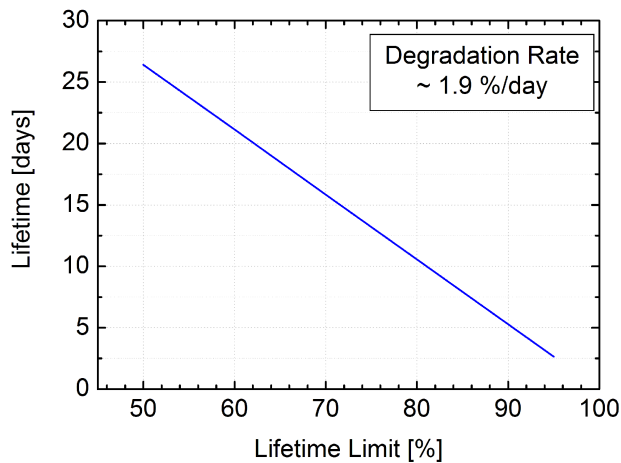


Figure 7.3: Lifetime  $t_L$  of a solar cell vs. lifetime limit as calculated from equation 7.2. A linear degradation rate  $R_D$  is assumed for the whole lifetime. The end of lifetime is reached (“lifetime limit”) if the power output drops below a certain percentage  $L_D$  of the initial power output.

### 7.2.1 Surface Roughness

The influence of sodium on the structure of the  $\text{Cu}(\text{In,Ga})\text{Se}_2$  absorber was investigated by SEM, SIMS and scanning laser microscopy (cf. sections 5.2, 5.5 and 5.6, respectively).

The surface roughness of the samples with varying sodium content was determined via scanning laser microscopy and confirmed by image analysis from SEM (cf. section 5.6). If sodium was introduced via post-deposition treatment, the surface roughness of the solar cell was not influenced by the sodium content. However, if sodium was introduced via co-evaporation of NaF during CIGSe deposition, the surface roughness of the solar cell was affected. From that comparison it is evident that the presence of sodium during  $\text{Cu}(\text{In,Ga})\text{Se}_2$  growth affects the surface roughness of the solar cell. It can be assumed that the surface roughness of the solar cell is altered due to an influence of the sodium during CIGSe growth on the surface roughness of the absorber (which then influences the roughness of the layers deposited subsequently). SEM images of the surface of the absorber, solely covered by the thin CdS layer, confirm that assumption.

In the case of NaF co-evaporation it was found that the surface becomes smoother the more sodium is present during absorber growth (cf. figure 5.19).

An exception from this observation was the sample with the highest sodium content from batch 2A-1209 ( $1.31 \times \text{Na}$ ) which had a significantly higher roughness compared to the four other samples with lower sodium content (cf. table 5.6). Looking at the IV data for these cells (cf. table 5.4), the samples with the highest sodium content stand out as well. While the optimum efficiency was reached for samples with  $1.00 \times$  sodium content, the efficiency drops for higher sodium contents. This leads to the hypothesis that surface smoothness correlates with the efficiency of the solar cell.

A potential explanation for this correlation can be found in the PhD thesis by Greiner who investigated the degradation behavior of ZnO:Al layers under damp heat [94]. The term “extended grain boundary”<sup>5</sup> is introduced to describe localized layers of small grains within the TCO layer that have non-perpendicular crystallographic axes and a higher percentage area of grain boundaries as compared to the rest of the TCO layer (which consists of compact grains with grain boundaries in parallel). By comparing ZnO:Al layers on smooth and rough substrates<sup>6</sup>, it was found that the formation of extended grain boundaries is triggered by the substrate roughness and causes a reduction of the DC conductivity of about two orders of magnitude.

Assuming the existence of extended grain boundaries in the TCO of our samples,

---

<sup>5</sup>Greiner uses the term “Makrokorngrenze” and describes it as follows: “Ausgehend von Röntgendiffraktometrie sowie Raster- und Transmissionselektronenmikroskopie wurde ein Strukturmodell für die inhomogene ZnO:Al-Schicht abgeleitet, nach dem die Schicht aus kompakt gewachsenen Körnern mit parallel angeordneten Korngrenzen sowie aus lokalisierten, durch Substratrauheiten induzierten Makrokorngrenzen mit kleineren Körnern, nicht senkrecht ausgerichteten kristallografischen Ebenen und einem größeren Flächenanteil an Korngrenzen besteht.” [94].

<sup>6</sup>The “smooth substrate” was silicon (mean roughness  $R_a < 1 \text{ nm}$ ) and the “rough surface” textured silicon ( $R_a = 525 \text{ nm}$ ).

the above described correlation between solar cell efficiency and surface smoothness can be interpreted as follows. With increasing sodium content in the absorber the surface roughness of the Cu(In,Ga)Se<sub>2</sub> layer decreases (cf. figure 5.19). Hence, less extended grain boundaries are formed upon ZnO:Al deposition, thus, leading to a front contact with increased conductivity. The overall efficiency of the solar cell increases<sup>7</sup>. However, if the surface roughness is very high (as it was the case for the samples with 1.31× sodium content in figure 5.19), more extended grain boundaries are formed and the thusly reduced TCO conductivity limits the efficiency of the solar cell (cf. figure 5.12).

The beneficial influence of the sodium on the TCO conductivity (and thus via series resistance and fill factor on the efficiency of the solar cell) via absorber roughness is independent of beneficial influences of sodium on the absorber that have been described in section 1.3.3. Most certainly both effects are in superposition.

## 7.2.2 Sodium Depth Distribution

SIMS measurements showed that the elemental gradients of the chalcopyrite constituents within the CIGSe absorber are stable under damp heat treatment (cf. section 5.5)<sup>8</sup>. This strongly indicates that the chalcopyrite Cu(In,Ga)Se<sub>2</sub> crystal itself is stable under damp heat and is in accordance with the literature (cf. section 2.4).

Initially (untreated samples), sodium exhibited a distinct gradient from the front towards the back of the cell with two aggregations at the interfaces between CdS/CIGSe and CIGSe/Mo, respectively (cf. figure 5.16). Since fluorine was similarly aggregated at the back contact interface (CIGSe/Mo), the presence of NaF as a compound may be suspected.

As shown in section 5.5, after damp heat treatment, the sodium aggregation at the back contact interface decreased significantly. For the sodium contents 1.00× and 1.05× it almost vanished. It seems that while involved in a corrosion process (cf. section 7.1.5 and 7.1.4), the sodium has been transported towards the back contact and substrate. This may have happened by diffusion as an ion or as a compound in solution (e.g. NaF). A slight increase of the sodium as well as the fluorine signal at the CdS/CIGSe interface after damp heat may indicate the presence of NaF, possibly as a consequence of the aforementioned transport process during damp heat.

While similarly distributed before and after damp heat throughout the absorber, the oxygen concentration differed slightly at the CIGSe/Mo interface and within the back contact. This might indicate a (partial) oxidation of the molybdenum.

---

<sup>7</sup>An increase in sodium content has multiple influences on the CIGSe solar cell and its absorber, e.g. on its doping and the presence of defects [142, 13]. Generally, the efficiency increases with increasing sodium content.

<sup>8</sup>Section 7.2.2 is based on a conference paper by Daume et al. [137].

### 7.2.3 Electrical Degradation

#### Sodium Co-Evaporation

The degradation behavior of the  $\text{Cu(In,Ga)Se}_2$  solar cells with respect to sodium content was studied for both methods of sodium introduction, i.e. co-evaporation (cf. section 5.3) and post-deposition (cf. section 5.4). First, the case of sodium co-evaporation will be discussed.

In a first experiment (batch 2A-1173; cf. section 5.3.1), samples with the lower sodium content ( $0.52\times \text{Na}$ ) had degraded by 13 % of their initial efficiency while samples with the high sodium content ( $11.33\times \text{Na}$ ) had degraded by 63 % after approximately 50 h of damp heat (cf. table 5.2). In a second experiment (batch 2A-1225; cf. section 5.3.2), the samples had degraded by 4 %, 7 % and 33 % of their initial efficiencies after 50 h of damp heat exposure for sodium contents of  $0.43\times$ ,  $0.71\times$  and  $1.14\times$ , respectively (cf. table 5.3). In a third experiment (batch 2A-1173; cf. section 5.3.1), after 85 h of damp heat, the samples had degraded by 55 % for the lowest sodium content in this experiment ( $0.61\times \text{Na}$ ) and up to 90 % for the samples with the highest sodium content ( $1.31\times \text{Na}$ ; cf. table 5.4).

It can thus be concluded that the degradation under damp heat proceeds faster for  $\text{Cu(In,Ga)Se}_2$  solar cells with higher sodium contents from NaF co-evaporation. In all three experiments the degradation was driven mainly by the fill factor, which decreased due to increases in the series resistance of the cells, and some decrease in  $V_{OC}$  (cf. section 4.2.1).

#### Sodium Post-Deposition

In the case of sodium post-deposition, the same tendency between sodium content and degradation was observed (cf. section 5.4). However, the degradation of the unencapsulated  $\text{Cu(In,Ga)Se}_2$  solar cells was significantly lower. After 50 h of damp heat exposure the samples with the lowest sodium content within the experiment ( $0.14\times \text{Na}$ ) had actually increased by 7 % in efficiency, while the samples with the highest sodium content ( $0.84\times \text{Na}$ ) had degraded by 6 % in efficiency (cf. table 5.5). Even after 200 h of exposure to damp heat the samples with sodium contents between  $0.14\times$  and  $0.26\times$  had increased in efficiency while the samples with the highest sodium content had degraded by moderate 36 % of their initial efficiency.

It can be concluded that solar cells with higher sodium contents from NaF post-deposition degrade faster under damp heat exposure. However, their damp heat stability was higher in comparison to cells where sodium was introduced via co-evaporation.

### Optimization of the sodium content

The initial efficiency of the solar cells tends to increase with increasing sodium content, as it was shown concordantly for cells with sodium co-evaporation (cf. section 5.3) and for cells with sodium post-deposition (cf. section 5.4). The beneficial nature of sodium for the initial efficiency of Cu(In,Ga)Se<sub>2</sub> solar cells is in agreement with the literature. It has been proven for CIGSe solar cells on glass in the case of co-evaporation [143, 39] and post-deposition [40] as well as for CIGSe solar cells on flexible polyimide substrates [144, 142]. Rudmann et al. pointed out that in the case of post-deposition sodium only altered the electronic properties while in the case of co-evaporation also the growth kinetics was influenced and thus the structural and electronic properties of the CIGSe modified [145].

While sodium is beneficial for the initial efficiency it was just carved out that an increasing sodium content is detrimental for the damp heat stability of the CIGSe solar cell. Given a certain damp heat stress, the sodium content can be chosen such that it guarantees the best compromise between initial efficiency and long-term stability<sup>9</sup> (cf. section 5.3.3). For the samples in this thesis (batch 2A-1209) the very sodium content was 1.00× (as normalized from LIBS).

#### 7.2.4 Origin of the Degradation

##### Relation between Sodium, Roughness & Degradation

It could be shown that the surface roughness of our samples decreased with increasing sodium content if the sodium was present during absorber growth (sodium co-evaporation). No relation between sodium content and surface roughness was found for samples with sodium post-deposition. Rudmann et al. reported a reduction of the CIGSe grain size with increasing sodium supply during growth [39] while no structural influence was found for sodium post-deposition [145]. Hence, the relation between grain size (the smaller) and surface roughness (the smoother) suggests itself.

Given the relation between grain size and surface roughness, it can be concluded that a smoother surface is also an indication for more grain boundaries within the absorber. In that case it seems likely that the permeability of the absorber increases since more “diffusion channels” are available. Degrading species such as water could therefore penetrate the absorber more easily and propagate along the grain boundaries towards the back contact. Due to the higher diffusivity degradation processes would be enhanced.

Based on the influence of sodium on the grain size of the absorber, this is a convenient way to explain the more pronounced degradation of CIGSe solar cells with higher sodium contents. On the contrary, for cells with sodium post-deposition, this relationship fails as a single explanation. If sodium is introduced via post-deposition, i.e. not

<sup>9</sup>If the acceleration factor (between damp heat testing and field testing) was known, a precise adjustment of the initial sodium content would be possible in order to adjust the solar cell to a certain expected stress in the field.

present during absorber growth, no influence on the roughness was measured. Given the relation between grain size and roughness, it can be concluded that the grain sizes are independent of the sodium content. This is plausible (and in accordance with the literature [145]) since no sodium was present during absorber growth, hence, it could not influence the grain size. Nevertheless, an influence of the sodium content on the damp heat stability of the CIGSe solar cells with sodium post-deposition was found (cf. section 5.4). It can therefore be concluded that the sodium dependent degradation is independent of the roughness of the solar cell.

While this appears to be in contrast to the above described explanation, the following interpretation is suggested. The initial sodium content has a direct influence on the degradation behavior of the CIGSe solar cell, i.e. the more sodium is present, the more pronounced the degradation is. The nature of this degradation path will be discussed below. It is present irrespective of the method of sodium incorporation. However, if sodium is present during absorber deposition, it alters the morphology of the CIGSe, i.e. smaller grains are formed for higher sodium contents [39]. More grain boundaries in the absorber come along with smaller grains thus facilitating the diffusivity for degrading species within the absorber. Therefore, sodium influences the degradation behavior of a CIGSe solar cell (at least) in two ways.

### **Corrosion at the CIGSe/Mo interface**

As it has been argued in section 7.1.4 and 7.1.5, there are many indications that the degradation facilitated by sodium occurs as a corrosion at the CIGSe/Mo interface. A summary on this argument based on evidence from electrical measurements as well as structural analysis will be given in this section.

A roll-over behavior of the IV characteristic of the CIGSe solar cell after damp heat at low temperatures was observed. This current blocking behavior was interpreted as the result of the change from an ohmic to a non-ohmic behavior of the back contact interface during damp heat exposure. Since a commonly observed MoSe<sub>2</sub> layer between absorber and back contact is being held responsible for the ohmic behavior of the back contact interface [135] it was argued that a damage of the MoSe<sub>2</sub> layer during damp heat causes the loss of the ohmic behavior of the interface (cf. section 7.1.4). Further aspects of the chemical nature of the corrosion at the CIGSe/Mo interface are discussed in the next section.

Another indication for the thesis of a corrosion at the CIGSe/Mo interface arises from the CV measurements. In section 7.1.5 it was argued that a partial corrosion of the interface area between absorber and back contact occurred. As a consequence of the lower effective interface area, the capacitance of the solar cell decreased. Another consequence of this laterally inhomogeneous corrosion (with locally increased contact resistances at the CIGSe/Mo interface) was the appearance of dark (cloud-like) spots in the electroluminescence images (cf. section 6.1). The fraction of the cell area of the

dark spots matched the relative change in capacitance which was taken as an indication that both observations have the same origin (cf. section 7.1.5).

From experiments regarding the damp heat stability of the molybdenum back contact it could be concluded that the bulk of the molybdenum does not degrade (cf. section 7.1.6). Due to the experimental limitations no information could be gathered on the contact resistance between molybdenum and CIGSe. It is, however, known from the literature that molybdenum oxidizes easily and that its oxides are soluble in water [139, 85]. Thus the surface of the back contact can corrode easily.

Evidence from structural analysis for the CIGSe/Mo interface corrosion thesis was obtained from SIMS measurements. Out of two aggregations found in the depth gradient of sodium, one at the CdS/CIGSe interface and another at the CIGSe/Mo interface, only the latter was significantly diminished after damp heat (cf. section 5.5). Since the electrical degradation of the solar cells is correlated with the initial sodium content and a change in sodium concentration was seen at the CIGSe/Mo interface another indication is given for the corrosion of the back contact interface.

As discussed in section 7.2.2, the combined analysis of the sodium and the fluorine gradients indicated that NaF may be present at the back contact interface as well. Within voids it may exist as a compound. Since NaF is hygroscopic [143] it would have an influence on the damp heat stability of the solar cell. If present at the CIGSe/Mo it could be a driving force for moisture ingress into the cell.

SIMS measurements potentially gave indication for an oxidized molybdenum back contact after damp heat treatment (cf. section 5.5). While this observation should be verified with another method (such as X-ray Photoelectron Spectroscopy on lift-off samples), it might be another evidence for a corroded CIGSe/Mo interface.

### Potential Reaction Pathways

The electrical, electro-optical and structural measurements discussed so far provided multiple indications that lead to the conclusion of a corrosion at the CIGSe/Mo interface. However, direct evidence for this thesis can only be obtained with measurement techniques sensitive to the chemistry at the CIGSe/Mo interface. While an outlook on further investigations on this subject will be given in section 7.4.2, potential reaction pathways that may lead to the discussed corrosion at the back contact interface will be discussed here briefly, based on results reported in the literature.

As an easy assessment of the chemical environment during damp heat the pH-value was measured within the climate chamber. It turned out to be neutral ( $pH = 7$ ). On the one hand this appears counter-intuitive: since the climate chamber is operating with deionized water where acidic pH-values should be expected (down to  $pH = 5$  due to the dissolution of  $CO_2$  from the air). On the other hand, the presence of aluminum (mountings) within the climate chamber could compensate such an pH-value due to its alkaline influence.

Another source of alkaline chemicals that could neutralize the expected acidic ambience could be hydroxides that were reported to form on  $\text{CuGaSe}_2$  solar cells even under ambient conditions (cf. section 2.4.4). Furthermore, the formation of  $\text{Zn(OH)}_2$  due to the hydrolysis of  $\text{ZnO:Al}$  under damp heat is possible [78].

Although several studies are available on the oxidation of CIGSe [124] (in the presence of sodium [146, 147]), only Braunger et al. reported on the oxidation of CIGSe in the presence of sodium *and* humidity. As summarized in section 2.4.6, the authors reported that the oxidation of sodium at high temperatures had little or no effect of the efficiency of the solar cell. However, if the solar cells were oxidized in humid air at room temperature, the efficiency dropped significantly. This degradation was attributed to elemental selenium that was formed during this (incomplete) oxidation of CIGSe and  $\text{Na}_2\text{Se}_x$  (from intergranular segregations) [50]. Following the argument by Braunger et al. and assuming the presence of intergranular  $\text{Na}_2\text{Se}_x$  within the absorber and near the back contact in our samples as well, the described chemical reactions provide a potential reaction pathway for the observed corrosion at the CIGSe/Mo interface.

Wennerberg et al. reported that molybdenum oxidizes easily [85] (e.g. within isolation scribes of the CIGSe solar cell) and these oxides are water soluble [139]. Finally, the sequence of oxidation of the back contact (at the interface with the absorber) due to diffusion of oxygen into the solar cell and the dissolution of these oxides due to humidity that penetrates the solar cell may reduce the conductivity of the CIGSe/Mo interface significantly or even lead to delamination of the absorber from the molybdenum. If this process proceeds laterally inhomogeneously (e.g. due to locally different diffusivities) the inhomogeneities observed in the degradation process (cf. chapter 6) were easy to explain.

## 7.3 Lateral Inhomogeneities During Degradation

### 7.3.1 Electroluminescence Imaging

Electroluminescence imaging was employed to study the lateral homogeneity of the solar cell properties before and after damp heat treatment (cf. section 6.1). Exposure to damp heat reduced the overall EL intensity of the samples (cf. figure 6.1 and 6.2). This was in agreement with the degradation of the solar cell efficiency due to damp heat exposure.

The formation of darker cloud-like areas in EL images of damp heat treated solar cells was found. It can be concluded that the degradation proceeded faster in these parts of the solar cell (cf. section 6.2). Thus, the degradation must be seen as a laterally inhomogeneous process.

Furthermore, solar cells with different sodium contents were imaged with electroluminescence after damp heat exposure. In accordance with the IV behavior of the samples it was observed that the overall EL intensity of the solar cells decreased stronger the higher the initial sodium content was. The higher the sodium content of the solar cells



the more inhomogeneous was the distribution of the EL intensity after damp heat exposure (cf. figure 6.3, 6.4 and 6.5).

### 7.3.2 Differential Diagnosis with Different Imaging Techniques

In section 6.2 the advantages of a “differential diagnosis”, i.e. the combination of complementary imaging techniques, were demonstrated by combining three common imaging techniques (EL, DLIT and LBIC). They are non-destructive and allow a fast data acquisition (except for LBIC).

Electroluminescence, by itself, is widely used in solar cell research and production [148]. For silicon solar cells EL images allow conclusions on various defective production steps, such as ingot production, cell or module handling, installation, operation. For thin film solar cells typical error patterns that can be detected are local shunts, moisture ingress, and cell breakdown (the latter two in modules). Additionally, procedures for the quantitative analysis of EL images are available (cf. section 7.3.3).

Lock-in thermography is most commonly used for the detection of shunts. However, quantitative analysis procedures are available as well and allow the investigation of local variations in the diode parameters [149].

Light beam induced current measurement allows a mapping of the current contribution of each point of the solar cell. Due to the testing time for large area solar cells, LBIC is a more common tool in research and development rather than an in-line characterization tool for production.

While all three aforementioned characterization methods are well established for thin film solar cell and have been combined partially [150, 151], there are no reports on the combined application of all three methods on Cu(In,Ga)Se<sub>2</sub> solar cells, yet. However, by combining the laterally resolved methods, EL, DLIT and LBIC, the distinction of certain failure patterns became feasible:

- Shunt: leads to a local distortion of the current collection within solar cell (cf. section 6.2.1)
- Severe shunt: located such that the current collection is distorted on a significant fraction of the solar cell’s area (cf. section 6.2.2)
- Corroded area: 2-dimensional distortion of the current collection that is not originating from a single point<sup>10</sup> (cf. section 6.2.3)

Since different error patterns lead to similar appearances in one imaging technique, analyzing only one method typically leaves room for interpretation. Only the combined evaluation of the three techniques and the comparison of specific error patterns allowed

---

<sup>10</sup>As suggested in section 6.2.3, likely causes for a “corroded area” may be a degradation of the pn-junction or of the planar contacts or their respective interfaces with the pn-junction.

to distinguish between certain defects, like a severe shunt and a locally corroded area (cf. section 6.2).

### 7.3.3 Series Resistance Mapping

Two imaging techniques based on voltage dependent electroluminescence (cf. section 3.2.3) were applied to flexible CIGSe thin film solar cells<sup>11</sup>. While common for silicon solar cells [121, 122], these methods were applied to Cu(In,Ga)Se<sub>2</sub> solar cells for the first time<sup>12</sup>.

The results of the calculation with the method by Hinken et al. [121] were shown in section 6.3.2 and those of the calculation with the method by Breitenstein et al. [122] were shown in section 6.3.3. A comparison is given below.

#### Comparison of Two Methods

Comparing the similarities of both calculation methods that allow to spatially resolve the series resistance, the obtained values match well. The average of all local series resistance values<sup>13</sup> obtained with Hinken's method (cf. section 6.3.2) is  $2.98 \Omega \text{ cm}^2$  compared to  $4.25 \Omega \text{ cm}^2$  from the IV measurement of the sample. Since Breitenstein's method (cf. section 6.3.3) does not yield absolute values, the average of the series resistance map calculated with that method was scaled to the series resistance obtained from the IV measurement. This is a major drawback of the method by Breitenstein et al. because the calculation of an absolute value for  $R_S$  in the method by Hinken et al. allow a validation of the result. The series resistance mapping calculated with the method by Hinken et al. (cf. figure 6.10) can be interpreted as a valid result since the average  $R_S$  calculated from this electro-optical measurement (EL) matches the value for  $R_S$  from a purely electrical measurement (IV) very well.

The distribution of the local series resistance is slightly different for both methods as shown in histograms in figure 7.4. The values from Breitenstein's method center on the global value of the series resistance with a tail towards lower resistances whereas the values from Hinken's method have their highest density at slightly lower resistances with a tail towards larger values. The tails in the histograms in figure 7.4 originate from extreme values of the local series resistances at the edges of the solar cell in the respective mappings (figures 6.10 and 6.11). Due to potential cutting damages at the edges of the solar cell it appears more obvious to assume an increased series resistance at the edges of the solar cell thus leaving the tail of the local series resistances to higher values (Hinken's method) more plausible.

---

<sup>11</sup>Section 6.3 is based on a conference paper by Daume et al. [120].

<sup>12</sup>Quantitative electroluminescence analysis on Cu(In,Ga)Se<sub>2</sub> modules has been shown before [152].

<sup>13</sup>This is a simple approximation, neglecting the circuitry of the local series resistances.

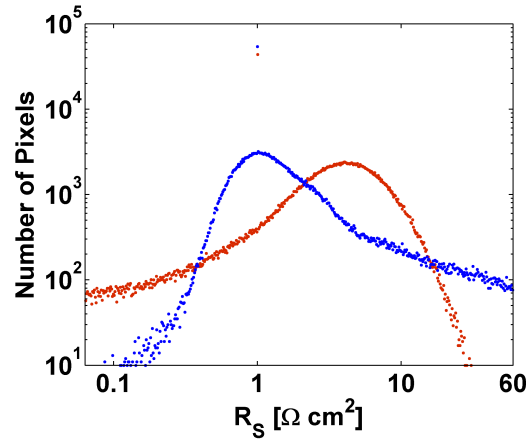


Figure 7.4: Histogram of series resistances in the mappings calculated with Hinken's method (blue) and Breitenstein's method (red). Note the logarithmic scaling.

Looking at a line scan (figure 7.5) through both mappings similar features were observed, indicating consistency between the two calculation methods. In both line scans periodic increases of the series resistance between the grid fingers are mapped. This is due to the limited conductivity of the TCO and hence a generally higher luminescence close to the (well conducting) grid fingers. It should be kept in mind that due to the definition of the local series resistance<sup>14</sup> such a behavior is expected even if homogeneous sheet resistances were assumed across the grid fingers.

For both methods, unity was assumed as diode ideality factor which might not be true locally. Hinken et al. point out that this assumption is valid as long as lateral variations in the effective bulk lifetime are negligible [121]. The authors claim that this is a good assumption for monocrystalline cells and may lead to errors for polycrystalline material<sup>15</sup>. However, it should be noted that for our setup the area on the cell covered by one pixel of the camera is about  $10^4 \times$  larger than the estimated grain size of the absorber. Hence, the spatially resolved series resistance is an average over many grains of the polycrystalline CIGSe microstructure. By averaging over a large number of grains with potentially individual properties the assumption of negligible variations in the bulk properties can be seen as fulfilled.

A main difference between the two methods is the need for only two EL images in the Breitenstein method. This advantage goes along with a much faster calculation

<sup>14</sup>The local series resistance  $R_s^{x,y}$  mapped by the pixel at point  $(x, y)$  is the resistance that the current fraction (that recombines to EL light emission) faces on its path from the outer contacts of the solar cell to this point  $(x, y)$  [121, 122].

<sup>15</sup>This was expressed for silicon originally. Nevertheless Cu(In,Ga)Se<sub>2</sub> absorbers are polycrystalline (with much smaller grains).

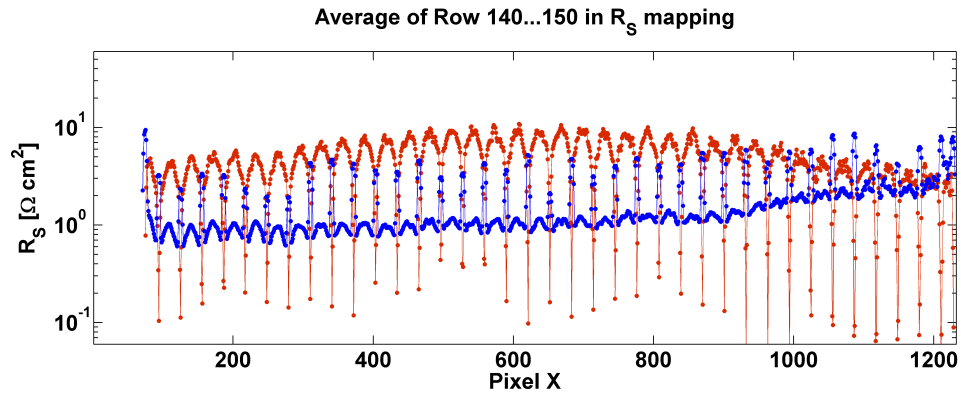


Figure 7.5: Line scan through the series resistance mapping calculated with Hinken's method (blue) and Breitenstein's method (red). Local maxima of the series resistance occur between the grid fingers. The deceptive spikes of the series resistance occur at or close to the grid fingers (calculation errors).

(factor 100 in calculation time) for the latter method. Moreover, Breitenstein's method allows to spatially resolve the series resistance and additionally the saturation current. This allows to differ between absorber (CIGSe) and planar contact (e.g. TCO) related effects on the observed electroluminescence and the solar cell performance, respectively. However, Hinken's method does not require a scaling of the calculated series resistance map to the global series resistance from IV while this is necessary for Breitenstein's method.

Having scaled the mean value of the local series resistances  $R_S^{x,y}$  to the global series resistance of the cell, the mean value of the calculated local saturation current densities  $j_0^{x,y}$  does not match the global saturation current density as determined from IV. This is in contradiction to the example of an industrial multicrystalline cell given by Breitenstein et al. where the saturation current densities match [122]. The offset seen here (which is in fact several orders of magnitude) leads to doubts about the applicability of Breitenstein's method to the Cu(In,Ga)Se<sub>2</sub> material system.

### Applicability to Damp Heat Treated Samples

As described in section 6.1.1, the overall EL intensity decreases after damp heat exposure. In order to calculate series resistance mappings, EL images at different voltages (or injection currents, respectively) are necessary (e.g. two images for the calculation following Breitenstein's method; cf. figure 6.9). At low injection currents the EL intensity after damp heat got as low as the background noise level (even at longer camera exposure times). For that reason the calculation method by Hinken et al. was not applicable to the solar cells after damp heat exposure. In order to conduct that calculation multiple

images below the threshold voltage of the pn-junction were necessary, however, at these low injections the EL images from the present experimental setup were too noisy.

An example for the calculation of a series resistance mapping via Breitenstein's method was shown in section 6.3.4. The interpretation of the obtained series resistance mapping is tempting. The dark spots seen in EL apparently do not originate from an increased series resistance (cf. figure 6.14). In combination with the calculated saturation current mapping (cf. figure 6.15) the spots may rather be explained by a degradation of the pn-junction, i.e. by a local increase in the saturation current density by one to two orders of magnitude in the area of the dark spots.

However, it must be kept in mind that the mean saturation current density from the mapping (cf. figure 6.15) does not even match the order of magnitude of the value from IV (approximately  $1.3 \times 10^{-5} \text{ A/cm}^2$ ). Thus, as discussed in the previous section, the applicability of the calculation method by Breitenstein et al. must be doubted. The apparent explication regarding the origin of the dark spots in EL images after damp heat is not reliable. At this point the only sure insight obtained with this method is the lateral inhomogeneity of the degradation process that, admittedly, had been obvious from the plain electroluminescence images already.

## Conclusion

Two methods providing spatially resolved information on the series resistance from voltage dependant electroluminescence measurements that had reportedly been used for silicon solar cells were successfully tested for CIGSe solar cells.

The obtained mean series resistance values from Hinken's method matched with the global series resistance from current-voltage measurement. This was taken as an indication for the validity of the method. From the series resistance map it could be concluded that darker areas in the EL images originate from a locally increased series resistance.

Breitenstein's calculation method outrivalled Hinken's method in time consumption for data acquisition as well as calculation, additionally it provided a mapping of the saturation current density. The latter, however, was not plausible since the mean saturation current density from the mapping did not match the value from IV testing. Thus the method should not be applied to CIGSe solar cells in its current form.

Instead Hinken's method can be applied to study the lateral homogeneity of the series resistance of  $\text{Cu(In,Ga)Se}_2$  solar cells. After damp heat exposure, the EL intensity was too low to obtain images with a sufficient signal-to-noise ratio. That disadvantage might be overcome by the replacement of the infrared camera in the given setup (cf. section 3.2.3) with a model more sensitive to the EL spectrum of the CIGSe solar cell<sup>16</sup>.

---

<sup>16</sup>Standard industrial infrared cameras with silicon CCD (charge-coupled device) sensors have a rather low sensitivity for EL in the range of approximately 1 eV from CIGSe solar cells. A camera with an InGaAs sensor would serve better due to its lower bandgap. However, to date no InGaAs based

## 7.4 Conclusions

The conclusions of the discussion in this chapter are summarized in the form of theses in section 7.4.1. In section 7.4.2 an outlook including suggestions for improvements of the damp heat stability, as well as further research topics on the stability of CIGSe solar cells is given.

### 7.4.1 Theses

**Sodium present during  $\text{Cu(In,Ga)Se}_2$  growth (sodium co-evaporation) influences the roughness of the solar cell surface: sodium $\uparrow \rightarrow$ roughness $\downarrow$ .**

This was experimentally confirmed via laser scanning microscopy as well as the analysis of SEM images of the surface of the solar cell (cf. section 5.6). In contrast, solar cells in which sodium was introduced via post-deposition, did not show a dependence of the surface roughness on the sodium content. In the discussion (cf. section 7.2.1) it was thus concluded that sodium has an influence on the absorber (and thus solar cell surface) roughness if present during absorber growth. The beneficial influence of a smoother surface on the efficiencies of the solar cell was ascribed to the conductivity of the TCO. According to Greiner [94] aluminum doped zinc oxide grown on rough surfaces forms more “extended grain boundaries” which limit the DC conductivity (cf. section 7.2.1).

**Damp heat does not cause structural changes in  $\text{Cu(In,Ga)Se}_2$  solar cells.**

No physical damage was visible after damp heat treatment. SIMS measurements showed identical gradients for the constituents of the CIGSe absorber. It was concluded that the chalcopyrite crystal structure is stable under damp heat. The comparison of SEM images (cross section and top view) as well as laser scanning microscopies of the solar cell surface showed no differences neither before nor after damp heat (cf. section 7.1.1). It was concluded that damp heat exposure up to 200 h (ex-situ experiments<sup>17</sup>) or 700 h (in-situ experiments<sup>18</sup>) of CIGSe solar cells leads to “mild” damage only, i.e. influences on the electrical properties of the solar cell but no influence on the morphology. Optical properties may be influenced by damp heat, but they were beyond the scope of the utilized measurement techniques. It was concluded in the discussion that the degradation of the CIGSe solar cell mainly happens at interfaces (including grain boundaries) and the planar contacts.

---

CCDs are commercially available that match the resolution of silicon based CCDs.

<sup>17</sup>An ex-situ experiment refers to a sequence IV measurement, damp heat exposure, IV measurement (and so forth) and was described in section 5.3.1.

<sup>18</sup>An in-situ experiment refers to the (repeated) IV measurement under damp heat and was described in section 4.3.

**Cu(In,Ga)Se<sub>2</sub> solar cells on polyimide substrates degrade under the influence of damp heat while water plays a role in the degradation process.**

It was found that CIGSe solar cells degraded under damp heat while they showed stable IV parameters under exposure to dry heat for the same time (cf. section 4.1). As discussed in section 7.1.3 and in accordance with the literature, it was concluded that humidity plays a leading role in the degradation process of CIGSe solar cells.

**Aging mechanisms with opposing trends allow the identification of two stages of aging of the Cu(In,Ga)Se<sub>2</sub> solar cell, i.e. an initial improvement followed by the continuous degradation.**

While a cyclic ex-situ experiment gave a first indication (cf. section 5.3.1), in-situ measurements of the IV characteristic under damp heat confirmed that characteristic of CIGSe solar cell aging (cf. section 4.3.3). Different hypotheses to explain the initial improvement (stage 1) were discussed in section 7.1.7. The nature of the degradation in stage 2 was subject to further investigation and will be summarized below.

**Sodium promotes the aging of Cu(In,Ga)Se<sub>2</sub> solar cells:  
sodium $\uparrow$ →aging $\uparrow$ .**

In multiple experiments it was shown that the degradation of CIGSe proceeds faster, the higher the initial sodium content of the solar cell was. Three ex-situ experiments showed this relation for solar cells with co-evaporated sodium (cf. section 5.3). Another ex-situ experiment with solar cells with post-deposited sodium confirmed this finding (cf. section 5.4) and thus proved that this relation is independent of the method of sodium introduction.

From in-situ IV measurements under damp heat degradation rates were fitted. No significant difference in the degradation rate (in stage 2) was found between three different sodium contents (cf. section 4.3). However, the onset of stage 2 and thus the characteristic of stage 1 differed between the different sodium contents.

Since sodium is on the one hand beneficial for the initial CIGSe solar cell efficiency and, on the other hand, detrimental for the damp heat stability, the initial sodium content allows to tune an optimum between initial efficiency and long-term stability (cf. sections 5.3.3 and 7.2.3).

**The sodium promoted degradation occurs due to a corrosion at the CIGSe/Mo interface.**

Indications to support this thesis were obtained from structural, electrical and optical measurements.

With SIMS measurements it was shown that sodium tends to aggregate at the CIGSe/Mo interface within the Cu(In,Ga)Se<sub>2</sub> solar cell. This aggregation vanishes after exposure to damp heat (cf. section 7.2.2).

IV measurements showed that the efficiency after damp heat degrades because of an increase in series resistance (cf. section 7.1.2). This effect and thus the degradation of fill factor and efficiency was more pronounced the higher the initial sodium content of the solar cell was (cf. section 5.3.1). The degradation of the IV parameters of the Cu(In,Ga)Se<sub>2</sub> solar cell was dependent on the sodium content irrespective of its method of introduction (sodium co-evaporation or post-deposition, cf. section 7.2). In low-temperature IV measurements a current blocking behavior in forward direction was found for damp heat treated samples. In the discussion in section 7.1.4, this roll-over was ascribed to a non-ohmic contact at the back contact interface between molybdenum and CIGSe after damp heat exposure (cf. section 7.1.4). From CV measurements it was concluded that the back contact or its interface with the CIGSe absorber corrodes under damp exposure of the solar cell (cf. section 7.1.5). However, resistivity measurements of the molybdenum before and after damp heat ruled out a degradation of the bulk of the back contact (cf. section 7.1.6).

Laterally resolved EL measurements proved that the degradation of the solar cell proceeds laterally inhomogeneously (cf. section 7.3.1). Darker areas in the EL images that appeared after damp heat were identified as corroded areas (planar contacts or their interfaces with the pn-junction) by comparing different laterally resolved measurements, i.e. EL, LBIC and DLIT (cf. section 6.2.3). Series resistance mappings obtained from voltage dependent electroluminescence showed that darker areas in EL typically result from locally increased series resistances (cf. section 7.3.3).

### **The solar cell degradation (aging) process is a superposition of multiple processes.**

A first indication for this superposition was given by the observation of two stages in the aging process, as described above, an initial improvement and the continuous degradation. While potential explanations on the nature of the initial improvement in stage 1 were discussed in section 7.1.7, evidence was gathered in this thesis that the degradation in stage 2 itself is a superposition of different detrimental mechanisms.

One contribution to the overall degradation of the solar cell is a corrosion at the CIGSe/Mo interface (as discussed above). It must be stressed that the bulk of the molybdenum is not subject to degradation while the interface with the absorber is vulnerable (cf. section 7.1.6). Another degradation mechanism is the degradation of the ZnO:Al front contact (cf. section 7.1.6). A third mechanism is the degradation of the contact between aluminum doped zinc oxide and grid. While the resistance of the bulk of the TCO increased by almost one order of magnitude the contact resistance between grid and TCO increased by two orders of magnitude (after 384 h of damp heat on un-encapsulated solar cells; cf. section 7.1.6). The contact resistance (between grid and



TCO) comprises the (bulk) resistance of the grid with a certain share and may thus be an indication for another degradation mechanism, i.e. the degradation of the grid.

In other words, the degradation of the solar cell is the sum of the degradation processes of each individual layer and interface of the thin film solar cell as well as their interaction. By studying the solar cell as one device with different measurement techniques as well as by performing measurements on individual layers of the planar contacts (cf. section 4.4), several degradation mechanisms could be identified. It is possible that further degradation mechanisms are contributing to the solar cell degradation, however, the above mentioned seem to dominate the degradation since they were superimposing other (potential) mechanisms with their intensity.

### **The solar cell degradation is a laterally inhomogeneous process.**

Laterally resolved measurements before and after damp heat exposure of Cu(In,Ga)Se<sub>2</sub> solar cells provided evidence for this thesis. Electroluminescence images revealed that some areas within the solar cell degraded faster than their surrounding (darker areas in EL images; cf. section 7.3.1). From series resistance mappings (calculated from voltage dependent electroluminescence images) it was concluded that darker areas in EL originate from locally increased series resistances in the cell (cf. section 7.3.3). With a “differential diagnosis”, i.e. by combining different laterally resolved measurement techniques, darker areas (as seen after damp heat exposure) in the EL images could be identified as corroded areas (cf. section 6.2.3).

## **7.4.2 Outlook**

### **Corrosion & Chemical Aspects**

The research within this thesis was conducted with electrical (IV, CV, TLM, Hall) and electro-optical (EL, LIT, LBIC) as well as structural (SEM, SIMS, LIBS, scanning laser microscopy) measurement methods. These techniques lead to a significant progress in the understanding of the degradation of flexible thin-film Cu(In,Ga)Se<sub>2</sub> solar cells. By combining the results of the different techniques, it could be differentiated between multiple degradation mechanisms (cf. section 7.4.1). However, the chemistry behind these processes remained subject to indirect conclusions and speculation. In order to assess the nature of the corrosion process at the CIGSe/Mo interface, whose potential chemical origin was discussed in section 7.2.4, measurements methods sensitive to the interface chemistry were necessary. In order to understand the changes that the back contact interface undergoes during damp heat exposure of the CIGSe solar cell, an analysis of the elements present at the interface as well as their bonding states would be necessary. X-ray photoelectron spectroscopies on both surfaces of lift-off<sup>19</sup> samples

---

<sup>19</sup>A lift-off sample is prepared by gluing the surface of the solar cell to a transfer substrate and by pulling the polyimide substrate (with the molybdenum back contact) off the CIGSe absorber [13].

before and after damp heat could serve that purpose.

As shown in chapter 6 and discussed in section 7.3, the degradation of the  $\text{Cu}(\text{In,Ga})\text{Se}_2$  solar cell proceeds laterally inhomogeneously. Thus, a 3-dimensional model of the solar cell as a device seems necessary in order to pass a certain level of knowledge. Many common measurement methods, such as IV, CV and TLM, disregard lateral effects, i.e. two out of three dimensions, and yield averaged results (over the whole area of the solar cell) instead. It is obvious that spatially resolved methods are required to better understand the degradation mechanisms in solar cell or any thin film device. This is particularly relevant as solar cell areas increase from lab scale ( $\approx 1 \text{ cm}^2$ ) to industrial scale ( $\approx 60 \text{ cm}^2$  in our case) or if the degradation of modules is studied ( $\approx 10\,000 \text{ cm}^2$ ). Basic approaches to measure electrical parameters locally have been demonstrated [153].

### Hypothesis

Two hypothesis that unfold from the discussion of the experimental results in this thesis are as follows. The damp heat experiments in section 5.3 were carried out ex-situ, i.e. measurements were followed by damp heat treatments which were followed by measurements (and so forth). The periods after which the solar cell efficiencies had degraded to a certain level within this cyclic approach were lower compared to the in-situ, i.e. IV measurements during damp heat exposure, experiments that were presented in section 4.3.

It can thus be conjectured that **(i) a continuous treatment for a given damp heat exposure  $\Delta t$  is less harmful to a CIGSe solar cell than a cyclic treatment interrupted by ex-situ measurements that adds up to the same damp heat exposure time  $\Delta t$ .** It remains subject to further investigation whether, e.g., heating and cooling or humidification and drying, respectively, or handling or delays between damp heat and IV measurements could evoke such a difference in the degradation behavior.

On the other hand, bearing the above described difference between ex-situ and in-situ experiments in mind, it can be conjectured that **(ii) damp heat exposure under illumination is less harmful to CIGSe solar cells than in the dark.** In order to check both hypotheses, a direct comparison with identical samples (same batch) under damp heat exposure could be carried out between in-situ and ex-situ IV measurements. Furthermore, the influence of light (and with respect to the application in the field also the load at maximum power point) on the solar cell during damp heat could be studied.

### Strategies to Improve the Stability of the Solar Cell

The necessity to encapsulate  $\text{Cu}(\text{In,Ga})\text{Se}_2$  solar cells in order to protect them from humidity is a broad agreement in the literature and was confirmed in this thesis. The

---

Two samples are obtained: transfer substrate/TCO/CdS/CIGSe and Mo/polyimide.

necessary protection that an encapsulation must provide in order to meet certain lifetime requirements was discussed in section 7.1.8. However, from the findings regarding the degradation behavior of flexible CIGSe solar cells, that were discussed above, strategies can be derived to increase the damp heat and thus long-term stability of unencapsulated CIGSe solar cells:

- A corrosion at the CIGSe/Mo interface was identified as one contribution to the degradation of the CIGSe solar cell. Thus, one strategy to improve the damp heat stability at this interface is to improve the damp heat stability of the molybdenum back contact. A potential route to reach this goal might be the doping of the molybdenum sputter target with aluminum [154].
- Since sodium was identified as a factor that influences the damp heat stability of the solar cells, the precise control of the initial sodium content is a strategy to influence the long-term stability of the solar cell. As discussed in section 5.3.3, the sodium content can be utilized to optimize the CIGSe solar cell for highest initial efficiency and long-term stability. The precise control of the initial sodium content may also affect the aggregation of the sodium at the back contact interface (that was found in SIMS; cf. section 7.2.2), and thus the corrosion or damp heat stability, respectively, at this interface.
- The solar cells with post-deposited sodium had a better damp heat stability than those with co-evaporated sodium (cf. section 7.2.3). Although further research is necessary to understand that difference, it seems reasonable to apply that method of sodium introduction. The option of a combined “alkali doping” with sodium and potassium that lead to the latest CIGSe efficiency world record [54, 55] should be evaluated with respect to its damp heat stability as well.
- The degradation of the TCO was identified as another contribution to the degradation of the CIGSe solar cell (cf. section 7.1.6). Hence, an improvement of the long-term stability of the transparent conductive oxide (TCO) is desirable. One strategy could be the replacement of the ZnO:Al with ITO or a multi-layer front contact with ITO as top layer. Another strategy could be the optimization of the surface roughness of the CIGSe solar cell with respect to a better damp heat stability of the TCO (cf. section 7.2.1).
- The damp heat stability of the grid and its contact resistance to the TCO gives scope for further improvements of the long-term stability of the CIGSe solar cell (cf. section 7.4.1). E.g., studies showed that the capping of the widely used Ni/Al (50 nm/2 to 3  $\mu$ m) grid with an additional Ni layer (50 nm) significantly improved the damp heat stability of the grid [85].

- The application of protective layers onto the solar cell can be seen as an intermediate step towards the encapsulation within a module. Different approaches such as the the direct application of inorganic barrier layers [104] or the application of inorganic barrier layers via organic precursors [155] on top of the solar cell have been demonstrated. This strategy directly protects the TCO as well as exposed parts of the molybdenum (e.g. isolation scribes) and slow down the ingress of moisture into the CIGSe solar cell.

## 8 Summary

The degradation of flexible Cu(In,Ga)Se<sub>2</sub> (CIGSe) solar cells was studied within this thesis. Thin film solar cell samples deposited on plastic substrates were fabricated by an industrial pilot–production line by *Solarion AG*. It is known from previous studies that humidity is the main threat to CIGSe solar cells. Thus, damp heat was used as accelerated lifetime test for unencapsulated samples.

The assessment of the damp heat induced degradation showed that no structural changes were caused. No physical damage was visible after exposure to damp heat. Electron microscopies neither showed differences in the surface texture nor in cross sections before and after damp heat. The elemental depth gradients of copper, indium, gallium and selenium (measured with SIMS) were not influenced by damp heat. From these findings it was concluded that the chalcopyrite CIGSe absorber, in particular, and the microstructure of the whole solar cell, in general, are stable under damp heat. The elemental depth profiles, however, revealed changes in the trace elements such as sodium (as summarized below).

Current–voltage measurements were carried out while the solar cells were exposed to damp heat. The damp heat degradation of the IV parameters could thus be observed in–situ for the first time for flexible Cu(In,Ga)Se<sub>2</sub> solar cells. These measurements revealed a two stage behavior of the degradation kinetics. In a first stage, the efficiency of the solar cell improved. Different hypotheses on this beneficial effect, that was mainly driven by open circuit voltage and fill factor, were discussed. In a second (and final) stage, the solar cell degraded. While papers on the degradation of CIGSe solar cells were published before, the initial improvement is being reported for the first time and should be subject to further research as well. Furthermore, the in–situ approach allowed the determination of degradation rates in stage two. Given a certain lifetime limit (percentage of the initial power), these degradation rates of unencapsulated CIGSe solar cells allowed to estimate lifetimes of solar cells and may help to estimate the lifetime of CIGSe modules in the future.

The research in this thesis showed that the series resistance of the solar cell was a main driver of the actual degradation (stage two). Due to an increase in series resistance after damp heat exposure, the fill factor of the solar cell was diminished and thus the efficiency as well. It could be shown that this degradation originated from the superposition of different degradation processes within the solar cell. Besides a corrosion at the Mo/CIGSe interface, the degradation of the ZnO:Al and the degradation of the contact between ZnO:Al and grid were identified as such detrimental processes. Further

degradation processes might be present (e.g. the degradation of the grid was suspected) but were superimposed by the aforementioned processes.

While sodium doping is a key to achieve high-efficiency solar cells little was known about its influence on the long-term stability before. For the first time, the role of sodium on the damp heat stability was studied for both fundamental doping methods of CIGSe solar cells grown on sodium-free substrates, i.e. sodium co-evaporation and sodium post-deposition. It was found that sodium promotes the degradation of Cu(In,Ga)Se<sub>2</sub> solar cells, regardless of how sodium was introduced to the solar cell. The samples with sodium post-deposition were more stable under damp heat exposure than those with sodium co-evaporation. In-situ degradation rates were fitted for the latter and revealed that the degradation rates were independent of the sodium content. Instead, the degradation kinetics between the cells with different sodium content differed in the onset of stage two of the degradation.

By combining the results of electrical, optical and structural measurement techniques, the sodium promoted degradation could be attributed to a corrosion at the back contact interface between molybdenum and CIGSe.

With regard to the deployment of CIGSe solar cells on large areas and with respect to the fact that the individual solar cells in this thesis had areas up to approximately 60 cm<sup>2</sup>, the lateral homogeneity of the degradation process was studied. It was shown that the degradation under damp heat proceeds laterally inhomogeneously. Specifically for higher sodium contents, some parts of the solar cell degraded faster than their surrounding. By combining three laterally resolved measurement techniques (EL, DLIT, LBIC), the areas that appeared darker in the EL images after damp heat exposure, were identified as corroded areas. For the first time, two methods to calculate series resistance mappings from voltage dependent electroluminescence images were applied to CIGSe solar cells. It could be concluded that darker areas within the EL images originated from locally increased series resistances in the solar cell.

From these findings, several recommendations how to improve the damp heat stability of unencapsulated flexible Cu(In,Ga)Se<sub>2</sub> solar cells were given: improve the damp heat stability of the molybdenum back contact (to improve the stability at the Mo/CIGSe interface), precisely control the initial sodium content (to balance between initial efficiency and damp-heat stability), apply sodium in a post-deposition treatment, improve the stability of the TCO and the grid.

Even more room for improvements on the stability of the CIGSe solar cell may be gained from further research on the degradation behavior of this type of thin film solar cell. Based on the findings in this thesis, investigations on the improving mechanism in stage one of the degradation process, on the chemical nature of the corrosion at the Mo/CIGSe interface, on the stability of the grid and its interplay with the TCO, on the difference between continuous and cyclic damp heat treatments and on the influence of light and bias during damp heat, may yield further insights into the degradation of Cu(In,Ga)Se<sub>2</sub> solar cells under damp heat.

# Appendix A

## Solar Cell Data

### Definition

In order to quantify the stoichiometry during absorber deposition, different ratios between the constituent elements are monitored. Following the convention at *Solarion AG* they are defined as follows. The ratio of gallium to group three elements (indium and gallium) is denoted as  $db$ . The gallium to indium plus gallium ration  $db$  determines the band gap of the  $\text{Cu}(\text{In},\text{Ga})\text{Se}_2$  absorber (cf. equation 1.8).

$$db = \frac{Ga}{In + Ga} \quad (\text{A.1})$$

The ratio of the cations  $dk$  characterizes the copper content of the absorber layer.

$$dk = \frac{Cu}{Ga + In} \quad (\text{A.2})$$

The selenium ratio  $ds$  characterizes the selenium deficiency of the absorber.

$$ds = \frac{2Se}{3(Ga + In) + Cu} - 1 \quad (\text{A.3})$$

### Samples in this Thesis

Tables A.1 and A.2 summarizes the stoichiometries, including sodium contents, and IV parameters of all solar cells that were studied in this thesis. The stoichiometries of the samples were obtained via in-situ XRF measurements during absorber deposition of the CIGSe absorber layers. Sodium contents were obtained from ex-situ LIBS measurements as described in section 5.1. The IV parameters were obtained from automatic flash solar simulator measurements after production of the solar cells.

Process	Cells	Na	db	dk	ds
2A-1173	9	0.52	0.232 ± 0.001	0.775 ± 0.006	-0.127 ± 0.002
2A-1173	6	11.33	0.226 ± 0.003	0.769 ± 0.006	-0.118 ± 0.002
2A-1209	3	0.61	0.234 ± 0.002	0.766 ± 0.001	-0.099 ± 0.000
2A-1209	3	0.75	0.231 ± 0.001	0.770 ± 0.001	-0.098 ± 0.002
2A-1209	3	1.00	0.229 ± 0.001	0.753 ± 0.000	-0.095 ± 0.001
2A-1209	3	1.05	0.223 ± 0.000	0.763 ± 0.002	-0.092 ± 0.000
2A-1209	3	1.31	0.227 ± 0.002	0.756 ± 0.002	-0.090 ± 0.001
2A-1225	6	0.43	0.229 ± 0.001	0.750 ± 0.004	-0.111 ± 0.000
2A-1225	11	0.71	0.230 ± 0.001	0.763 ± 0.007	-0.108 ± 0.001
2A-1225	6	1.14	0.232 ± 0.001	0.780 ± 0.002	-0.108 ± 0.001
2A-1233	1	0.44	0.231 ± 0.000	0.766 ± 0.000	-0.103 ± 0.000
2A-1233	2	0.66	0.231 ± 0.001	0.793 ± 0.001	-0.103 ± 0.001
2A-1233	1	0.86	0.227 ± 0.000	0.772 ± 0.000	-0.100 ± 0.000
2A-1234	6	0.14	0.229 ± 0.000	0.767 ± 0.001	-0.105 ± 0.000
2A-1234	11	0.22	0.232 ± 0.001	0.772 ± 0.006	-0.103 ± 0.001
2A-1234	12	0.26	0.230 ± 0.002	0.771 ± 0.004	-0.104 ± 0.001
2A-1234	15	0.47	0.235 ± 0.007	0.764 ± 0.012	-0.105 ± 0.002
2A-1234	12	0.77	0.232 ± 0.001	0.768 ± 0.006	-0.104 ± 0.000
2A-1234	12	0.84	0.232 ± 0.001	0.769 ± 0.007	-0.103 ± 0.002

Table A.1: Overview of all samples studied in this thesis, including the number of solar cells, sodium contents (as obtained from LIBS) and stoichiometries ( $\pm$  standard deviations).



Process	Na	$V_{OC}$ [V]	$J_{SC}$ [mA/cm <sup>2</sup> ]	FF	$\eta$ [%]	$R_S$ [ $\Omega$ cm <sup>2</sup> ]	$R_P$ [k $\Omega$ cm <sup>2</sup> ]
2A-1173	0.52	0.498 ± 0.014	35.3 ± 0.4	0.564 ± 0.008	9.9 ± 0.4	2.08 ± 0.09	0.000 ± .01
2A-1173	11.33	0.567 ± 0.006	33.1 ± 0.4	0.614 ± 0.025	11.5 ± 0.4	2.33 ± 0.39	0.020 ± .04
2A-1209	0.61	0.505 ± 0.007	33.2 ± 0.2	0.559 ± 0.015	9.4 ± 0.4	4.41 ± 0.39	12.67 ± 16.63
2A-1209	0.75	0.516 ± 0.010	33.1 ± 0.1	0.589 ± 0.022	10.1 ± 0.6	3.93 ± 0.35	21.30 ± 17.03
2A-1209	1.00	0.528 ± 0.007	32.8 ± 0.1	0.644 ± 0.012	11.1 ± 0.2	3.19 ± 0.19	24.38 ± 14.37
2A-1209	1.05	0.544 ± 0.012	31.0 ± 1.1	0.611 ± 0.010	10.3 ± 0.4	3.59 ± 0.28	19.82 ± 10.84
2A-1209	1.31	0.542 ± 0.008	27.9 ± 1.2	0.414 ± 0.023	6.3 ± 0.2	6.15 ± 0.37	6.404 ± .13
2A-1225	0.43	0.474 ± 0.001	33.0 ± 0.3	0.568 ± 0.020	8.9 ± 0.3	3.74 ± 0.30	4.140 ± .76
2A-1225	0.71	0.510 ± 0.008	32.4 ± 0.3	0.638 ± 0.012	10.6 ± 0.3	2.69 ± 0.10	4.802 ± .95
2A-1225	1.14	0.536 ± 0.002	30.6 ± 0.5	0.629 ± 0.022	10.3 ± 0.5	2.64 ± 0.15	5.463 ± .75
2A-1233	0.44	0.474 ± 0.001	33.0 ± 0.0	0.617 ± 0.000	10.3 ± 0.0	3.12 ± 0.00	37.91 ± 0.00
2A-1233	0.66	0.510 ± 0.008	32.6 ± 0.1	0.635 ± 0.001	10.7 ± 0.0	3.21 ± 0.03	11.30 ± 7.70
2A-1233	0.86	0.536 ± 0.002	28.2 ± 0.0	0.617 ± 0.000	9.4 ± 0.0	3.17 ± 0.00	2.140 ± .00
2A-1234	0.14	0.351 ± 0.019	29.2 ± 1.4	0.407 ± 0.029	4.2 ± 0.6	6.09 ± 0.78	8.665 ± .48
2A-1234	0.22	0.387 ± 0.032	31.5 ± 1.3	0.484 ± 0.026	5.9 ± 0.9	4.49 ± 0.37	9.405 ± .48
2A-1234	0.26	0.373 ± 0.048	30.4 ± 1.5	0.461 ± 0.037	5.3 ± 1.3	4.81 ± 0.54	10.96 ± 10.99
2A-1234	0.47	0.425 ± 0.051	31.4 ± 1.4	0.530 ± 0.052	7.2 ± 1.7	3.96 ± 0.63	9.428 ± .23
2A-1234	0.77	0.466 ± 0.040	32.2 ± 0.4	0.579 ± 0.072	8.8 ± 1.8	3.36 ± 0.98	11.23 ± 8.12
2A-1234	0.84	0.495 ± 0.017	32.8 ± 0.4	0.642 ± 0.035	10.4 ± 1.0	2.59 ± 0.39	13.67 ± 12.08

Table A.2: Overview of all samples studied in this thesis, including sodium contents (as obtained from LIBS) and IV parameters of the solar cells ( $\pm$  standard deviations). Parallel resistances were measured in the dark (except for process 2A-1173).



# Appendix B

## List of Publications

All articles (research papers and conference records) which I wrote or that I contributed to are listed below. Furthermore, all posters that I presented and all talks I gave are named.

### B.1 Research Articles (own and contributed work)

- H. Zachmann, S. Puttnins, **F. Daume**, A. Rahm, K. Otte, R. Caballero, C.A. Kaufmann, T. Eisenbarth, H.W. Schock;  
*Incorporation of Na in low-temperature deposition of CIGS flexible solar cells*;  
Thin Solid Films; 2009;  
DOI: <http://dx.doi.org/10.1557/PROC-1210-Q03-02>
- H. Zachmann, S. Puttnins, **F. Daume**, A. Rahm, K. Otte;  
*Generation of electrical defects in ion beam assisted deposition of Cu(In,Ga)Se<sub>2</sub> thin film solar cells*;  
Thin Solid Films; 2010;  
DOI: <http://dx.doi.org/10.1016/j.tsf.2010.12.215>
- **F. Daume**, C. Scheit, S. Puttnins, A. Rahm, M. Grundmann;  
*Application of series resistance imaging techniques to Cu(In,Ga)Se<sub>2</sub> solar cells*;  
Proceedings of the 26<sup>th</sup> EU-PVSEC (Hamburg); 2011;  
DOI: <http://dx.doi.org/10.4229/26thEUPVSEC2011-3DV.2.13>
- S. Puttnins, S. Jander, K. Pelz, S. Heinker, **F. Daume**, A. Rahm, A. Braun, M. Grundmann;  
*The Influence of Front Contact and Buffer Layer Properties on CIGSe Solar Cell Breakdown Characteristics*;  
Proceedings of the 26<sup>th</sup> EU-PVSEC (Hamburg); 2011;  
DOI: <http://dx.doi.org/10.4229/26thEUPVSEC2011-3CO.4.6>

- S. Puttnins, M. Purfürst, M. Hartung, H.K. Lee, **F. Daume**, L. Hartmann, A. Rahm, A. Braun, M. Grundmann;  
*The influence of sodium on CIGSe solar cell breakdown characteristics*;  
Proceedings of the 27<sup>th</sup> EU-PVSEC (Frankfurt); 2012;  
DOI: <http://dx.doi.org/10.4229/27thEUPVSEC2012-3CO.2.6>
- J. Cesar, S. Puttnins, **F. Daume**, A. Braun, A. Rahm;  
*Temperature-Dependent IV and EQE measurements on CIGSe solar cells with varying sodium content*;  
Proceedings of the 27<sup>th</sup> EU-PVSEC (Frankfurt); 2012;  
DOI: <http://dx.doi.org/10.4229/27thEUPVSEC2012-3CV.1.31>
- **F. Daume**, A. Rahm, A. Braun, M. Grundmann;  
*Sodium in the Degradation Process of Cu(In,Ga)Se<sub>2</sub> Solar Cells*;  
Proceedings of the 28<sup>th</sup> EU-PVSEC (Paris); 2013;  
DOI: <http://dx.doi.org/10.4229/28thEUPVSEC2013-3BO.7.3>
- S. Puttnins, H. Kempa, S. Englisch, R. Karsthof, **F. Daume**, A. Rahm, A. Braun, M. Grundmann;  
*Voltage Dependent Photocurrent in Low-Temperature Deposited CIGSe Solar Cells*;  
Proceedings of the 28<sup>th</sup> EU-PVSEC (Paris); 2013;  
DOI: <http://dx.doi.org/10.4229/28thEUPVSEC2013-3BV.6.49>
- S. Puttnins, S. Jander, A. Wehrmann, G. Benndorf, M. Stölzel, A. Müller, H. von Wenckstern, **F. Daume**, A. Rahm, M. Grundmann;  
*Breakdown characteristics of flexible Cu(In,Ga)Se<sub>2</sub> solar cells*;  
Solar Energy Materials & Solar Cells; 2013;  
DOI: <http://dx.doi.org/10.1016/j.solmat.2013.09.031>
- S. Puttnins, S. Levenco, K. Schwarzburg, G. Benndorf, **F. Daume**, A. Rahm, A. Braun, M. Grundmann, T. Unold;  
*Effect of Sodium on Material and Device Quality in Low Temperature Deposited Cu(In,Ga)Se<sub>2</sub>*;  
Solar Energy Materials & Solar Cells; 2013;  
DOI: <http://dx.doi.org/10.1016/j.solmat.2013.08.029>
- **F. Daume**, S. Puttnins, C. Scheit, H. Zachmann, A. Rahm, A. Braun, M. Grundmann;  
*Damp heat treatment of Cu(In,Ga)Se<sub>2</sub> solar cells with different sodium content*;  
Materials; 2013;  
DOI: <http://dx.doi.org/10.3390/ma6125478>

- S. Puttnins, M.S. Hammer, J. Neerken, I. Riedel, **F. Daume**, A. Rahm, A. Braun, M. Grundmann, T. Unold;  
*Impact of Sodium on the Device Characteristics of Low Temperature-Deposited Cu(In,Ga)Se<sub>2</sub>-Solar Cells*;  
Thin Solid Films; 2014;  
DOI: <http://dx.doi.org/10.1016/j.tsf.2014.07.048>
- M. Theelen, N. Barreau, **F. Daume**, H. Steijvers, V. Hans, A. Liakopoulou, Z. Vroon, M. Zeman;  
*Accelerated Performance Degradation of CIGS Solar Cell Determined by In-situ Monitoring*;  
Proceedings of the SPIE Optics + Photonics Conference (San Diego); 2014;  
DOI: <http://dx.doi.org/10.1117/12.2059951>
- C.A. Kaufmann, D. Greiner, S. Harndt, R. Klenk, S. Brunken, R. Schlatmann, M. Nichterwitz, H.W. Schock, T. Unold, K. Zajac, S. Brunner, **F. Daume**, C. Scheit, S. Puttnins, A. Braun, A. Rahm, R. Wuerz, F. Kessler, M. Günthner, M. Pscherer, S. Ihlow, G. Motz, H. Morgner, R.G. Schmidt, A. Lambrecht, J.T. Grundmann, P. Spietz, P. Schülke;  
*Flexible Cu(In,Ga)Se<sub>2</sub> Thin Film Solar Cells for Space Applications – Recent Results from a German Joint Project (PIPV2)*;  
Proceedings of the 29<sup>th</sup> EU-PVSEC (Amsterdam); 2014;  
DOI: <http://dx.doi.org/10.4229/EUPVSEC20142014-3AO.5.4>
- M. Theelen, A. Liakopoulou, V. Hans, **F. Daume**, H. Steijvers, N. Barreau, Z. Vroon, M. Zeman;  
*Determination of the Temperature Dependency of the IV Characteristics of CIGS Solar Cells*;  
Manuscript in preparation.
- M. Theelen, **F. Daume**;  
*Stability of Cu(In,Ga)Se<sub>2</sub> Solar Cells: A Literature Review*;  
Manuscript in preparation.

## B.2 Posters (only own)

- F. Daume, S. Puttnins, H. Zachmann, A. Rahm, M. Grundmann;  
*Influence of Damp and Heat on Roll-Over Effect in Cu(In,Ga)Se<sub>2</sub> Solar Cells*;  
E-MRS Spring Meeting(Strasbourg); 2010
- F. Daume, C. Scheit, S. Puttnins, A. Rahm, M. Grundmann;  
*Series resistance mapping of Cu(In,Ga)Se<sub>2</sub> solar cells by voltage dependent electroluminescence*;  
DPG Frühjahrstagung (Dresden); 2011
- F. Daume, S. Puttnins, H. Zachmann, A. Rahm, M. Grundmann;  
*Damp heat treatment of Cu(In,Ga)Se<sub>2</sub> solar cells with different sodium content*;  
E-MRS Spring Meeting (Nice); 2011
- F. Daume, C. Scheit, S. Puttnins, A. Rahm, M. Grundmann;  
*Application of series resistance imaging techniques to Cu(In,Ga)Se<sub>2</sub> solar cells*;  
26<sup>th</sup> EU-PVSEC (Hamburg); 2011
- F. Daume, S. Puttnins, C. Scheit, H. Zachmann, A. Rahm, A. Braun,  
M. Grundmann;  
*Damp heat treatment of Cu(In,Ga)Se<sub>2</sub> solar cells with different sodium content*;  
BuildMoNa Symposium (Leipzig); 2012
- F. Daume, S. Puttnins, A. Rahm, A. Braun M. Grundmann;  
*Influence of Na on flexible Cu(In,Ga)Se<sub>2</sub> solar cells under damp heat treatment*;  
E-MRS Spring Meeting (Strasbourg); 2012
- F. Daume, A. Rahm, M. Grundmann;  
*Sodium in the Degradation Process of Cu(In,Ga)Se<sub>2</sub> Solar Cells*;  
BuildMoNa Symposium (Leipzig); 2013
- F. Daume, A. Rahm, S. Puttnins, A. Braun, M. Grundmann;  
*Sodium in the Degradation Process of Cu(In,Ga)Se<sub>2</sub> Solar Cells*;  
MRS Spring Meeting (San Francisco); 2013
- F. Daume, M. Theelen, H. Steijvers, L. Hartmann, A. Rahm, A. Braun,  
M. Grundmann;  
*Damp heat degradation rates of flexible Cu(In,Ga)Se<sub>2</sub> solar cells*;  
BuildMoNa Symposium (Leipzig); 2014

### B.3 Talks (only own)

- F. Daume, S. Puttnins, H. Zachmann, A. Rahm, M. Grundmann;  
*Influence of sodium on the electrical properties of flexible CIGSe solar cells*;  
DPG Frühjahrstagung (Regensburg); 2010
- F. Daume, A. Rahm, M. Grundmann;  
*Application of series resistance imaging techniques to Cu(In,Ga)Se<sub>2</sub> solar cells*;  
DPG Frühjahrstagung (Berlin); 2012
- F. Daume, A. Rahm, A. Braun;  
*Sodium in Cu(In,Ga)Se<sub>2</sub> solar cells: beneficial influences & damp heat stability*;  
3<sup>rd</sup> International Workshop on CIGS Solar Cell Technology (Berlin); 2012
- F. Daume, S. Puttnins, A. Rahm, A. Braun M. Grundmann;  
*The Influence of Sodium on the Long-term Stability of Cu(In,Ga)Se<sub>2</sub> Solar Cells*;  
BuildMoNa Workshop (Burgstädt); 2012
- F. Daume, A. Rahm, M. Grundmann;  
*Admittance Spectroscopy Cu(In,Ga)Se<sub>2</sub> Solar Cells with respect to Na content*;  
DPG Frühjahrstagung (Regensburg); 2013
- F. Daume, A. Rahm, A. Braun, M. Grundmann;  
*Sodium in the Degradation Process of Cu(In,Ga)Se<sub>2</sub> Solar Cells*;  
28<sup>th</sup> EU-PVSEC (Paris); 2013
- F. Daume;  
*Flexible CIGS: Research & Production*;  
5<sup>th</sup> International Workshop on CIGS Solar Cell Technology (Berlin); 2014





## Bibliography

- [1] Peter Würfel. *Physik der Solarzellen*. Spektrum Akademischer Verlag, 2<sup>nd</sup> edition, 2000.
- [2] Marius Grundmann. *The Physics of Semiconductors: An Introduction Including Devices and Nanophysics*. Springer, 2006.
- [3] M. Burgelman, P. Nollet, and S. Degraeve. Modelling polycrystalline semiconductor solar cells. *Thin Solid Films*, 361–362:527–532, 2000.
- [4] D. M. Chapin, C. S. Fuller, and G. L. Pearson. A New Silicon pn Junction Photocell for Converting Solar Radiation into Electrical Power. *Journal of Applied Physics*, 25(5):676–677, 1954.
- [5] PHOTON Publishing GmbH, 2011.
- [6] Jef Poortmans and Vladimir Arkhipov, editors. *Thin Film Solar Cells - Fabrication, Characterization and Applications*. Wiley, 2006.
- [7] Brian O'Regan and Michael Grätzel. A low-cost, high-efficiency solar cell based on dye-sensitized colloidal TiO<sub>2</sub> films. *Nature*, 353:737–740, 1991.
- [8] Martin A. Green, Keith Emery, Yoshihiro Hishikawa, Wilhelm Warta, and Ewan D. Dunlop. Solar cell efficiency tables (version 44). *Progress in Photovoltaics: Research and Applications*, 22(7):701–710, 2014.
- [9] William Shockley and Hans J. Queisser. Detailed Balance Limit of Efficiency of p–n Junction Solar Cells. *Journal of Applied Physics*, 32(3):510–519, 1961.
- [10] Zentrum für Sonnenenergie und Wasserstoff Forschung Baden Württemberg (ZSW). ZSW holt Weltrekord zurück nach Stuttgart – Neuer Dünnschichtsolar-Bestwert mit 21,7 Prozent Wirkungsgrad. Press Release, September 2014.
- [11] Martin A. Green, Keith Emery, Yoshihiro Hishikawa, Wilhelm Warta, and Ewan D. Dunlop. Solar cell efficiency tables (version 42). *Progress in Photovoltaics: Research and Applications*, 21(5):827–837, 2013.

- [12] Roland Scheer and Hans-Werner Schock. *Chalcogenide Photovoltaics: Physics, Technologies, and Thin Film Devices*. Wiley–VCH, 2011.
- [13] Felix Daume. Die elektrische Charakterisierung des Absorbers Cu(In,Ga)Se<sub>2</sub> von flexiblen Solarzellen (und Korrelation mit Materialparametern), 2009. Diplomarbeit, Universität Leipzig.
- [14] Yoshihiro Hamakawa. *Thin–Film Solar Cells*. Springer, 2003.
- [15] Karsten Otte. *Einfluss niederenergetischer Ionenstrahlen auf die Defektchemie von Cu(In,Ga)(Se,S)<sub>2</sub>*. PhD thesis, Universität Leipzig, 2002.
- [16] R. Herberholz, U. Rau, H. W. Schock, T. Haalboom, T. Gödecke, F. Ernst, C. Beilharz, K. W. Benz, and D. Cahen. Phase segregation, Cu migration and junction formation in Cu(In,Ga)Se<sub>2</sub>. *The European Physical Journal Applied Physics*, 6(2):131–139, 1999.
- [17] U. Rau and H.W. Schock. Electronic properties of CIGS heterojunction solar cells – recent achievements, current understanding, and future challenges. *Applied Physics A: Materials Science & Processing*, 69(2):131–147, 1999.
- [18] P. Migliorato, J.L. Shay, H.M. Kasper, and S. Wagner. Analysis of the electrical and luminescent properties of CIS. *Journal of Applied Physics*, 46(4):1777–1782, 1975.
- [19] Noufi, Axton, Herrington, and Deb. Electronic properties versus composition of thin films of CuInSe<sub>2</sub>. *Applied Physics Letters*, 45:668–670, 1984.
- [20] S. B. Zhang, Su-Huai Wei, Alex Zunger, and H. Katayama-Yoshida. Defect physics of the CIS chalcopyrite semiconductor. *Physical Review B*, 57(16):9642–9656, 1998.
- [21] L. L. Kazmerski. Atomic Imaging, Atomic Processing and Nanocharacterization of CIS Using Proximal Probe Techniques. *Japanese Journal of Applied Physics*, 32:25–34, 1993.
- [22] M. Altosaar, K. Ernits, J. Krustok, T. Varema, J. Raudoja, and E. Mellikov. Comparison of CdS films deposited from chemical baths containing different doping impurities. *Thin Solid Films*, 480–481:147–150, 2005.
- [23] Yasunori Okano, Tokio Nakada, and Akio Kunioka. XPS analysis of CdS/CuInSe<sub>2</sub> heterojunctions. *Solar Energy Materials & Solar Cells*, 50(1–4):105–110, 1998.
- [24] A. Niemegeers, M. Burgelman, R. Herberholz, U. Rau, D. Hariskos, and H.-W. Schock. Model for electronic transport in CIGS solar cells. *Progress in Photovoltaics: Research and Applications*, 6(6):407–421, 1998.

- 
- [25] Susanne Siebentritt. Wide gap chalcopyrites: material properties and solar cells. *Thin Solid Films*, 403–404:1–8, 2002.
- [26] Wei and Zunger. Band offsets and optical bowings of chalcopyrites and Zn-based II–VI alloys. *Journal of Applied Physics*, 78:3846, 1995.
- [27] G. Hanna, A. Jasenek, U. Rau, and H. W. Schock. Influence of the Ga-content on the bulk defect densities of CIGS. *Thin Solid Films*, 387(1–2):71–73, 2001.
- [28] J. E. Phillips and W. N. Shafarman. Analysis of Cu(In,Ga)Se<sub>2</sub> solar cells: Why performance decreases with increasing Ga content. *AIP Conference Proceedings*, 462(1):120–125, 1999.
- [29] Landolt-Börnstein, editor. *Phase Equilibria, Crystallographic and Thermodynamic Data of Binary Alloys*, volume Group IV, Volume 5. Springer, 2007.
- [30] W.K. Metzger, I.L. Repins, M. Romero, P. Dippo, M. Contreras, R. Noufi, and D. Levi. Recombination kinetics and stability in polycrystalline Cu(In,Ga)Se<sub>2</sub> solar cells. *Thin Solid Films*, 517:2360–2364, 2009.
- [31] M. Nishitani, T. Negami, N. Kohara, and T. Wada. Analysis of transient photocurrents in Cu(In,Ga)Se<sub>2</sub> thin film solar cells. *Journal of Applied Physics*, 82:3572–3575, 1997.
- [32] J. Hedström, H. Ohlsen, M. Bodegard, A. Kylner, L. Stolt, D. Hariskos, M. Ruckh, and H.-W. Schock. ZnO/CdS/Cu(In,Ga)Se<sub>2</sub> Thin Film Solar Cells With Improved Performance. In *Proc. of the 23<sup>rd</sup> IEEE Photovoltaic Specialist Conference*, 1993.
- [33] J.E. Granata, J.R. Sites, S. Asher, and R.J. Matson. Quantitative Incorporation of Sodium in CuInSe<sub>2</sub> and Cu(InGa)Se<sub>2</sub> Photovoltaic Devices. In *Proc. of the 26<sup>th</sup> IEEE Photovoltaic Specialist Conference*, 1997.
- [34] Marika Bodegard, Karin Granath, Lars Stolt, and Angus Rockett. The behaviour of Na implanted into Mo thin films during annealing. *Solar Energy Materials & Solar Cells*, 58(2):199–208, 1999.
- [35] P. Bommersbach, L. Arzel, M. Tomassini, E. Gautron, C. Leyder, M. Urien, D. Dupuy, and N. Barreau. Influence of Mo back contact porosity on co-evaporated Cu(In,Ga)Se<sub>2</sub> thin film properties and related solar cell. *Progress in Photovoltaics: Research and Applications*, 21(3):332–343, 2013.
- [36] Lorelle M. Mansfield, Ingrid L. Repins, Stephen Glynn, Joel W. Pankow, Matthew R. Young, Clay DeHart, Rajalakshmi Sundaramoorthy, Carolyn L. Beall, Bobby To, Michael D. Carducci, and David M. Honecker. Sodium-Doped Molybdenum Targets for Controllable Sodium Incorporation in CIGS Solar Cells. In *Proc. of the 37<sup>th</sup> IEEE Photovoltaic Specialists Conference*, 2011.

- [37] P. Blösch, S. Nishiwaki, L. Kranz, C.M. Fella, F. Pianezzi, T. Jäger, C. Adelhelm, E. Franzke, S. Buecheler, and A.N. Tiwari. Sodium-doped molybdenum back contact designs for Cu(In,Ga)Se<sub>2</sub> solar cells. *Solar Energy Materials & Solar Cells*, 124:10–16, 2014.
- [38] Marika Bodegard, Karin Granath, and Lars Stolt. Growth of Cu(In,Ga)Se<sub>2</sub> thin films by coevaporation using alkaline precursors. *Thin Solid Films*, 361–362:9–16, 2000.
- [39] D. Rudmann, G. Bilger, M. Kaelin, F. J. Haug, H. Zogg, and A. N. Tiwari. Effects of NaF coevaporation on structural properties of Cu(In,Ga)Se<sub>2</sub> thin films. *Thin Solid Films*, 431–432:37–40, 2003.
- [40] D. Rudmann, A. F. da Cunha, M. Kaelin, F. Kurdesau, H. Zogg, A. N. Tiwari, and G. Bilger. Efficiency enhancement of Cu(In,Ga)Se<sub>2</sub> solar cells due to post-deposition Na incorporation. *Applied Physics Letters*, 84(7):1129–1131, 2004.
- [41] V. Probst, J. Rimmasch, W. Riedl, W. Stetter, J. Holz, H. Harms, F. Karg, and H.W. Schock. The Impact of Controlled Sodium Incorporation on Rapid Thermal Processed Cu(InGa)Se<sub>2</sub>-Thin Films and Devices. In *Proc. of the 24<sup>th</sup> IEEE Photovoltaic Specialist Conference, 1<sup>st</sup> World Conference*, 1994.
- [42] P.S. Vasekar and N. G. Dhere. Effect of sodium addition on Cu-deficient CuIn<sub>1-x</sub>Ga<sub>x</sub>Se<sub>2</sub> thin film solar cells. *Solar Energy Materials & Solar Cells*, 2008.
- [43] R. Herberholz, H.W. Schock, U. Rau, J.H. Werner, T. Haalboom, T. G6decke, F. Ernst, C. Beilharz, K.W. Benz, and D. Cahen. New Aspects of Phase Segregation and Junction Formation in CuInSe<sub>2</sub>. In *Proc. of the 26<sup>th</sup> IEEE Photovoltaic Specialist Conference*, 1997.
- [44] Raquel Caballero, Christian A. Kaufmann, Tobias Eisenbarth, Thomas Unold, Susan Schorr, Raik Hesse, Reiner Klenk, and Hans-Werner Schock. The effect of NaF precursors on low temperature growth of CIGS thin film solar cells on polyimide substrates. *physica status solidi (a)*, 206(5):1049–1053, 2009.
- [45] P. T. Erslev, J. W. Lee, W. N. Shafarman, and J. David Cohen. The Influence of Na on Metastable Defect Kinetics in CIGS Materials. *Thin Solid Films*, 517:2277–2281, 2009.
- [46] David W. Nilas, Mowafak Al-Jassim, and Kannan Ramanathan. Direct observation of Na and O impurities at grain surfaces of CuInSe<sub>2</sub> thin film. *Journal of Vacuum Science & Technology A*, 17(1):291–296, 1999.

- 
- [47] V. Lyahovitskaya, Y. Feldman, K. Gartsman, H. Cohen, C. Cytermann, and David Cahen. Na effects on CuInSe<sub>2</sub>: Distinguishing bulk from surface phenomena. *Journal of Applied Physics*, 91(7):4205–4212, 2002.
- [48] C. Heske, D. Eich, R. Fink, E. Umbach, S. Kakar, T. van Buuren, C. Bostedt, L. J. Terminello, M. M. Grush, T. A. Callcott, F. J. Himpsel, D. L. Ederer, R. C. C. Perera, W. Riedl, and F. Karg. Localization of Na impurities at the buried CdS/Cu(In, Ga)Se<sub>2</sub> heterojunction. *Applied Physics Letters*, 75(14):2082–2084, 1999.
- [49] Su-Huai Wei, S. B. Zhang, and Alex Zunger. Effects of Na on the electrical and structural properties of CuInSe<sub>2</sub>. *Journal of Applied Physics*, 85(10):7214–7218, 1999.
- [50] D. Braunger, D. Hariskos, and H.-W. Schock. Na-Related Stability Issues in Highly Efficient Polycrystalline Cu(In,Ga)Se<sub>2</sub> Solar Cells. In *Proc. of the 2<sup>nd</sup> World Conference and Exhibition on Photovoltaic Solar Energy Conversion*, volume 1, pages 511–514, 1998.
- [51] David Cahen and Rommel Noufi. Defect chemical explanation for the effect of air anneal on CdS/CuInSe<sub>2</sub> solar cell performance. *Applied Physics Letters*, 54(6):558–560, 1989.
- [52] R. Scheer, I. Luck, M. Kanis, R. Kurps, and D. Krüger. Effect of sodium and oxygen doping on the conductivity of CuInS<sub>2</sub> thin films. *Thin Solid Films*, 361–362:468–472, 2000.
- [53] R. Wuerz, A. Eicke, F. Kessler, S. Paetel, S. Efimenko, and C. Schlegel. CIGS thin-film solar cells and modules on enamelled steel substrates. *Solar Energy Materials & Solar Cells*, 100(0):132–137, 2012. Photovoltaics, Solar Energy Materials, and Technologies: Cancun 2010.
- [54] Adrian Chirilă, Patrick Reinhard, Fabian Pianezzi, Patrick Bloesch, Alexander R. Uhl, Carolin Fella, Lukas Kranz, Debora Keller, Christina Gretener, Harald Hagerdorfer, Dominik Jaeger, Rolf Erni, Shiro Nishiwaki, Stephan Buecheler, and Ayodhya N. Tiwari. Potassium-induced surface modification of Cu(In,Ga)Se<sub>2</sub> thin films for high-efficiency solar cells. *Nature Materials*, 12:1107–1111, 2013.
- [55] Philip Jackson, Dimitrios Hariskos, Roland Wuerz, Wiltraud Wischmann, and Michael Powalla. Compositional investigation of potassium doped Cu(In,Ga)Se<sub>2</sub> solar cells with efficiencies up to 20.8%. *physica status solidi (RRL)–Rapid Research Letters*, 8(3):219–222, 2014.
- [56] P. Reinhard, S. Buecheler, and A.N. Tiwari. Technological status of Cu(In,Ga)(Se,S)<sub>2</sub>-based photovoltaics. *Solar Energy Materials & Solar Cells*, 119(0):287–290, 2013.

- [57] Mirjam Theelen and Felix Daume. Stability of Cu(In,Ga)Se<sub>2</sub> Solar Cells: A Literature Review. *Manuscript in preparation*.
- [58] Dennis J. Coyle. Life prediction for CIGS solar modules part 1: modeling moisture ingress and degradation. *Progress in Photovoltaics*, 21(2):156–172, 2011.
- [59] George Makrides, Bastian Zinsser, Markus Schubert, and George E. Georghiou. Performance loss rate of twelve photovoltaic technologies under field conditions using statistical techniques. *Solar Energy*, 103(0):28–42, 2014.
- [60] Neelkanth G. Dhere, Ashwani Kaul, and Shirish A. Pethe. Long-term performance analysis of CIGS thin film PV modules. In *Proc. SPIE*, volume 8112, pages 81120R–81120R–6, 2011.
- [61] HD Musikowski and AZ Styczynski. Analysis of the operational behavior and long-term performance of a CIS PV system. In *Proc. of the 25<sup>th</sup> European Photovoltaic Solar Energy Conference*, pages 3942–3946, 2010.
- [62] J.A. del Cueto, S. Rummel, B. Kroposki, C. Osterwald, and A. Anderberg. Stability of CIS/CIGS modules at the outdoor test facility over two decades. In *Proc. of the 33<sup>rd</sup> IEEE Photovoltaic Specialist Conference*, 2008.
- [63] D.C. Jordan and S.R. Kurtz. Thin-film reliability trends toward improved stability. In *Proc. of the 37<sup>th</sup> IEEE Photovoltaic Specialists Conference*, pages 000827–000832, 2011.
- [64] Daryl R Myers, Ibrahim Reda, Stephen Wilcox, and Afshin Andreas. Optical radiation measurements for photovoltaic applications: instrumentation uncertainty and performance. In *Proc. SPIE*, volume 5520, pages 142–153, 2004.
- [65] Shigeru Niki, Miguel Contreras, Ingrid Repins, Michael Powalla, Katsumi Kushiya, Shogo Ishizuka, and Koji Matsubara. CIGS absorbers and processes. *Progress in Photovoltaics: Research and Applications*, 18:453–466, 2010.
- [66] J.H. Ermer, J. Hummel, C.L. Jensen, C.V. Fredric, D. Pier, D. Tarrant, and K. Mitchel. Advances in Large Area CuInSe<sub>2</sub> Thin Film Modules. In *Proc. of the 21<sup>st</sup> IEEE Photovoltaic Specialist Conference*, 1990.
- [67] Dale E Tarrant and Robert Rowell Gay. *Process R&D for CIS-based thin-film PV*. National Renewable Energy Laboratory, 2006.
- [68] Katsumi Kushiya, Satoru Kuriyagawa, Kenichi Tazawa, Tadashi Okazawa, and Masayuki Tsunoda. Improved stability of CIGS-based thin-film PV modules. In *Proc. of the 4<sup>th</sup> WCPSEC*, 2006.

- 
- [69] C. Radue and E.E.van Dyk. Degradation analysis of thin film photovoltaic modules. *Physica B*, 404:4449–4451, 2009.
- [70] D. C. Jordan and S. R. Kurtz. Photovoltaic Degradation Rates – an Analytical Review. *Progress in Photovoltaics: Research and Applications*, 21(1):12–29, 2013.
- [71] International Electrotechnical Commission (IEC) 61646 ed. 2.
- [72] C. R. Osterwald and T. J. McMahon. History of Accelerated and Qualification Testing of Terrestrial Photovoltaic Modules: A Literature Review. *Progress in Photovoltaics: Research and Applications*, 17:11–33, 2009.
- [73] Thomas Carlsson and Andy Brinkman. Identification of degradation mechanisms in field-tested CdTe modules. *Progress in Photovoltaics: Research and Applications*, 14(3):213–224, 2006.
- [74] T. J. McMahon. Accelerated testing and failure of thin-film PV modules. *Progress in Photovoltaics: Research and Applications*, 12(2-3):235–248, 2004.
- [75] F. J. Pern and R. Noufi. Stability of CIGS solar cells and component materials evaluated by a step-stress accelerated degradation test method. In *Proc. SPIE*, volume 8472, pages 84720J–84720J–14, 2012.
- [76] Mirjam Theelen, Nicolas Barreau, Felix Daume, Henk Steijvers, Vincent Hans, Aikaterini Liakopoulou, Zeger Vroon, and Miro Zeman. Accelerated performance degradation of CIGS solar cell determined by in-situ monitoring. In *Proc. SPIE*, volume 9179, pages 91790I–91790I–11, 2014.
- [77] John Pern and Rommel Noufi. An investigation of stability issues of ZnO and Mo on glass substrates for CIGS solar cells upon accelerated weathering and damp heat exposures. In *Proc. of the DOE SETP Review Meeting*, volume 4, pages 17–19, 2007.
- [78] F.J. Pern, B. To, C. DeHart, X. Li, and S.H. Glick. Degradation of ZnO Window Layer for CIGS by Damp-Heat Exposure. In *Proc. of the SPIE PV Reliability Symposium*, 2008.
- [79] Johan Wennerberg, John Kessler, and Lars Stolt. Degradation mechanisms of Cu(In,Ga)Se<sub>2</sub>-based thin film PV modules. In *Proc. of the 16<sup>th</sup> European Photovoltaic Solar Energy Conference*, pages 309–312, 2000.
- [80] Mirjam Theelen, Krista Polman, Mathieu Tomassini, Nicolas Barreau, Henk Steijvers, Jurgen van Berkum, Zeger Vroon, and Miro Zeman. Influence of deposition pressure and selenisation on damp heat degradation of the Cu(In,Ga)Se<sub>2</sub> back contact molybdenum. *Surface and Coatings Technology*, 252(0):157–167, 2014.

- [81] Dieter Schmid, Martin Ruckh, and Hans Werner Schock. A comprehensive characterization of the interfaces in Mo/CIS/CdS/ZnO solar cell structures. *Solar Energy Materials & Solar Cells*, 41–42:281–294, 1996.
- [82] M. Theelen, S. Harel, M. Verschuren, M. Tomassini, A. Hovestad, N. Barreau, J. van Berkum, Z. Vroon, and M. Zeman. Degradation mechanisms of the molybdenum back contact for CIGS solar cells. *Submitted to Applied Surface Science*.
- [83] J.-F. Guillemoles, L. Kronik, D. Cahen, U. Rau, A. Jasenek, and H.-W. Schock. Stability Issues of CIGS Based Solar Cells. *Journal of Physical Chemistry B*, 104(20):4849–4862, 2000.
- [84] J.F Guillemoles. The puzzle of Cu(In,Ga)Se<sub>2</sub> (CIGS) solar cells stability. *Thin Solid Films*, 403-404(0):405–409, 2002. Proceedings of Symposium P on Thin Film Materials for Photovoltaics.
- [85] J. Wennerberg, J. Kessler, M. Bodegard, and L. Stolt. Damp heat testing of high performance CIGS thin film solar cells. In *Proc. of the 2<sup>nd</sup> world conference on photovoltaic energy conversion*, 1998.
- [86] Johan Wennerberg, John Kessler, and Lars Stolt. Cu(In,Ga)Se<sub>2</sub>-based thin-film photovoltaic modules optimized for long-term performance. *Solar Energy Materials & Solar Cells*, 75:47–55, 2003.
- [87] M. Schmidt, D. Braunger, R. Schaffler, H. W. Schock, and U. Rau. Influence of damp heat on the electrical properties of Cu(In,Ga)Se<sub>2</sub> solar cells. *Thin Solid Films*, 361–362:283–287, 2000.
- [88] C. Deibel, V. Dyakonov, and J. Parisi. Defect Spectroscopy on Damp-Heat Treated ZnO/CdS/Cu(In,Ga)(S,Se)<sub>2</sub>/Mo Heterojunction Solar Cells. *Zeitschrift für Naturforschung*, 58a:691–702, 2003.
- [89] F.J. Pern, B. Egaas, B. To, C.-S. Jiang, J.V. Li, S. Glynn, and C. DeHart. A study on the humidity susceptibility of thin-film CIGS absorber. In *Proc. of the 34<sup>th</sup> IEEE Photovoltaic Specialists Conference*, pages 000287–000292, 2009.
- [90] R. Würz, A. Meeder, D. Fuertes Marrón, Th. Schedel-Niedrig, and K. Lips. An Electron Paramagnetic Resonance and Photoelectron Spectroscopy Study on the Native Oxidation of CuGaSe<sub>2</sub>. In *MRS Proceedings*, volume 865, 2005.
- [91] C. Heske, U. Groh, L. Weinhardt, O. Fuchs, B. Holder, E. Umbach, C. Bostedt, L. J. Terminello, S. Zweigart, T. P. Niesen, and F. Karg. Damp-heat induced sulfate formation in Cu(In,Ga)(S,Se)<sub>2</sub> based thin film solar cells. *Applied Physics Letters*, 81:4550, 2002.



- 
- [92] J. Malmström, J. Wennerberg, and L. Stolt. A study of the influence of the Ga content on the long-term stability of Cu(In,Ga)Se<sub>2</sub> thin film solar cells. *Thin Solid Films*, 431–432:436–442, 2003.
- [93] Felix Daume, Stefan Puttnins, Christian Scheit, Hendrik Zachmann, Andreas Rahm, Alexander Braun, and Marius Grundmann. Damp Heat Treatment of Cu(In,Ga)Se<sub>2</sub> Solar Cells with Different Sodium Content. *Materials*, 6(12):5478–5489, 2013.
- [94] Dieter Greiner. *Ursache der Leitfähigkeitsabnahme nach künstlicher Alterung in feuchter Wärme bei hochdotierten Zinkoxid-Schichten für die Dünnschichtfotovoltaik*. PhD thesis, Freie Universität Berlin, 2010.
- [95] Mirjam Theelen, Supratik Dasgupta, Zeger Vroon, Bas Kniknie, Nicolas Barreau, Jurgen van Berkum, and Miro Zeman. Influence of the atmospheric species water, oxygen, nitrogen and carbon dioxide on the degradation of aluminum doped zinc oxide layers. *Thin Solid Films*, 565(0):149–154, 2014.
- [96] Tadatsugu Minami, Toshihiro Miyata, Yuusuke Ohtani, and Takeshi Kuboi. Effect of thickness on the stability of transparent conducting impurity-doped ZnO thin films in a high humidity environment. *physica status solidi (RRL)–Rapid Research Letters*, 1(1):R31–R33, 2007.
- [97] T. Tohsophon, J. Hupkes, S. Calnan, W. Reetz, B. Rech, W. Beyer, and N. Sirikulrat. Damp heat stability and annealing behavior of aluminum doped zinc oxide films prepared by magnetron sputtering. *Thin Solid Films*, 511–512:673–677, 2006.
- [98] D. Greiner, S.E. Gledhill, Ch. Köble, J. Krammer, and R. Klenk. Damp heat stability of Al-doped zinc oxide films on smooth and rough substrates. *Thin Solid Films*, 520(4):1285–1290, 2011.
- [99] Jiwen Xu, Zupei Yang, Hua Wang, Huarui Xu, and Xiaowen Zhang. Effect of growth temperature and coating cycles on structural, electrical, optical properties and stability of ITO films deposited by magnetron sputtering. *Materials Science in Semiconductor Processing*, 21(0):104–110, 2014.
- [100] Gao Mei-Zhen, Xin Ke, and Wolfgang R. Fahrner. Study of the morphological change of amorphous ITO films after temperature–humidity treatment. *Journal of Non-Crystalline Solids*, 355:2682–2687, 2009.
- [101] Kajsa Sols. Simulation of solar cell losses depending on cell design. Master’s thesis, Chalmers University of Technology Göteborg, Sweden, 2010.
- [102] Johan Wennerberg, John Kessler, and Lars Stolt. Design of grided Cu(In,Ga)Se<sub>2</sub> thin-film PV modules. *Solar Energy Materials & Solar Cells*, 67:59–65, 2001.

- [103] J. S. Britt, E. Kanto, S. Lundberg, and M. E. Beck. CIGS device stability on flexible substrates. In *Proc. of the IEEE Photovoltaic Energy Conversion, 4<sup>th</sup> World Conference*, volume 1, 2006.
- [104] Paul R. Elowe, Matthew A. Stempki, Steve J. Rozeveld, and Marty W. DeGroot. Development of Direct Cell Inorganic Barrier Film Technology Providing Exceptional Device Stability for CIGS Solar Cells. *Chemistry of Materials*, 23:3915–3920, 2011.
- [105] F.J. Pern, L. Mansfield, C. DeHart, S.H. Glick, F. Yan, and R. Noufi. Thickness effect of Al-doped ZnO window layer on damp-heat stability of CuInGaSe<sub>2</sub> solar cells. In *Proc. of the 37<sup>th</sup> IEEE Photovoltaic Specialists Conference*, pages 002798–002803, 2011.
- [106] T. Walter, R. Herberholz, C. Muller, and H. W. Schock. Determination of defect distributions from admittance measurements and application to CIGS-based heterojunctions. *Journal of Applied Physics*, 80(8):4411–4420, 1996.
- [107] R. Herberholz, M. Igalson, and H.-W. Schock. Distinction between bulk and interface in CuInSe<sub>2</sub> / CdS / ZnO by space charge spectroscopy. *Journal of Applied Physics*, 83:318, 1998.
- [108] C. Deibel, V. Dyakonov, and J. Parisi. Spectroscopy of electronic defect states in Cu(In,Ga)(S,Se)<sub>2</sub>-based heterojunctions and Schottky diodes under damp-heat exposure. *Europhysics Letters*, 66(3):399, 2004.
- [109] M. Igalson, M. Wimbor, and J. Wennerberg. The change of the electronic properties of CIGS devices induced by the damp heat treatment. *Thin Solid Films*, 403–404:320–324, 2002.
- [110] C. Deibel, V. Dyakonov, J. Parisi, J. Palm, S. Zweigart, and F. Karg. Influence of damp heat testing on the electrical characteristics of Cu(In,Ga)(S,Se)<sub>2</sub> solar cells. *Thin Solid Films*, 403–404:325–330, 2002.
- [111] Karsten Otte, Liudmila Makhova, Alexander Braun, and Igor Konovalov. Flexible Cu(In,Ga)Se<sub>2</sub> thin-film solar cells for space application. *Thin Solid Films*, 511–512:613–622, 2006.
- [112] H. Zachmann, S. Puttnins, F. Daume, A. Rahm, and K. Otte. Generation of electrical defects in ion beam assisted deposition of Cu(In,Ga)Se<sub>2</sub> thin film solar cells. *Thin Solid Films*, 519:7317–7320, 2011.
- [113] Hendrik Zachmann. Untersuchung der strukturellen und elektrischen Schichteigenschaften bei der ionenstrahlgestützten Abscheidung von CIGS, 2007.

- 
- [114] Hendrik Zachmann. *Elektrische Defekte bei der Ionenstrahlgestützten Abscheidung von Cu(In,Ga)Se<sub>2</sub>*. PhD thesis, Universität Leipzig, 2011.
- [115] Christian Scheit. *Experimentelle Untersuchungen zur Kontaktierung flexibler Cu(In,Ga)Se<sub>2</sub>-Dünnschichtsolarzellen mittels polymerer Dickschichttechnik*. PhD thesis, Technische Universität Dresden, 2013.
- [116] Daniel Abou-Ras, Thomas Kirchartz, and Uwe Rau. *Advanced Characterization Techniques for Thin Film Solar Cells*. Wiley-VCH, 2011.
- [117] Steven S. Hegedus and William N. Shafarman. Thin-film solar cells: device measurements and analysis. *Progress in Photovoltaics: Research and Applications*, 12(2-3):155–176, 2004.
- [118] Keithley Instruments, Inc., 28775 Aurora Road, Cleveland, Ohio 44139, USA. *Model 2601A/2602A – System SourceMeter Specifications*, 2011.
- [119] Sensovation AG, Markthallenstrasse 5, 78315 Radolfzell, Germany. *Datasheet SensoCam Series*.
- [120] Felix Daume, Christian Scheit, Stefan Puttnins, Andreas Rahm, and Marius Grundmann. Application of series resistance imaging techniques to Cu(In,Ga)Se<sub>2</sub> solar cells. In *Proc. of the 26<sup>th</sup> European Photovoltaic Solar Energy Conference*, 2011.
- [121] David Hinken, Klaus Ramspeck, Karsten Bothe, Bernhard Fischer, and Rolf Brendel. Series resistance imaging of solar cells by voltage dependent electroluminescence. *Applied Physics Letters*, 91(18):182104–3, 2007.
- [122] O. Breitenstein, A. Khanna, Y. Augarten, J. Bauer, J.-M. Wagner, , and K. Iwig. Quantitative evaluation of electroluminescence images of solar cells. *Phys. Status Solidi RRL*, 4(1):7–9, 2010.
- [123] Agilent Technologies, Inc., 5301 Stevens Creek Blvd, Santa Clara CA 95051, USA. *Agilent 4284A Precision LCR Meter – Data Sheet*, 2004.
- [124] U. Rau, D. Braunger, R. Herberholz, H. W. Schock, J.-F. Guillemoles, L. Kronik, and David Cahen. Oxygenation and air-annealing effects on the electronic properties of CIGS films and devices. *Journal of Applied Physics*, 86(1):497–505, 1999.
- [125] Otwin Breitenstein, Wilhelm Warta, and Martin Langenkamp. *Lock-in Thermography: Basics and Use for Evaluating Electronic Devices and Materials*. Springer, 2010.

- [126] Marcel Hartung. Lock-in IR-Thermographie-Messungen an Dünnschichtsolarzellen. Master's thesis, HTWK Leipzig, 2012.
- [127] Sascha Kipping. Aufbau eines Messplatzes zur topografischen Untersuchung von CIGS Solarzellen. Master's thesis, Hochschule Mittweida, 2010.
- [128] Matthias Brandt, Holger von Wenckstern, and Rainer Pickenhain. *Praktikum Halbleiterphysik, Experimentelle Methoden der Halbleiterphysik, A4: Freie Ladungsträger*. Universität Leipzig, 2009.
- [129] Reinhard Noll. *Laser-Induced Breakdown Spectroscopy*. Springer, 2012.
- [130] M. Theelen, M. Tomassini, H. Steijvers, Z. Vroon, N. Barreau, and M. Zeman. In-situ analysis of the degradation of Cu(In, Ga)Se<sub>2</sub> solar cells. In *Proc. of the 39<sup>th</sup> IEEE Photovoltaic Specialists Conference*, pages 2047–2051, 2013.
- [131] M. Theelen, A. Liakopoulou, V. Hans, F. Daume, H. Steijvers, N. Barreau, Z. Vroon, and M. Zeman. Determination of the Temperature Dependency of the IV Characteristics of CIGS Solar Cells. *Manuscript in preparation*.
- [132] David Nečas and Petr Klapetek. Gwyddion: an open-source software for SPM data analysis. *Central European Journal of Physics*, 10(1):181–188, 2012.
- [133] Johan Wennerberg. *Design and Stability of Cu(In,Ga)Se<sub>2</sub> – Based Solar Cell Modules*. PhD thesis, Uppsala University, 2002.
- [134] T. Eisenbarth. *Identifikation von Defekten und Metastabilitäten in CIGS-Dünnschichtsolarzellen*. PhD thesis, Freie Universität Berlin, 2010.
- [135] T. Wada, N. Kohara, S. Nishiwaki, and T. Negami. Characterization of the CIGS/Mo Interface in CIGS Solar Cells. *Thin Solids Films*, 387:118–122, 2001.
- [136] J. Cesar, S. Puttnins, F. Daume, A. Braun, and A. Rahm. Temperature-Dependent IV and EQE Measurements on CIGSe Solar Cells with Varying Sodium Content. In *Proc. of the 27<sup>th</sup> European Photovoltaic Solar Energy Conference and Exhibition*, 2012.
- [137] Felix Daume, Andreas Rahm, Alexander Braun, and Marius Grundmann. Sodium in the Degradation Process of Cu(In,Ga)Se<sub>2</sub> Solar Cells. In *Proc. of the 28<sup>th</sup> European Photovoltaic Solar Energy Conference*, 2013.
- [138] D.J. McClure. Polyimide film as a vacuum coating substrate. *SVC Bulletin*, 2010.
- [139] D. Abou-Ras, D. Mukherji, G. Kostorz, D. Brémaud, M. Kälin, D. Rudmann, M. Döbeli, and A. N. Tiwari. Dependence of the MoSe<sub>2</sub> Formation on the Mo

- Orientation and the Na Concentration for Cu(In,Ga)Se<sub>2</sub> Thin-Film Solar Cells. In *Mater. Res. Soc. Symp. Proc.*, volume 865 F, pages 8.1.1 – 8.1.6, 2005.
- [140] S. Ishizuka, K. Sakurai, A. Yamada, K. Matsubara, H. Shibata, M. Yonemura, S. Nakamura, H. Nakanishi, T. Kojima, and S. Niki. Effects of water vapor introduction during Cu(In<sub>1-x</sub>Ga<sub>x</sub>)Se<sub>2</sub> deposition on thin film properties and solar cell performance. *physica status solidi (a)*, 203(11):2609–2614, 2006.
- [141] Dennis J. Coyle, Holly A. Blaydes, James E. Pickett, Rebecca S. Northey, and James O. Gardner. Degradation Kinetics of CIGS Solar Cells. In *Proc. of the 34<sup>th</sup> IEEE Photovoltaic Specialists Conference*, pages 001943–001947, 2009.
- [142] H. Zachmann, S. Puttnins, F. Daume, A. Rahm, K. Otte, R. Caballero, C.A. Kaufmann, T. Eisenbarth, and H.-W. Schock. Incorporation of Na in low-temperature deposition of CIGS flexible solar cells. In *Mater. Res. Soc. Symp. Proc.*, volume 1210, 2009.
- [143] Karin Granath, Marika Bodegard, and Lars Stolt. The effect of NaF on Cu(In, Ga)Se<sub>2</sub> thin film solar cells. *Solar Energy Materials & Solar Cells*, 60(3):279–293, 2000.
- [144] D. Rudmann, D. Bremaud, H. Zogg, and A. N. Tiwari. Na incorporation into Cu(In,Ga)Se<sub>2</sub> for high-efficiency flexible solar cells on polymer foils. *Journal of Applied Physics*, 97(8):084903, 2005.
- [145] D. Rudmann, D. Bremaud, A.F. da Cunha, G. Bilger, A. Strohm, M. Kaelin, and A.N. Tiwarid H. Zogga. Sodium incorporation strategies for CIGS growth at different temperatures. *Thin Solid Films*, 480–481:55–60, 2005.
- [146] L. Kronik, U. Rau, J. F. Guillemoles, D. Braunger, H.-W.Schock, and D. Cahen. Interface redox engineering of CIGS – based solar cells: Oxygen, Sodium, and chemical bath effects. *Thin Solid Films*, 361–362:353–359, 2000.
- [147] C. Heske, R. Fink, E. Umbach, W. Riedl, and F. Karg. Na-induced effects on the electronic structure and composition of Cu(In,Ga)Se<sub>2</sub> thin-film surfaces. *Applied Physics Letters*, 68(24):3431–3433, 1996.
- [148] Bernhard Weinreich. Elektrolumineszenz: Was kommt ans Licht, was bleibt im Dunkeln? *Sonne, Wind & Wärme*, 10:160–165, 2010.
- [149] Jan Bauer, Otwin Breitenstein, and Jan-Martin Wagner. Lock-in Thermography: A Versatile Tool for Failure Analysis of Solar Cells. *Electronic Device Failure Analysis*, 3:6–12, 2009.

- [150] T. M. H. Tran, B. E. Pieters, M. Schneemann, J. P. Theisen, R. Schäffler, A. Gerber, and U. Rau. Classification of defects in CIGS solar cells and modules using electroluminescence and thermography techniques. In *Proc. of the 27<sup>nd</sup> European Photovoltaic Solar Energy Conference*, 2012.
- [151] Karsten Bothe, David Hinken, Klaus Ramspeck, Bernhard Fischer, and Rolf Brendel. Combined quantitative analysis of electroluminescence images and LBIC mappings. In *Proc. of the 22<sup>nd</sup> European Photovoltaic Solar Energy Conference*, 2007.
- [152] Anke Helbig, Thomas Kirchartz, Raymund Schaeffler, Jürgen H. Werner, and Uwe Rau. Quantitative electroluminescence analysis of resistive losses in Cu(In,Ga)Se<sub>2</sub> thin-film modules. *Solar Energy Materials & Solar Cells*, 94:979–984, 2010.
- [153] Christian Kramer. Ortsaufgelöste Messung elektrischer Kenngrößen von Dünnschichtsolarzellen. Master’s thesis, Hochschule für Technik, Wirtschaft und Kultur Leipzig, 2013.
- [154] Chih-Liang Wang, Wen-Chieh Shih, Chia-Hsiang Chen, Yi-Chang Chen, Song-Fu Hong, Chih-Pin Tsai, Yung-Chung Wu, and Chih-Huang Lai. Enhanced Reliability of Molybdenum by Al Doping after Damp-Heat Exposure for CIGS Solar Cells. *Proceeding of the 35<sup>th</sup> IEEE Photovoltaic Specialists Conference*, 2010.
- [155] C. A. Kaufmann, D. Greiner, S. Harndt, R. Klenk, S. Brunken, R. Schlatmann, M. Nichterwitz, H.-W. Schock, T. Unold, K. Zajac, S. Brunner, F. Daume, C. Scheit, S. Puttnins, A. Braun, A. Rahm, R. Wuerz, F. Kessler, M. Guenther, M. Pscherer, S. Ihlow, G. Motz, H. Morgner, R. G. Schmidt, A. Lambrecht, J. T. Grundmann, P. Spietz, and P. Schülke. Flexible Cu(In,Ga)Se<sub>2</sub> thin film solar cells for space applications – recent results from a german joint project (PIPV2). In *Proc. of the 29<sup>th</sup> European Photovoltaic Solar Energy Conference*, 2014.
- [156] Alexander Koch. Vergleich von verschiedenen Defektuntersuchungsmethoden an Cu(In,Ga)Se<sub>2</sub>-Solarzellen am Beispiel einer Variation des Galliumgehaltes, 2011. Bachelorarbeit, Ernst-Abbe-Fachhochschule Jena.
- [157] Oliver Leutert. Charakterisierung Damp Heat behandelter Cu(In,Ga)Se<sub>2</sub> Dünnschichtsolarzellen, 2012. Bachelorarbeit, Ernst-Abbe-Fachhochschule Jena.
- [158] Lisa Paller. Drive-Level Capacitance Profiling on Cu(In,Ga)Se<sub>2</sub>-based Thin Film Solar Cells. Master’s thesis, Universität Leipzig, 2014.

## Abbreviations & Symbols

$\eta$	efficiency [%]
$A$	area [cm <sup>2</sup> ]
$db$	ratio of gallium to group three elements: $db = \frac{Ga}{In+Ga}$
$dk$	ratio of the cations: $dk = \frac{Cu}{Ga+In}$
$ds$	selenium deficiency: $ds = \frac{2Se}{3(Ga+In)+Cu} - 1$
$FF$	fill factor
$I_{SC}$	short circuit current [mA]
$J_0$	dark saturation current density [mA/cm <sup>2</sup> ]
$J_{MPP}$	current density at maximum power point [mA/cm <sup>2</sup> ]
$J_{Ph}$	photo current density [mA/cm <sup>2</sup> ]
$J_{SC}$	short circuit current density [mA/cm <sup>2</sup> ]
$n$	diode ideality
$P_{MPP}$	electric power at maximum power point [W]
$P$	electric power [W]
$P_{opt}$	power of the illumination at the solar cell [W]
$R_P$	parallel (shunt) resistance [ $\Omega$ cm <sup>2</sup> ]
$R_S$	series resistance [ $\Omega$ cm <sup>2</sup> ]
$T_{NaF}$	temperature of the NaF crucible [°C]
$V_{MPP}$	voltage at maximum power point [V]
$V_{OC}$	open circuit voltage [V]

## *Abbreviations & Symbols*

---

AC	alternating current
ALT	accelerated lifetime testing
CdS	cadmium sulfide
CdTe	cadmium telluride
CGSe	$\text{CuGaSe}_2$
CIGSe	$\text{Cu(In,Ga)Se}_2$
CIGSSe	$\text{Cu(In,Ga)(S,Se)}_2$
CISE	$\text{CuInSe}_2$
CV	capacitance–voltage measurements
DC	direct current
DH	damp heat
DLIT	dark lock–in thermography
EL	electroluminescence
ITO	indium tin oxide
IR	infrared
IV	current–voltage measurement
ILIT	illuminated lock–in thermography
i-ZnO	intrinsic zinc oxide
LBIC	light beam induced current
LED	light–emitting diode
LIBS	laser induced breakdown spectroscopy
LIT	lock–in thermography
ODC	ordered defect compound (also denoted as “OVC”, ordered vacancy compound)
PV	photovoltaics



---

SIMS secondary ion mass spectrometry  
SEM scanning electron microscopy  
TLM transfer length measurement  
TCO transparent conductive oxide  
XRF X-ray fluorescence  
ZnO:Al aluminum doped zinc oxide



# List of Figures

1.1	Band diagram of a pn-junction . . . . .	3
1.2	Market share of different solar cell technologies in 2011 . . . . .	4
1.3	Thin film technologies . . . . .	5
1.4	Equivalent circuit – ideal solar cell . . . . .	6
1.5	Equivalent circuit – real solar cell . . . . .	7
1.6	Influence of $R_S$ and $R_P$ on the IV characteristic . . . . .	7
1.7	Determination of IV parameters . . . . .	8
1.8	Solarion CIGSe solar cell . . . . .	9
1.9	Chalcopyrite crystal structure and phase diagram . . . . .	12
1.10	Absorption coefficients . . . . .	15
1.11	Phase diagram Na–Se . . . . .	18
2.1	Parameters of the cost competitiveness of electricity from PV . . . . .	21
2.2	Degradation rates of CIGSe solar cells . . . . .	25
2.3	Band diagram CIGSe solar cell before and after damp heat . . . . .	36
2.4	$V_{OC}$ vs. bulk defect density before and after damp heat . . . . .	37
3.1	Solarion roll-to-roll process . . . . .	39
3.2	Photograph and SEM cross section of a Solarion solar cell . . . . .	40
3.3	Solarion solar cell contacted for IV measurement . . . . .	41
3.4	Simulation of the EL intensity $\phi_{EL}$ vs. T & V . . . . .	44
3.5	TLM method . . . . .	48
3.6	Sample holders for in-situ IV under damp heat . . . . .	52
4.1	Damp vs. dry heat treatment . . . . .	54
4.2	Damp heat IV statistics . . . . .	55
4.3	Example of IV curves vs. damp heat time . . . . .	56
4.4	Low temperature IV measurements after damp heat . . . . .	57
4.5	Solar cell equivalent circuit with additional blocking diode . . . . .	57
4.6	Roll-over resistance . . . . .	58
4.7	Net doping vs. sodium content . . . . .	59
4.8	CV measurements vs. damp heat . . . . .	60
4.9	In-situ IV curves under damp heat . . . . .	61
4.10	$V_{OC}$ & $J_{SC}$ vs. DH from in-situ measurement . . . . .	62

4.11	FF & efficiency vs. DH from in-situ measurement . . . . .	63
4.12	Two stages of aging . . . . .	65
4.13	Linear fit of degradation rate . . . . .	66
4.14	DH degradation rates from in-situ IV measurements . . . . .	67
4.15	Molybdenum – TLM short damp heat . . . . .	69
4.16	Molybdenum – TLM extended damp heat . . . . .	70
4.17	Hall measurements – molybdenum . . . . .	71
4.18	TCO – TLM short damp heat . . . . .	72
4.19	TCO – TLM extended damp heat . . . . .	73
4.20	Hall measurements – TCO . . . . .	74
5.1	Sodium content from LIBS . . . . .	77
5.2	Fit of sodium content from LIBS . . . . .	78
5.3	SEM images from process 2A-1173 (cross section) . . . . .	79
5.4	SEM images from process 2A-1173 (top view) . . . . .	80
5.5	SEM images from process 2A-1209 (top view) . . . . .	81
5.6	SEM comparison before & after DH from process 2A-1209 (cross section) . . . . .	82
5.7	SEM comparison before & after DH from process 2A-1209 (top view) . . . . .	83
5.8	IV parameters vs. DH exposure for two sodium contents . . . . .	85
5.9	$R_S$ vs. DH exposure for two sodium contents . . . . .	86
5.10	IV vs. sodium (DH) . . . . .	87
5.11	IV vs. DH (sodium) . . . . .	88
5.12	IV optimization of the sodium content . . . . .	91
5.13	Na content from LIBS (post-deposition) . . . . .	93
5.14	$V_{OC}$ , $J_{SC}$ , $FF$ vs. DH (Na post-deposition) . . . . .	94
5.15	efficiency, $R_S$ , $R_P$ vs. DH (Na post-deposition) . . . . .	95
5.16	Elemental depth profiles (SIMS) . . . . .	97
5.17	Integral Na content from SIMS . . . . .	99
5.18	Scanning laser microscopy of solar cell surface . . . . .	100
5.19	Roughness of sample surface . . . . .	102
6.1	EL vs. damp heat (batch 2A-1173, Na 0.52×) . . . . .	105
6.2	EL vs. damp heat (batch 2A-1173, Na 11.33×) . . . . .	105
6.3	EL before damp heat (batch 2A-1225) . . . . .	106
6.4	EL after 50 h of damp heat (batch 2A-1225) . . . . .	106
6.5	EL vs. sodium vs. damp heat (batch 2A-1209) . . . . .	108
6.6	Images of a solar cell with a shunt . . . . .	110
6.7	Images of a solar cell with a severe shunt . . . . .	112
6.8	Images of a solar cell with a corroded area . . . . .	114
6.9	Voltage dependant electroluminescence images . . . . .	115
6.10	$R_S$ -mapping from Hinken’s method . . . . .	116

6.11	$R_S$ -mapping from Breitenstein's method . . . . .	116
6.12	$J_0$ -mapping from Breitenstein's method . . . . .	117
6.13	EL image after damp heat for $R_S$ mapping . . . . .	118
6.14	$R_S$ -mapping from Breitenstein's method after damp heat . . . . .	118
6.15	$J_0$ -mapping from Breitenstein's method after damp heat . . . . .	118
7.1	Hypothesis about $V_{OC}$ increase . . . . .	129
7.2	Lifetime vs. Degradation Rate . . . . .	131
7.3	Lifetime vs. Lifetime Limit . . . . .	131
7.4	$R_S$ -mapping histogram . . . . .	141
7.5	$R_S$ -mapping line scan . . . . .	142



## List of Tables

1.1	Champion efficiencies of different solar cell technologies . . . . .	6
1.2	Point defects in CISE . . . . .	13
1.3	Energetic depth of point defects in CISE . . . . .	14
2.1	Module degradation rates . . . . .	22
2.2	Failure modes of CIGSe PV . . . . .	24
3.1	Measurement conditions for IV sweeps . . . . .	42
3.2	Measurement parameters for LIT . . . . .	46
3.3	Measurement conditions for LIBS . . . . .	51
4.1	Solar cell degradation rates . . . . .	68
5.1	Sodium content from LIBS measurements . . . . .	76
5.2	Samples of sodium experimental batch 2A-1173 . . . . .	84
5.3	Samples of sodium experimental batch 2A-1225 . . . . .	86
5.4	Samples of sodium experimental batch 2A-1209 . . . . .	89
5.5	Samples of sodium (post-deposition) experimental batch 2A-1234 . . . . .	92
5.6	Surface mean square roughness of samples from batch 2A-1209 . . . . .	101
A.1	Overview of stoichiometry of all samples . . . . .	154
A.2	Overview of IV parameters of all samples . . . . .	155





# Acknowledgement

Mein erster Dank gilt Professor **Dr. Marius Grundmann**, meinem Doktorvater, und **Dr. Andreas Rahm**, meinem langjährigen Chef und Betreuer innerhalb der *Solarion AG*. Durch die Erarbeitung dieser Dissertation in einer Firma war ich ein Wandler zwischen zwei Welten: einerseits die Kolleginnen und Kollegen in Forschung, Entwicklung und Produktion bei der *Solarion AG* und andererseits die universitäre Arbeitsgruppe Halbleiterphysik um Professor Grundmann an der *Universität Leipzig*. Beiden Arbeitsgruppen möchte ich für viele Jahre kollegiale und ausgezeichnete Arbeitsatmosphäre danken.

Namentlich möchte ich folgenden Personen für Ihre Unterstützung meiner Arbeit danken:

- **Lars Hartmann** für seine Hilfe bei Probenpräparationen und Messungen aller Art, für unzählige hilfreiche Diskussionen und die Unterstützung bei allen großen und kleinen Problemen im Doktorandenalltag
- **Lisa Paller** für die Messung (IV) und Auswertung der Proben aus Prozess 2A–1234 sowie **Marcel Hartung**, **Oliver Leutert** und **Hendrik Schmidt** für ihre Messungen (DLIT, IV, LBIC) an Proben aus Prozess 2A–1225
- **Mirjam Theelen** für die Zusammenarbeit und viele wertvolle Diskussionen zum Thema CIGSe Degradation sowie gemeinsam mit **Henk Steijvers** für gemeinsame in-situ Messungen von Degradationsraten bei *TNO* in Eindhoven
- **Fabian Klüpfel**, **Dr. Kerstin Brachwitz**, **Daniel Splith**, **Michael Bonholzer** und **Dr. Holger von Wenckstern** für ihre Unterstützung bei Messungen (Hall, 3D-Mikroskopie) an der *Universität Leipzig*
- **Dietmar Hirsch** vom *IOM* in Leipzig für SEM und SIMS Messungen
- **Dr. Iver Lauer** und **Dr. Alexander Grimm** für gemeinsame Messungen am *BESSY* in Berlin
- **Dr. Heiko Kempa** und **Dr. Helmut Herrnberger** für hilfreiche Diskussionen und gute Ratschläge
- Meinen Doktorandenkollegen **Dr. Hendrik Zachmann**, **Dr. Christian Scheit**, **Stefan Puttnins**, **Annegret Reithe**, **Christian Guhr** und **Stefan Ribbe** für viele hilfreiche Diskussionen und zahlreiche heitere Situationen im Büro

- Den von mir bei der *Solarion AG* betreuten Studenten **Marco Augustin**, **Agnes Holtz**, **Robert Karsthof**, **Alexander Koch** [156], **Christian Kramer** [153], **Oliver Leutert** [157], **Lisa Paller** [158], **Thorsten Schultz** und **Megan Tsai**, durch deren Neugier, Fragen und Sichtweisen ich viel gelernt habe
- **Dr. Alexander Braun** und **Dr. Karsten Otte** für deren Einsatz für die Firma *Solarion AG* und damit den finanziellen Rückhalt für meine Arbeit.

Außerdem bedanke mich beim gesamten Team der *Solarion AG* für Ihre Mitwirkung an der Herstellung der untersuchten Solarzellen.

Für das Korrekturlesen des Manuskriptes dieser Dissertation gilt mein besonderer Dank **Dr. Andreas Rahm**, **Dr. Heiko Kempa**, **Lars Hartmann**, **Lisa Paller** und **Anne Schrader**.

Bei meiner Freundin **Tina**, meinen Eltern **Maritta** und **Ludwig**, sowie meinen Freunden und meiner gesamten Familie möchte ich mich herzlich für ihre Unterstützung bedanken. Sie haben mir den Rücken frei gehalten, mich im richtigen Maß von der Arbeit abgelenkt und zu den richtigen Zeitpunkten motiviert. Ohne sie wäre ich nicht so weit gekommen. Danke!

# Curriculum Vitae

## Personal Information

Name Felix Daume  
Date of birth 6.2.1984  
Place of birth Leipzig, Germany

## Education & Scientific Activities

1990–1994 Primary school  
1994–2002 High school  
(Gymnasium Neue Nikolaischule Leipzig)  
June 2002 Abitur  
2003–2009 Studies of physics at Universität Leipzig  
2006–2007 Studies of physics at Kent State University (Ohio, USA)  
2007 International summer school program at Hahn–Meitner–  
Institut Berlin (“Photoluminescence measurements on  
Cu(In,Ga)Se<sub>2</sub> solar cells”, advisor: Dr. Thomas Unold)  
2008 DAAD Taiwan summer institute program (internship at  
National Taiwan Normal University in Taipei, Taiwan)  
2008–2009 Diploma thesis “Die elektrische Charakterisierung des  
Absorbers Cu(In,Ga)Se<sub>2</sub> von flexiblen Solarzellen (und  
Korrelation mit Materialparametern)”  
(semiconductor physics group of Prof. Grundmann at  
Universität Leipzig, industrial partner: Solarion AG)  
2009 International summer school on photovoltaics and new  
concepts of quantum solar energy conversion “Quantsol”  
in Hirschegg, Austria  
November 2009 Diploma in physics  
since 2010 R&D employee at Solarion AG  
2010–2014 PhD student at Universität Leipzig  
(thesis advisor: Prof. Grundmann),  
since 2011 Member of the graduate school BuildMoNa



# Selbstständigkeitserklärung

Hiermit versichere ich, dass

- die vorliegende Arbeit ohne unzulässige Hilfe und ohne Benutzung anderer als der angegebenen Hilfsmittel angefertigt wurde und dass die aus fremden Quellen direkt oder indirekt übernommenen Gedanken in der Arbeit als solche kenntlich gemacht wurden;
- alle Personen genannt wurden, von denen ich bei der Auswahl und Auswertung des Materials sowie bei der Herstellung des Manuskripts Unterstützungsleistungen erhalten habe;
- außer den genannten keine weiteren Personen bei der geistigen Herstellung der vorliegenden Arbeit beteiligt waren, insbesondere nicht die Hilfe eines Promotionsberaters in Anspruch genommen wurde und weitere Personen von mir oder meinem Auftrag weder unmittelbar noch mittelbar geldwerte Leistungen für Arbeiten erhalten haben, die im Zusammenhang mit dem Inhalt der vorgelegten Dissertation stehen;
- die vorgelegte Arbeit weder im Inland noch im Ausland in gleicher oder in ähnlicher Form einer anderen Prüfungsbehörde zum Zwecke einer Promotion oder eines anderen Prüfungsverfahrens vorgelegt und in ihrer Gesamtheit noch nicht veröffentlicht wurde.

Leipzig, den 30. Januar 2015

---

FELIX DAUME